COOLED TURBINE TIP DESIGN: AERÓTHERMAL OPTIMIZATION FOR ENGINE TRANSIENTS

by

Valeria Andreoli

A Dissertation

Submitted to the Faculty of Purdue University

In Partial Fulfillment of the Requirements for the degree of

Doctor of Philosophy

School of Mechanical Engineering

West Lafayette, Indiana

August 2019

THE PURDUE UNIVERSITY GRADUATE SCHOOL
STATEMENT OF COMMITTEE APPROVAL

Dr. Guillermo Paniagua, Chair

School of Mechanical Engineering

Dr. Daniel DeLaurentis

School of Aeronautics and Astronautics

Dr. Tomas Grönstedt

Chalmers University of Technology

Dr. Neera Jain

School of Mechanical Engineering

Dr. Tom Shih

School of Aeronautics and Astronautics

Dr. Matthew Bloxham

Rolls-Royce Corporation

Approved by:

Dr. Jay Gore

Head of the Graduate Program

ACKNOWLEDGMENTS

I want to thank Prof. Paniagua for being one of the most inspired and inspiring Professors I have ever met. His love for science and passion for teaching are what lead me to and helped me stayed motivated through my Ph.D. I will never forget the wisdom, the knowledge, the experience (and the crazy ideas) that he shared with me in these years. I would like to thank the members of my Committee for the feedback and suggestions that helped me to transform ideas into the work you are about to read. This path would not have been possible without the support of Rolls-Royce Indianapolis. Through our partnership, I have been privileged to work with the most talented engineers, and I grew up technically and personally through these interactions.

This journey has been a great experience thanks to my team, the current, past, and future PETAL team that I am part of, and that is part of me. I learned so much from each of you, in all the good, funny, stressed moments. I know that today I see things differently from the beginning, and it is thanks to each of you. I am sure that we are PETAL today, and we will feel PETAL for life.

In particular James has been through this with me since day 1, and of course, he would be angry if I do not dedicate him at least a paragraph in this section. He is the most genuine, wild mind I have ever had the privilege to know. He has the power to make everything sound like a new exciting adventure, and he always managed to make me feel better about every technical or personal issue.

The Ph.D. struggle has been much less, thanks to all the magnificent ladies that I met through the Women in Engineering Program. GWEN has made my weeks, months, and years better and better, and I met inspiring women and great friends for life. I would like to thank all my VKI friends, even though our paths departed, you are still with me in everything I do. A particular acknowledgment goes to Sergio who taught me a lot of the things that I know today and Cis who will never recognize it but has always been a mentor to me. I would like to thank all my friends, who had to get used never to see me, and always have late replies from me. I may not be the most present person, but my heart is always with you.

I would of course not be here without the love and sacrifices of my family. My grandparents, uncles and aunts, my cousins and my in-law family are my first fans, my biggest supporters. Even though we are far, every time I see them, I feel that sense of belonging like if time had never passed. My parents made me the person I am today, through their teaching but most of all, through their example. They showed me that no matter how hard a challenge is, there is nothing that could not be achieved with hard work and the right attitude. They taught me that before being a good scientist, what really matters it is to be a good person, and this motivates me to stay true to myself wherever I go. I would like to thank Alessandro, my little brother, who has always been my big brother. In many occasions, you were way wiser than I was, and if it were not for you I would probably not be here. Becoming someone you could be proud of has always motivated me through my path, even though our roads lead us apart. Spending some moments with you, even if in between flights and only for some hours, is the biggest joy of my life.

I finally want to thank David; I waited so long before writing this section so that I can finally call you my husband. You are the best person in this world; there is no other way to describe you. I wish one day you could see yourself through my eyes and understand how deeply you marked my path. This achievement is mine but is actually also yours. Thanks for choosing to be in my life.

TABLE OF CONTENTS

LIST OF TABLES

LIST OF FIGURES

NOMENCLATURE

A	Area [m^2]
a	Speed of sound [m/s]
CFD	Computational fluid dynamics
c_{ax}	Axial chord [m]
C_P	Heat capacity [kg m^2/K s^2]
DGF	Discrete Green's Function
DoE	Design of experiments
G	Discrete Green's function matrix
G^{-1}	Inverse Discrete Green's function matrix
g	Green's function coefficient
h	Convective heat transfer coefficient [W/m^2-K]
k	Thermal Conductivity [W/m-K]
L	Characteristic length
LE	Leading edge
M	Mach number ($M = V/a$)
$\dot{m}$	Mass flow [kg/s]
Nu	Nusselt number [-]
P	Pressure [Pa]
PS	Pressure side
PSP	Pressure Sensitive Paint
Q	Heat flux [W/m^2]
RANS	Reynolds average Navier-Stokes

Re	Reynolds number ($Re = \rho VL/\mu$)
RPM	Shaft rotational speed [rpm]
SS	Suction side
SST	Shear stress transport
T	Temperature [K]
TE	Trailing edge
V	Absolute velocity [m/s]
W	Relative velocity [m/s]
y^+	Non-dimensional first cell height
z	Axial coordinate [m]

Greek symbols

β	Relative flow angle ($\tan^{-1}(W_t/V_z)$
γ	Heat capacity ratio
τ	Torque [Nm]
ω	Shaft rotational speed [rad/s]
ρ	Density [kg/m^3]
η	Efficiency
μ	Dynamic viscosity [Ns/m^2]

Subscripts

0	Total
1	Plane 1 (Vane inlet)

2	Plane 2 (Vane exit)
3	Plane 3 (Rotor exit)
01,02,03	Total quantity at vane inlet, vane exit, rotor exit
0r	Total relative quantity
adiabatic	Adiabatic
aw	Adiabatic wall
cool	Coolant
exp	Experiment
i,j	Indices for Green's function matrix
inlet	Inlet
leakage	Over-tip leakage
norm	Normalized
passage	Passage
ref	Reference value
rel	Relative
s	Static
tip	Tip
vane	Vane
rotor	Rotor

ABSTRACT

Author: Andreoli, Valeria. PhD
Institution: Purdue University
Degree Received: August 2019
Title: Cooled Turbine Tip Design: Aerothermal Optimization for Engine Transients
Committee Chair: Guillermo Paniagua

The current doctoral dissertation addresses the optimization of cooled high-pressure turbines during the aircraft mission. To comply with the ambitious targets set by ACARE 2050, the overall propulsive system should be optimized along the trajectory. Hence, a global model of the engine is needed to quantify the overall engine performance and select the optimal turbine along the trajectory, which highlights the interconnection between optimization and engine modeling. The detailed analysis of the turbine components is however vital to analyze the aerothermal phenomena. This thesis presents optimal cooled turbine tip designs that demonstrate a superior performance during an entire engine transient. The improvement of efficiency is obtained by optimizing the shape of the cooled turbine tip, considering all the phenomena associated with clearance variations. Optimal turbine blade tip designs not only enhance the aerodynamic performance, but they also reduce the thermal loads on one of the most vulnerable parts of the gas turbine. A multi-objective optimization was performed using a differential evolution strategy and Computational Fluid Dynamics software to solve Reynolds-Averaged Navier-Stokes equations. The results showed the strong impact of the over-tip coolant flows on the over-tip flow field. A detailed model for the scaling of tip convective heat flux based on Green's functions was developed to predict the overtip heat flux at various gaps and engine conditions. The turbine aerothermal models integrated with the mathematical model of the entire engine were used to assess the effect of an improved turbine design on the overall gas turbine performance. Finally, this thesis proposes an experimental approach to validate the numerical models of the turbine aerothermal performance. This experimental procedure relies on an extensive computational analysis which resulted in the development of an unprecedented facility. This new facility, built at Purdue University, will be extensively used to evaluate transients with ad-hoc instrumentation designed using CFD. This work proposes a methodology to extrapolate the experimental results to engine conditions, in terms of aerothermal performance focusing on tip flow.

CHAPTER 1. INTRODUCTION

1.1 Background

During recent years, the dynamic analysis of jet engines has become key to the design and optimization of future engines [1]. Compared to steady-state simulations, the modeling of engine transients presents additional challenges [2]. Critical features to be modeled are:

- Variation of tip clearance in response to changes in terms of mechanical and thermal loads.
- The transient heat transfers due to variations in flow and metal temperatures.
- Change of coolant ratio during a transient.

These effects become even more relevant when dealing with compact engines [3]. The rotating blades are smaller, however, the running gap between stationary and moving parts cannot be miniaturized beyond a certain level. Therefore, the resulting relative size of the gap is higher than in conventional engines. Because the area-to-volume ratio increases, the heat transfer is enhanced, which requires a precise estimation. It has been shown how scaling down an engine significantly impacts component efficiencies and cooling requirements [4].

In high-pressure turbines, the gap between the casing and the rotor tip, called tip gap, is responsible for about 1/3 of the energy loss [5]. The optimization of the turbine tip geometry offers wide potential to improve the performance of the turbine stage and as a result the specific fuel consumption of the entire gas turbine. Results in the literature [6] show that an increase of 0.001" in the tip clearance, causes an increase of 0.1% of SFC. The trend becomes even more relevant for transients of military aircraft, where maneuvers are even more abrupt, and the engine conditions are extreme. Kawecki [7] indicates that the High-Pressure Turbine (HPT) is the component where we can observe the most significant impact of the variation of clearance in terms of performance. Furthermore, the turbine tip surface is subjected to high levels of heat transfer, which limit the operational life of the component [8]. The increase of tip clearance in high-pressure turbines has been proven to be one of the major contributors to the degradation of engine performance [9].

To constrain the over-tip flow different solutions can be proposed. Shrouded turbines demand special cooling and result in high stresses to the blade root [10]. Unshrouded rotor designs such as flat tips and squealer-like geometries are less constrained from thermal or mechanical stresses but penalize the rotor aerodynamic performance. Alternative designs, such as winglets, can increase efficiency [11] but suffer from increased cooling demands [12].

The turbine overtip flow is characterized by tight clearances, with pressure gradients counterbalanced by viscous effects. Hence, non-dimensional analysis based on the boundary layer is inadequate and therefore, the use of an adiabatic wall temperature is questionable. Hence, the complex heat transfer requires a detailed analysis which cannot be expressed using the classical Newton heat convection approach. An alternative approach to predict the convective heat transfer problem across the turbine rotor tip is offered by Discrete Green's Functions, applying linearity of the energy equation in the solid domain with constant thermal properties. The Discrete Green Function is a matrix of coefficients that relate the increment of temperature observed in a surface with the heat flux integrated on the same surface. The coefficients are calculated using the temperature response of the cell to a heat flux pulse imposed at different locations, relying on the superposition principle.

1.2 Research Objectives

The aim of this work is organized into a primary objective and three secondary objectives.

- The main aim is the development of a dynamic model of compact engines to evaluate the turbine performance during the transient.

The three secondary objectives are:

- The aerothermal optimization of a cooled turbine tip over a given trajectory. This objective includes the development of tools to analyze the performance of a high-pressure turbine during transient operation. The analysis will consider the variation of clearance, and cooling requirements during a transient.
- The development of models based on Green's Functions to retrieve rotor tip convective heat flux. When dealing with tight clearances, the traditional models of convective heat flux fails. Hence, we must build models that are scalable for various inlet conditions and values of tip gap.
- The development of experimental procedures for future validation of the dynamic engine model. This objective includes methods to validate the turbine performance prediction, the heat flux calculations and the model of the turbine component.

1.3 Research Methodology

To achieve the objectives of this work, the following research strategy is adopted:

Aerothermal optimization of the tip shape for a cooled high-pressure turbine.

The first step is the development of an optimization methodology for a fixed clearance and for a given cooling configuration. The tip shape will be parametrized to design a number of rims, with arbitrary shape. For each rim configuration, the code will build the associated fluid domain, mesh it, and solve it with RANS simulations. This procedure will give a set of optimized tips, for a given flight condition.

The second step of the procedure is an analysis of the “robustness” of the design to inlet flow and geometrical parameters. This study will indicate how the performance enhancements hold when, simulating a real flight trajectory, we perturb the turbine cooling and the clearance.

The third step is the optimization of the tip shape considering the variability of the tip clearance during an engine transient. A set of tip clearance will be identified, based on a collocation method, and multiple CFD simulations in these points will be run. The procedure will give tip geometries that perform optimally not in a single point but over the entire envelope. These sections are based on numerical tools, specifically RANS-based CFD.

Scalable models of rotor heat flux

In conventional models for convective heat transfer, the local heat flux is expressed as a linear function of the local wall and adiabatic wall temperature (or inlet total temperature). This local approach does not account for all the physics phenomena when dealing with complex flows.

The first step of this section is to derive a methodology, based on Green’s Functions, that is suitable to model the heat flux in tight gaps. The blade tip and casing are subdivided into small elements where heat pulses are individually applied. Through numerical simulations based on RANS, the response of the walls in terms of heat flux is derived and assembled into a matrix.

The second step is to summarize the results into a matrix that will indicate how much the temperature in a single element affect the entire domain, and not only the element itself like in the traditional approach. This calculation will be repeated for multiple clearances to identify the dependence of the Green’s Function matrix on the value of clearance.

The third step is to investigate how the matrix scales when the turbine conditions are varied, and when the clearance changes. Several corrections for the matrix elements based on the wall temperature will be considered.

<u>Evaluate a compact engine during a transient.</u>

The first step of the engine analysis is the selection of the modeling strategy, the engine baseline, and the trajectory. A compact turbojet with a single shaft is designed, in order to isolate the effect of the turbine performance.

The second step is to integrate the modeling of the following modules into the T-MATS environment:

- Calculation of turbine performance in function of tip clearance, operating point, inlet conditions. The module implements the calculation of the turbine map, based on these inputs.
- Calculation of convective heat flux in function of tip clearance, cooling effectiveness, inlet temperature. This module is based on the scaling of the Green's Function matrices.
- Simulation of the thermomechanical behavior of the components. This component allows retrieving the deformations of casing, rotor and blades and the consequent change in clearance.

The last step is to connect these three calculation blocks to the turbine component in the engine model and to couple the model with an iterative Newton-Raphson solver to simulate the engine performance over a transient.

After the numerical simulations of the engine transient, we will propose the design of an experiment in a new turbine facility at Purdue University [13] to validate the numerical predictions. A numerical model of the wind tunnel was developed, to model the experiments with the same approach used for the engine transient.

Efforts are dedicated to the selection of the experimental setup, to validate CFD. The experiment would allow to identify the flow features and verify that the CFD correctly predicts them. The work proposes a strategy for the measurements of tip flow topology in a cascade, considering the effect of the relative motion between blade and casing.

The last step is to add considerations for future experimental validation of the Green's function approach, assessing the uncertainty of the methodology, when associated with experimental measurement.

Figure 1.1 shows a summary of the proposed research methodology.

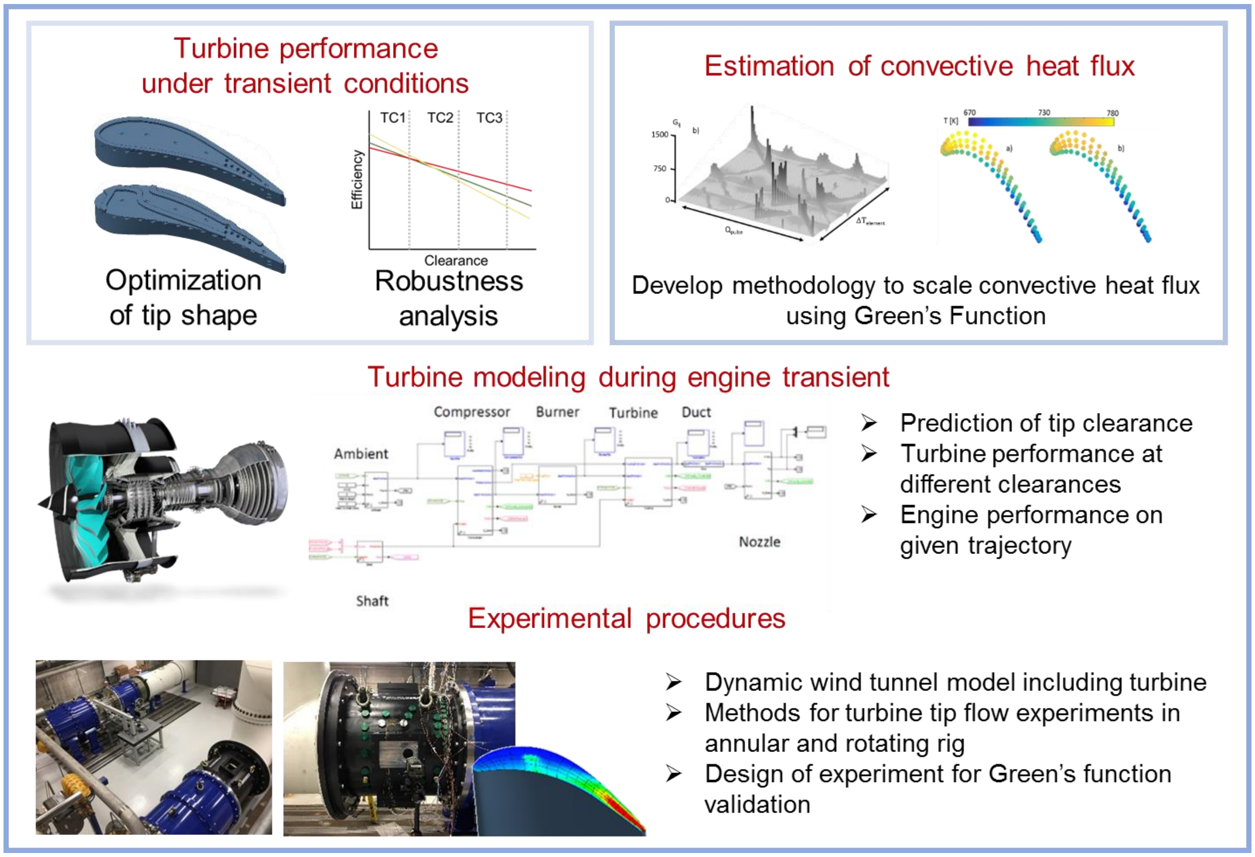

Figure 1.1: Summary of the methodology

1.4 Thesis Outline

This research proposal has been divided into three chapters, following the logic of the methodology:

- Chapter 2: this chapter explains the methodology and the results of the tip optimizations, and the robustness analysis. Detailed analysis of tip loss mechanism in optimal tips is presented, with quantification of leakage flow and its effect on the losses breakdown and an assessment of the effect of cooling.

- Chapter 3: shows the theoretical background, the methodology and the results of the calculation of convective heat flux based on Green's Function approach. A simple test case will be presented to demonstrate the method, which will then be applied to the turbine tip case. The final section will describe the scaling with tip gap and inlet flow.
- Chapter 4: will show the strategy for the implementation of the system modeling, based on the conclusions of the previous two chapters. The modules will be included in a transient engine model, whose structure will be described. The chapter will first present a steady analysis of the engine sensitivity to turbine tip variations and will then move to the transient analysis of the engine performance in a deceleration-reacceleration trajectory.
- Chapter 5: the last chapter will summarize the main conclusions, highlighting the results from each chapter and their connections.

CHAPTER 2. TIP DESIGN FOR TRANSIENTS OF HIGH-PRESSURE TURBINES

2.1 Tip Flows in High-Pressure Turbines

Numerous experimental and numerical studies have shown the effect of the tip gap on heat flux and efficiency of unshrouded turbines. The nature of the flow within the tip gap can be transonic or even feature complex supersonic shock structures [14] depending on the running clearance [15]. When the clearance is relatively large, the flow distribution in the over-tip gap is conventional, with flow passing from pressure to suction side. At tight clearances, however, viscous effects dominate, and the profile is divided into several inlet and outlet regions. Consequently, tailored strategies to reduce the tip losses must be adapted to the configuration and running conditions.

In the past few years, this approach has motivated numerous researchers to optimize the turbine tip shape to enhance rotor aerothermal performance [16]. De Maesschalck et al. documented a reduction in the over-tip heat flux using carved geometries, and more recently, three-dimensional optimization of uncooled tip geometries with special squealer designs showed significant benefits in terms of heat flux and efficiency [17]. The decrease in heat flux and increase in efficiency was due to a change of the flow field within the tip gap region. The authors above used evolutionary optimization algorithms to retrieve geometries in a timely manner.

Additionally, the operating conditions of modern high-pressure turbines often require dedicated airfoil cooling. As turbine inlet temperatures continue to rise, the judicious usage of coolant flow becomes vital [18]. However, this coolant flow will interact significantly with the tip gap flow [19]. Hence, it is essential to optimize the tip structures with all relevant coolant feeds also modeled [20].

The main contributions to unshrouded turbine losses due to tip flows are:

- Potential flow due to the pressure gradient. The difference between high pressure on the pressure side and low pressure on the suction side drives the flow across the overtip region. This potential flow can be modeled for simplified geometries knowing the tip gap area, and the local discharge coefficient.
- Boundary layer in blade and shroud: due to the small size of the tip gap, a proper definition of the boundary layer may not be straightforward. The establishment of the boundary layer

and separations can cause acceleration and deceleration regions that affect the velocity profile in the entire gap.

- Scraping vortex due to viscous effect. The velocity profile close to the wall is twisted due to relative motion between blade and wall. The shear-induced by this motion causes scraping vortices that rotate in the opposite direction of the tip leakage vortex.

A description of tip losses mechanism is provided by Denton [21] for shrouded and unshrouded rotor blades. Bindon [22] explains how the quantity of leakage flow alone is not sufficient to explain the tip losses, providing a breakdown of the losses (tip, mixing and secondary) based on traverse measurement in a turbine cascade.

A total number of 10 RANS CFD simulations were run to characterize the effect of tip gap on the tip leakage and rotor performance. The simulations were performed with FINE/Turbo, a solver that will be described and validated in the Appendix. Different sets of boundary conditions were used to assess the dependency of the flow characterization on the wall condition.

Most of the analysis available in the literature focuses on medium to large tip gaps, which are investigated with either numerical tools or in annular cascades neglecting the blade rotation. These studies conclude that the viscous effects are confined in a very small region close to the casing, and that most of the flow field is dominated by the pressure gradient. In large gaps, the typical tip flow will enter on the pressure side and move with a constant angle towards the suction side. The air starts flowing over the pressure side, where a small recirculation bubble starts to develop due to the large gap. The flow reattaches right after the bubble, and then migrates with constant angle towards the suction side. These characteristics can be observed in the Mach number contours in Figure 2.1, which shows the tip flow topology is depicted in a plane aligned with the tip flow direction. Three tip gaps (0.55, 1.0 and 1.45%) are shown. On the top, there is a representation of the Mach number in the entire tip gap from PS to SS. We can clearly see how the flow accelerates from a low Mach number on the PS to a higher one on the SS, but in this case still lower than the Mach number of the main flow close to the top portion of the blade suctions side (colored in orange/light red in the contours). Below, there is a zoom on the pressure side region, to better highlight the flow entrance area and the separation bubble. It can be noticed that when the gap is small, on the left column, there is almost no recirculation bubble. As the distance between blade and casing increases, the bubble starts growing till occupying approximately 20% of the gap in the radial direction. As the recirculation region grows in height, it also grows in length, pushing the reattachment line further away from the pressure side. On the bottom of Figure 2.1, the isolines of Mach number are added to the contour. This allows visualizing the effect of the recirculation bubble on the acceleration profile of the overtip flow.

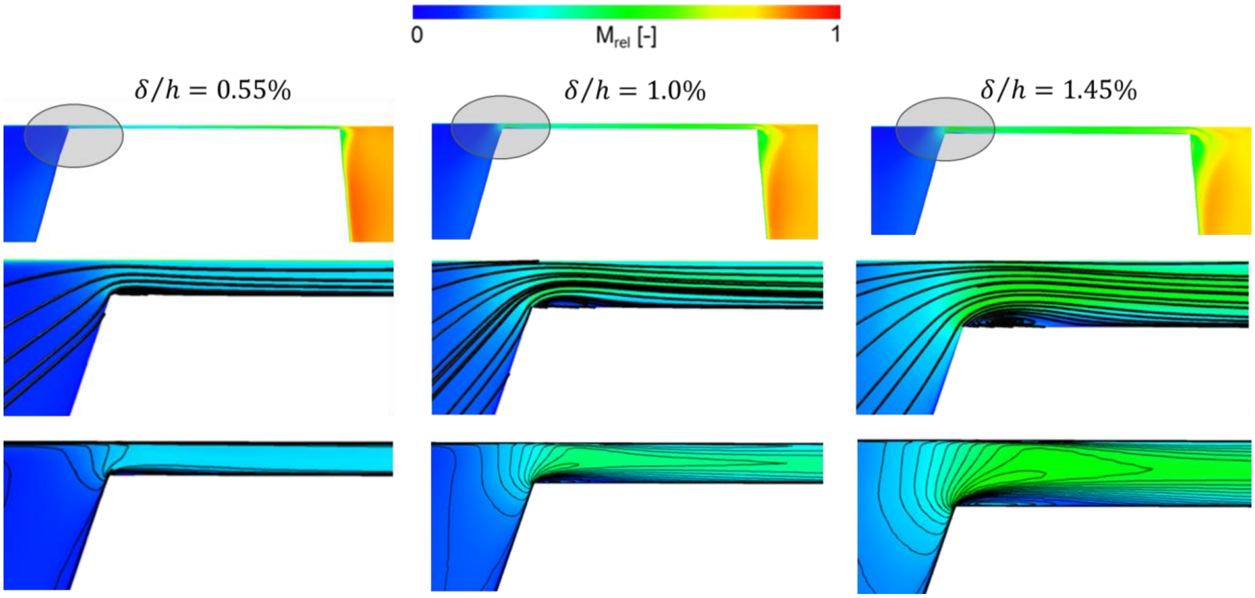

Figure 2.1: Mach number contours in a section perpendicular to the axis for three clearances. The entire section is shown on top, a zoom on the pressure side area is depicted in the center with streamlines and in the bottom with isolines of Mach number.

The reattachment lines associated with the separation bubble, which are also visible in the large gap geometries in the bottom of Figure 2.2, progress continuously from leading to trailing edge, close to the pressure side. However, the flow topology manifests different characteristics when the tip clearance becomes tighter [15]. Figure 2.2 describes the tip surface flow features for different values of clearance. The color contours represent wall pressure and are used to qualitatively describe the pressure gradient across the blade tip surface. The surface streamlines are vector lines based on the shear stress vector, and they represent the local direction of the velocity close to the wall. On the top left corner, the blade with the smallest clearance is reproduced. When the gap is only 0.1% of the blade span, the flow field appears to be dominated by viscous effects. The front portion of the suction side is an inlet, and a portion of flow enters on the suction side and is ejected right after still from the suction side. Analogously, due to viscous forces induced by the rotation of the shroud, a fraction of leakage flow enters on the suction side in the leading edge area and exits on the pressure side.

Only the rear section of the airfoil presents a "typical" flow field with flow passing from pressure to suction side, driven by the pressure gradient. This flow topology shows that for small gaps the effect of the relative motion between blade and casing affects the entire flow field, while for large tip gaps the rotation effects stay confined in the casing region due to the small size of the boundary layer (like shown in [22]).

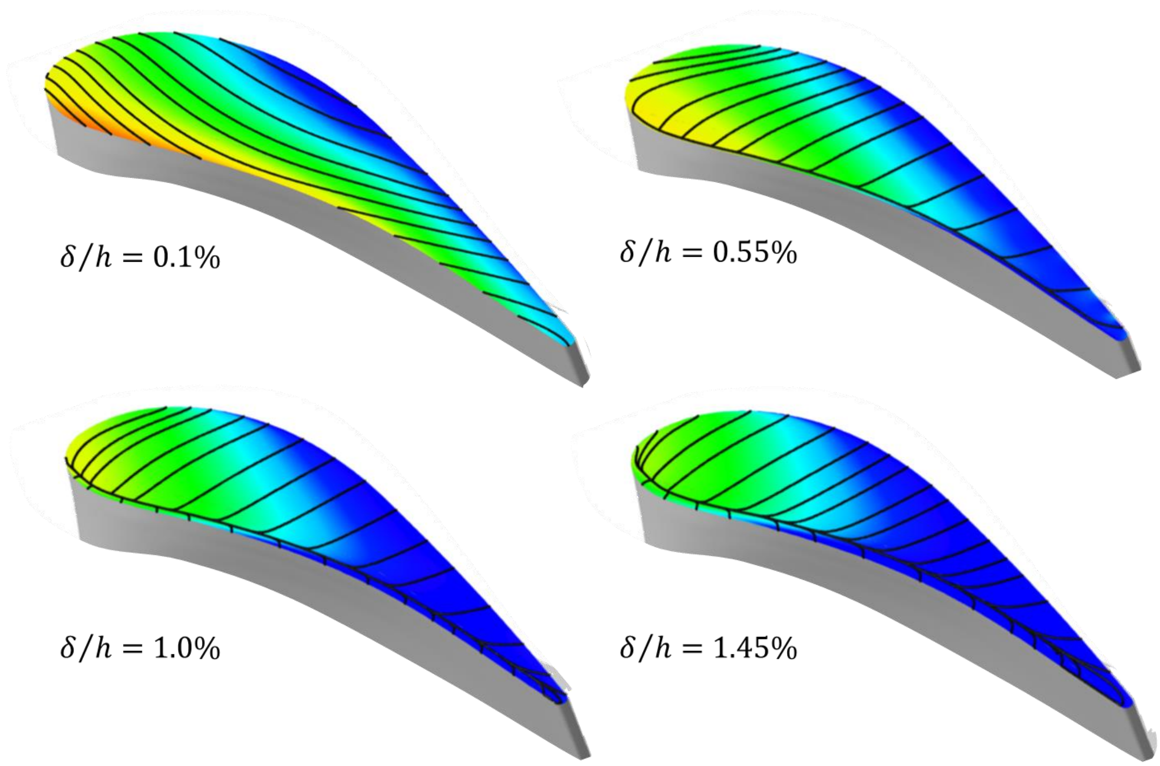

Figure 2.2: Tip surface streamlines for 4 different tip gaps, with isothermal walls, over contours of static pressure.

On the top right corner, the figure depicts an intermediate clearance case with $\delta/h = 0.55\%$. As the gap grows larger, the flow close to the tip starts feeling less the presence of the rotating casing. The pressure side is now entirely an inlet, while most of the suction side, approximately the rear 80%, is an outlet. The only region characterized by a non-conventional flow field is the leading edge area, where the flow enters and exit on the front 20% of the suction side. The two contours on the bottom of the figure represent two relatively large tip clearances ($\delta/h = 1.0\%$ and 1.45% on the left and right respectively). The main difference between the 1.0 and the 1.45 clearance lies in the extension of the separation bubble, which is larger on the second case. This can be observed as well in Figure 2.1.

In the tight gap, we have concluded that the relative rotation of the shroud has a large effect on the flow topology. In order to demonstrate it, three different simulations were run with different boundary conditions. The surface streamlines are depicted in Figure 2.3.

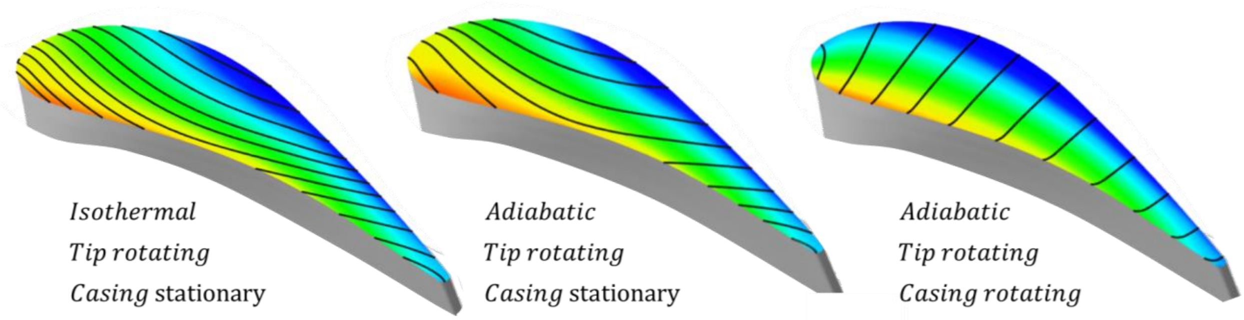

Figure 2.3: Tip surface streamlines for tight gap (δ/h 0.1%) with isothermal walls (left), with adiabatic walls (center) and with adiabatic walls and rotating casing (right).

On the left, the isothermal case previously showed in Figure 2.2 is reported as reference. The same rotor geometry is then simulated with adiabatic walls (center image) and with adiabatic wall and a casing rotating with the same rotational speed as the blade. It can be observed that without heat flux the viscous effects are slightly less important than in the isothermal case. In the central figure, the front portion of the suction side is still an outlet but the extent of this area is reduced compared to the left plot. The inflection point, where the gas begins to leave the airfoil is shifted upstream due to the lack of heat flux. This suggests that the heat transfer between fluid and wall modifies the flow properties, the velocity and consequently the static pressure distribution as depicted in the colored contour. The right figure illustrates the flow topology in absence of relative motion between blade and casing. Even though the gap is still tight, the viscous effects, i.e. the presence of a boundary layer, does not modify the direction of the leakage flow since the shear stress on the tip is aligned with the direction of the pressure gradient.

We analyze the rotor performance at each clearance in the isothermal and adiabatic case. The mechanical efficiency is calculated in each case as:

$$\eta = \frac{\tau\omega}{\dot{m}_{in} C_P T_{02}\left[1 - \left(\frac{P_{03}}{P_{02}}\right)^{\frac{\gamma-1}{\gamma}}\right]} \tag{2.1}$$

The results are plotted Figure 2.4, where on the abscissa the tip clearance is reported as a percentage of the blade span. On the ordinate, $\Delta\eta$ is calculated by subtracting the efficiency at zero clearance in the isothermal case to the efficiency in each case.

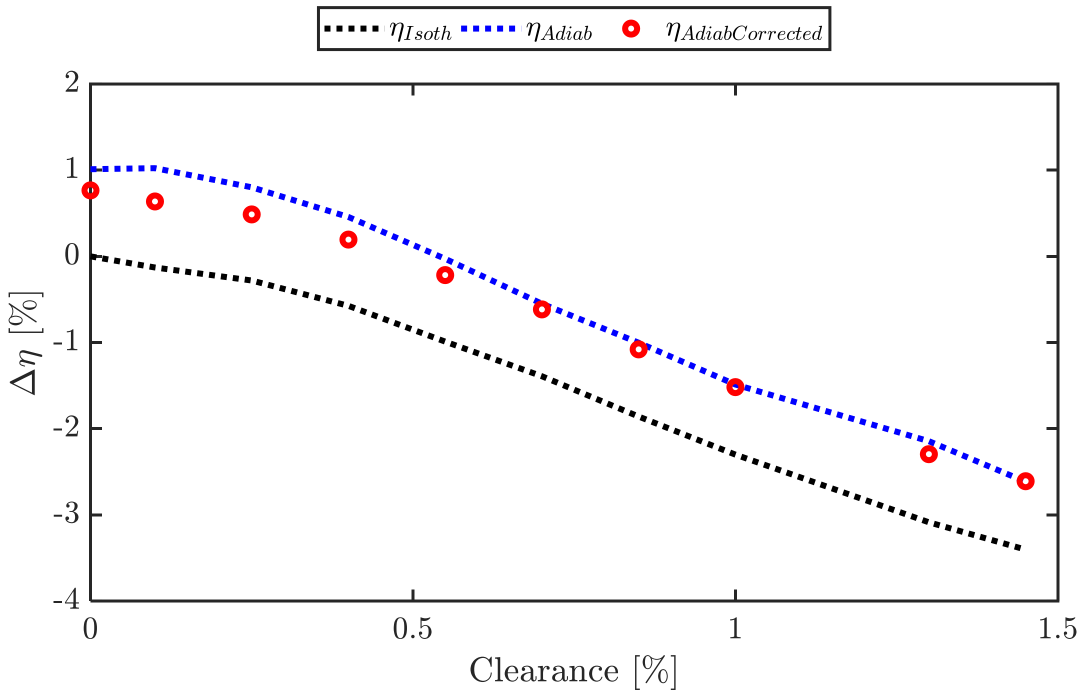

Figure 2.4: Variation of efficiency in function of clearance.

The black dotted line represents the isothermal efficiency for a range of clearance ranging from 0 to 1.45% of the blade span. The curve decreases monotonically as the clearance increases, showing a fairly linear trend, with a slightly smaller slope for tight clearances. The meaning of the slope in this kind of graph is the tip clearance exchange rate: an increase of 1.0% of clearance is traded with 2.0% of efficiency. The blue line shows the efficiency in the adiabatic case; in this configuration, the efficiency is higher because there is no energy loss in the transferring process to the wall. The difference between the blue and the black lines is approximately constant over the range of clearances under examination. Hence, the effect of heat flux on rotor performance is qualitatively independent of the tip clearance. The red dots represent the adiabatic efficiency retrieved from the isothermal case using the method described in [23]. The equation used in this calculation is:

$$\Delta H = T_{03}\left(\frac{q_{stator}}{T_{01}} + \frac{q_{rotor}}{(T_{02}+T_{03})/2}\right) \tag{2.2}$$

The adiabatic case with the rotating casing is included in Figure 2.5, colored in gold. The difference with the adiabatic case is larger for tight clearances, below 0.3%, or large clearances, larger than 0.8%, while the two curves are closer for intermediate gaps. This indicates that the effect of relative motion has a large effect on rotor performance even for large gaps. The effect of casing motion will be investigated in depth in the following sections.

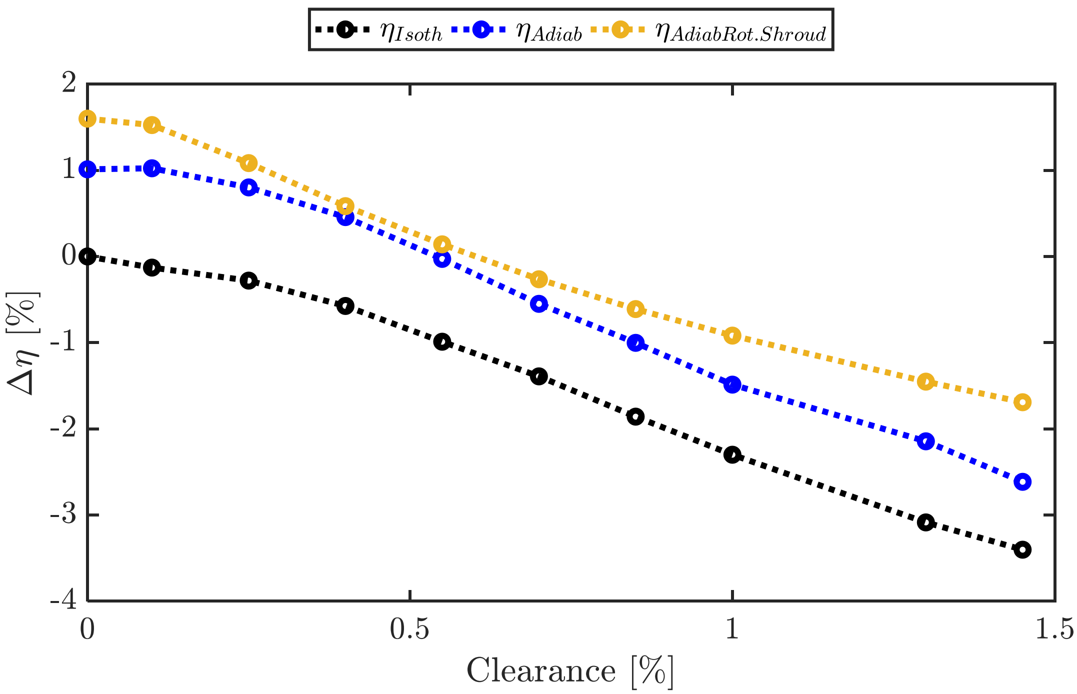

Figure 2.5: Variation of efficiency in function of clearance for isothermal rotor, adiabatic rotor and adiabatic rotor with rotating casing.

For the turbine operation, the efficiency is not the only relevant parameter. The engine operating point will be affected by the changes to the turbine map, i.e. the machine capacity as well. When the tip gap is modified, the leakage flow over the blade intuitively increases. The flow has indeed a larger effective area to leak through, and the pressure gradient is not expected to have major modifications. However, the tip flow has an effect also on the passage mass flow as described in [21]. Figure 2.6 shows the variation of tip leakage mass flow with an increase of tip gap. The curve initiates in zero, which is clearly the case of null tip clearance, and continuously increases with the size of the gap. The trend is overall linear, except for the tight clearances. On the right, the variation of mass flow in the entire passage is plotted. While the leakage flow increases, the total mass flow increases monotonically with the rise of the tip gaps.

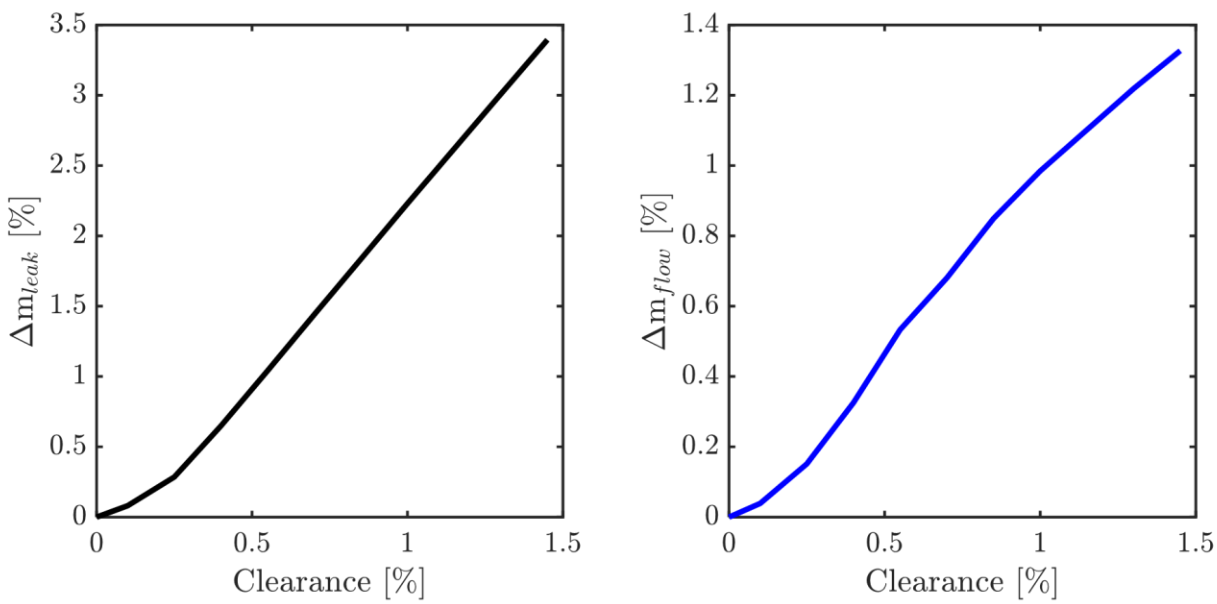

Figure 2.6: Leakage mass flow (left) and passage mass flow (right) as a function of the tip clearance.

The change in mass flow is due to a variation of the flow direction at the rotor outlet. In other words, the leakage flow causes a blockage that is a function of the tip clearances and can reduce the stage mass flow.

Figure 2.7 depicts the flow angle variations from different values of tip clearances. The black dotted line is the mass flow-averaged flow angle extracted from the CFD, while the red line shows the flow angle calculated using the correlation proposed by Hubert [24]. The empirical correlation, based on experiments in a cascade and described in Section 4.2.1, consistently overpredicts the changes of flow angle compared to the CFD. Nonetheless, the range of angles estimated is similar and goes from zero to a maximum of three degrees in the case of the RANS simulations, and 5 degrees in the case of the correlation.

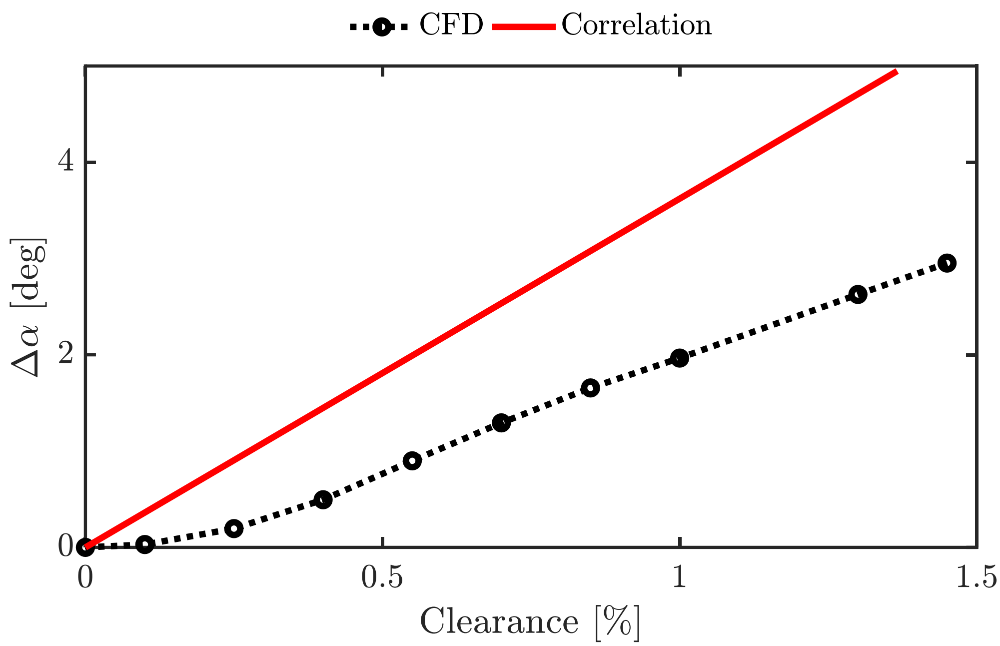

Figure 2.7: Variation of flow angle at the rotor exit; calculated with CFD (black dashed line), vs. predicted with correlation proposed by Hubert [24] (red line).

2.2 Tip Design for Enhancement of Turbine Performance

Optimal turbine blade tip designs have the potential to enhance aerodynamic performance while reducing the thermal loads on one of the most vulnerable parts of the gas turbine. This section focuses on the modeling of turbine tips, and the optimization of turbine performance with novel tip designs. A novel optimization strategy of the tip shape of a cooled high-pressure turbine blade is proposed; where the simultaneous enhancement of the stage aerodynamic efficiency is targeted while minimizing the blade tip heat load.

2.2.1 Single Clearance Tip Optimization*

Initially, this work introduces a novel strategy to perform a multi-objective optimization of the tip geometry of a cooled turbine blade. A parameterization strategy generates arbitrary rim shapes around the coolant holes on the blade tip. Each tip geometry performance is assessed using steady Reynolds-Averaged Navier-Stokes simulations with the k-ω SST model for turbulence closure. The fluid domain is discretized with hexahedral elements, and the entire optimization is performed using identical mesh characteristics in all simulations. This is done to ensure an adequate comparison among all investigated designs. Isothermal walls are imposed at engine-representative levels to compute the convective heat flux for each case. The optimization objectives are a reduction in heat load and an increase in turbine stage efficiency. The multi-objective optimization is performed using a differential evolution strategy. Improvements were achieved in both the aerodynamic efficiency and heat load reduction, relative to a conventional squealer tip arrangement. Furthermore, this work demonstrates that the inclusion of over-tip coolant flows impacts the over-tip flow field and that the rim-coolant interaction can be used to create a synergistic performance enhancement.

Figure 2.8 shows the baseline CFD configuration, integrating a fully cooled rotor with a standard squealer tip. The boundary conditions included inlet radial profiles of total pressure and total temperature, together with an exit radial profile of static pressure (Table 1). The blade was cooled with multiple rows of cooling holes along the pressure side and several cooling holes on the tip cap. The inlet conditions for the cooling holes were modeled using total pressure, total temperature and a velocity direction.

* Section partially published in Andreoli, V., Braun, J., Paniagua, G., De Maesschalck, C., Bloxham, M., Cummings, W. and Langford, L., 2019. Aerothermal Optimization of Fully Cooled Turbine Blade Tips. Journal of Turbomachinery, 141(6), p.061007.

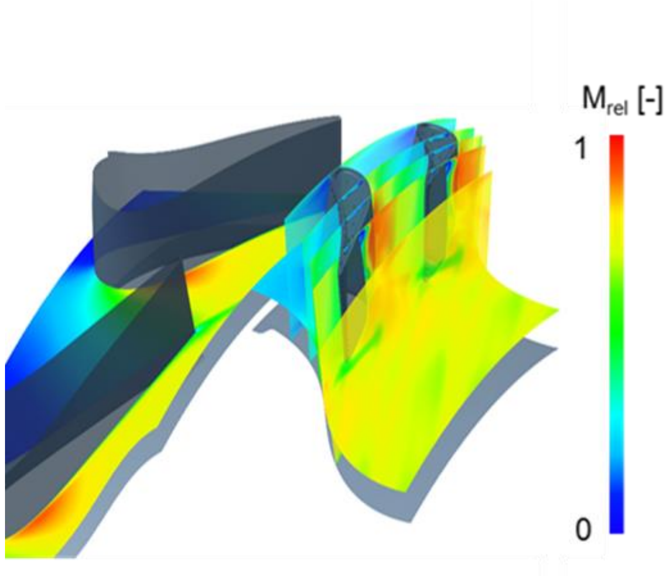

Figure 2.8: Baseline stage.

Table 2.1: CFD boundary conditions.

Boundary	***Condition***
Inlet	P_0, T_0
Outlet	Static pressure profile
Cooling holes	P_0, T_0, velocity direction
Hub/casing/blade	No slip isothermal wall

The baseline was meshed in Numeca Hexpress using 10.5 million cells and a y+ below one to guarantee to model the viscous sublayer. A grid sensitivity study was performed to ensure insensitivity to the discretization size. The flow field was calculated with Numeca FINE/Open by solving the RANS equations with the k-omega-SST turbulence model as closure equations.

In order to reduce the computational cost of the optimization, the entire stage was simulated only for the baseline tip; the alternative tip geometries were then assessed with CFD calculations of the rotor only. Data from the inlet rotor plane of the baseline were extracted (Figure 2.9a) and imposed at the inlet of the rotor only simulation, similar to the strategy used by De Maesschalck et al. [17]. The different geometries were discretized following a two-domain strategy: a lower block (b, grey) was meshed only once and used for all the tip designs, while an upper block (in red in Figure 2.9b) was generated for each geometry.

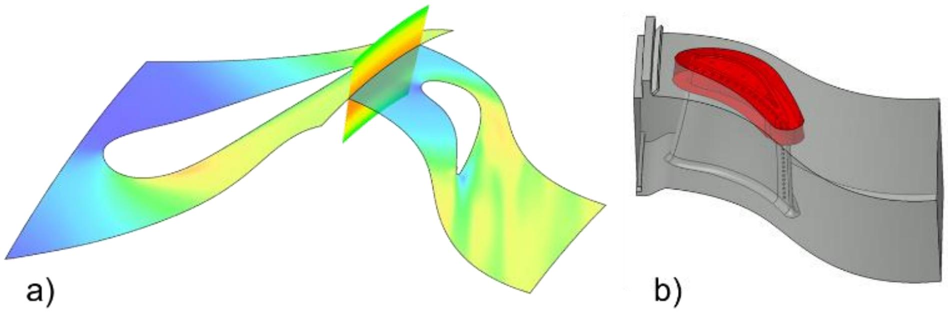

Figure 2.9 Rotor mesh strategy.

Optimization routine

Figure 2.10 shows the overall optimization strategy, which is used to generate, mesh, solve and post-process a random rotor tip geometry from 40 design parameters. This routine is coupled to a multi-objective differential evolution optimizer CADO [25], which is based on the NSGA-II algorithm [26]. The optimizer is initialized by a Design of Experiments [DoE], which used a fractional factorial approach [27]. For this optimization, minimum heat load and maximum efficiency are selected as the two competing objectives. The optimization was performed on a tip clearance to span ratio of 0.73%.

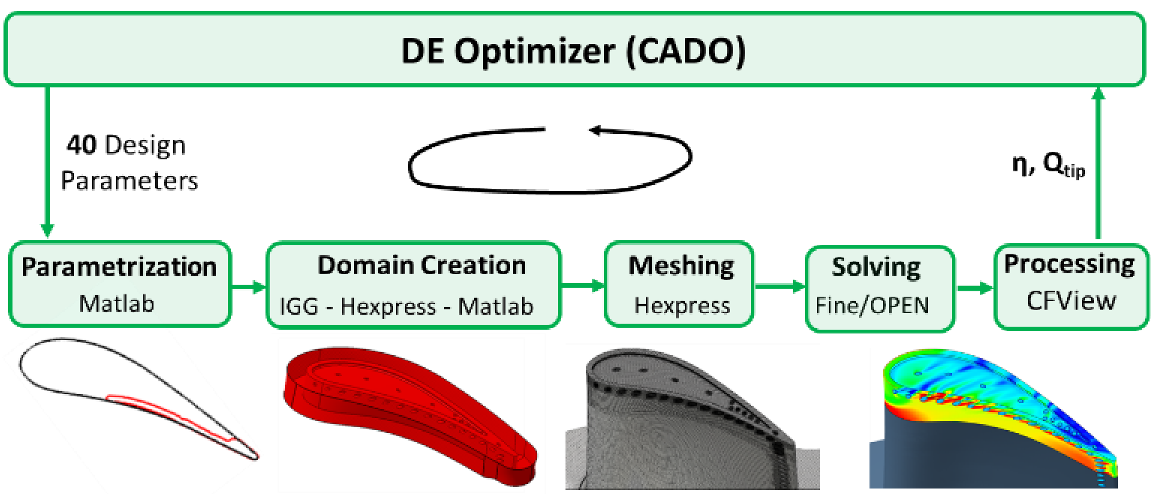

Figure 2.10: Full optimization routine.

The purpose of the parameterization is to build geometries with arbitrary numbers of rims and shapes. Figure 2.11 is a visual representation of the parameterization strategy used to obtain the random rim profiles. A description of each step is provided below.

- A Bezier surface is constructed in a square domain with a set number of control points (Figure 2.11a), where each of the control points can vary between 0 and 1. All the points of the iso-line at 0.5 are identified and used to define the centerline of the rims (e.g. black line in Figure 2.11a).
- The centerline of the rims is mapped to the blade tip profile. The centerline is adjusted to guarantee a minimum thickness of the rims.
- In accordance with manufacturing limitations, rims are merged when they are too close and sharp corners are smoothed (Figure 2.11c).
- An additional step is included to ensure that none of the rims pass over or interfere with the cooling holes. If the rims are too close to a cooling hole, the rim is moved until the interference is eliminated (Figure 2.11d).
- A constant thickness is added to the centerline to define the solid boundaries of the rim (Figure 2.11e).
- The rim outer lines are smoothed, extracted (Figure 2.11f), and projected from the two-dimensional plane onto the three-dimensional blade profile.

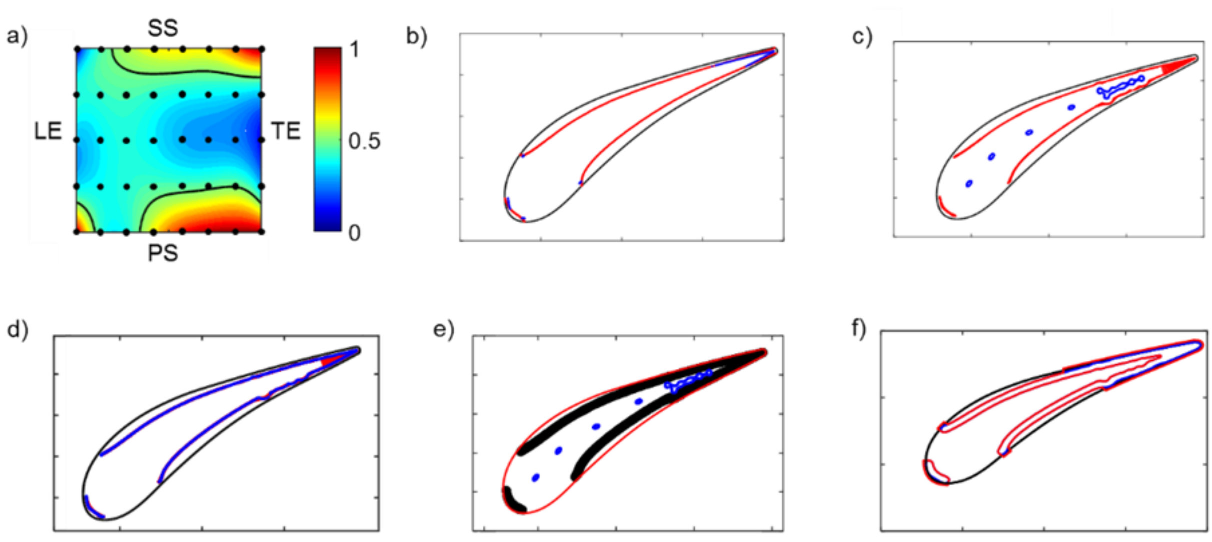

Figure 2.11: Rim parameterization.

A sensitivity analysis was performed to determine the number of control points for the optimization. A good compromise between variability of the rim shape and the quantity of optimization design parameters was achieved with 40 control points (5 control points across the airfoil thickness and 8 control points along the airfoil chord).

The fluid domain is generated in three steps. First, the borders of each rim from the parameterization are passed to the geometry modeler Numeca IGG as lofted surfaces, closed by a top and a bottom surface at the blade and cavity radius respectively. Second, each rim from the previous step is intersected with a flat blade tip. Third, the rims are subtracted from the base fluid domain. Using these steps, any rim configuration created by the parameterization control points (Figure 2.12a) can be used to generate a fluid domain for CFD analysis (Figure 2.12b).

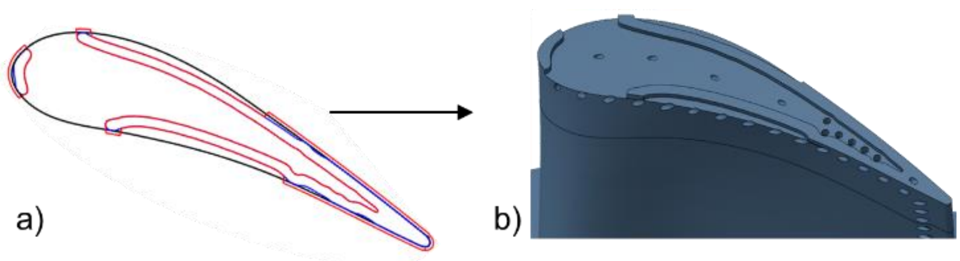

Figure 2.12: Fluid domain creation.

An unstructured hexahedral mesh is generated for the upper block and connected to the lower block via a non-matching boundary condition. The grid is refined close to the blade tip, in order to resolve the small-scale flow structures in the tip gap.

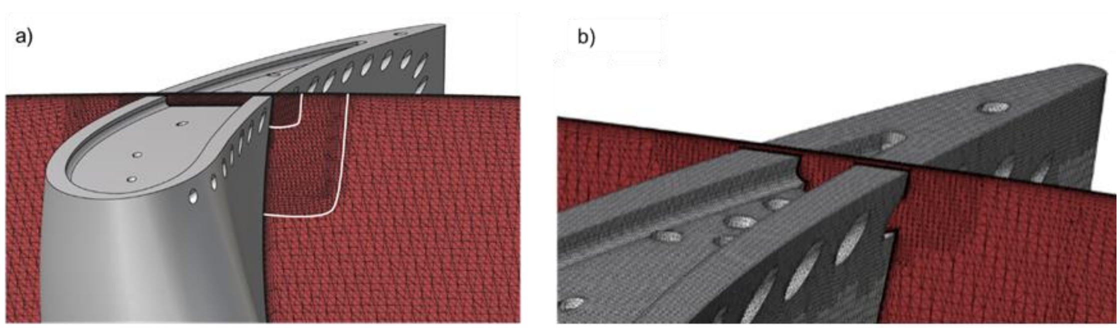

Figure 2.13: Mesh generation.

Figure 2.13a illustrates the three levels of refinement in the passage, and Figure 2.13b shows a close-up of the grid in the tip gap. For all solid walls, a wall refinement with a y+ below 1 was achieved. Figure 6b depicts a detailed view of the coolant holes at the trailing edge of the blade. The number of cells was between 3.5 and 4.5 million cells for the upper block, depending on the specific geometry under considerations, and 3.3 million for the lower block.

The steady RANS equations are solved within the reference frame of the rotor, using Numeca FINE/Open coupled with the k-omega-SST turbulence model and constant gas properties. The solver was validated in previous publications on a cooled high-pressure turbine with squealer tip [17], where the static pressure and tip heat flux predicted by CFD show good agreement with the experiments in a transient wind tunnel. Post-processing of the simulations is done using Numeca CFView at the locations shown in Figure 2.14 below. Rotor efficiency and integrated heat load on the top section of the blade are chosen as objectives of the optimization and fed back to the optimizer. The efficiency was calculated from the extracted mass flow averaged quantities using Equation 1 [28], which includes the expansion of the coolant flow from its own individual feed pressure to the downstream stage pressure.

$$\eta = \frac{\tau\omega}{\dot{m}_{in} C_P T_{02}\left[1-\left(\frac{P_{03}}{P_{02}}\right)^{\frac{\gamma-1}{\gamma}}\right] + \sum \dot{m}_c C_{P,c} T_{0,c}\left[1-\left(\frac{P_{03}}{P_{0,c}}\right)^{\frac{\gamma_c-1}{\gamma_c}}\right]} \tag{2.3}$$

A typical simulation was run on 8 cores of Intel Xeon-E5 processors and took about 11 hours to converge.

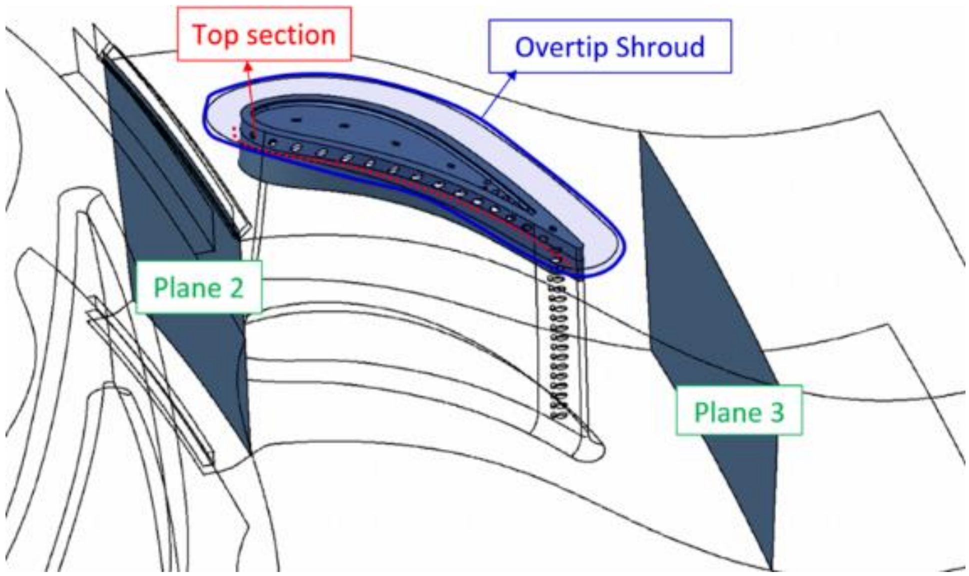

Figure 2.14: Post-processing details.

Pareto front evolution

Figure 2.15 shows the results of the DoE in terms of the optimization objectives, the aerodynamic efficiency and the integral heat flux on the rotor blade tip.

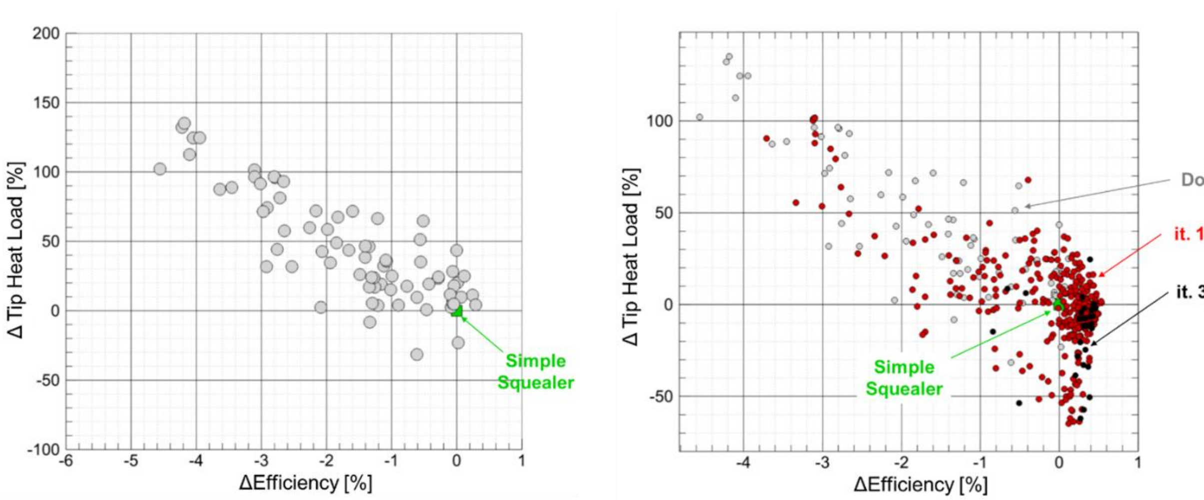

Figure 2.15: Left: results of Design of Experiment. Right: Pareto front evolution.

The values in the figure are referenced to the baseline geometry (green square). The 129 individuals of the DoE cover a range of 5% in efficiency and 170% in heat transfer. These preliminary results suggest improved designs compared to the simple squealer performance, with efficiency improvements up to +0.23% and tip heat load reductions up to 30%. After 32 optimization iterations and about 450 simulated profiles, significant improvements in efficiency and heat flux are observed. Figure 2.15, right combines results from the DoE (Figure 2.15, left) with the subsequent 32 optimization iterations (note that each optimization iteration contains 20 individuals). The first 30 iterations are colored red, while symbols for the last 2 optimization loops are colored black. The final Pareto front illustrates that the simple squealer is outperformed by several novel shapes with heterogeneous geometrical features. Throughout the iterations, the populations move towards the lower-right region of the chart, combining low heat transfer levels with high efficiencies. The individuals of the last two populations are closely concentrated on the Pareto front, confirming the convergence of the optimization.

A majority of the geometries of the last two populations offer improved efficiency and a simultaneous decrease in heat flux relative to the baseline. Figure 2.16 shows a close-up view of the Pareto front. It also highlights the geometries that offer the most efficiency improvement for a fixed heat load level. Provisional and non-provisional patents have been submitted for the geometries shown in Figure 2.16.

The tip geometry offering the optimal aerodynamic performance (red diamond) has an increase in efficiency of 0.53% with respect to the simple squealer (green square). This enhancement of performance is achieved without a considerable change in the tip heat load compared to the baseline case. The tip geometry with the lowest heat load, indicated with a blue circle, decreases the blade tip heat flux by 65% while increasing the aerodynamic efficiency by 0.25%.

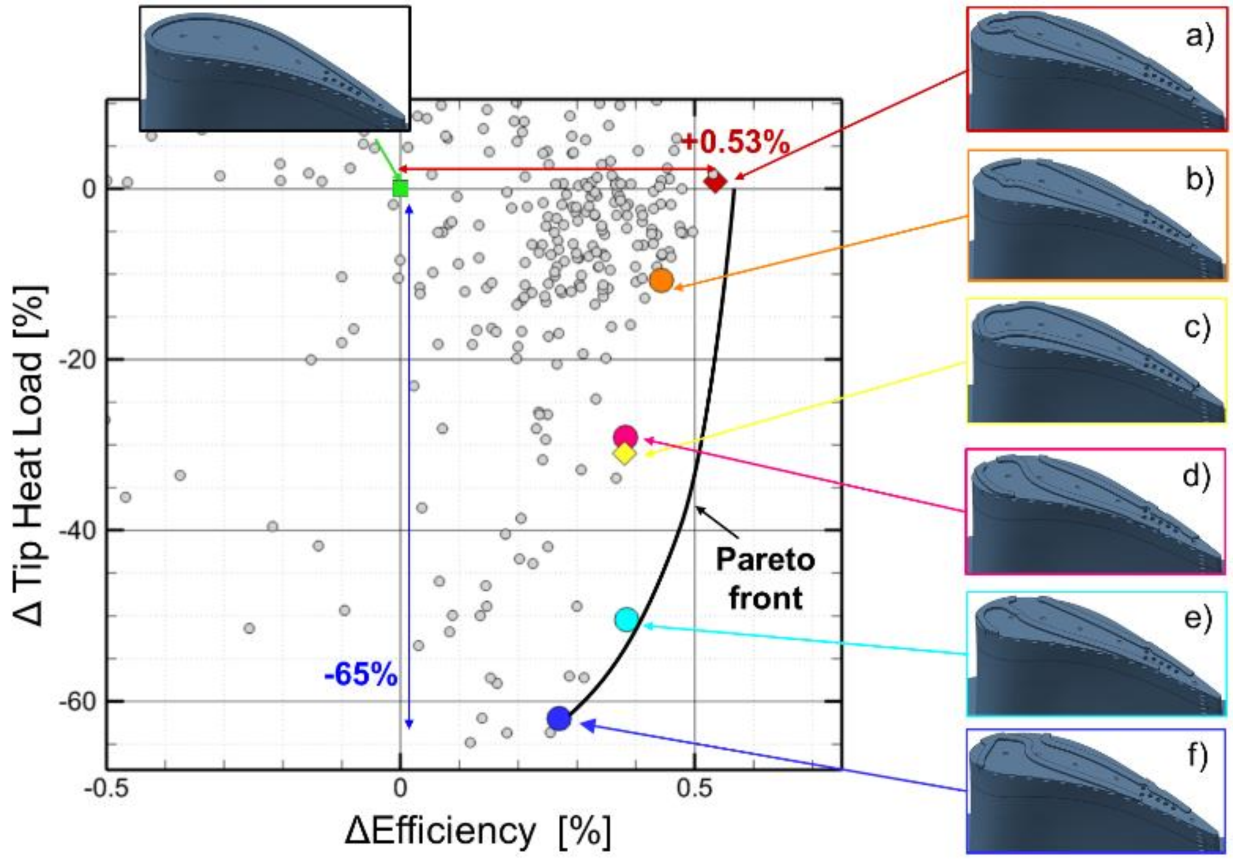

Figure 2.16: Results of optimization – Geometry details.

Starting with geometry 'a' in Figure 2.16, the highest efficiency is provided by a squealer-like profile with a single rim. The rim starts near the trailing edge, which is open and extends along the length of the pressure side with a recess or shelf that becomes larger towards the leading edge. The rim almost moves in a straight line across the airfoil to the suction surface except for an abrupt change near the airfoil max thickness. The abrupt change can be attributed to the rim navigating around a cooling hole. Once the rim reaches the suction surface it turns and moves aft along the suction side. The rim creates a small recess or shelf in the region adjacent to the blade passage throat. After the shelf, the rim remains on the suction side until it ends near the trailing edge.

Geometry 'a' introduces some features that are common to all the tip geometries with enhanced aerodynamic performance, including open trailing edges and single continuous, or quasi-continuous rims (see geometries 'a', 'b', and 'c' in Figure 2.16). Geometries 'a', 'b', and 'c' also show that the efficiency and heat flux decrease as the pressure side rim moves closer to pressure surface and leading edge. More optimal heat flux configurations introduce additional design characteristics including a rim in the front part of the blade to protect the leading edge area from the direct ingestion of hot gas, a suction side recess or shelf, and a rim that passes between the most forward tip cap cooling holes.

Geometry 'f', which offers the best heat flux performance, consists of two rims and has an open trailing edge. The first rim has the shape of a shepherd's hook. The hook extends along the leading edge and then wraps around the upstream cooling hole location. Aft of the forward cooling hole, the rim turns in the direction of the pressure side and then runs along the pressure side until the aft tip cap cooling holes. The second rim is located on the suction side. It begins near 25% axial chord on the suction side edge of the tip cap. It also creates a small shelf or recess that extends about a third of the airfoil downstream. The second rim then resides on the suction side edge of the tip cap until it terminates near the most aft tip cap cooling hole. The detailed analysis of the flow features and the loss mechanism will be part of the future work.

2.2.2 Tip Optimization for Multiple Clearances

When operating during an engine transient, the rotating and stationary components experience continuous deformations. This implies that the rotor will not operate at a specified clearance, but over a range of different tip gaps. In order to take this into account in our performance optimization, tip clearance sensitivity studies for efficiency and heat flux were performed on flat tips and optimal designs.

In these simulations, the casing radius is fixed, and the blade radius is adjusted to set the desired value of tip clearance. In the case of optimized tips, given the complexity of the geometry generation procedure, three values of tip clearance are selected with a collocation method based on Hermite polynomial [29]. Figure 2.17 shows a sketch of the geometry for different tip clearances, with a plot of the expected result. The nondimensional tip gap, in abscissa, is normally used to characterize the flow topology and the effect on efficiency.

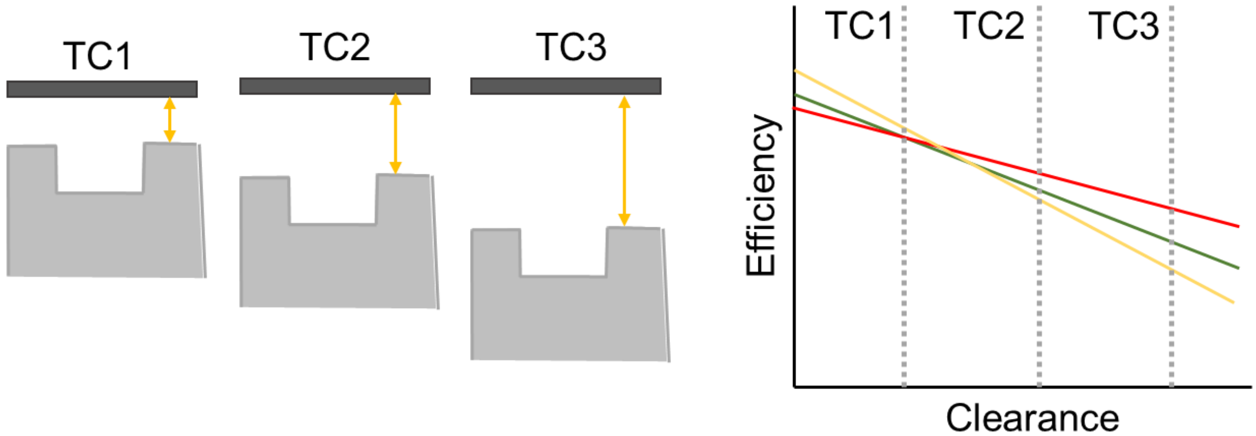

Figure 2.17: Collocation method and clearance variation.

The objective of this section is to use the three selected clearances to characterize the trend of efficiency and heat flux over the entire range of tip gaps. In order to decouple the effect of gap from the effect of off-design performance, all simulations were run at design RPM and inlet conditions.

The analysis is initially run on the profiles identified during the previous tip optimization. In particular, we want to verify if the gain of efficiency and the reduction of heat flux are guaranteed also for larger clearance than the optimization one. The results are shown graphically in Figure 2.18, where the green, red, and blue lines represent the baseline, optimal efficiency, and optimal heat flux designs, respectively. The abscissa in the graph is the tip clearance.

The ordinate axis of Figure 2.18 is the change in efficiency. It should be noted that the optimizations were performed at the lowest clearance values shown in the plot. The optimal designs shown in Figure 2.18 maintain their original efficiency benefits relative to the baseline for only a few thousandths of an inch. At some point, the slopes of the baseline and optimal heat flux designs change, while the optimal efficiency sensitivity is constant slope across the interrogated range. The slope change allows the baseline design to overtake the heat flux design somewhere between a clearance change of 0.001” and 0.009”. Additional simulations are required to identify the intersection more clearly.

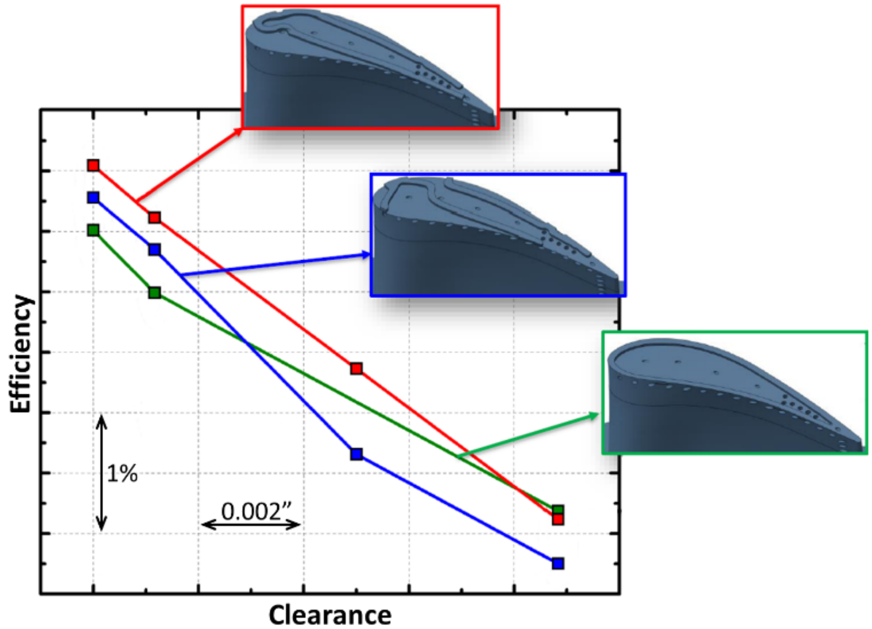

Figure 2.18: Tip clearance sensitivities to turbine efficiency for the baseline (green curve), optimal efficiency (red curve), and optimal heat flux (blue curve).

The baseline shape overtakes the optimal efficiency once the tip clearance is opened ~0.009" from the original tip clearance. These preliminary results indicate the need to optimize over a range of clearances instead of a single value if we want a profile that outperforms a baseline over an engine transient. The approach of optimizing turbine geometries to desensitize tip clearance variations has been proven beneficial in compressors in [30].

Figure 2.19 illustrates how the optimization strategy for single clearance is adapted to handle a range of clearances. The procedure used to generate, mesh, and solve the individuals is analogous to the one described in the previous section. The domain creation, in this case, is automatized to generate a fluid domain with an arbitrary tip radius. The blade is generated first, using a cylinder with a constant radius to cut the blade at the right height. The rims are added to the blade, and the cooling holes are subtracted. This blade is then used as a tool to subtract the solid part from the fluid domain.

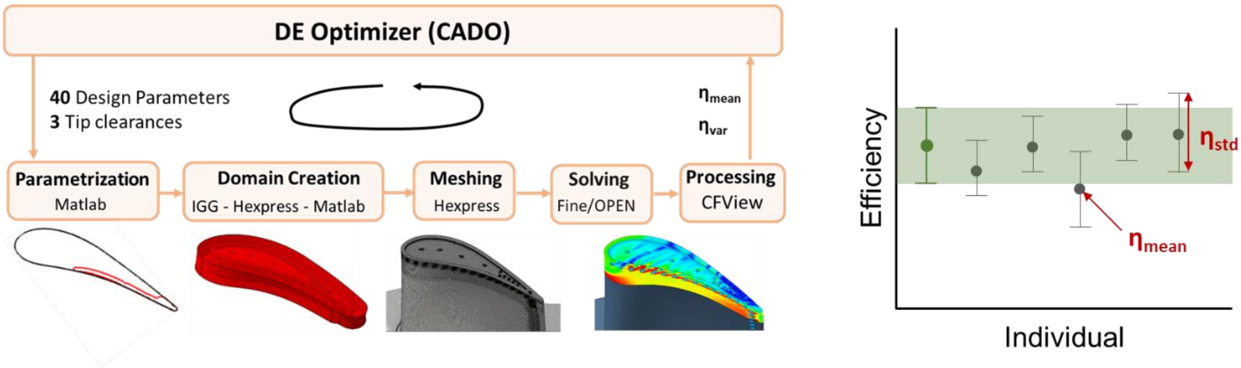

Figure 2.19: Methodology of optimization for multiple clearances.

Three different simulations, at the three clearances identified in the previous section, are run. The simulations give then multiple values of efficiencies, one for each clearance.

The selected objectives for the optimization are:

- Weighted mean of efficiency: we want to maximize the mean efficiency over the entire range of tip gaps, and not on the single value. This value is marked in Figure 2.19, right with a circle.

$$\eta_{mean} = \frac{\sum w_i \eta_i}{\sum w_i} \tag{2.4}$$

  In this optimization, all the weights will be set to one for simplicity. However, different weights can be applied based on the engine mission. In case there is a design clearance that should be prioritized, the relative weight can be increased.

- Standard deviation of the efficiency: we want to minimize the variance of the efficiency over the range of clearances, to ensure a satisfactory level of performance for different clearances. This value will be marked with the error bars on Figure 2.19, right. The standard deviation is calculated as:

$$\eta_{std} = \sqrt{\frac{\sum(\eta_i - \eta_{mean})^2}{N-1}} \tag{2.5}$$

Figure 2.20 depicts the evolution of the optimization results. A total of ~400 different geometries at three different clearances were simulated. 128 individuals composed the initial Design of Experiments and are used as a database to start the iterations of the optimization. The populations have 30 individuals each, and the optimization was stopped after a total of 8 iterations.

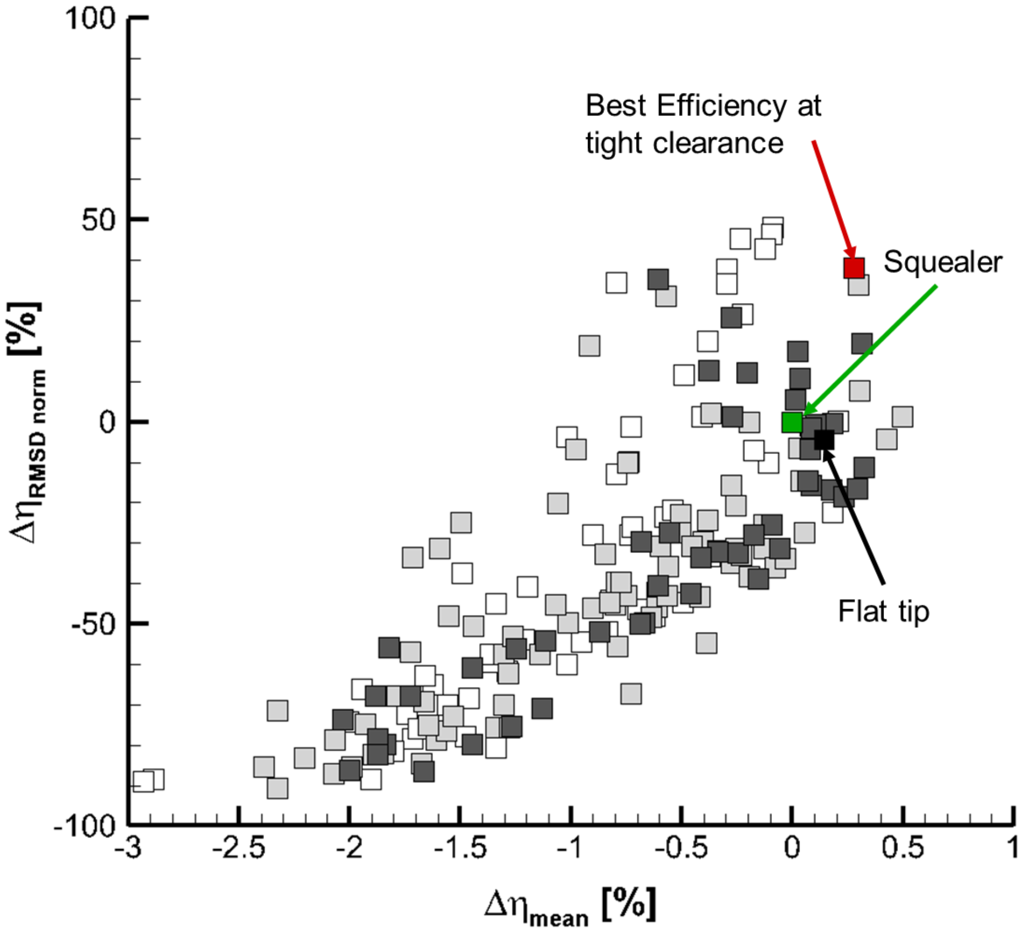

Figure 2.20: Optimization results. The DoE is indicated with white squares, light grey squares indicate populations 1 to 5, and dark grey squares indicate populations from 5 to 8. The green, red and black squares represent the simple squealer, best efficiency from previous optimization and flat tip respectively.

Populations from 1 to 4 are indicated in light grey, while iterations 5-8 are colored in dark grey to highlight the evolution towards a Pareto front. Additionally, three reference geometries are included in the plot: a flat tip (black square), a simple squealer (green square) and the optimal geometry at tight clearance (red square).The performance of the simple squealer is used as a reference for both quantities. $\Delta\eta_{mean}$ is calculated as the difference between the efficiency of each geometry and the reference efficiency. $\Delta\eta_{RMSD}$ is calculated as the difference between the RMSD and the reference value, normalized with the reference value. The design space is characterized by variability of approximately 4% in terms of mean efficiency, and 150% in terms of variations of RMSD. A Pareto front can be identified, composed of those geometries where the mean efficiency cannot be further increased without increasing the variability of the efficiency for different clearances. The Pareto front is highlighted in Figure 2.21, where optimal individuals are marked with different colors.

The individuals along the Pareto front are identified by colors ranging from blue to orange, and the respective geometries are depicted around the central plot in clockwise order (from a to f). The geometry marked with a) offers the highest mean efficiency, while maintaining the same performance variability offered by the simple squealer. This tip design contains three distinct rims in the central area: one on the pressure side, one on the suction side and one at the center of the airfoil. The central and PS (pressure side) rims merge in the front area towards the leading edge region. Both PS and SS rims do not follow the border of the airfoil but they have a recess that allows a small pocket to create. These pockets are features that have already been identified as optimal features in the previous optimization. Moving towards individual b) we reduce the mean efficiency but at the same time the slope of efficiency in terms of clearance decreases. For this geometry, only two rims can be identified. These two walls have distinct origin in the leading edge region, and they proceed almost in parallel towards the trailing edge. Compared to the previous geometry, the pocket on the pressure side has been heavily reduced, and it is almost disappeared while the SS recess has increased. The pressure side rim extends almost till the trailing edge while leaving the final part of the trailing edge open. The rim on the suction side interrupts before the last cluster of cooling holes. Profile c) presents similar features to b), with two rims with slightly increased recesses. It is an interesting trend that the SS wall starts to depart from the airfoil and move towards the camber line, where the tip cooling holes are located. This rim keeps migrating towards the pressure side in geometries from d to i, trespassing the cooling holes. Additionally, geometries ‘f’ to ‘i’ present and additional rim, that may be merged with the pressure side one, and covers only the front part of the suction side.

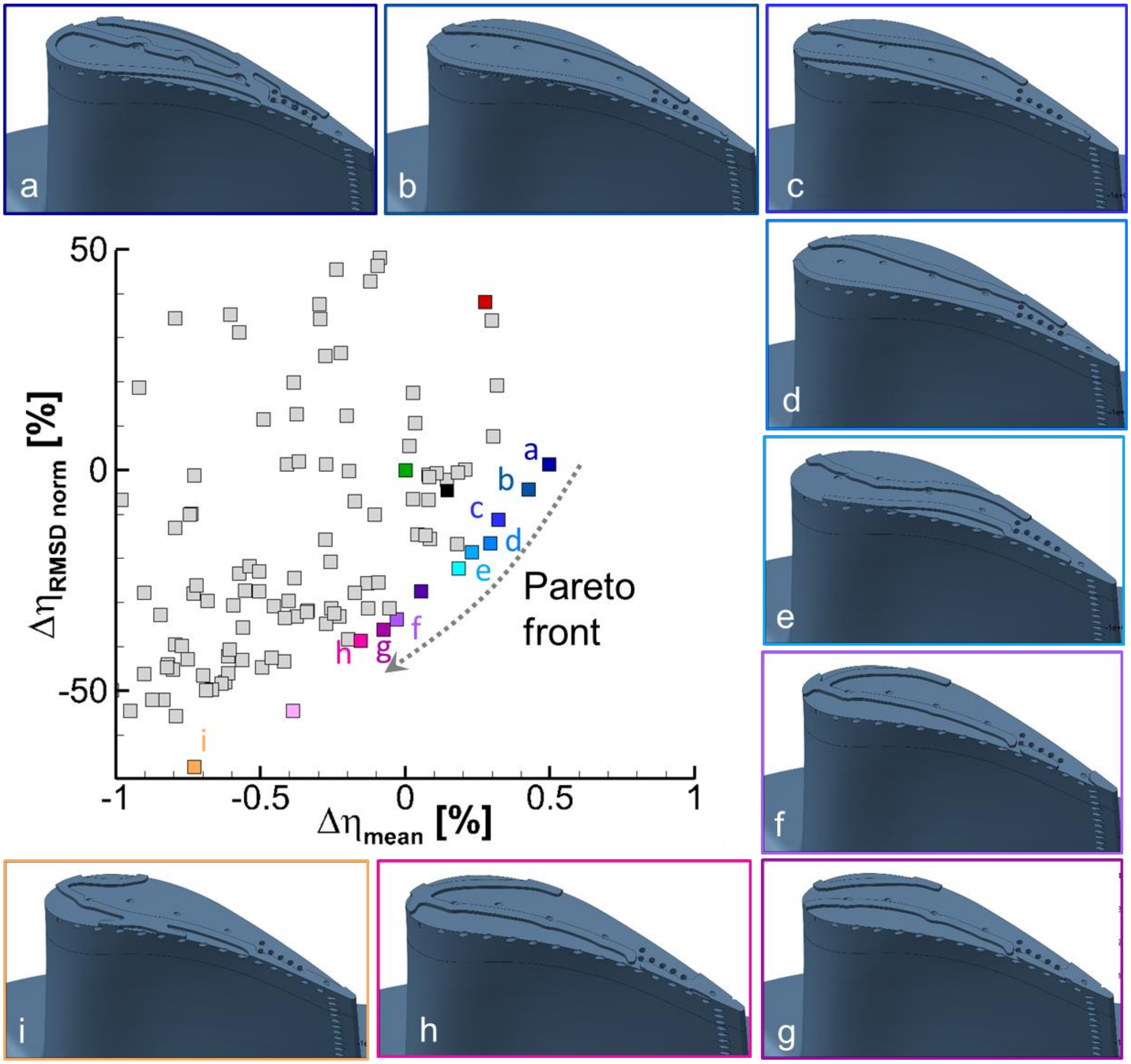

Figure 2.21: Zoom of the optimization results to highlight the Pareto front. The green, red and black squares indicate the simple squealer, best efficiency from previous optimization and flat tip respectively. The geometries located along the Pareto front (indicated with colored squares) are depicted in the figures a-i.

Conceptually, geometries that can be found at the top of the Pareto front (like a, b…) offer large efficiency improvements exploiting flow features at tight clearance. For this reason, the obtained high levels of efficiency degrade faster with the magnitude of tip gap. On the other hand, profiles in the lower region of the Pareto front do not enhance the overall mean performance but make it more stable over a given clearance variation. This means that the tip features are selected to make the tip flow more insensitive to the actual distance between blades and casing.

Considering the actual operation in an engine, it is important to quantify the variations in stage mass flow for the set of derived airfoils. Figure 2.22 shows the Pareto front described in the previous graphs (with the same axis as Figure 2.20), but contoured with mean mass flow over 3 clearances (left) and RMSD of mass flow (right).

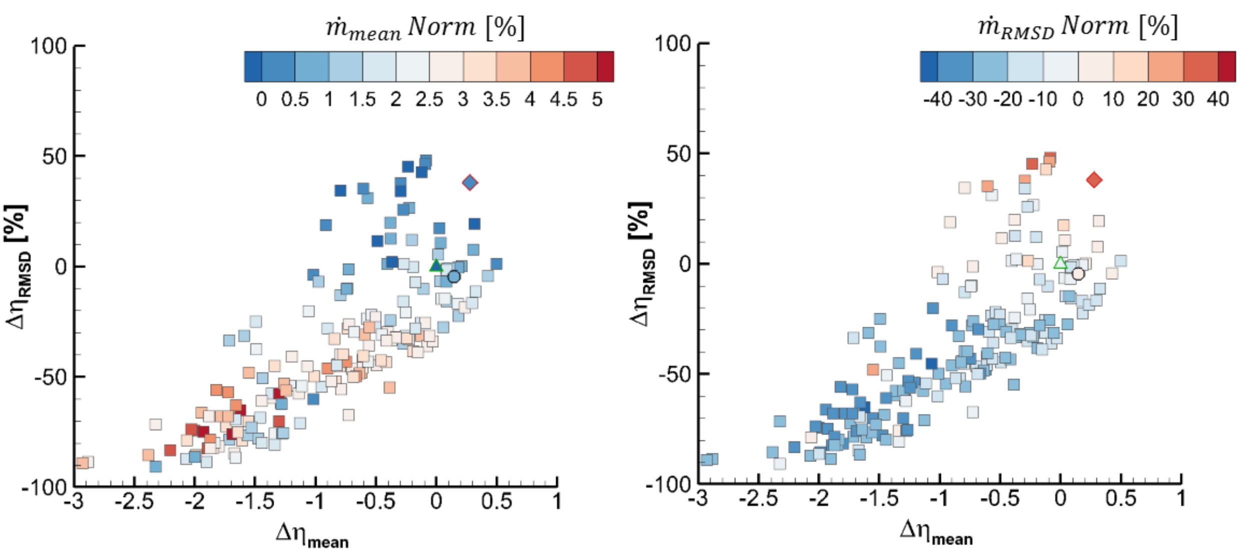

Figure 2.22: Optimization results contoured with mean mass flow (left) and mass flow RMSD (right).

In this figure, the squealer (reference geometry) is marked as a triangle with a green border, the flat tip is a circle with black border and the optimal geometry from the previous optimization is a diamond with red border. In the left figure, we can see that individuals with high variability of efficiency have a reduced mass flow, i.e., component capacity. Geometries that offer more stable performance, at the expense of mean efficiency, have a larger stage mass flow. This result shows that the tip geometry has an effect not only on the tip leakage vortex but also on the overall rotor flow field and can produce mass flow variations of more than ~5%. On the right graph, we can see a similar graph but colored with the RMSD of the mass flow. This value is extremely relevant because it shows how not only the efficiency but the engine operability is affected by variations of tip clearance. As in the previous plots, the squealer design is considered the reference value, and the RMSD is normalized. The tip designs that have low variations of efficiency (bottom part in the plot) also have lower variations of mass flows. This result is consistent with the intuitive idea that a flow field that is robust to tip gaps variation will provide more stable performance in terms of both efficiency and capacity.

Figure 2.23 depicts similar plots, but the contours are mean value and RMSD of heat flux. For this optimization, in opposition to what done in the previous single-point optimization, the heat flux is not accounted for in the objectives. However, even though it has been decided to prioritize the aerodynamic performance, the heat flux is considered for the selection of the optimal geometry.

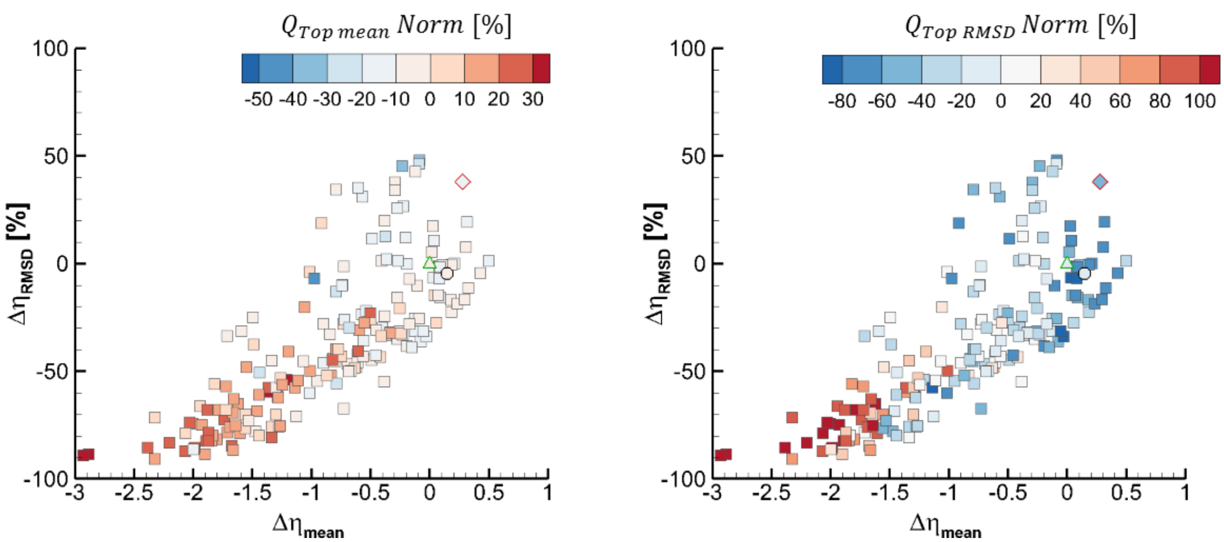

Figure 2.23: Optimization results contoured with mean tip heat flux (left) and tip heat flux RMSD (right).

The Q_{Top} indicated in the graph is the integral value of heat flux over the top portion of the blade. The considered region is the same previously included in the objective of the optimization. High values of both mean and variation of heat flux (red regions) can be found in the lower regions of the plots on left and right respectively. This means that profile that have lower variability of efficiency have higher mean heat transfer, but also higher variations of heat flux in function of the tip gap. Figure 2.24 on top shows the relation between the slope of a line passing through the three efficiencies at each clearance. On the abscissa, we can find the efficiency RMSD while on the ordinate, we find the slope calculated based on the three geometries.

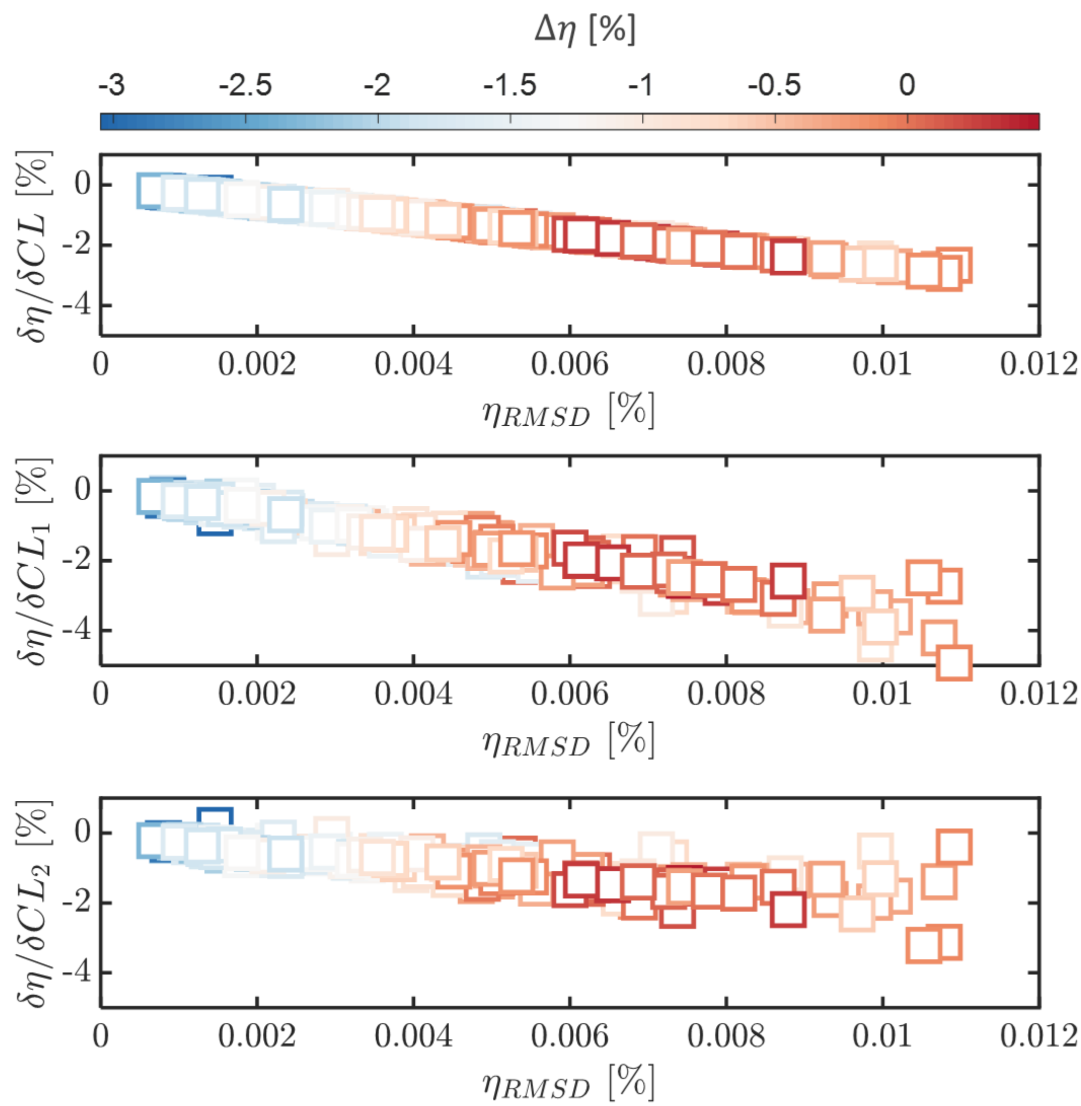

Figure 2.24: Variation of tip clearance exchange rate.

As expected, there is a reasonably linear trend between the line slope and the RMSD of efficiency. In the middle plot, the slope is calculated based on the first two clearances only. Hence the significance of $\delta\eta/\delta CL_1$, in the ordinate in the central figure, is the exchange rate for tight clearances. On the bottom plot, the slope is calculated only based on large clearances, so $\delta\eta/\delta CL_2$ is the exchange rate for large clearances. It is interesting to notice a large scatter of geometries in the two lower figures, showing that a large number of tip designs can offer different behavior at tight or large tip gaps.

2.3 Loss Mechanism in Optimal Tip Designs*

The initial analysis is based on the profiles found in the single-point optimization. The first set of selected optimal designs are of the baseline geometry, geometry ‘a’ (optimal efficiency), and geometry ‘f’ (optimal heat flux) in Figure 2.16. Figure 2.25 shows the flow field features in these three tip designs (baseline, best efficiency and best heat flux from left to right).

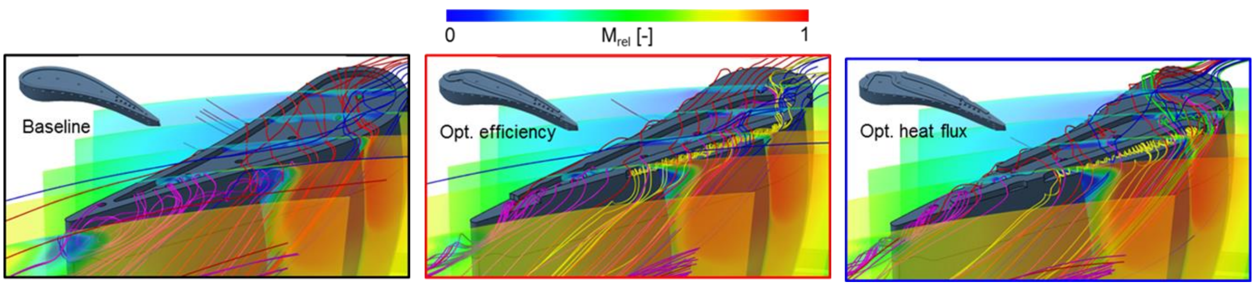

Figure 2.25: Details of turbine aerodynamics.

The five axially-spaced cut planes are colored with contours of relative Mach number and are included to illustrate the influence of the over-tip leakage on the freestream flow field. The cut planes are positioned at 20, 40, 60, 80, and 110% axial chord. To aid in the discussion, the cut planes will be referred to by their relative axial position with the first and fifth cut planes being the most axially forward and aft planes, respectively. Tip gap streamlines are provided to illustrate the characteristics of the over-tip leakage flow.

At the location of the third axial cut plane, the influence of the over-tip leakage on the freestream flow-field is clearly visible as a region of low relative Mach flow near the tip. This low relative Mach region coincides with the over-tip leakage vortex, which increases in size in the subsequent cut planes. The tip vortex or low Mach region of the optimal geometry is smaller than the baseline tip vortex on the third plane. On the fourth cut plane, located at 80% axial chord, the difference between the two flow fields is clearly visible. At this axial location, the tip vortex of the baseline geometry is twice as large as the optimal efficiency geometry. The differences in the size and magnitude of the low relative Mach number regions persist as illustrated by a comparison of the fifth cut planes of the baseline and optimal efficiency tip geometries. In this case, the baseline geometry still has a large concentrated vortex, while the optimal geometry has a much smaller region of low momentum.

* Section partially published in Andreoli, V., Braun, J., Paniagua, G., De Maesschalck, C., Bloxham, M., Cummings, W. and Langford, L., 2019. Aerothermal Optimization of Fully Cooled Turbine Blade Tips. Journal of Turbomachinery, 141(6), p.061007.

For the baseline tip geometry, a majority of the over-tip leakage flow crosses straight over the tip, and re-enters the primary gas-path on the suction side. The streamlines that originate in the cooling holes are immediately entrained by the over-tip leakage flow. The streamlines that originate near the leading edge cross over the squealer rim and are immediately turned toward the suction side. These streamlines move directly to the suction side rim and cross it returning to the primary gas path.

The optimal efficiency geometry has no rims on the pressure side close to the leading edge. Consequently, a large part of the incoming flow (red streamlines) enters the tip region and travels along the length of the airfoil. The streamlines continue on the same trajectory until they approach the pressure side rim, where the flow finally turns and crosses over the rim. Once the flow enters the channel created by the rim system, it again moves down the length of the airfoil until it reaches the suction side rim. It then crosses the suction side rim and re-enters the primary gas path.

It is noteworthy to compare the gas path re-entry locations of the leading edge streamlines between the baseline and optimal efficiency geometries. The baseline geometry leading edge streamlines re-enter the primary gas-path between 40 and 60% axial chord, while the optimal geometry streamlines re-enter the primary gas-path much farther downstream. In this way, the interaction of the rims with the over-tip leakage delays the formation of the tip vortex. An additional advantage of the optimal efficiency tip rim system is seen by following the blue and yellow leading edge streamlines in the optimal efficiency figure within Figure 2.25. Both of these streamline sets form vortices within the rim system. The blue streamlines form a small vortex within the leading edge portion of the rim channel. This vortex prevents the flow from immediately crossing over the suction side rim. The optimal geometry's suction side shelf also houses a long vortex system (yellow streamlines). It is believed that these vortex systems help to promote blockage, but perhaps more importantly, help to turn the over-tip flow in the direction of the primary gas path at the point of re-entry.

The optimal heat flux flow field has characteristics of both the baseline and the optimal efficiency fields. Similar to the baseline, the streamlines of the optimal heat flux geometry move more in a straight line across the blade tip. Similar to the optimal efficiency field, the formation of multiple tip rim vortex structures is also noted.

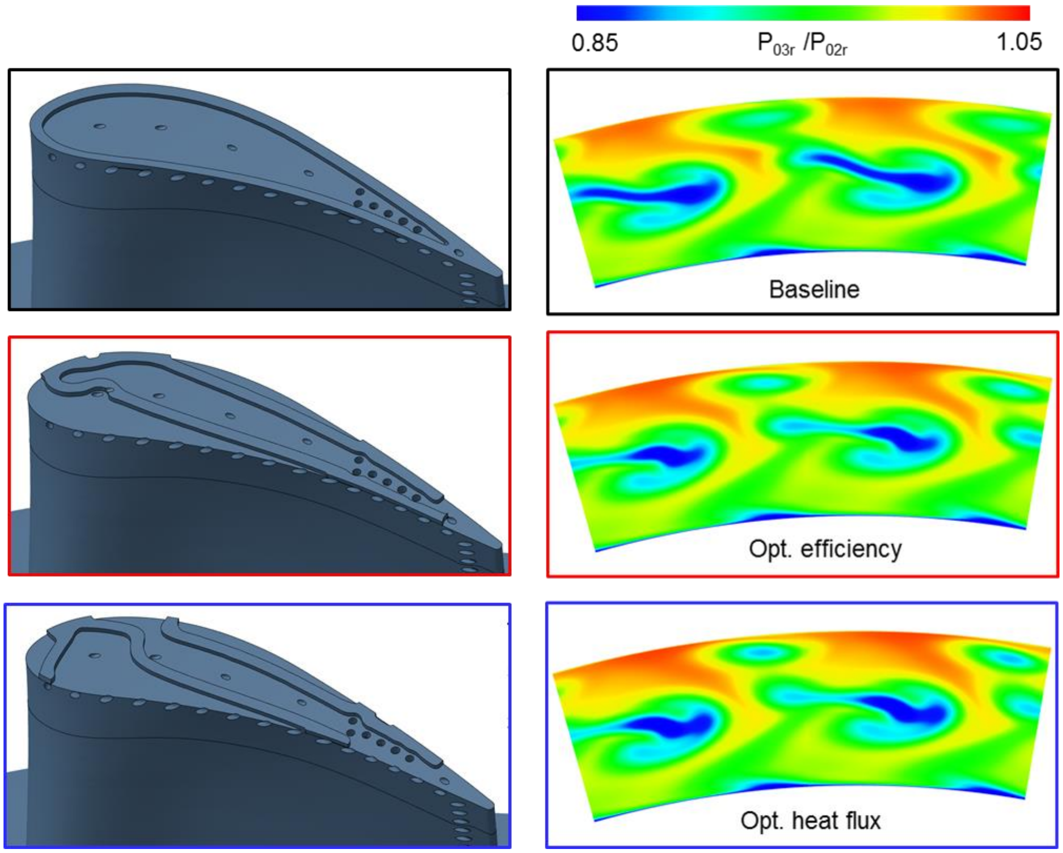

Figure 2.26: Contours of relative total pressure 50% c_{ax} downstream of trailing edge.

Figure 2.26 contains relative total pressure contours 50% c_{ax} downstream of the trailing edges of the baseline, optimal efficiency, and optimal heat flux designs. Starting with the baseline results, the loss cores of the tip vortex and the hub and case passage vortices are clearly visible. The hub and case passage vortexes have clearly merged. The outer bands of the tip vortex loss core touch the outer bands of the passage vortex system, indicating vortex interaction.

In contrast, the optimal efficiency geometry tip vortex is almost completely detached from the passage vortex. This does not only have an effect on the size of the tip vortex but also appears to impact the extent and location of the loss cores of the passage vortices, which are much larger and more concentrated relative to both the optimal efficiency and the optimal heat flux contours.

Figure 2.27 depicts the radial distribution of the pitch-wise average of relative total pressure at three axial locations labeled ‘a’, ‘b’, and ‘c’. At axial location ‘a’, located approximately at 50% of the rotor axial chord, the main differences in relative total pressure lie within the tip region (see

Figure 2.27a). This is attributed to the different jet exit conditions in the tip region on the suction side. More than 90% of the blade span is relatively unaffected by the changes in the tip geometry.

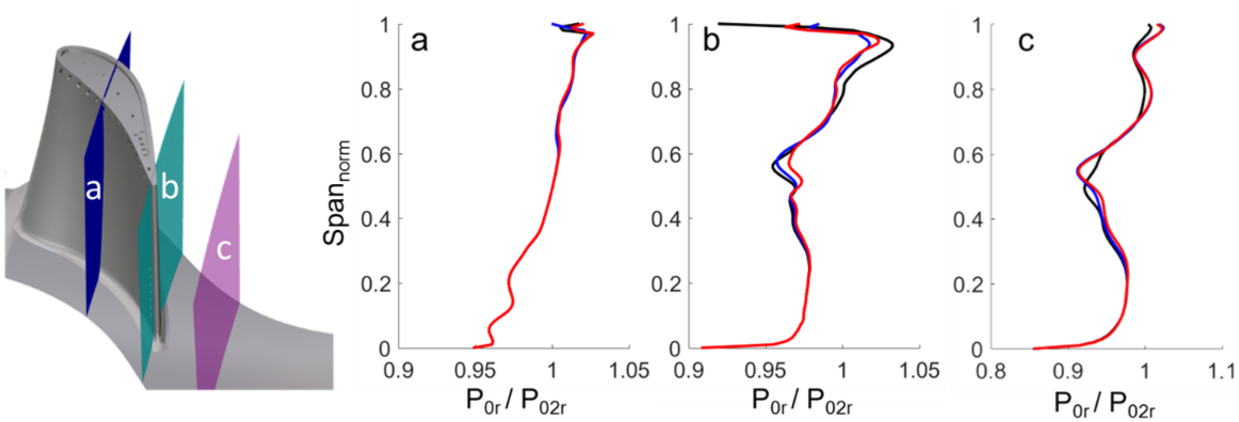

Figure 2.27: Radial distributions of relative total pressure of the baseline (black lines), optimal efficiency (red lines) and optimal heat flux (blue lines) tip geometries.

At the trailing edge (location 'b', see Figure 2.27b), three main differences in the radial relative total pressure profiles are noted. First, the relative total pressure between 98-100% span is much lower for the simple squealer. Second, between 75-98% span, the relative total pressure is higher for the simple squealer. Third, between 30-60% span, the relative total pressure of the baseline is lower than the optimized tips.

At location 'c', 50% axial chord downstream of the trailing edge, significant mixing has occurred. At this location, the relative total pressure loss across the span is lower for the optimized geometry except between 55-60% span due to the radial movement of the passage vortex loss cores. In Figure 2.27c we can see similar trends for the two optimal geometries, an indication that the optimal tip geometries similarly impact the mid-span flow field.

2.3.1 Effect of Geometry Variations

To understand the key design features that improve the aerodynamic performance in optimized blades, the optimal geometry is slightly modified to obtain 3 different variants. This is also important to guide the design iterations and understand which geometrical features are key to the design and which can be sacrificed if needed. In Figure 2.28, the 4 different versions of the optimal geometry are depicted.

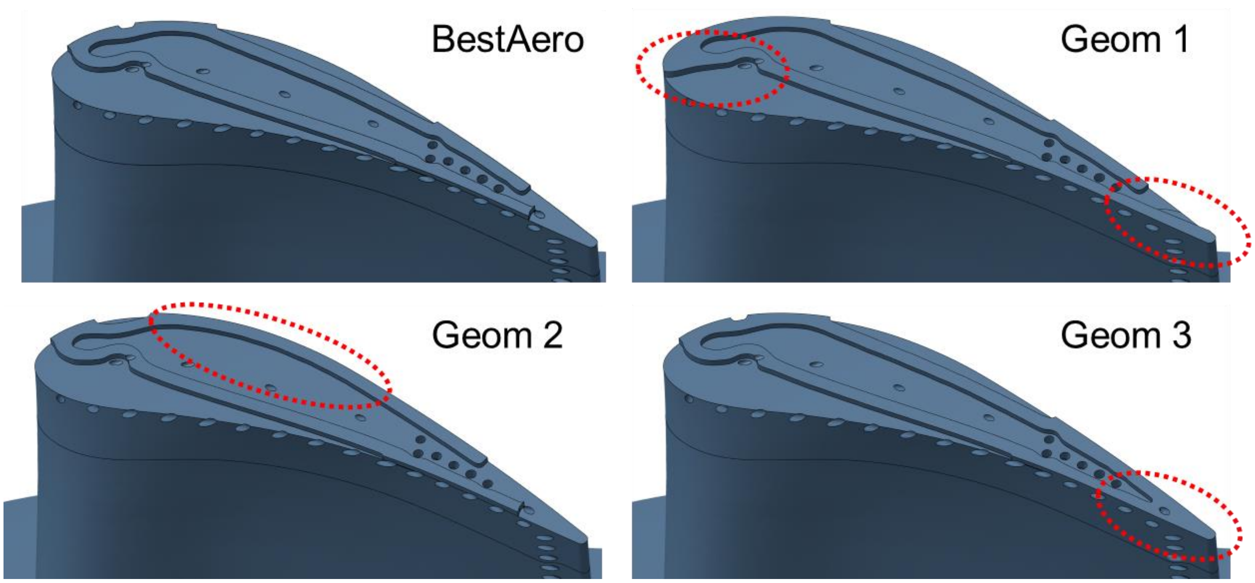

Figure 2.28: Variants of optimized geometry.

The design on the top left is the one obtained from the optimization; on the top right the front rim is extended towards the pressure side, and the leading edge on the pressure side is closed; on the bottom left (indicated as 'Geom 2') the pocket on the suction side is closed, so that there is no recess; 'Geom 3' is identical to BestAero except for the trailing edge that is completely closed.

Figure 2.29 reports the variations of efficiency (left) and mass flow (right) with respect to the simple squealer.

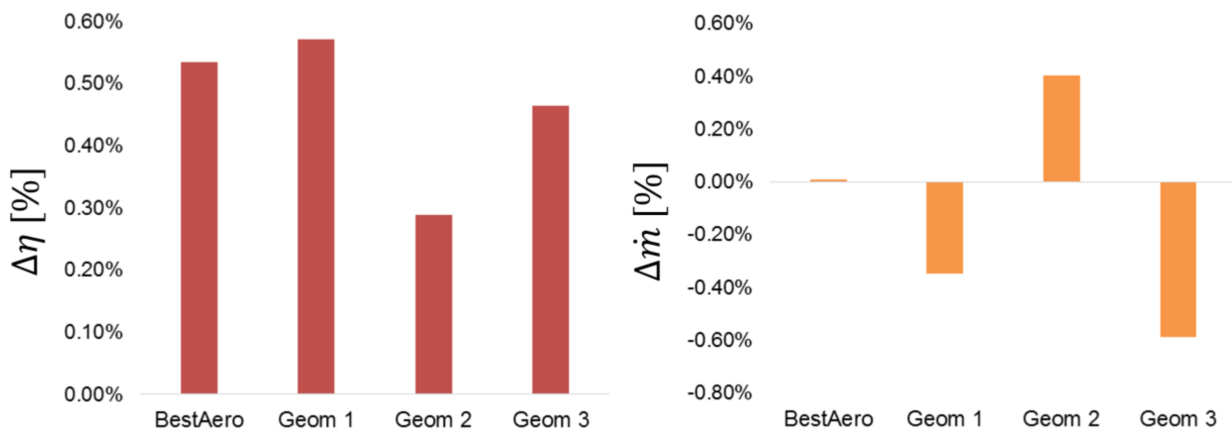

Figure 2.29: Results for geometry variations.

The efficiency of 'BestAero' on the left chart is the result that we already found during the optimization. 'Geom 1' manages to slightly improve this efficiency. This shows that if we extend the rims on the pressure side, to cover the entire axial chord, the efficiency is not penalized. 'Geom 3' provides an efficiency very close to the optimization one, showing once again that the performance enhancement is not due to the open trailing edge in the original configuration. The only geometry where we observe a drastic drop of efficiency increase is the 'Geom 2'. This shows that the pocket on the suction side is key to the achievement of optimal performance. This result also indicates that a possible source of improvement lies in the mixing mechanism between main flow and tip leakage flow, after the ejection point in the suction side.

The change of geometry has an effect on the turbine capacity as well, as shown on the right plot. While the 'BestAero' configuration has an almost null mass flow variation with respect to the squealer, the 3 variants seem to provide up to +0.50% variation (on case of 'Geom 2') or -0.50% variations (for 'Geom 1' and 'Geom 3') of passage mass flow.

Several methods have been proposed over the past years to identify vortical structures. For the following analysis, the Q-criterion [31] is used to identify tip vortex and passage vortex. The topology identified with this method has then been compared to the one obtained using a λ_2 criterion. Similar structures can be distinguished, as shown in Figure 2.30.

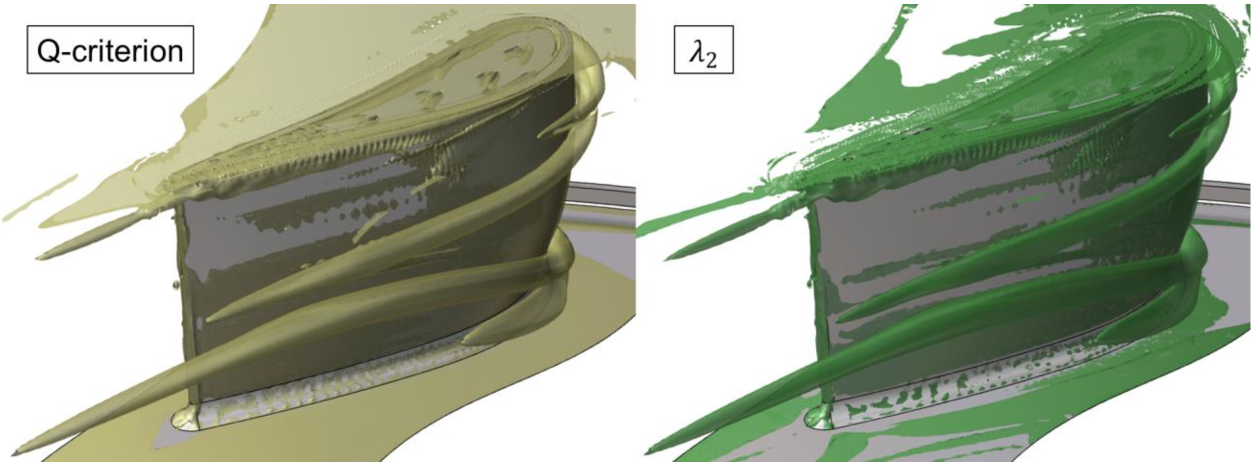

Figure 2.30: Vortical structure for Q-criterion (on the left) and λ_2 criterion (right).

This is consistent with the results discussed in the literature [32]. Even though operating with non-zero threshold introduces arbitrary choices in the application of the methods, it has been studied how qualitatively they identify similar vortex core structures. The thresholds used for the results in Figure 2.30 are selected based on the suggestions in [32].

The Q-criterion is then selected and used to visualize the vortex topology for simple squealer and optimized geometries. Figure 2.31 shows iso-surfaces of Q-criterion contoured with the sign of the streamwise viscosity. In this way, we can identify simultaneously the individual vortices but also their sense of rotation (whether clockwise or counter-clockwise). Please note that the iso-surface were cut around mid-gap to remove the uniform vorticity field due to the relative motion of the casing.

On the left, the baseline airfoil is showed. The upper and lower passage vortices can be clearly distinguished. Given the low aspect ratio of the blade, the passage vortex has a large axial extent and it migrates towards midspan. As expected, the lower and upper passage vortices have an opposite sense of rotation, highlighted by positive and negative vorticity (red and blue colors). Close to the trailing edge the secondary flow dominates the entire flow field and a clean flow can no longer be distinguished. Focusing on the tip region, a continuous tip vortex can be identified. The leakage flow passes over the continuous rim on the suction side and rolls in clockwise direction. The growth of this vortex is continuous over the entire suction side. We can also distinguish the scraping vortex on top of this leakage vortex, due to the shear induced by the movement of the casing. This vortex, rotating in a counter-clockwise direction, is confined close to the casing because of the blockage of the tip flow.

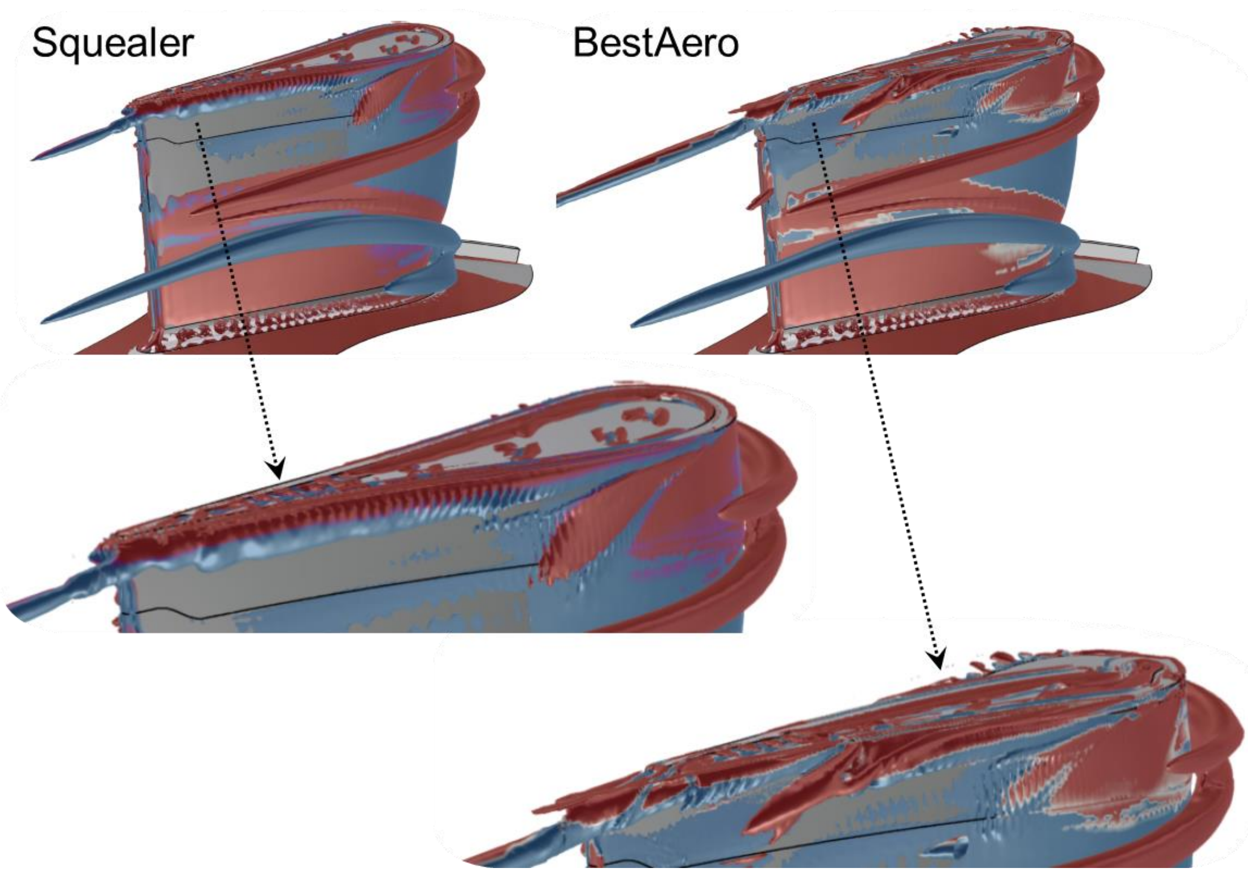

Figure 2.31: Q criterion iso-surface for simple squealer and optimized airfoil.

On the right, the secondary flow for the optimized tip is shown. Upper and lower passage vortex can still be identified, and they are qualitatively similar to the baseline configuration. The zoom on the tip region, highlighted in the bottom right, allows identifying two main differences. The tip leakage vortex starts now to develop in the recess on the suction side, which provides a platform for the vortex growth and keeps it blocked close to the tip region. Once the pocket is over, and the rim reaches the suction side, the vortex is interrupted and it migrates towards midspan. The blockage induced by the developing tip vortex is drastically reduced, and this leaves room for the scraping vortex to grow and migrate towards a lower radius. As the tip vortex starts to grow again, is limited in intensity compared to the one in the baseline design. Moreover, it is confined to a higher radius thanks to the blockage induced by the scraping vortex. Being counter-rotating, the two vortices do not merge limiting therefore the losses due to the combined secondary/tip flow. These characteristics can be encountered in Figure 2.32, where the surface shear stress vector lines are depicted over contours of static pressure.

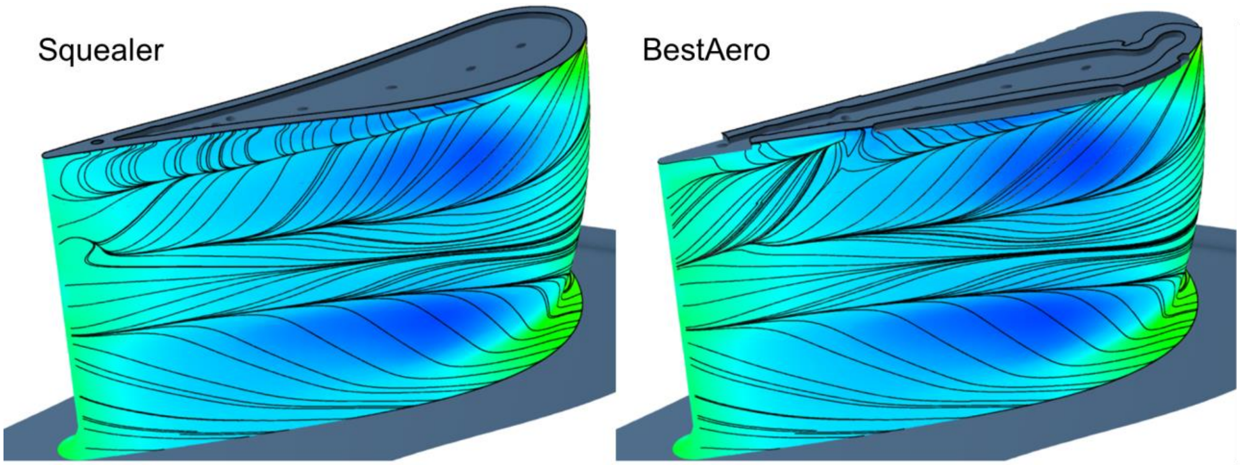

Figure 2.32: Shear stress vector lines over contours of wall pressure for simple squealer (left) and optimal tip (right).

The surface streamlines are consistent with the vortex cores identified with the Q criterion. On the left it can be seen that for the simple squealer the tip vortex grows continuously along the suction side until reaching the trailing edge. On the right, we can see that the tip leakage vortex is clearly divided into two branches. There is a first half below the suctions ide pocket that is then abruptly interrupted. There is a second tip vortex growing in the rear part of the airfoil, which does not mix with the first branch.

Eventually, based on simple turbomachinery theory, the work extracted by a turbine can be described as Euler's work:

$$\Delta H = U_2 V_{t2} - U_3 V_{t3} \tag{2.6}$$

Hence, it is relevant to investigate the tangential velocity downstream of the turbines. Figure 2.33 contains a histogram plot of the tangential velocity in a plane half axial chord downstream of the rotor trailing edge. The height of each bar represents how much mass flow has that level of tangential velocity. So if the flow were uniform, there would be a single bar with the height of the total mass flow. Hence the spread of the bars represents the non-homogeneity of the flow.

The black bars refer to the simple squealer, while the red bars stand for the optimized geometry. First, we can see a large velocity variability in terms of range, since the V_t ranges from less than -150m/s to +180 m/s. The averaged values in the two geometries are close, but the distributions show different regions (around 50 m/s and for velocities higher than 100 m/s).

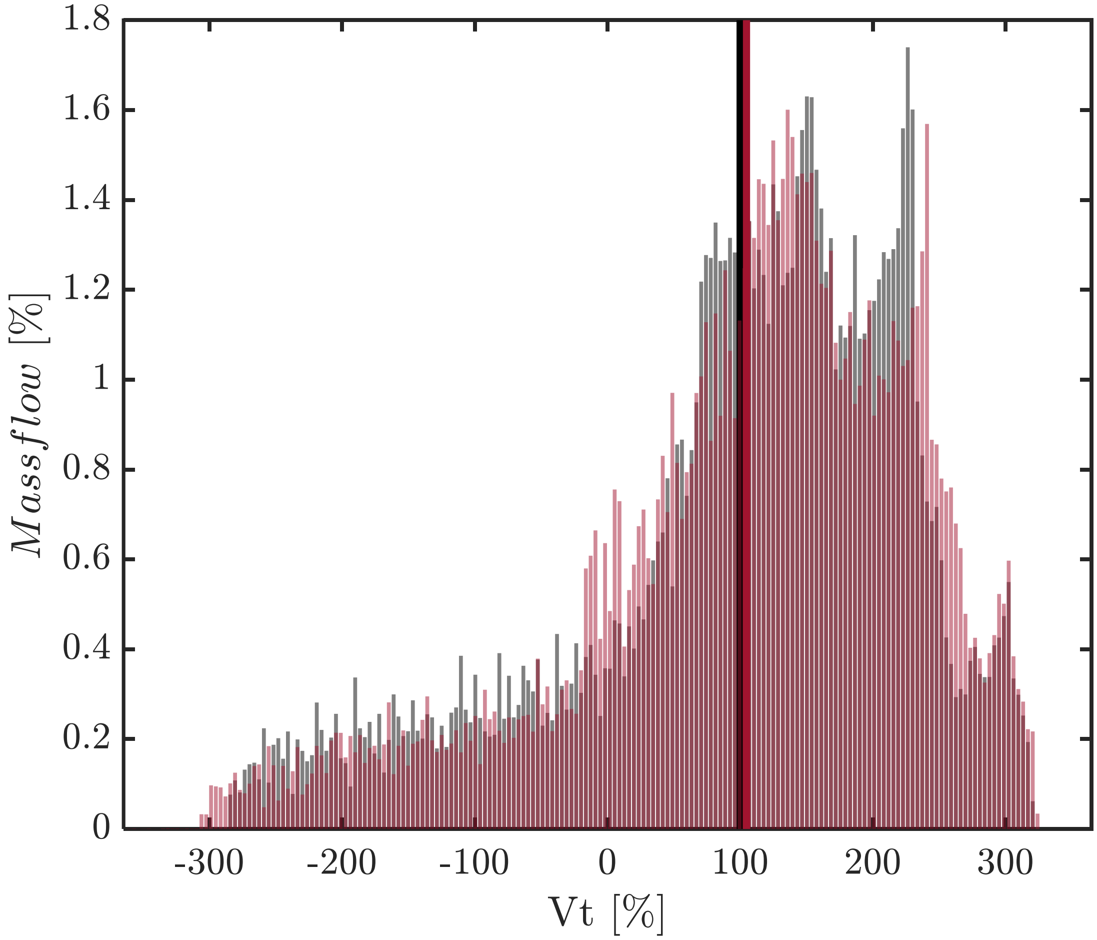

Figure 2.33: Histogram of absolute tangential velocity at the turbine outlet for baseline (black bars) and optimal geometry (red bars).

Based on Equation 2.6, it can be concluded that a higher tangential velocity at the rotor outlet will cause a larger enthalpy drop and consequently a larger work extraction from the turbine.

2.3.2 Analysis of Optimal Profiles for Multiple Clearances

In this section, we analyze the features that characterize the Pareto front obtained in Chapter 2.2.2.

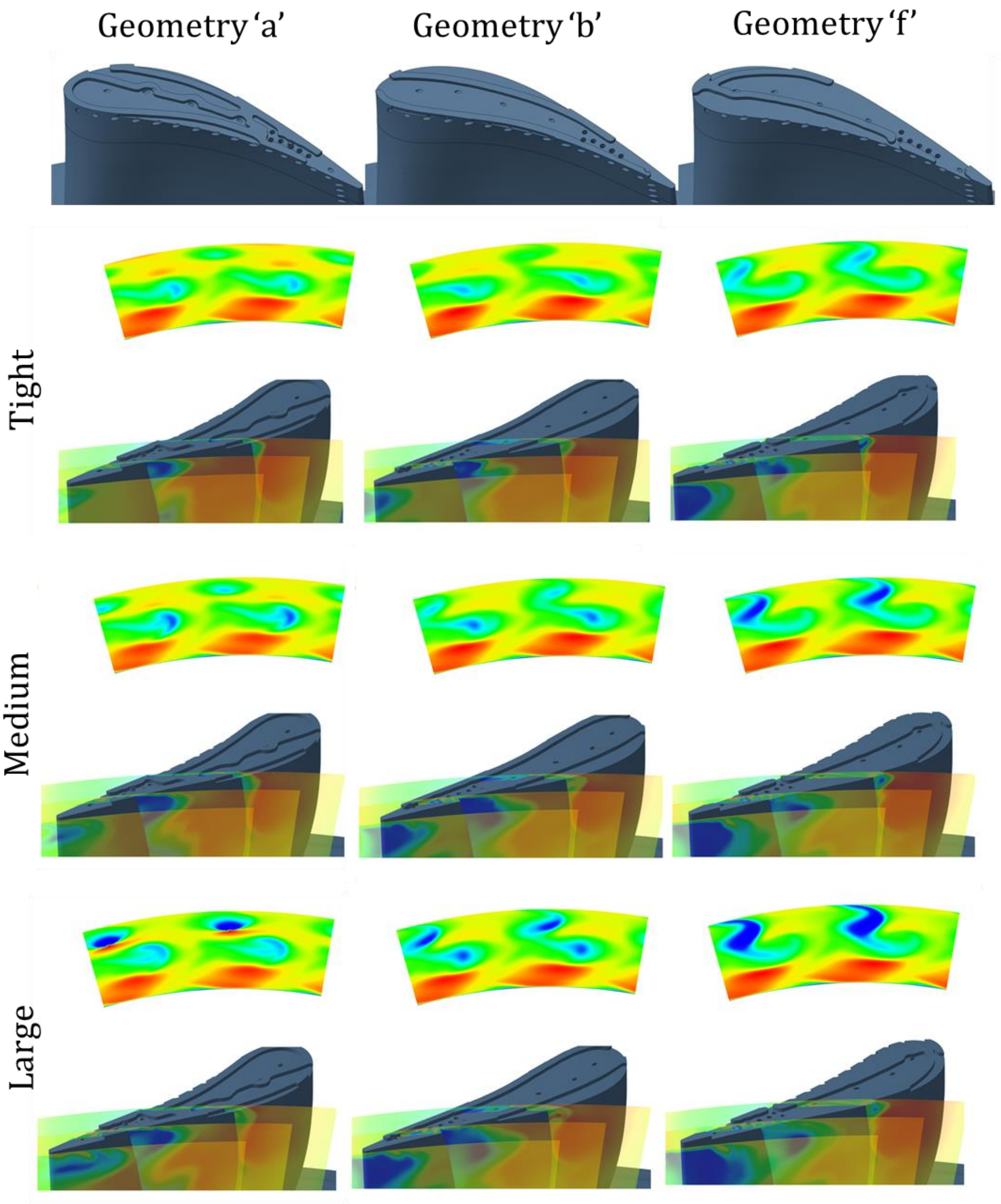

Figure 2.34: Relative Mach number contours at the outlet and in the tip for geometry 'a', 'b' and 'f'. The different geometries are on each row, and the three clearances are on each column.

Figure 2.34 shows three different geometries, coming from the Pareto front identified in Figure 2.21. The three geometries are identified with ‘a’, ‘b’ and ‘f’ on the plot.

The geometry ‘a’ has the highest mean efficiency, and its topology is similar to the tip designed with the single-point optimization. The geometry has a rim on suction side that is slightly recessed. This feature allows the leakage vortex to start growing, and analogously with the previous discussion is interrupted at around 70% of the axial length. The scraping vortex has room to migrate downwards and it locates between the passage vortex and the leakage flow. This is visible in the contour of relative total pressure downstream of the blade, where the two vortex cores are clearly identifiable and separate. For the large clearance, geometry ‘a’ still shows two separate vortices, but their strength appears to be increased. Hence, the efficiency variability at large clearances. As we move to the other two geometries, we have tips that offer a more constant performance but with lower mean values. The geometry ‘b’ has a rim close to the suction side, but the recess is larger. In this case the vortex and the passage vortices are merged together but seem to have distinct cores. The cores appear to be more energized than the previous geometry. Finally the third geometry is characterized by a single large vortex that incorporates the incoming secondary flow and the tip leakage. This geometry offers low mean efficiency but maintains pretty constant performance over a wider range of clearances. It seems that for this type of geometries, the losses reduction does not involve phenomena connected to viscous effects that vanish for large clearances. For a tip-insensitive performance, the tip should exploit features that involve leakage reduction.

2.3.3 Leakage Characteristics

In the following analysis, the optimal profiles from Chapter 2.2.1 will be considered. Figure 2.35 visualizes the two optimal geometries (optimal efficiency and optimal heat flux) and the baseline case. The mass flow in the tip gap is integrated in the radial direction along the profile for each geometry (Figure 2.35a). The red color indicates mass flow entering the tip gap region, while the blue color represents mass flow exiting the tip gap region. The vectors indicate the flow direction and are proportional in size to the amount of local mass flow. Figure 2.35b illustrates the surface streamlines on the blade tip. The yellow color contour on the blade highlights the regions with high heat flux (higher than the 175% of the average heat flux on the tip of the baseline squealer).

Two main phenomena drive the over-tip gap flow field: the pressure gradients and the viscous forces. The pressure gradient drives the flow across the tip gap from pressure to suction side. Within the reference frame of the rotor, the case has a tangential speed opposed to the blade. Due to the fluid viscosity, the case drags a layer of flow from suction to pressure side, against the pressure gradient. The size of the tip clearance is one of the main factors that determine the relative importance of each phenomenon. For tight clearances the flow is mainly driven by viscosity, while for large tips gaps the gas follows the pressure gradients from pressure to suction side.

The simple squealer is characterized by a leading edge region which acts as an uninterrupted inlet. Most of the incoming gas is ingested near the leading edge. The inlet extends along the suction surface with the flow monotonically decreasing until an inflection point, indicated by the dashed ellipse. The inflection point coincides with the end of the high heat flux region shown in Figure 2.35b. After this point the suction side acts as an outlet. This distribution is consistent with the streamline plots in Figure 2.35b. The first 25% of the blade axial chord of the pressure side also acts as inlet, after which small regions of inlets and outlets alternate. Near the trailing edge flow again enters the blade tip region. The mass flow distributions for the three geometries suggest the influence of both viscous and pressure forces. This is illustrated by the higher number of inflection points and abrupt changes in the magnitude of mass flow as seen in Figure 2.35a.

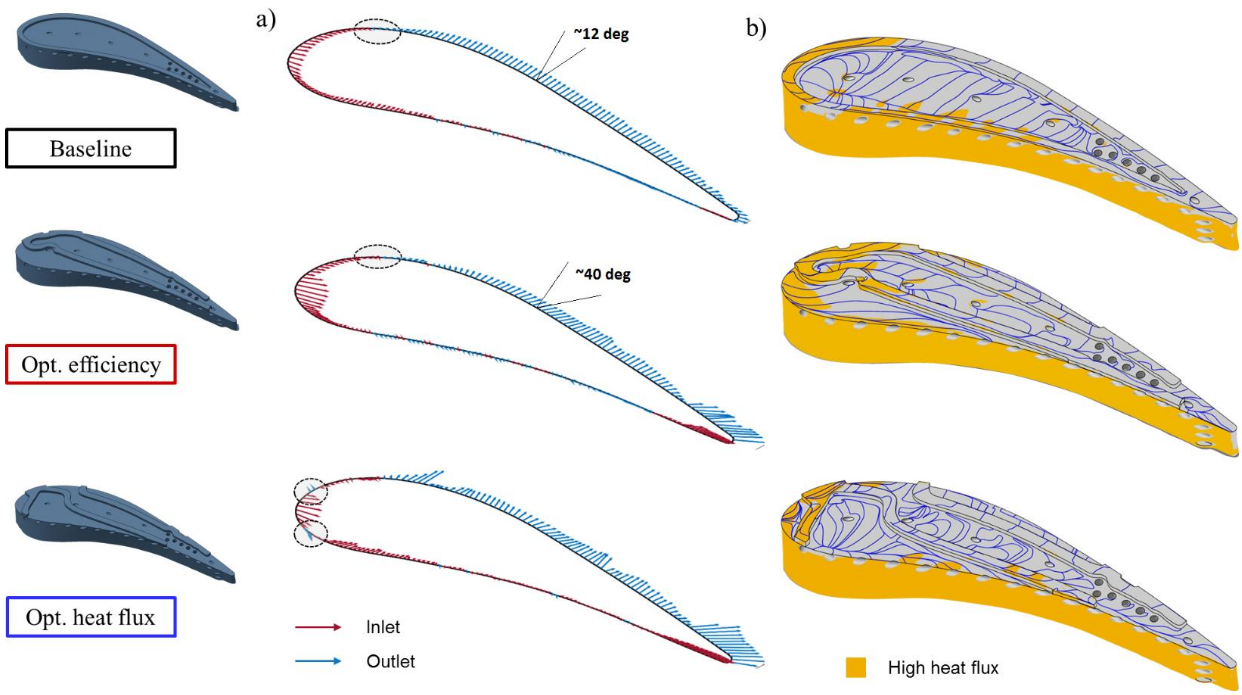

Figure 2.35: Tip leakage characteristics.

As previously shown, the optimal efficiency geometry has a large amount of mass flow entering from the leading edge due to the absence of the leading edge rim. The leading edge inlet region is more concentrated than the baseline. Minimal over-tip leakage is seen entering along the entire length of the pressure side with the exception of the trailing edge region. This suggests a balance between the viscous and pressure forces. The suction side is characterized by a continuous outlet with non-uniform distribution of mass flow. As shown previously, the mass flow exits the suction side farther downstream. The large pressure side inlet and suction side outlet are a direct result of the absence of a rim.

In Denton's seminal work on turbomachinery loss, he shows that the rate of entropy generation for the mixing of over-tip leakage flow and the gas-path flow is a function of the stagnation temperatures of the flows, the ratio of the velocities, the ratio of the flow rates, the Mach of the primary flow stream, and the injection angle of the leakage flow. The optimal efficiency configuration has a radially-averaged re-entry angle more aligned with the freestream flow field (see the angle callouts of Figure 2.35b). According to Denton's work, this reduces the entropy generation due to the reintroduction of the leakage flow. This entropy generation reduction is a source of efficiency improvement.

The leading edge region of the optimal heat flux design is characterized by a large inlet, bordered by two small outlets at each extremity of the rim. A large outlet on the suction side is observed adjacent to the gap between the suction and pressure side rims just downstream of the leading edge. Based on the streamlines from Figure 2.25, this outlet is comprised of leading edge and cooling flow. The leading edge flow takes a circuitous route to arrive at this outlet, with most of it navigating around the pressure side of the leading edge rim and then crossing the airfoil. Downstream of this outlet, the flow field is similar to the optimal efficiency geometry.

Modifications to the tip geometry have a direct impact on the overall tip leakage as the relative blockage of the tip gap changes with varying rim placement. In addition, varying rim placement changes the blade tip pressure distribution, which changes the tip coolant flow rates given the applied boundary conditions described earlier in Table 1. Table 2 summarizes the tip leakage and tip coolant levels for the baseline, optimal efficiency, and optimal heat flux designs. The tip leakage and tip coolant flow rates are normalized by the total inlet flow rate of the rotor.

Table 2.2: Tip leakage and cooling flow accounting.

	Baseline	***Optimal Efficiency***	***Optimal Heat Flux***
$\dot{m}_{tip,leakage}/\dot{m}_{passage}$ [%]	0.70%	1.06%	1.19%
$\dot{m}_{tip,cool}/\dot{m}_{passage}$ [%]	1.03%	0.99%	1.13%
$\dot{m}_{tip,leakage}/\dot{m}_{tip,cool}$	0.67	1.07	1.06

As Table 2 shows, both the optimal efficiency and optimal heat flux designs significantly increase the over tip leakage flow, while the overall coolant flow is less influenced by the rim changes. The increase in turbine efficiency for the optimal geometry designs coupled with the increase in tip leakage flows suggest that the negative effects of over-tip leakage flow can be minimized with careful re-introduction of the leakage flow to the primary gas path.

A comparison of the ratio of the tip leakage and the tip coolant flow rates is interesting. In the case of the optimal efficiency, the leakage rate increases dramatically (50%), while the coolant flow rate remains similar to the baseline. In spite of this large increase in tip leakage relative to tip coolant, the average heat flux of the blade tip remains relatively the same as the baseline (see Figure 2.16). The optimal heat flux design also has a significant increase in over-tip leakage (70%)

and an increase in the tip coolant flow (10%). In this case, the blade tip heat flux still decreases 65%.

2.3.4 Losses Breakdown

A simplified explanation of the generation of losses due to tip flow is given by Denton [21]. In Denton's work, the tip vortex is described as an angled jet that mixes with the main flow. This approach may be practical for flat blade tips but may not appropriately describe the complex flow fields [33] occurring in non-flat tip geometries (e.g., squealer tip designs) [34].

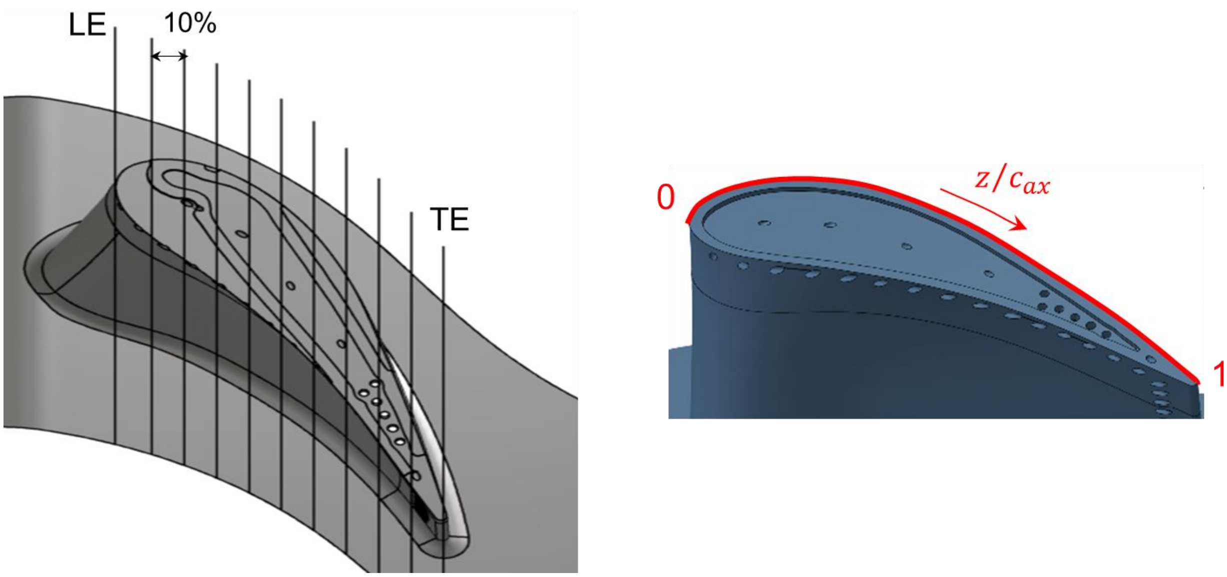

Figure 2.36: Schematic of the optimized blade with details of axial coordinate.

To understand the tip losses it is necessary to quantify not only the leakage flow, but also the leakage characteristics when the jet mixes with the main flow. Figure 2.36 shows a top view of the blade, with details of the turbine tip rails. The black lines originate from the leading edge and are scattered till the trailing edge with intervals of 10% of the axial chord. These lines will be useful for the interpretations of the following graphs where the abscissa is expressed in terms of axial location as a percentage of the axial chord.

First, the leakage flow through the baseline and the optimized blade are analyzed in Figure 2.37. This quantity is a quantitative representation that corresponds to the tip leakage characteristics qualitatively showed in Figure 2.35.

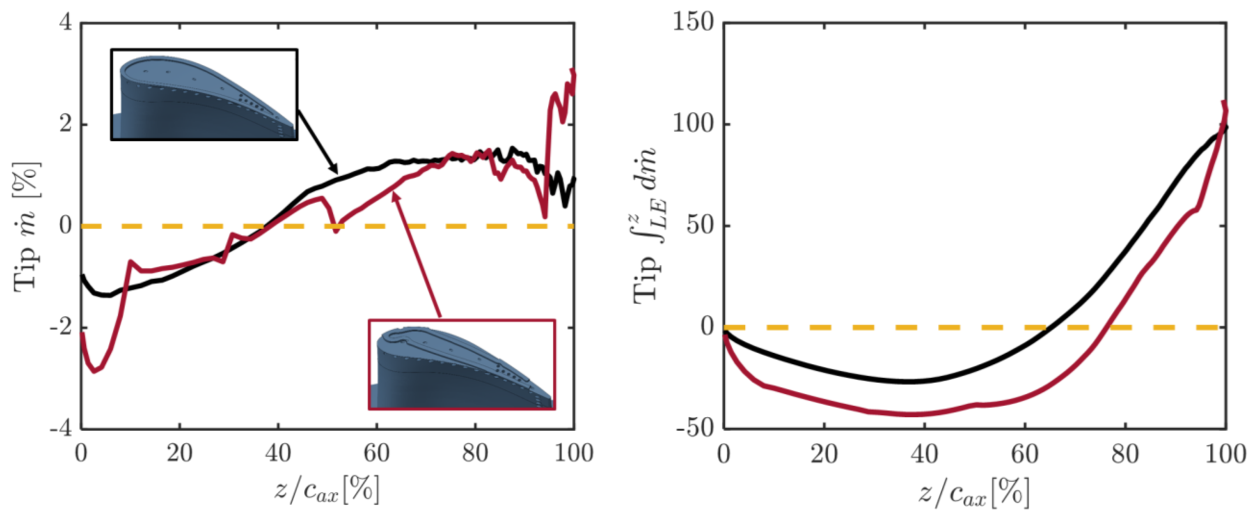

Figure 2.37: Left, Tip leakage mass flow for optimized geometry (red) and simple squealer (black). Right, Cumulative tip mass flow for optimized geometry (red) and simple squealer (black).

On the left, we can find the local mass flow through the suction side of the baseline and the optimized blade. The line at zero mass flow is marked with gold, to have a reference to identify the inlet and outlet regions. First of all, it is interesting that a large portion of the suction side, approximately the front 40%, is an inlet (negative mass flow) instead of an outlet. This detail is consistent with the streamline visualization described in Figure 2.25. The best efficiency geometry, indicated with red, has an inlet mass flow in the front 10% of the axial chord that is double than the baseline value. While the two geometries tend to have a similar behavior between the 40% and 50% of the blade, the two trends become sensitively different between the 50% and 80% of the axial chord. A final significant difference between the two geometries can be identified in the trailing edge region (rear 10% of the axial chord). This feature is due to the best efficiency geometry having an open trailing edge vs. the closed trailing edge of the simple squealer.
On the right, we can see the cumulative integral of leakage mass flow as a function of the axial chord. For each axial location, the cumulative sum of mass flow is computed as:

$$\int_{LE}^{z} d\dot{m} \Big/ \int_{LE}^{TE} d\dot{m}_{base} = \sum_{LE}^{i(z)} d\dot{m} \Big/ \sum_{LE}^{TE} d\dot{m}_{base} \tag{2.7}$$

Since the curves are both normalized with the baseline total mass flow, both lines have origin in zero but only the squealer goes precisely to 100% of the leakage mass flow at the trailing edge. The difference between the red and the black line at 10% of the axial chord should match the difference in leakage flow, as reported in Table 2.2. Consistently with the plots on the left, the optimized geometry has a negative leakage flow in the first portion of the blade, which generates a difference between the two curves that propagates until the very last portion of the blade, close to the trailing edge. This result is an indication that is not only the total leakage flow to determine tip losses, but also the location where this flow is injected into the flow.

According to the model of mixing between two angled jets, the angle of injection plays a significant role in the mechanism of generation of losses. For this scope, in Figure 2.38 on the left, the flow angle in the tangential direction is shown for both the overtip region and the main flow in the passage. On the right graph, we calculate the difference between the leakage flow angle and the main flow angle. The closest this value to zero, the more the leakage is aligned to the flow, which would imply a reduction of the mixing losses.

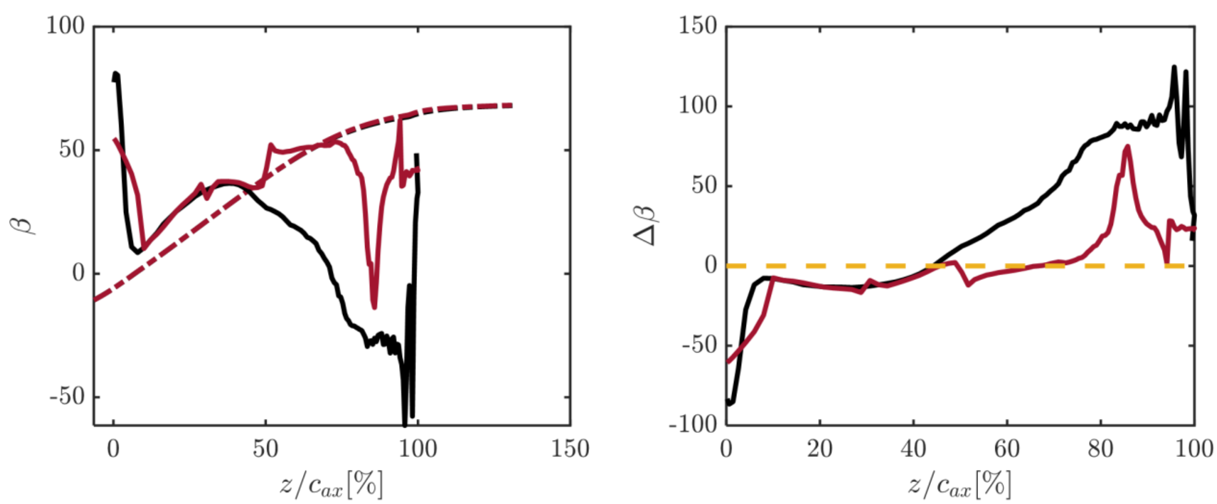

Figure 2.38: Relative velocity angle for optimized geometry (red) and simple squealer (black) in the main passage (dashed lines) and tip (solid lines) against axial location.

In the front part, the angle distribution is similar between the two geometries. However, in the second half of the blade, the two trends depart. The black line (simple squealer) continuously decreases until the trailing edge, increasing the difference with main flow angle as a consequence. For the optimal geometry, indicated in red, the value of the flow angle stays high and relatively close to the angle of the main flow. This trend is then interrupted at approximately 80% of the axial chord, where the rim on the suction side stops and the tip becomes fully open.

The relative Mach number plays a role as well in the mixing phenomenon. In particular, Denton [21] shows that the injection at higher Mach number can be more detrimental. Figure 2.39 represents the distribution of Mach number along the passage, dashed line, and in tip gap on the suction side, solid lines. Again, the trends are similar in the first half of the blade for the optimized blade and the simple squealer. However, there is a significant difference between 50 and 80% of the blade. In the optimized blade, the leakage flow is more accelerated in the region where the relative angle is minimal, which seems to be advantageous to reduce the mixing losses.

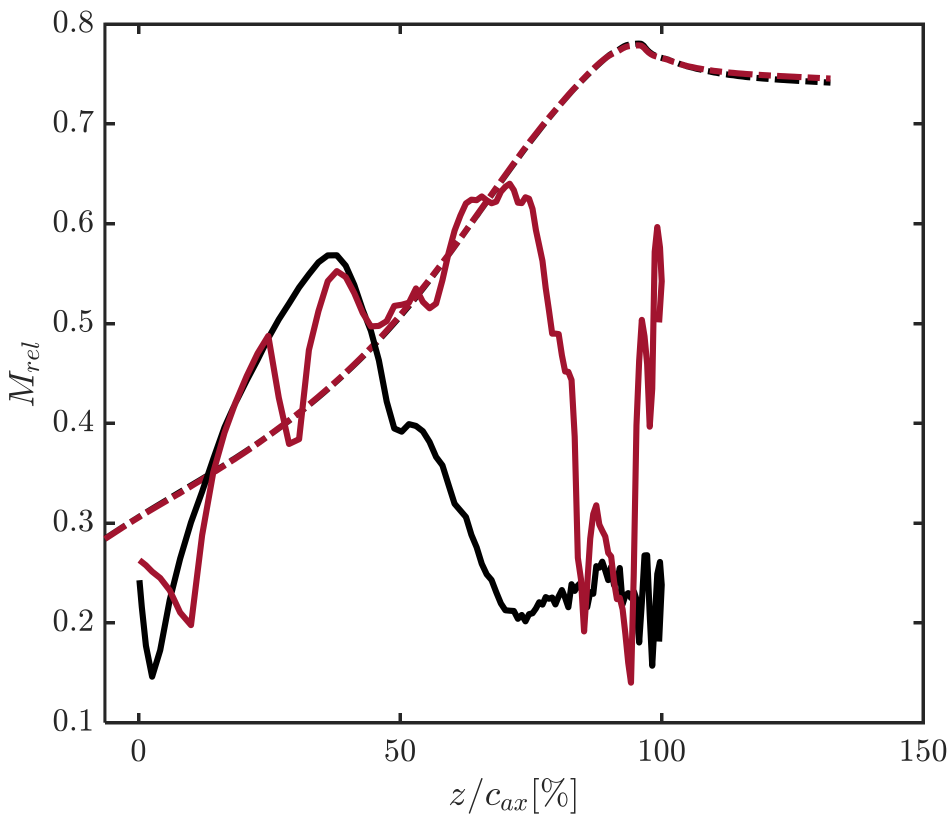

Figure 2.39: Relative Mach number for optimized geometry (red) and simple squealer (black) in the main passage (dashed lines) and tip (solid lines) against axial location.

Finally, the different sources of losses are summarized in Figure 2.40. Previous studies have applied this model to analyze tip losses with a simplified approach [35, 36]. The passage is discretized into a series of small control volumes in the axial direction, and the following equation is assessed in each of them:

$$\Delta s = c_p \frac{\dot{m}_{leak}}{\dot{m}_m}\left[\left(1 + \frac{(\gamma - 1)}{2} M_m^2\right)\frac{T_{0c} - T_{0m}}{T_m} + (\gamma - 1) M_m^2 \left(1 - \frac{V_c}{V_m}\cos\alpha\right)\right] \tag{2.8}$$

In Figure 2.40, Δs_i indicates the different sources of losses in the previous equation, where the index ‘i ‘goes from 1 to 5. The first term is the ratio of the leakage mass flow and the passage mass flow. Hence, the larges the leakage, the higher the entropy raise. The second term is proportional to the square of the Mach number at which the mixing is taking place. If the mixing happens at a higher Mach number, the model predicts larger losses. The third term becomes relevant when the small jet and the main flow have different temperatures. In uncooled turbine blades, this term is normally small or even negligible. However, in cooled turbine rotors, the redistribution of leakage flow causes different blockage in the overtip gap which affects the coolant flow. Hence, in cooled tips, the difference between leakage temperature and main flow temperature can be significant.

$$\Delta s = c_p \overbrace{\frac{\dot{m}_{leak}}{\dot{m}_m}}^{\Delta s_1}\left[\left(1+\overbrace{\frac{(\gamma-1)}{2}M_m^2}^{\Delta s_2}\right)\overbrace{\frac{T_{0c}-T_{0m}}{T_m}}^{\Delta s_3} + (\gamma-1)M_m^2\left(1-\overbrace{\frac{V_c}{V_m}}^{\Delta s_4}\overbrace{\cos\alpha}^{\Delta s_5}\right)\right]$$

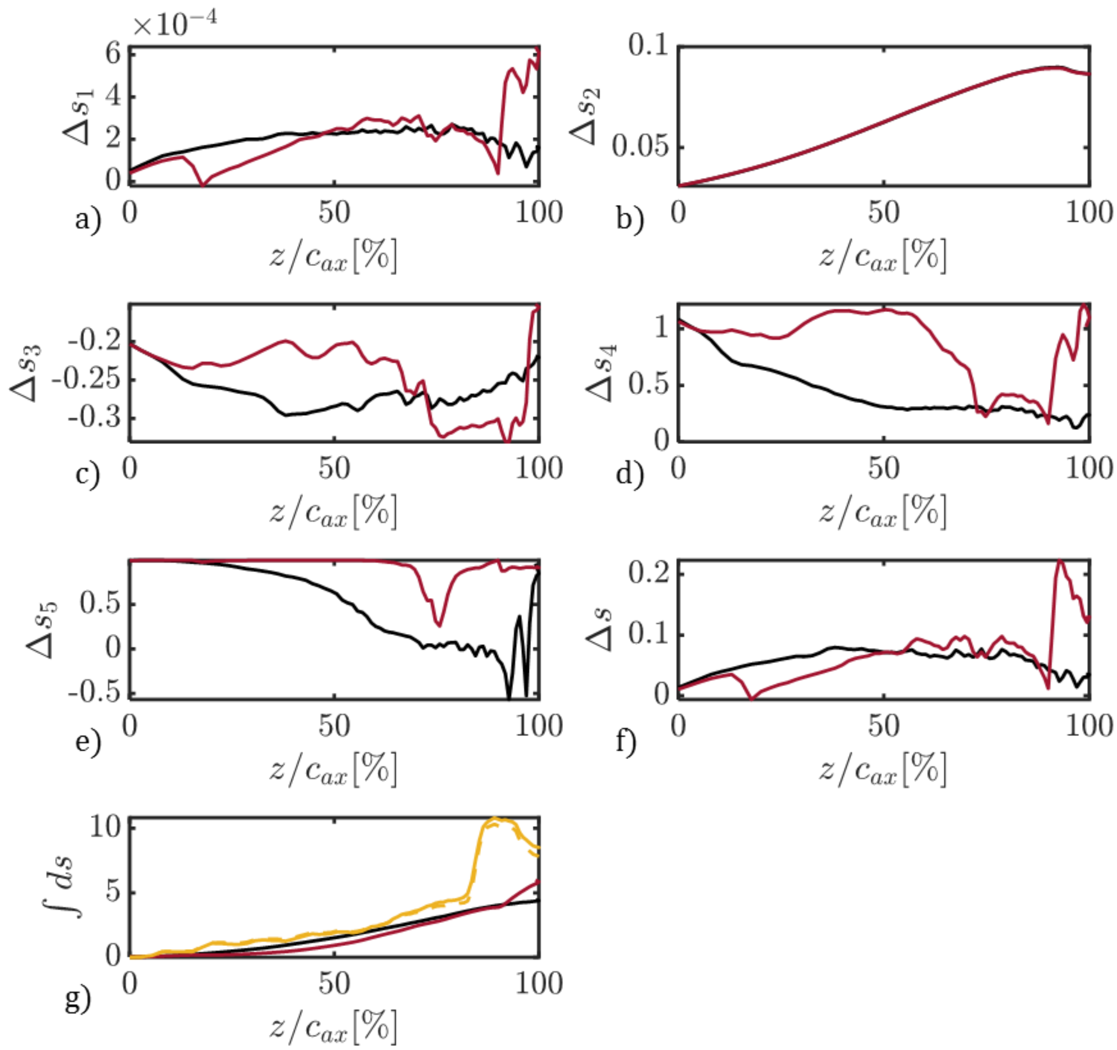

Figure 2.40: Loss model based on the method described by Denton [21].

The forth term is proportional to one minus the ratio between the leakage velocity and the passage velocity and the fifth term is the cosine of the relative angle between the two flows. These terms indicates that the losses are reduced if the two velocities have comparable magnitude, or if the angle between the two flows is null. The limiting case has two aligned jets with the same velocity, where the second term of the entropy equation would go to zero.

Figure 2.40, ‘a’ shows the first term related to the leakage flow ratio. As shown in the previous section, the optimized tip does not act through a leakage reduction. Hence we cannot expect this term to be the most beneficial in this analysis. In fact, we can see that even though the optimized tip works towards leakage reduction in some limited regions, the overall tip flow is higher compared to the baseline case. The term number three shows significant differences between the two geometries, highlighting the effect of the rails on the distribution of coolant. The term number four, which represents the velocity ratio, is close to 1 for the front 50% of the optimal tip, while for the squealer, the velocity ratio continuously decreases from leading to trailing edge. This gap is due to the recess on the suction side in the optimal tip, which allows the leakage flow to expand and accelerates before mixing. The difference between the two tip configurations is canceled out when the rim reaches the suction side, around the 80% of the blade. However, in the last 10% of the blade where the optimal trailing edge is fully open, the velocity in the optimized tip will suddenly increase again. In this section however, the leakage flow is not guided in the direction of the main flow but on the contrary is free to directly flow from pressure to suction side. The graph ‘e’ refers to the cosine of the relative flow angle. Hence, if the angle goes to zero this term will tend towards one. This graph shows the largest differences between optimized and baseline blade. The red curve lies above the black line everywhere in the suction side. In the squealer, the angle between the leakage and the main flow continuously increases from leading to trailing edge. For the optimized blade, the term is closed to one for the front 80% of the blade and only has a value drop close to the blade 80% where the pocket is abruptly interrupted. Finally, graph ‘f’ shows the local increase of entropy for the two geometries, and graph ‘g’ shows the resulting local entropy value as predicted by the model and by the CFD (colored in gold).

2.4 Effect of Coolant Injection on Optimized Tip Performance

The cooled rotor configuration used as baseline geometry contains both platform coolant injection and blade film cooling. To verify the extent of the results obtained from the optimization, we have to characterize the robustness to the amount and location of injected coolant. In particular it needs to be verified that performance enhancement due to tip shape can be extrapolated to different cooling configurations. In this analysis, two tip geometries are compared: the simple squealer, whose performance is always used as reference, and the optimal efficiency from the single point optimization (geometry ‘a’ in Figure 2.16).

Effect of Purge Flow

The first step is to individually turn off the platform cooling in each location. Figure 2.41 shows the difference of efficiency for squealer and optimal tip, colored in blue and orange respectively.

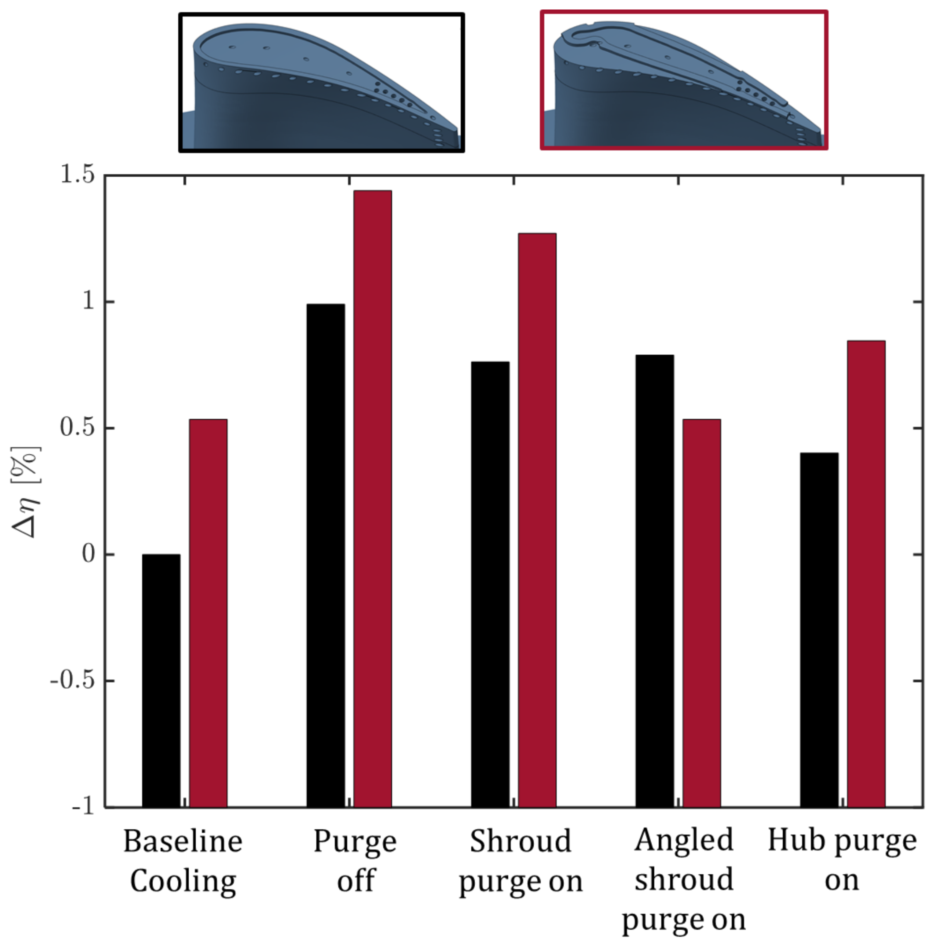

Figure 2.41: Effect of purge flow on turbine efficiency.

In the first column on the right, indicated with baseline, we find the performance of the two geometries in the configuration used for the optimization. The squealer bar is equal to 0% because this is the reference value, and the height of the orange bar indicates the efficiency enhancement found during the optimization. If all the purge channels are turned off, and the injected mass flow is set to null, we find an overall increase of efficiency (two bars indicated with Purge off). The difference between the two geometries is kept constant compared to the baseline configuration. This result indicates that the optimal geometry is still more efficient than the squealer, even without platform cooling. We then analyze individually the contribution of the three injection locations, by turning on the casing slot, the angles casing slot and the hub slot. The two straight injections at hub and casing do not modify the performance improvements due to the optimal shape while modifying the absolute values of efficiency. However, the injection of coolant at an angle appears to be detrimental for the optimized turbine performance, that in this case has an efficiency ~0.2% lower than the simple squealer.

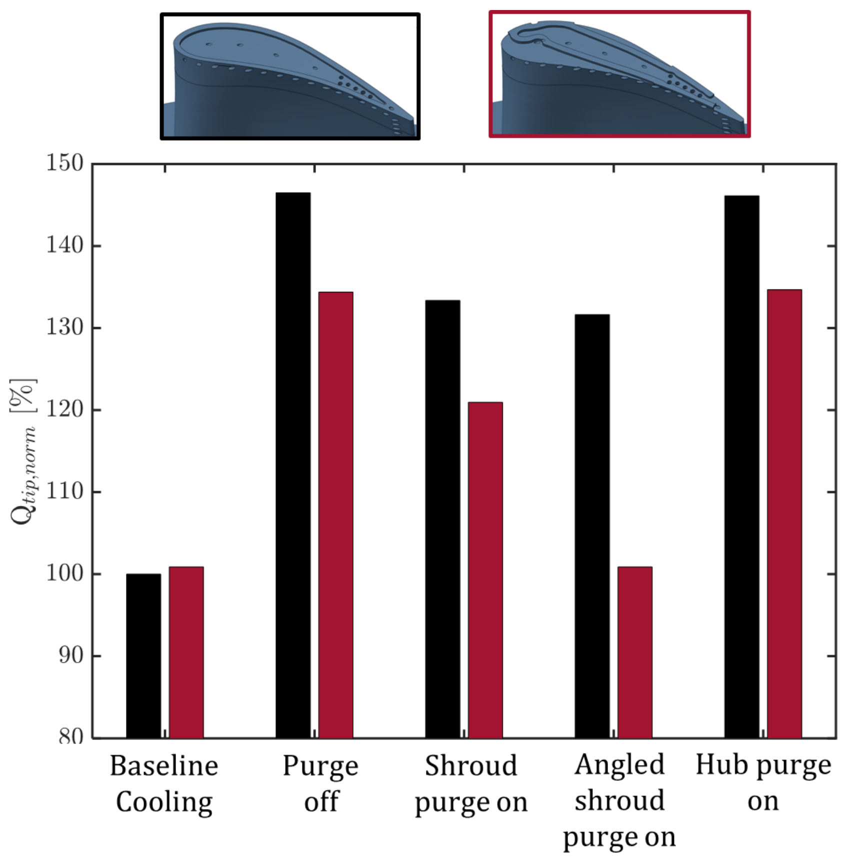

Figure 2.42: Effect of purge flow on blade heat transfer

The injection of platform cooling has a relevant effect on tip heat flux. Figure 2.42 shows the integral heat load on the top part of the blade with different purge configurations. The first column, indicated with baseline, refers again to the standard configuration. As seen in Figure 2.16, the optimal geometry and simple squealer have a similar tip heat load.

When all the purge slots are turned off, the tip heat load in the squealer increases of approximately 50% compared to the baseline configuration. In this case, the optimal geometry offers a reduction of the 10% of heat load. A similar trend can be seen if only the purge slot is active (last column on the right). This indicates that the hub purge does not have a relevant effect on the heat transfer phenomena in the tip part of the blade, which is intuitive.

Based on these results, it can be concluded that the improvements of efficiency that have been gained through a tip optimization are not hindered by variations of purge flow.

Effect of Film Cooling

After analyzing the purge, the effect of coolant injection in the blades is analyzed. There are multiple holes on the pressure side, close to the top portion on the blade and along the trailing edge. Additionally, there are several holes distributed on the blade tip surface, at various inclination. For this analysis, only the tip cooling holes were varied, while the rest of the cooling holes are maintained as in the baseline configuration. Figure 2.43 summarizes the results in terms of turbine efficiency. The two lines allow to identify the trend for an optimized blade and a simple squealer. The two lines can be approximated with linear trends with similar slopes. This allows to quantify and exchange rate between total pressure and efficiency. In particular, for pressure variations of approximately the 25%, there is an efficiency loss of the 0.6%.

In the same set of numerical simulations, the effect in terms of variations of heat flux is quantified. Also in this case, the two trends are similar, which allows to define a single slope value for both of them. In this case, a 25% change of coolant pressure makes the tip heat flux range from the 65% to the 110% of the design value.

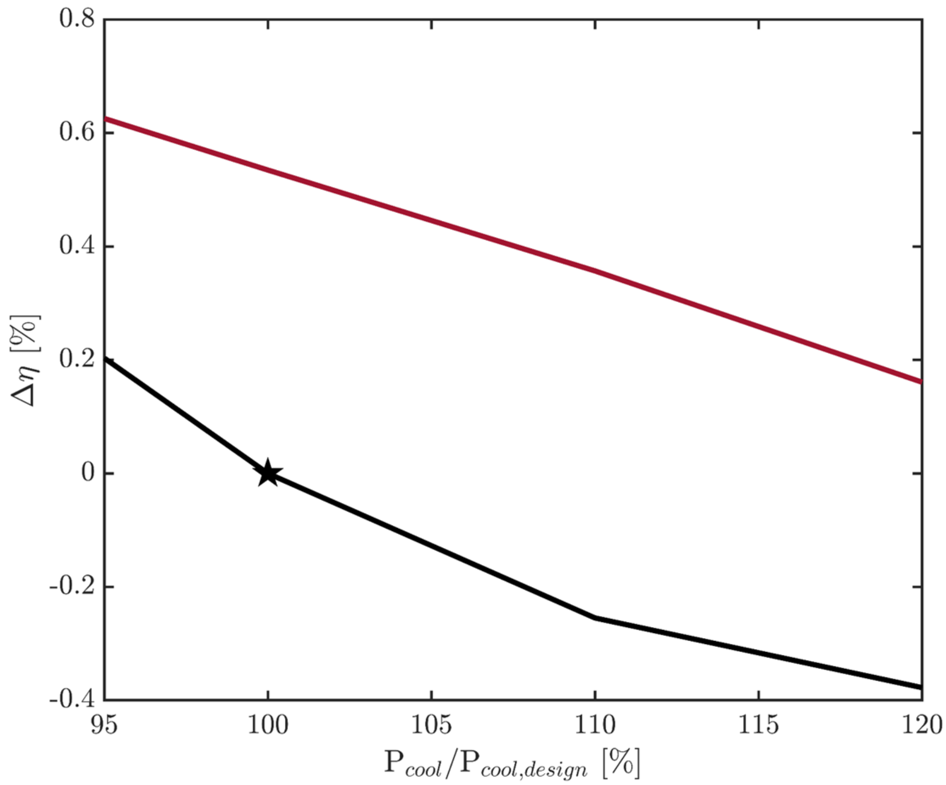

Figure 2.43: Effect of coolant pressure injection on turbine efficiency

To verify that the efficiency improvements will hold without cooling, a simulation without cooling in the tip region is performed. Figure 2.45 shows on the left a bar graph with efficiency, while on the right heat flux. The orange geometry refers to the optimized tip, while the blue bar refers to the squealer. On the left plot, we can see that for baseline cooling configuration the difference in terms of efficiency is around 0.5% while for the configurations without cooling it is around 0.3%. On the other hand, the heat flux that is the same for both geometries in the baseline configuration is suddenly much higher for the optimized tip once we remove the tip cooling. It is interesting that for the squealer, the absence of tip cooling only increases the tip heat flux of the 25%.

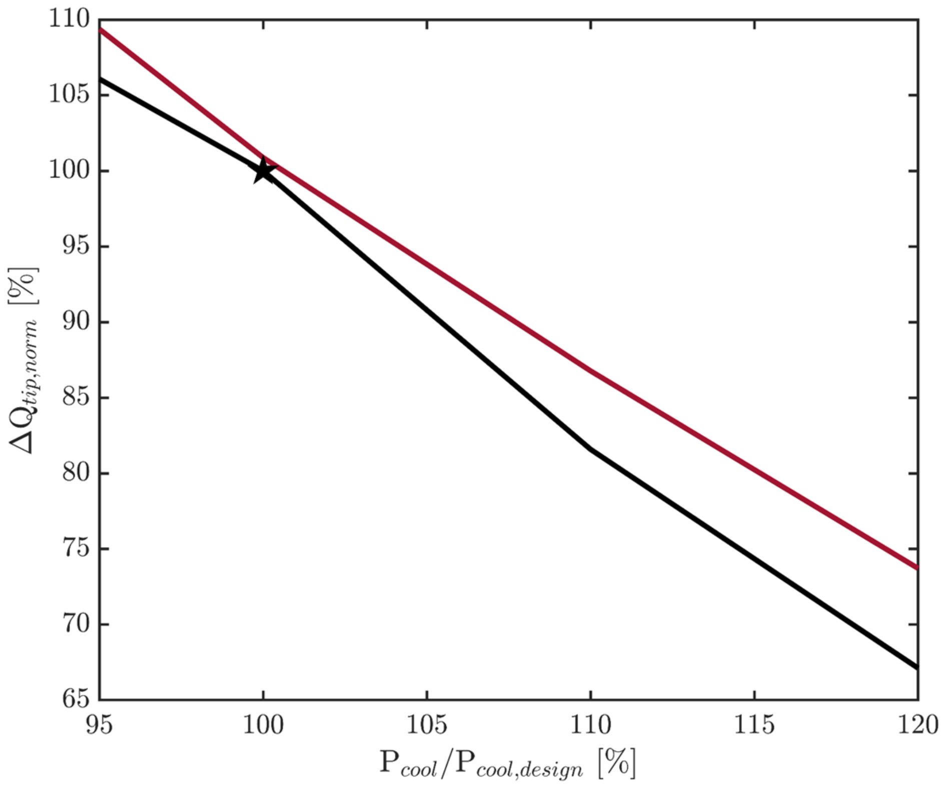

Figure 2.44: Effect of coolant pressure injection on turbine heat flux

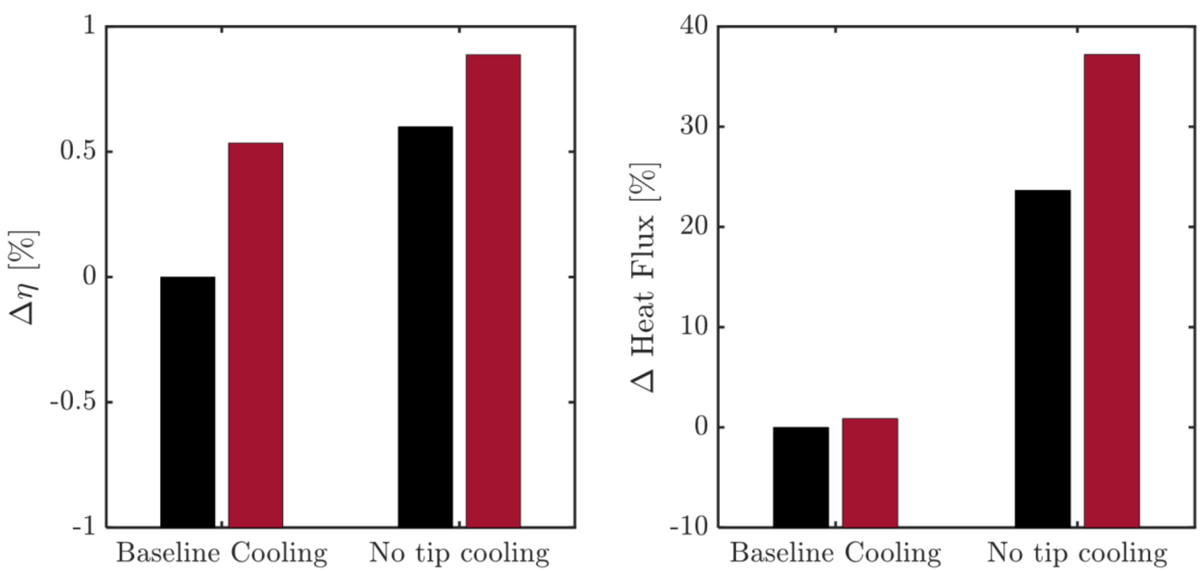

Figure 2.45: Effect of tip cooling on efficiency (left) and heat flux (right)

2.5 Conclusions

The effect of tip leakage has been assessed in a flat tip geometry at various tip clearances. The results indicate that while the flow is dominated by viscous effects when the gap becomes small. The size of the gap affects the amount of leakage flow, as well as on its direction. The changes in leakage impact the main flow, where the total flow is reduced when the leakage flow increases.

Then, the tip shape is optimized for a single tight clearance. A multi-objective optimization routine is implemented to maximize turbine efficiency while minimizing the tip integral heat load. Results show that by changing the number and shape of rail structures on the tip, the efficiency can be improved by 0.53% or the heat load can be reduced by 70%.

An analysis is performed to quantify the sensitivity of the enhanced performance to changes of tip clearance. The study highlights that the improvements obtained by optimizing the shape at tight clearances are not maintained when the gap grows larger.

Hence, it was decided to implement a multi-clearance optimization that would consider the turbine efficiency at three different gaps: a tight, a medium, and a large one. With this approach, the mean efficiency over the three conditions is maximized while reducing the efficiency sensitivity to the clearance.

The optimal profiles are analyzed to identify the mechanism involved in tip losses reduction and how is this related to the rim structure. Detailed quantification of tip leakage properties is performed, and the losses breakdown is discussed. The interaction between leakage vortex and passage vortex is considered to be particularly relevant in this family of small turbines.

Finally, the turbine performance sensitivity to the coolant is investigated. The purge flow and the film cooling are separately varied to assess the effect on turbine efficiency. Two geometries are considered: a squealer, and an optimized tip. Variations of coolant mass flows are obtained by varying the injection pressure. Results show a reasonably linear trend of performance in function of coolant flow. In particular, a variation of -10% of coolant total pressure corresponds to a decrease in the efficiency of 0.3% and a heat load reduction of 20%.

CHAPTER 3. SCALING OF CONVECTIVE HEAT FLUX

3.1 Modeling of Convective Heat Flux*

In order to calculate the convective heat transfer, we need to define an invariant which normally depends on the temperature difference between the flow and the wall. The simplest and most commonly used method is the Newton's law of cooling based in the definition of a convective heat transfer coefficient which multiplies the selected difference of temperatures as specified in Equation 5.

$$h = \frac{\dot{q}_{conv}/A}{T_{flow} - T_{surface}} \tag{4.1}$$

In turbomachinery, the definition of T_{flow} plays a major role in order to obtain the invariant coefficient due to the unsteady behavior of the flow in time and in space. If T_{flow} would be defined using the upstream total temperature of the vane or blade, spatial and temporal variations higher than 100% would be observed in the experimental calculation of the convective heat transfer [37]. These variations are considered not representative of the reality since the thermal boundary layer over the blade is much more stable. Therefore, T_{flow} is commonly defined as the temperature just above the thermal boundary layer known as adiabatic wall temperature T_{aw}, since it is the temperature that the wall reaches in adiabatic conditions. The invariant obtained with this reference flow temperature is the adiabatic convective heat transfer coefficient $h_{adiabatic}$. However, in areas where the boundary layer is not established, with temporal and spatial fluctuations and aero-thermal phenomena dominated by viscous forces, the application of the Newton's law of cooling is questionable. This is the case of the turbine blade tip region.

3.1.1 Green's Function Method

The alternative procedure that we introduce in this section is based on the Green Functions approach to calculate the convective heat flux through the turbine tip. This technique was initially introduced by Sellars [38], who developed the mathematical procedure for a laminar flow in a circular tube and a flat plate. Sellars proposed a linear and discretized function to calculate the

* Section partially published in Andreoli, V., Cuadrado, D.G. and Paniagua, G., 2018. Prediction of the Turbine Tip Convective Heat Flux Using Discrete Green's Functions. Journal of Heat Transfer, 140(7), p.071703.

increment of temperature due to an imposed distribution of heat flux based on the superposition kernel function, which is expressed in Equation 6.

$$(T_{wall} - T_{inlet})_{n,m} = \sum_{i=1}^{n} \sum_{j=1}^{m} \frac{\dot{q_{o,i,j}}}{c_p \dot{m}} g_{n-i,m-j} \tag{4.2}$$

Therefore, the increment of temperature is obtained multiplying a series of coefficients (g*) called superposition kernel function by the measured heat flux. These coefficients are structured in a matrix of n rows and m columns where i expressed the row location and j express the column location of each of the discretized areas. $q_{o,i,j}$ is the convective heat rate in the location i,j and $\dot{m}$ is the mass flow that is entering in the domain. In order to relate this superposition kernel function with the adiabatic convective heat transfer coefficient we need to separate the temperature increment in two parts [39].

$$(T_{wall} - T_{inlet})_{n,m} = (T_{wall} - T_{adiabatic})_{n,m} - (T_{adiabatic} - T_{inlet})_{n,m} \tag{4.3}$$

Where using the superposition kernel function the different parts can be rewritten into Equation 8 below. Equation 8 also expresses the relationship between the adiabatic convective heat transfer coefficient and the green function coefficients.

$$(T_{wall} - T_{adiabatic})_{n,m} = \frac{\dot{q_{o,n,m}}}{c_p \dot{m}} g_{i,i} \tag{4.4}$$

And

$$(T_{adiabatic} - T_{inlet})_{n,m} = \sum_{i=1}^{n} \sum_{j=1}^{m-1} \frac{\dot{q_{o,i,j}}}{c_p \dot{m}} g_{n-i,m-j} \tag{4.5}$$

Equation 4 shows the increment of temperature that each area of the geometry experiments due to heat flux provided in this individual area, while the equation 9 represents the variation of temperature due to the heat flux in the neighbor areas. Therefore, the coefficient $g_{i,i}$ is independent on the inlet temperature and the effect of the heat flux in the surrounding geometry. This coefficient is the nexus between the adiabatic convective heat transfer coefficient and the superposition kernel function which will be called from now on Discrete Green Function (DGF). Since the adiabatic Newton law of cooling is expressed as

$$(T_{wall} - T_{adiabatic})_{n,m} = \frac{\dot{q_{o,n,m}}}{h_{ad,n,m} \ A_{surface,n,m}} \tag{4.6}$$

Hence, the adiabatic convective heat transfer coefficient can be expressed as the Equation below, as a function exclusively of the diagonal terms of the Matrix of coefficients

$$h_{adiabatic,n,m} = \frac{c_p \dot{m}}{g_{i,i} \;\; A_{surface,n,m}} \tag{4.7}$$

For the sake of comparing different models and cases one can derive a local Nusselt number based on the Green Function coefficients. This local Nusselt number is derived from the traditional definition of the Nusselt number, and equation 12.

$$Nu_{adiabatic,n,m} = \frac{C \; c_p \dot{m} / \; g_{i,i} \;\; A_{surface,n,m}}{k} \tag{4.8}$$

Where reference length is the chord (C) and k is the conductivity of the fluid.

The Stanton number, expressed in Equation 4.9 [40], is determined using the coefficients of the DGF Matrix.

$$St_{ij} = \frac{g_{i,j}}{\rho \, U_\infty C_p} \tag{4.9}$$

The advantage of this approach with respect to the definition of the adiabatic convective heat transfer coefficient lies in the easy calculation of the coefficients, using individual heat transfer pulses, and in the accounting of the effect of the spatial neighbor points in the heat calculation of the point one is interested in.

The procedure has been used in a wide range of applications, not only in fundamental flow studies [41], but also concerning the convective heat transfer such us microelectronics cooling [39], [42], internal turbine blade cooling ([43], [44]) and even turbine film cooling [45]. The present methodology is derived from the implementation of linear superposition. The superposition can be experimentally achieved by an array of electrical heaters, releasing independent pulses of heat flux. The temperature field created by these heat flux pulses defines the Green Function coefficients. This approach is equivalent to the Duhamel's Theorem, widely used to solve analytically unsteady heat conduction problems.

A preliminary analysis of the flow and thermal field of a backward facing step was performed to evaluate the behavior of the method in recirculating and velocity-varying flows. The numerical validation and uncertainty analysis were carried out using Fluent and imposing different inlet temperatures, Mach numbers and inlet pressures.

This present procedure can be used in a wide variety of practical turbine applications. In general, a matrix of coefficients is required to express the relationship between localized heat flux pulses to temperature variations along the entire surface.

In this manuscript, we extend the application of the Green Functions methodology to turbine tip flows. The overtip gap is a delicate region in high-pressure turbines, difficult to cool since high-temperature gas enters in contact with the blade surface at high speed. In the tip region, the high loading acting on the blade combined with relevant viscous effects give rise to complex flow field characterized by high Mach number and significant heat flux variations ([14], [46]). In this scenario, the classical definition of aerodynamic and thermal boundary layers becomes not applicable, especially in case of small clearance, i.e. the gap between rotating blade tip and casing. It has been shown how this design parameter largely affects the turbine performance and the heat transfer distribution [47]. While turbines with relatively large clearance exhibit conventional flow topologies and heat transfer distributions, at smaller clearance the flow physics is completely modified [15]. For this reason, there is a need to develop ad-hoc techniques for the description of heat transfer phenomena in this area. Large efforts have been done in the past years to improve the techniques to retrieve experimentally the blade tip heat load with high accuracy ([48]–[52]) in the few laboratories in the world that have the capabilities to perform transient tests of turbines at engine similarity. The final purpose of this work is to numerically verify the feasibility of the Discrete Green Function approach for future applications in the Turbine Aerothermal Lab at Purdue University [13].

In this case of study, the numerical work was carried out using Numeca software with a widely studied rotor geometry [53] at two different clearances: a nominal and a tight geometry with clearances of 1% and 0.1% of the blade height respectively. The tip clearance is defined as the height of the gap between the tip of the rotor blade and the shroud internal casing. The selection of these two cases aims to the demonstration of this methodology in two extreme operations of the rotor blade. The coefficients of the Green Functions matrix were obtained by imposing numerical pulses of heat flux in each sub-element all along the turbine tip surface. The increments of temperature were estimated and compared against the heat flux applied over the surface for different cases.

The Discrete Green Function approach is a method that evaluates the effect of a spatially distributed heat flux on the increments of temperature. Basically, the differential equation is linearized and solved using the principle of superposition. The geometry must be discretized and a matrix of coefficients related with each discretized division is built assigning certain value of pulses of heat flux and extracting the increment of temperature. Therefore, the energy equation regarding convective heat flux can be written as

$$\dot{q}_{ij} = g_{ij}\Delta T_j, \tag{4.10}$$

Where g_{ij} is the element of G relating the average temperature increment on the element j to the heat flux imposed in the element i. Each one of these coefficients is calculated by imposing a pulse in each one of the discretized elements and retrieving the resulting temperature. The superposition technique is then used during the validation, considering that the net effect in heat flux on element i is the summation of the effect in each individual element, such as:

$$\dot{q}_i = \sum_{j=1}^{n} g_{ij}\Delta T_j \tag{4.11}$$

Or rewritten in matricial form

$$\dot{q} = G\Delta T \tag{4.12}$$

where ΔT is the vector which contains the increment of temperature at each individual division and $\dot{q}$ is the vector with the averaged heat flux in all the discretized points. The inverse Discrete Green's Function, G^{-1}, a matrix of dimension equal to G, allow the calculation of the increment of temperature from the provided heat flux, given an accurate estimate of the adiabatic wall temperature. Each element of the array is needed to fulfill [54]:

$$\Delta T_{ij} = g_{ij}^{-1}\dot{q}_j \tag{4.13}$$

Or written in matricial form

$$\Delta T = G^{-1}\dot{q} \tag{4.14}$$

The increments of temperature are expressed with respect to a reference temperature. A widely used approach to define this temperature is to use the adiabatic wall temperature. When dealing with numerical simulations, this temperature could be retrieved with a calculation with adiabatic walls. This strategy will be used in this research proposal. However, another strategy will be explored in order to consider the actual experimental feasibility of the proposed procedure for DGF. It is actually challenging to retrieve the adiabatic wall temperature with one experiment in a direct way. The coefficients of the Inverse Discrete Green Function can be written as:

$$g_{ij}^{-1} = \frac{T_{ij} - T_{ref\ i}}{\dot{q}_j} \tag{4.15}$$

All the coefficients g_{ij}^{-1} are organized in a matrix G^{-1}. In order to obtain the direct coefficients g of the DGF method we need to calculate the inverse of this matrix.

For the experimental application of the DGF, first the experiments to measure the T_{ij} will be necessary. After that, only one extra experiment will be needed to retrieve the reference temperature. The most convenient option would be to impose fixed level of heat fluxes over the surface, measure the temperature and then express Equation 20 in the form:

$$T_{exp} - T_{ref} -= g(T_{ref})^{-1}\dot{q}_{exp} \qquad (4.16)$$

Where with T_{exp} and $\dot{q}_{exp}$ are vectors of measured wall temperature and imposed heat flux. In this expression, T_{ref} is the only unknown and can be easily derived by solving the implicit linear system.

The experimental setup would consist of an array of electric heaters that would be powered individually to release a heat flux pulse at a given instant. The temperatures and heat fluxes would be measured in discrete points using a combination of thermocouples, high-frequency response thin film gauges (single-sided or double-sided), or a high-speed infra-red camera. The selection of the most adequate measurement technique is a trade-off between space and time resolution. Once the map of heat fluxes and temperatures are obtained for each heat flux, one can determine the matrix of coefficients.

3.1.2 Method Validation

To retrieve the matrix of coefficients we need to discretize the surface of interest in different zones and evaluate the increment of temperature in all zones due to a heat flux pulse. This heat flux pulse needs to be applied one at a time in each one of the regions giving as a result the rows of the Green function matrix of coefficients. This procedure was previously applied to a backward facing step in order to study the main effects of the boundary conditions in a simple geometry with a detached and reattached flow structure. Figure 3.1a) shows the evaluated fluid domain where only the bottom plate was analyzed.

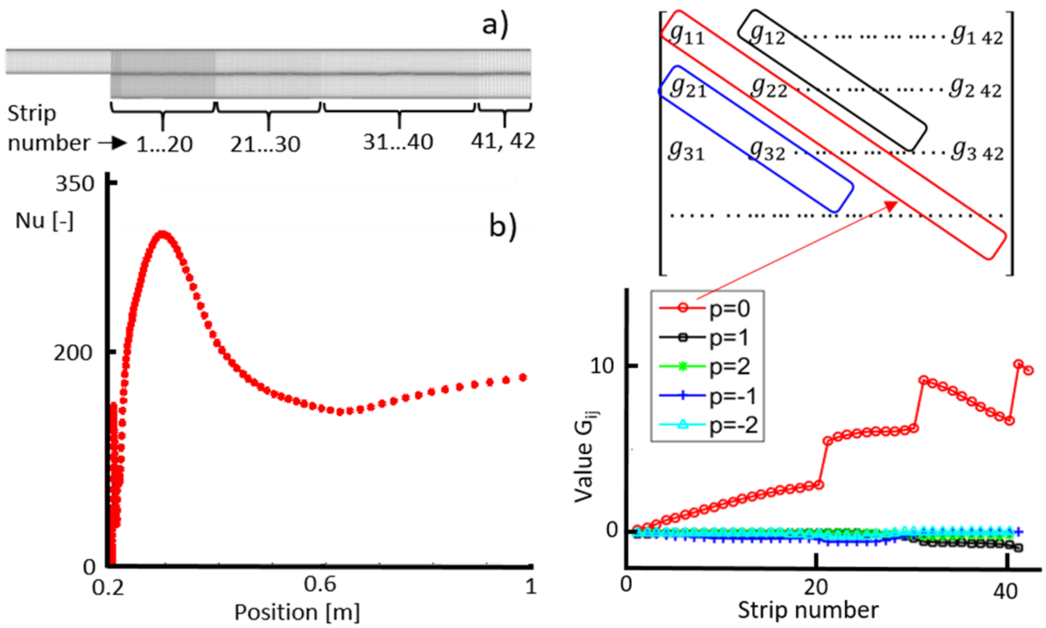

Figure 3.1: a) Numerical domain. b) Nusselt number for isothermal wall conditions. Right: Values of the DGF coefficients in the main diagonal, sub-diagonals and super-diagonals of the Green Function matrix for the baseline case.

For this reason, the bottom plate, located between the axial position 0.2m and 1m, was discretized in 42 strips taking into account the distribution of Nusselt number in the isothermal case, represented in Figure 3.1b). Therefore, in order to improve the accuracy, the finer strips were discretized in the proximity of the vertical wall of the step, increasing to coarser strips along the axial direction of the bottom plate.

The temperature distribution is obtained using 2D RANS calculations which were performed using ANSYS Fluent and imposing pulses of heat flux at each discretized strip. The simulations have been performed using Realizable k-epsilon turbulence model without wall functions.

The 2D RANS simulation allows retrieving the temperature distribution ΔT_{ji} at every cell. The Green's Function G_{ij} defines the following relationship [54]:

$$q_{i1} = G_{ij}\Delta T_{j1} \tag{4.17}$$

In different simulations, we have applied a heat flux pulse q_{im} of 10000 W/m^2 in each strip. Therefore, we have 42 different evaluations from which we can compute the 42^2 unknown elements in G_{ij} just tracking the increment of temperature ΔT_{jm}.

$$q_{im} = G_{ij}\Delta T_{jm} \tag{4.18}$$

In all these calculations the ΔT must be referenced to the adiabatic wall temperature, which has been calculated imposing adiabatic boundary conditions in the analyzed geometry.

The baseline calculation was performed at ambient pressure, with a flow inlet temperature of 400K and an initial wall temperature of 300K. The inlet Mach number was selected as 0.12.

Figure 3.2 shows the value of the Green Function coefficients of the main diagonal (p=0), two super-diagonals (p=-1 and p=-2) and two sub-diagonals (p=1 and p=2). The value of the main diagonal represents the effect of the pulse imposed in the temperature increase of the evaluated element. This is the term which is related to the adiabatic convective heat transfer coefficient. The super-diagonals, p = -1 and p = -2, represent the effect in the temperature rise of the pulse located in the upstream strips, the one imposed immediately upstream of the analyzed strip for the case of p=1 and the one located 2 positions upstream for the case of p=-2. The same explanation is applicable for the sub-diagonals p =1 and p=2, but in this case the effect is provided by the pulses located downstream of the analyzed element.

If we observe the values of the coefficients we can relate them with the aerodynamic phenomena occurring in the backward-facing steps. The point where the super-diagonals cross the sub-diagonals is the stagnation point where the flow is reattached. When the sub-diagonals are over the super-diagonals we observe that there is a stronger influence of the downstream pulses due to the recirculation bubble and the reverse flow. Downstream of the stagnation point, the flow is reattached and the effect of the upstream pulses is higher as the super-diagonals are over the sub-diagonals.

The procedure was validated using the measured Stanton number obtained in a backward-facing step by Eaton and Hacker [40], at a similar Reynolds number. Fig. 3 shows a good agreement between the experimental Stanton number and the evaluated Stanton using the GF calculation. We observe a large positive Stanton number at the location where the heat flux is applied, and negative values elsewhere. The effect of the local heating is mostly sensed upstream because the flow within the recirculating region travels upstream. The local heating influence on the Stanton number decays rapidly, and eventually becomes negligible.

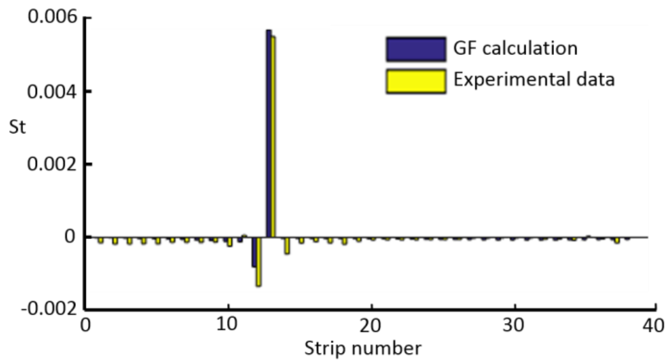

Figure 3.2: Comparison between experimental data of Eaton and Hacker [40] and the numerical calculation of the Stanton number in the recirculating region of the backward facing step.

The evaluation of the backward facing step was the first step in order to validate the procedure before assessing more complex geometries, like the overtip region of a high-pressure turbine.

3.2 Tip Convective Heat Flux*

The Green function methodology is applied to a state-of-the-art transonic turbine stage that was previously characterized in the open literature with numerical and experimental techniques [53]. This geometry was experimentally evaluated and the Nusselt number and isentropic Mach number were extracted at different locations along the blade span. Two values of tip clearance were considered, 1% and 0.1% of blade height respectively. The operational conditions have been computed to guarantee the similarity of the turbine to the original geometry in terms of dimensionless velocity triangles, Reynolds number and T_{blade}/T_{gas}. The stage inlet total temperature was selected considering the capabilities of the wind tunnel, and the remaining boundary conditions were derived by scaling the conditions of the original stage. Table 3.1 summarizes the turbine conditions selected for this study. Uniform total quantities are imposed at the stage inlet, while static pressure with radial equilibrium is imposed at the rotor outlet.

Table 3.1: Turbine operating conditions

	Unit	**Value**
T_{01}	[K]	600
P_{01}	[bar]	2.38
P_{s3}	[bar]	0.78
N	[rpm]	7226
T_{blade}/T_{gas}	[-]	0.67

The full Hex Multi-Block Structured Mesh of the stage fluid domain was generated using the software of the Numeca suite. The grid is particularly refined in the overtip gap in order to resolve this flow region with high detail. Since an accurate evaluation of the heat flux is crucial for the purpose of this work, the $y+$ is maintained below 1 everywhere (below 0.3 in most of the surfaces). The initial stage mesh was generated using Numeca/Autogrid5 [55]. The distribution of the grid in the tip gap was modified in Numeca/IGG in order to avoid any non-matching of the mesh in the rotor tip region. To compute the DGF coefficients, the tip surface was discretized in order to impose independent TBC on each patch. In particular, we want to impose a heat flux on a single portion of the tip and set the rest of the blade as adiabatic.

* Section partially published in Andreoli, V., Cuadrado, D.G. and Paniagua, G., 2018. Prediction of the Turbine Tip Convective Heat Flux Using Discrete Green's Functions. Journal of Heat Transfer, 140(7), p.071703.

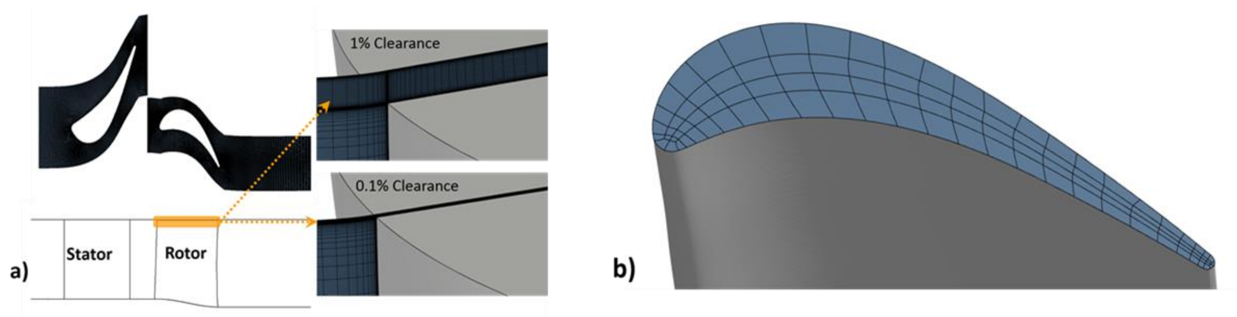

Figure 3.3: a) Stage mesh and tip gap details. b) Elements used to impose the heat pulses

Figure 3.3a) illustrates the stage composition, a blade to blade view of the computational grid, and the details of the mesh in the tip gap for the nominal and tight clearance. Figure 3.3b) shows the discretization use for the calculation of the DGF coefficients. The blade was divided in 100 elements of variable sizes that will be used for the pulses calculations. In order to select the appropriate grid, the effect of the mesh element size has been assessed for the stage and the rotor calculation. Beside the mesh used for the Green Function calculation, three meshes have been investigated: one finer, one coarser and one even coarser. The relevant quantities have been extracted and compared, following the approach suggested by Celik [56]**.**

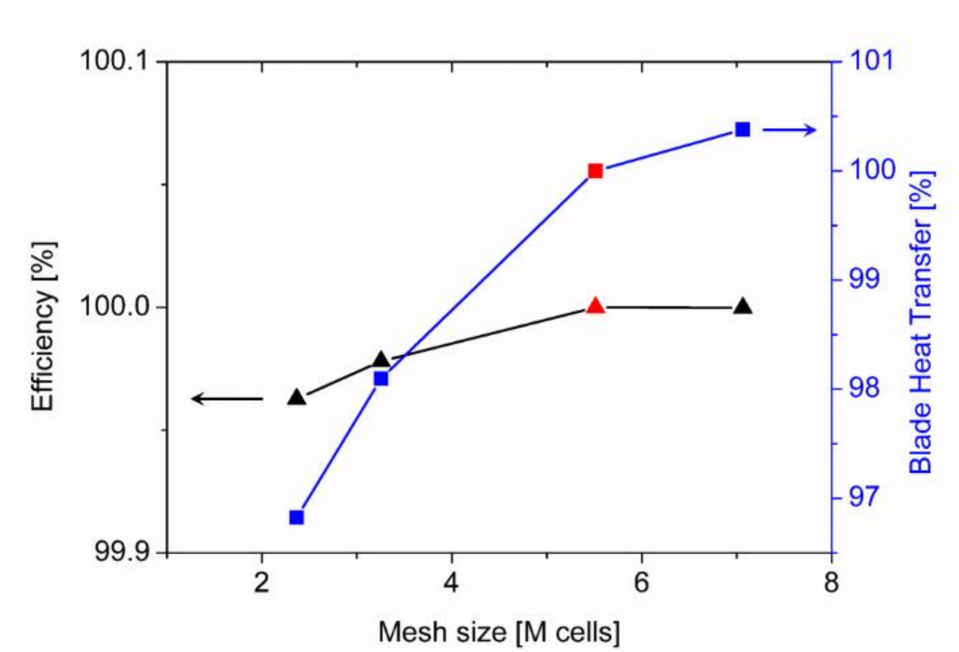

Figure 3.4: Grid sensitivity study

Figure 3.4 shows the effect of the grid size on the stage efficiency and the heat transfer in the blade tip region. All the values are expressed as a percentage of the reference efficiency and heat flux (marked in red) obtained with the selected mesh. While all the grids provide a good estimation of the efficiency, the convergence of the heat flux requires a relatively finer grid. For this reason, given the need for accurate computation of the heat transfer for this project, the mesh of 5.5M elements was selected.

The steady RANS simulations have been performed using the Numeca Fine/Turbo solver [57], with SST turbulence model. The turbulent kinetic energy and the turbulent dissipation have been computed considering a level of turbulence intensity of 2.5%. Stator-rotor interface was computed by the solver with a mixing plane approach, i.e. computing the pitchwise average at the stator outlet and imposing the profiles at the rotor inlet.

The turbine stage calculations performed with the CFD tool, the Reynolds Averaged Navier-Stokes solver developed by Numeca, were validated using the experimental data reported by Didier at al. [58] and the results are shown in Appendix A. Since the calculation of the Inverse Discrete Green Function requires a large number of numerical calculations, the reduction of computational cost of the single simulation has to be a priority. It is reasonable that by imposing a local heat flux in the blade tip the conditions at the stator-rotor interface will not be significantly affected. Therefore, the pitchwise averaged profiles at the mixing plane were extracted from a stage adiabatic calculation and imposed as inlet condition to the rotor calculations. For each pulse calculation then, only the rotor was modeled.

Isothermal simulations for both clearances were performed in order to assess the levels of heat flux per unit surface that take place in the tip region at nominal wall-to-gas temperature ratio. As previously discussed, this was one of the criteria used to select the magnitude of the pulse of heat flux that should be applied on each surface element. Adiabatic simulations were performed in order to retrieve the adiabatic wall temperature averaged on the surfaces for both geometries.

The simulations with the heat pulses were run using the converged adiabatic case as initial solution. The convergence of the DGF simulations have been monitored for some sample cases and a suitable number of iterations has been identified and selected for all the simulations. The quantities monitored for the convergence were the mass flow, the efficiency and the residuals together with the average of the blade surface temperature.

In order to simplify the calculation procedure, a semi-automatic procedure has been implemented to setup the calculations and post-process them.

3.2.1 Prediction of the Turbine Tip Temperature

The effects of the clearance on the rotor performance and heat transfer are investigated. The results of the two simulated geometry, with 1% and 0.1% clearance, show how the flow topology and heat flux distribution are deeply affected by the clearance. Figure 3.5a) and b) depict the shear stress vector lines on the blade tip surface and on the casing, while the color contours represent the heat flux per unit surface.

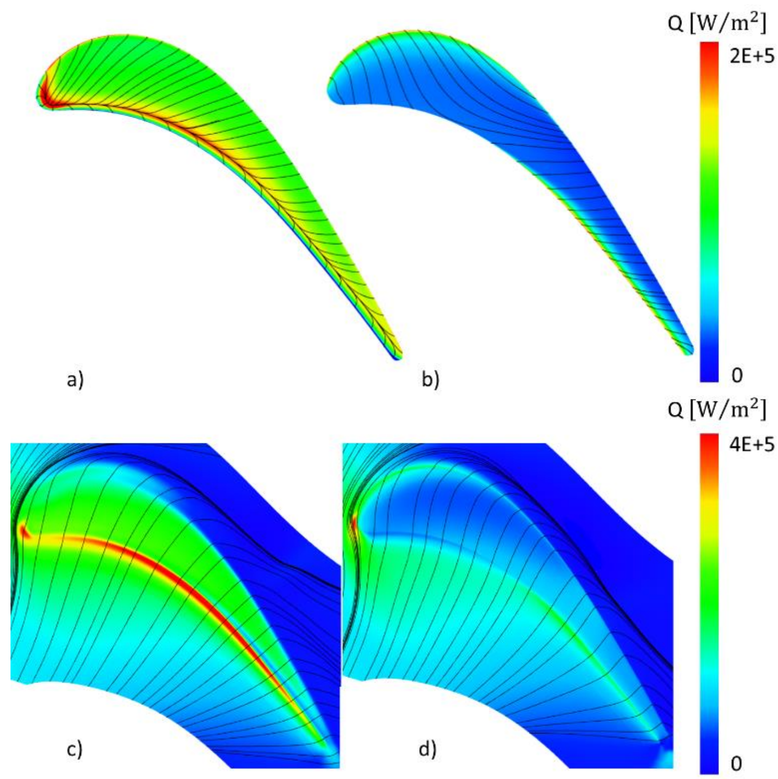

Figure 3.5: a) Shear stress lines and heat flux on blade tip for 1% and b) 0.1% clearance. c) Shear stress lines and heat flux on shroud for 1% and d) 0.1% clearance.

From the top left figure an almost uniform heat flux field can be identified over most part of the blade, especially close to the suction side. The highest levels of heat transfer can be distinguished close to the leading edge where the flow first impacts on the tip surface. From this region, two main areas are separated by a shear stress line that goes straight towards the trailing edge. In most of the blade, between this line and the suction side, the shear stress lines indicate a flow going almost straight from pressure to suction side. In the small region between the line and the pressure side the flow seems to go against the pressure gradient, towards the blade pressure side. The S-shaped surface streamlines, together with low levels of heat flux, suggest the presence of a small vortex that develops close to the leading edge and grows uninterrupted until the trailing edge.

When the gap between the blade and the casing becomes smaller, the viscous effects become predominant. While the pressure gradient that is established between the pressure side and the suction side of the blade would drive the flow towards the low-pressure region, the viscous stress works towards the opposite direction. In order to move through the overtip gap, the gas has to overcome the resistance due to the relative motion between blade and casing. In the case of a relatively large clearance (as in the case of the nominal clearance at 1% of blade height) the phenomenon is pressure driven in the majority of the flow field. For this reason, the portions of the blade that can be clearly identified as inlet and outlet are the pressure and suction side respectively, as intuition would suggest.

This idea is confirmed by the relative velocity vectors shown in Figure 3.5c) where the pressure side can be entirely identified as inlet, while the flow exits on the suction side. Hence, through the analysis of the flow topology, we can assert that there is a region where the viscous effects are confined and that a large portion of the flow is not majorly affected by them. However, in the case of tight clearance this is not valid anymore, since the whole overtip flow is dominated by viscous forces. It becomes impossible to distinguish a main flow and a boundary layer, since the whole flow in this thin region is entirely dragged by the relative motion between rotating and non-rotating components.

The flow structure generated in case of tight clearance in Figure 3.5b) shows that the blade can be divided into three regions. Two regions, in the front and aft part of the blade respectively, are characterized by straight shear stress lines. However, while in the aft part of the blade the flow direction is from pressure to suction side, in the front portion of the blade the gas, dragged by the viscous forces, flows in the opposite direction. There is a third region that can be clearly identified in the central part of the suction side, where the surface streamlines enter and exit from the suction side. This means that the effect of the relative motion of the shroud is perceived at the blade.

Considering the cut at mid-gap (Figure 3.5d) we can see that the flow is even more dominated by the viscous effects, since the portion of reverse flow becomes more significant.

The different flow topologies at the two clearances give origin to two completely different distributions of adiabatic wall temperature (Figure 3.6a, b).

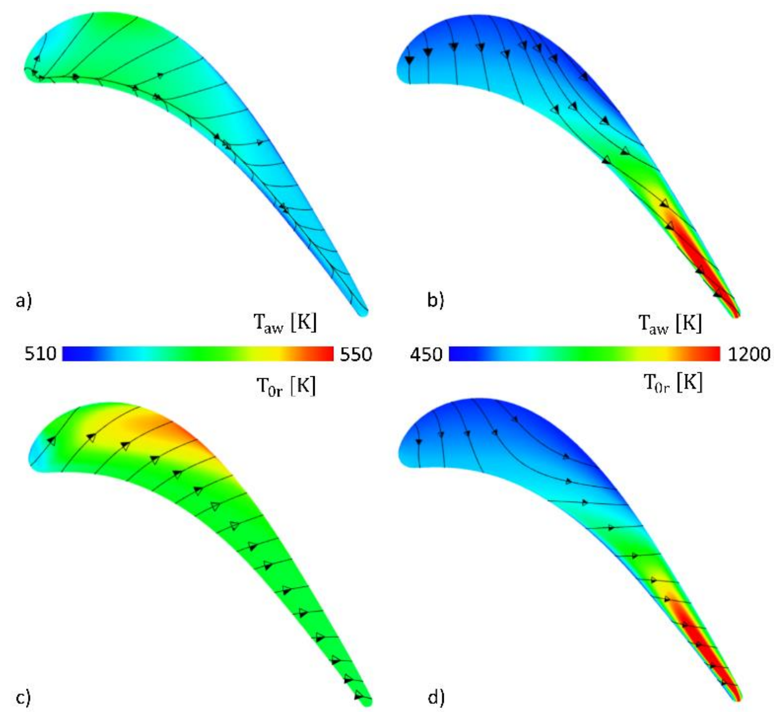

Figure 3.6: a) Adiabatic wall temperature (with shear stress lines) at 1% clearance and b) 0.1% clearance c) Relative total temperature with streamlines at 1% and d) 0.1% clearance

While for the 1% clearance the adiabatic wall temperature is similar in magnitude to the average total temperature at the rotor inlet, the tight geometry shows a remarkable increase of the adiabatic wall temperature. These results are in agreement with what documented in previous works about heat transfer phenomena in high pressure turbine with tight clearance [59].

The 3D-RANS calculations have been used to retrieve the components of the Inverse Discrete Green Function Matrix. The 3D-RANS calculations are then used to retrieve components of the Inverse Discrete Green Function matrix. To retrieve the temperature from a given heat flux profile, a similar procedure is applied to the turbine blade tip using the Inverse Discrete Green Function matrix. The procedure used for the backward-facing step is now applied to the turbine blade tip to retrieve the temperature from a given heat flux distribution. The same strategy can be applied however to retrieve the heat flux from temperature measurements. To validate this approach several heat distributions have been assessed.

Figure 3.7 shows the average of the surface temperature on each element as computed with CFD (a) and as retrieved using the IDGF (b) for the imposed heat flux distribution (c) on the geometry at nominal clearance.

Figure 3.7 compares the surface temperature distribution obtained using CFD and using the IDGF, using a given heat flux distribution. In (a) the surface temperature shown is computed using CFD, in (b) the surface temperature is computed using the IDGF. Figure 3.7 also shows the heat flux distribution that is imposed on the element (c). Finally, the relative error between the IDGF and CFD results is shown in (d).

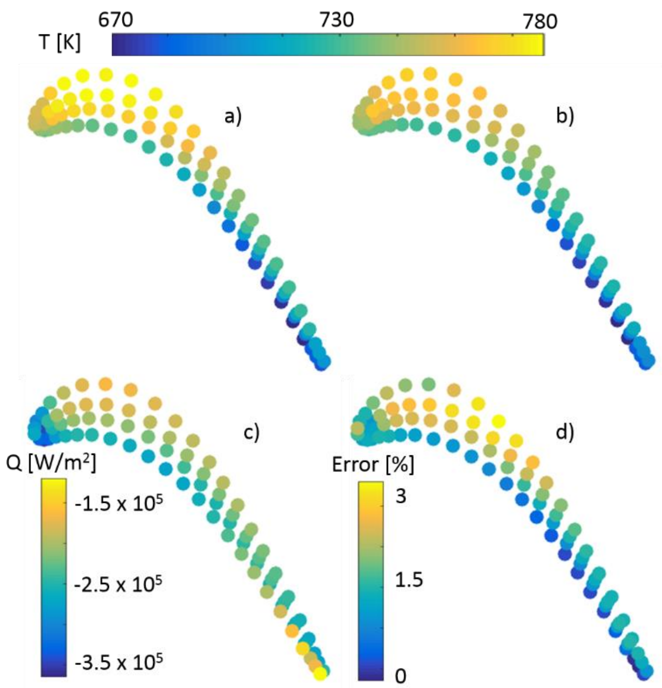

Figure 3.7: Nominal clearance validation case: a) Temperature distribution calculated with CFD b) Temperature distribution predicted with Green Function approach c) Heat flux distribution imposed on the tip surface d) Relative temperature error between the calculated CFD distribution and the predicted Green Function approach distribution.

In this case there is a good agreement between the temperature computed with CFD and the one retrieved from DGF. The error, expressed in percentage of the local temperature, is everywhere below 3%. The maximum levels of mismatch between the two temperature distributions can be localized at the central part of the suction side and close to the leading edge.

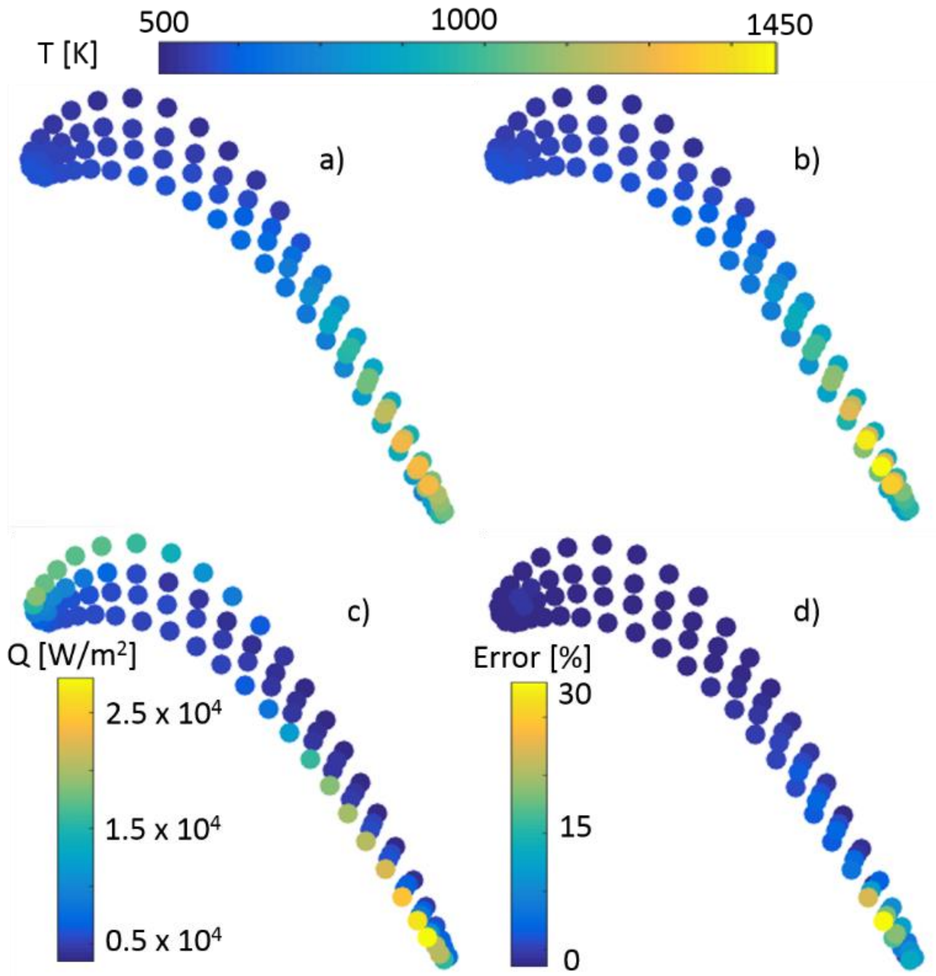

Figure 3.8: Tight clearance validation case: a) Temperature distribution calculated with CFD b) Temperature distribution predicted with Green Function approach c) Heat flux distribution imposed on the tip surface d) Relative temperature error between the calculated CFD distribution and the predicted Green Function approach distribution.

The equivalent color contours are shown in for the case of tight clearance. The error between the two temperature distributions has an average value of 2.9% over the entire blade and is below 10% almost everywhere. However close to the leading edge, where the elements are smaller, the error reaches values of 20% and the error percentage gets even higher when approaching the trailing edge. While in the previous case the variability of the blade temperature was limited to a range of 100K, in the case of the tight clearance the temperature of the blade goes from an average of 600K in the front part of the blade to peaks of more than 1400K close to the leading edge. This variability confirms the high nonlinearity of the heat transfer in this geometry, as already seen in the previous section. Moreover, it has to be considered that the adiabatic wall temperature in this case reaches high values. It is indeed well known from previous works in the open literature [42] that the methodology is sensitive to the errors in adiabatic wall temperature. Therefore, the accurate prediction of the temperature in the case of the tight clearance appears more challenging especially close to the trailing edge, where T_{aw} is large and the area of the sub-elements is small.

3.2.2 Scaling of Tip Heat Flux

Scaling with Clearance

In order to get better insights on the phenomena driving the heat transfer in the two cases, we can look at the structure of the respective SGD matrices. Figure 3.9 displays a 3D histogram of the matrix components, where the two axes indicate the row and column of the matrix and the bar elevation is proportional to the magnitude of the coefficient. If all the sub-elements of the surface were not interdependent, the only nonzero elements in the matrix would be along the diagonal. This means that a pulse of heat flux in a single element would cause an increase in temperature only on the element itself and no effect could be detected on other blade regions. In this scenario, using the Discrete Green Function methodology would be equivalent to the use of an adiabatic convective heat transfer coefficient h_{aw} and adiabatic wall temperature T_{aw}. If we depart from the ideal condition of the diagonal matrix, the DGF approach will give different results than the h_{aw}approach, because all the interactions between elements are considered. In case of nominal clearance (Figure 3.9a) the matrix retrieved from the pulses calculations reveals a structure fairly similar to a diagonal matrix. However, some small groups on nonzero extra-diagonal elements can be spotted. It is difficult to deduct the relative location of the elements from the matrix, since the geometry is complex and the elements are sorted in a column vector. This means that two elements that are not adjacent in the matrix can be in the same neighborhood in the blade geometry.

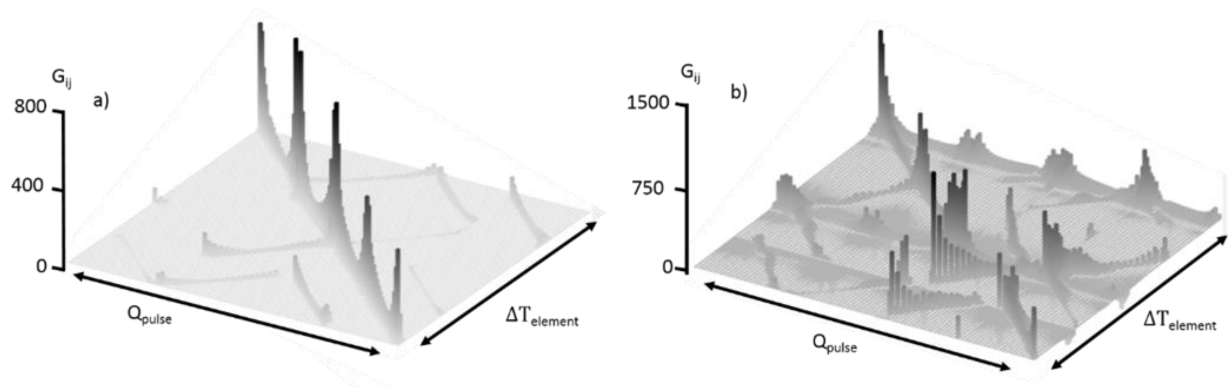

Figure 3.9: Histogram of the Inverse Discrete Green Function for a) 1% clearance and b) 0.1% clearance

Figure 3.9 left shows that the diagonal values are significantly larger than the rest of the values in the matrix. At clearances larger than 1% the local heat transfer is expressed as a function of the local temperature differences. This can be articulated using Equation 12, where the Nusselt number is a scaled value of the diagonal terms of the Matrix of coefficients. However, for tight clearances, Figure 3.9 right indicates that the local heat flux is also function of the temperature in multiple neighboring locations. Hence, attempts to express the convective heat transfer for tight clearances as a function of the adiabatic flow temperature and a wall temperature are deemed to fail.

When the clearance becomes smaller (Figure 3.9b) all the sub-elements are highly correlated. The histogram in this case shows how in some regions the extra-diagonal terms become even larger than the diagonal term in that row or column. The evidence of an important crosstalk between blade locations justifies the good agreement that can be obtained using the GDF methodology.

To gather a better understanding of the dependence of the Green's Function matrix on the tip gap, and additional clearance of 0.6% has been considered. For this additional clearance, the direct and inverse Discrete Green's Function matrices have been derived. The same methodology previously described has been implemented, and the results from more the 100 RANS calculations have been summarized into the matrix.

The data has been postprocessed and sorted so that the elements are organized with the same logic and the location of each element can be approximately the same independently on the tip clearance. Furthermore, the heat transfer is considered in terms of heat flux and not integral value. In this way, the magnitude of the matrix elements will have comparable values independently on the element size. The discretized areas are numbered from 1 to 104, where 1 is on the leading edge and 104 is on the trailing edge.

Figure 3.10 shows the results for the three clearances, 0.1% 0.6% and 1.0% at the top middle and bottom row respectively.

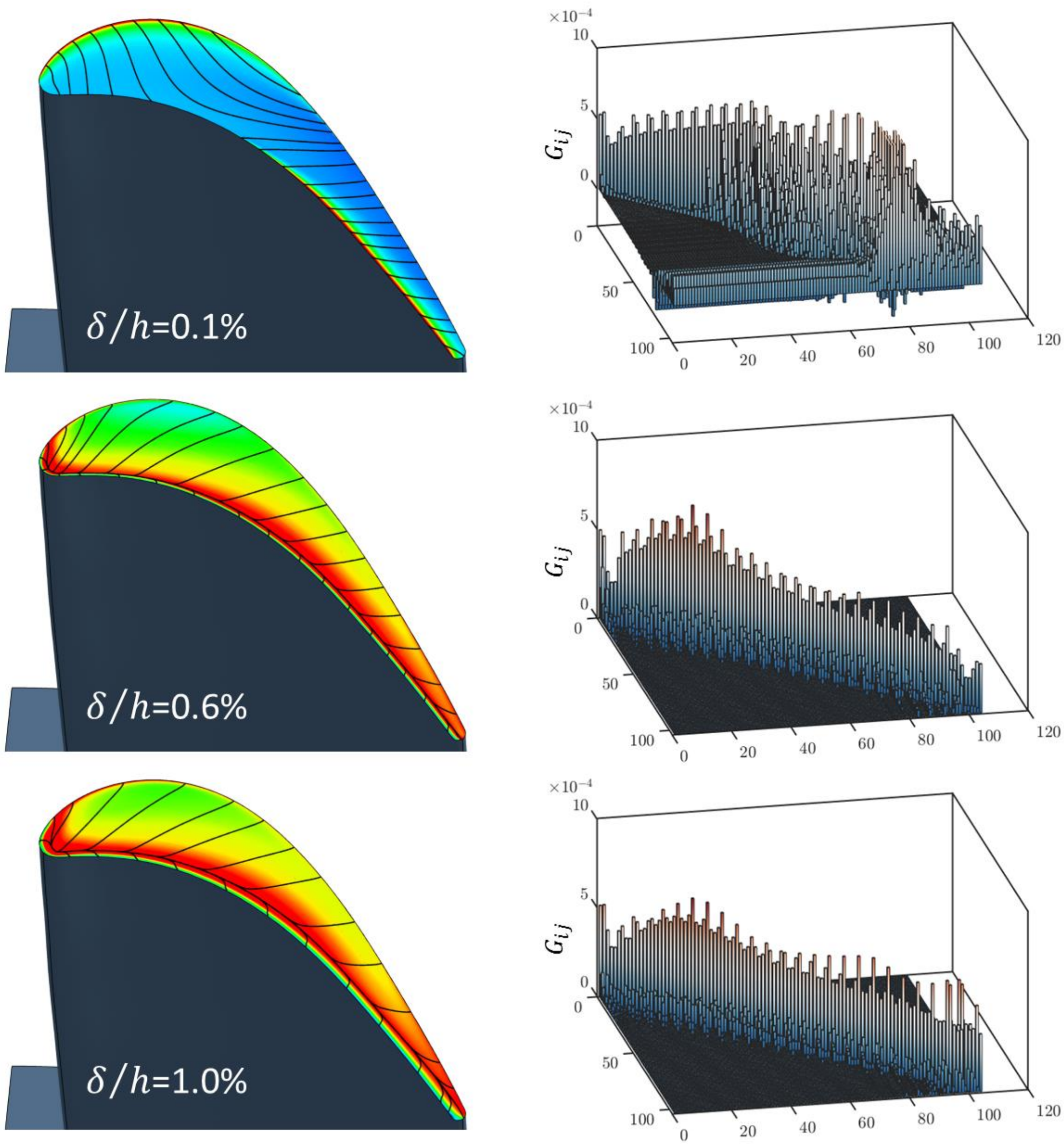

Figure 3.10: Comparison of three DGF matrices at three different tip gaps.

On the left there is a qualitative color contour of the tip heat flux, while on the right there is a representation of the Green's function matrix for each clearance. The top row is based on a relative tip clearance of 0.1%. The sorted matrix based on heat flux and not on integral values allow to better visualize the relevance of the small areas close to the trailing edge. In the region of the matrix where both the index 'i' and the index 'j' are less than approximately 50, i.e. in the top left quadrant of the matrix, the diagonal elements dominate. The extra-diagonal elements in that area are very small and seem to have non-zero value only immediately below and above the diagonal. In the middle region the elements out of the diagonal raise till having a value that is comparable to the diagonal terms. This region corresponds to the central part of the blade, where leakage flow enters and exits from the suction side. Finally, at the bottom right corner of the matrix we find the elements located at the blade trailing edge. Also in this region the cross-talking is dominating the heat transfer field but the bar height is in average decreasing.

As we moved to the 1.0% tip gap, the matrix is almost fully diagonal with small extra-diagonal terms located right below or above the diagonal terms. In this case, the main feature characterizing the heat transfer field is the height of the diagonal terms. The intermediate gap, shows a flow and matricial structure similar to the 1.0%. The separation bubble that can be distinguished on the pressure side of the large clearance is now reduced to at least ¼ of its length, which becomes more relevant in the trailing edge. While for the 1.0% gap, half of the TE is occupied by a recirculation bubble, in the 0.6% case this phenomenon is almost negligible. Consequently, most of the differences between the two matrices can be identified in the trailing edge region and in the magnitude of the extra-diagonal terms.

Scaling with Inlet Flow

According to Green's Function theory, the pulse should produce a consistent effect on the system. Hence, the coefficient calculated with different pulse amplitude should be the same as long as the value of the pulse is large enough. Figure 3.11 depicts the coefficients calculated based on five different pulses, ranging from 100 to 500 kW/m^2. When the value of the impulse grows, the coefficient decays with a trend similar to an exponential law, fitted by the red line. The overall coefficient variation is included in the 0.5% of the final value.

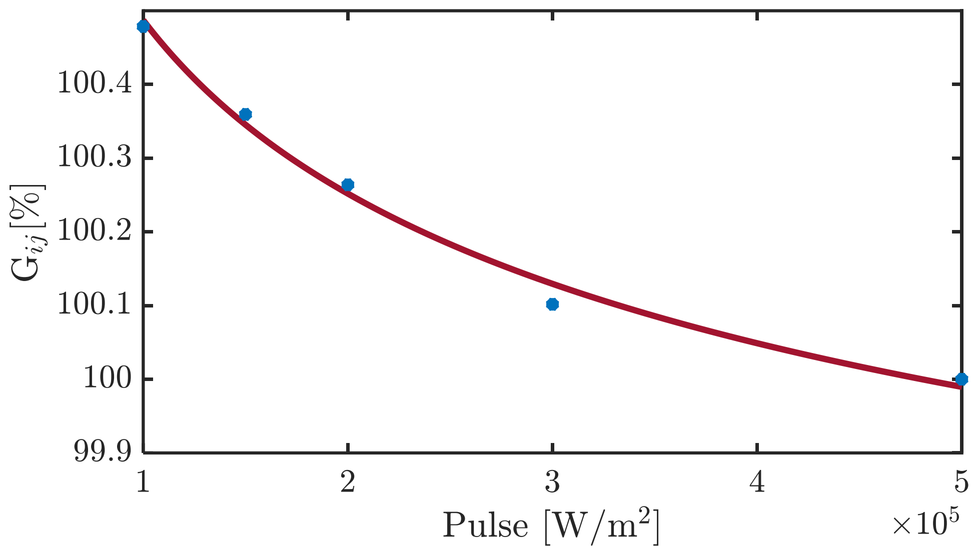

Figure 3.11: Trend between heat pulse and wall temperature.

There are different methods in the literature to scale the convective heat flux with the gas-to-wall temperature. Some examples are summarized in [60], where the authors propose various modeling approaches of h in function of T_w. One of these methods is based on the assumption that, if the relation between h and T_g/T_w, we can fit it based on 3 different conditions using the so-called 3-points method [61]. The power method, demonstrated by Lavagnoli et al. in tip flows [59], is applied in this case to evaluate how the exponent changes with the clearance. Since the temperature has an effect on the gas properties, like viscosity, tips with smaller gap may show a more relevant temperature dependence than large gaps. Figure 3.12 provides an example of the application of the power method correction to the tight clearance case. The non-linear expression allows to drop the fitting error to values between +20% and -20%.

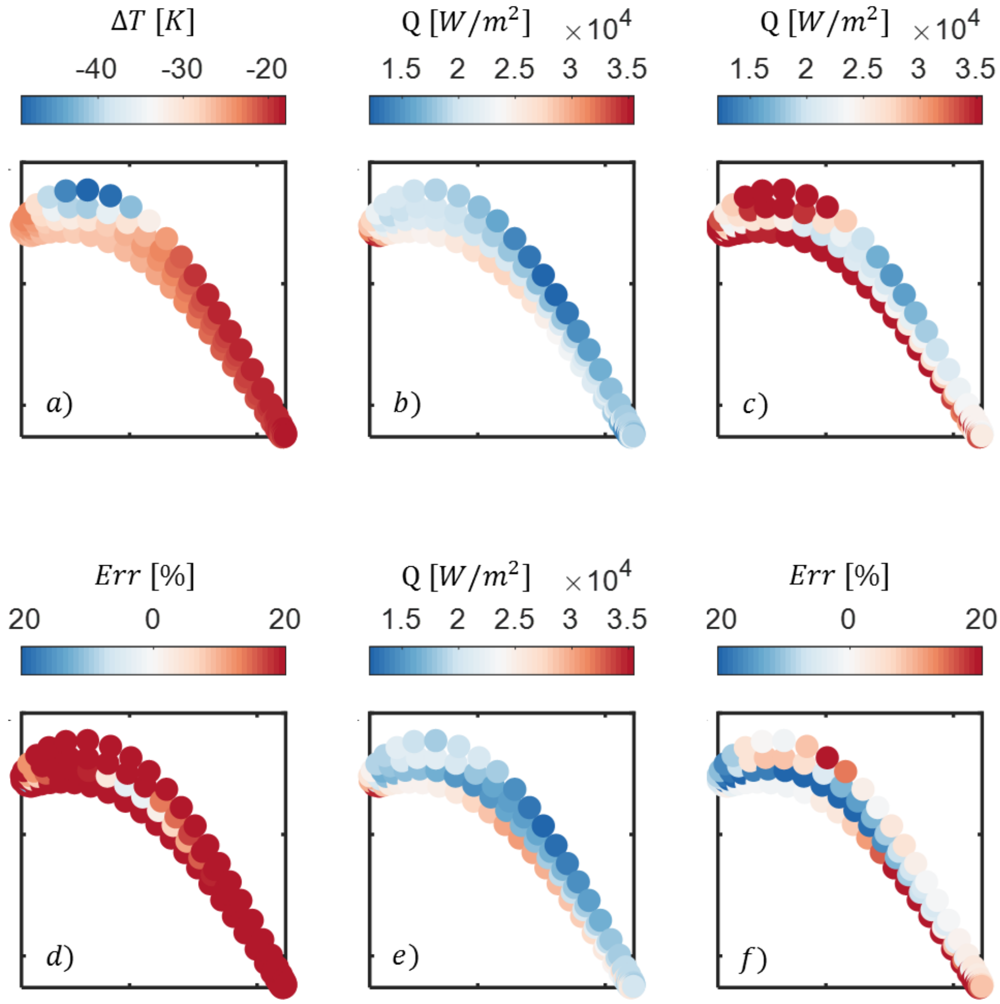

Figure 3.12: Correction of G matrix based on temperature ratio: a) difference of temperature, b) heat flux; c) calculated heat flux with the linear method and d) error; e) calculated heat flux with power method and f) error

However, the power law may bring to over predicting the trends far from the region where the law coefficients are calibrated. Hence, the use of power laws to extrapolate out of the characterized region may be challenging. Figure 3.13 shows that for a limited range of wall to gas temperature ratios, the linear approximation is satisfactory.

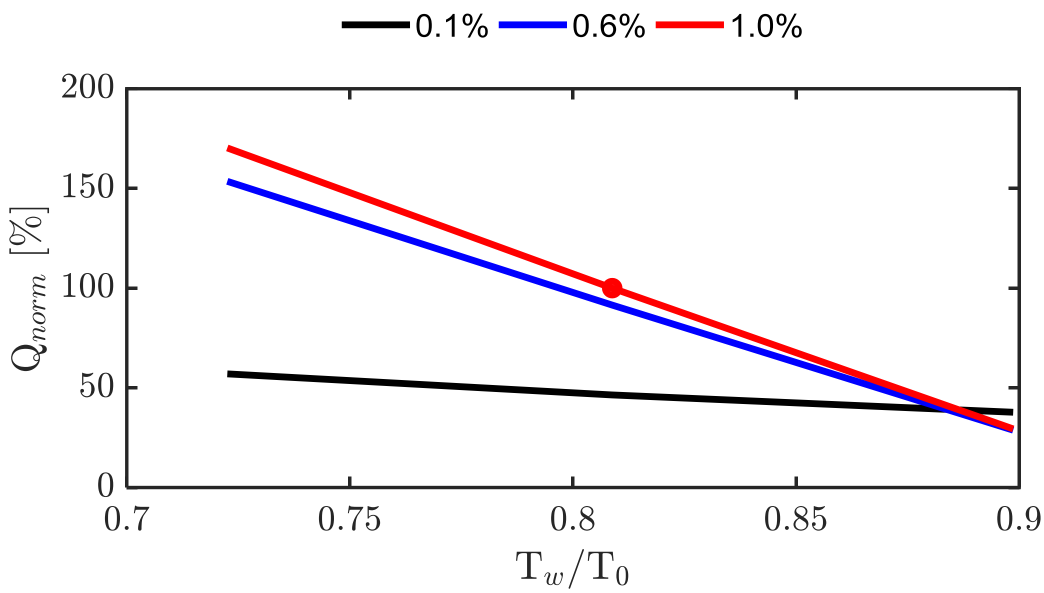

Figure 3.13: Trend of heat flux for three tip clearances at different temperature ratios

The graph shows the integral heat flux on the tip as a percentage of a reference value highlighted with a red dot. The three lines refer to the trends of heat flux in terms of wall-to-gas temperature ratio for three different clearances: a tight, a medium and a large one indicated with black, blue and red lines respectively.

3.3 Conclusions

In the first section of this chapter, an introduction about the Green's Function method is provided. The theoretical description is complemented with one test case that demonstrates the method's application. The procedure is successfully tested in a backward-facing step and compared to similar test cases in the literature.

In the second half of this chapter, the focus is on turbine tip convective heat flux. The challenges related to modeling of heat transfer phenomena in the overtip region are highlighted, and a Green's Function based methodology is proposed to overcome them.

Finally, the scaling of Green's functions over a range of turbine conditions is studied. In particular, the dependence on the tip gap and gas-to-wall temperature ratio are established.

CHAPTER 4. TURBINE MODELING AND EXPERIMENTAL PROCEDURES

4.1 Transient Modeling Approach

Over the trajectory of an engine, the tip clearance varies continuously due to a variety of different phenomena [62]. A typical trajectory can be seen in Figure 4.1, where the abscissa indicates the time of the mission, the right ordinate shows the shaft speed, and the left ordinate shows the tip clearance.

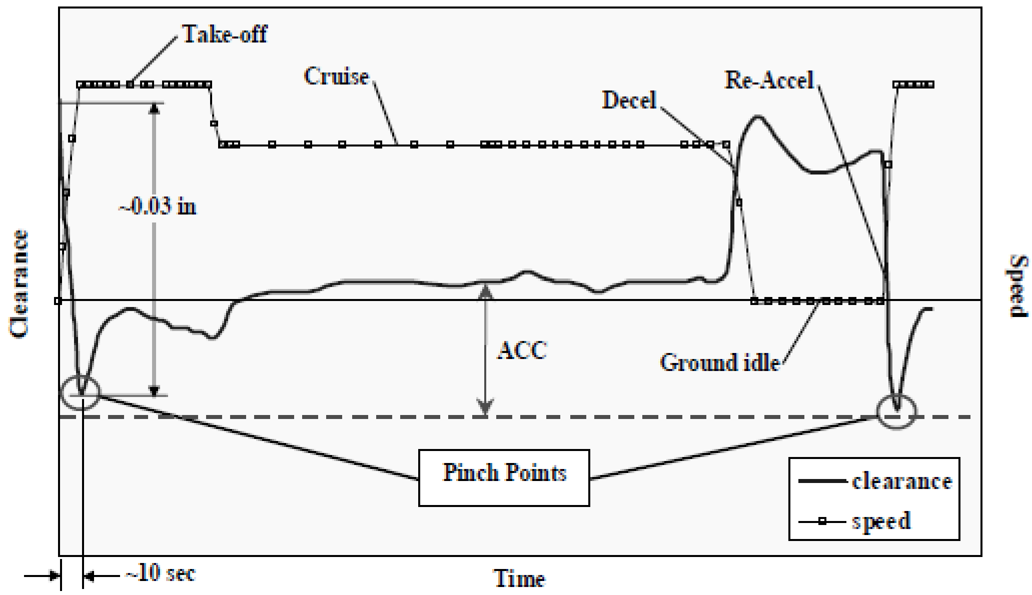

Figure 4.1: Variation of tip clearance over a given trajectory [62].

It is evident that changes in shaft rotational speed induce substantial variations in running clearance, which can be even +-100% of the clearance for cruise conditions. This change implies that even if the engine is designed for a safe running clearance at cruise, this may not be ensured over the trajectory and that optimizing the performance of turbomachinery for a given clearance may not be sufficient to an optimal performance over a range of RPM.

In the literature, turbomachinery deformations are broken down into two main categories:

- Axisymmetric deformation: due to thermal, centrifugal and aerodynamic loads, is the same for all the blades (symmetric in the circumferential direction)

- Non-axisymmetric deformation: caused by non-symmetric forces, produces an eccentricity of the rotor and therefore an unbalance of the loading on each blade

In general, the loads acting on the engine can be centrifugal, thermal, internal aerodynamic forces, thrust loads. These loads can induce both symmetric and non-symmetric deformations. Additionally, there are also loads due to flight conditions, like inertial, external aerodynamic forces, gyroscopic forces; these loads typically induce asymmetric deformations.

Given the complexity of the phenomena involved and the large variability of mechanical and thermal properties of the engine parts, each component has a different reaction to transient loading. This factor makes the dynamic modeling of tip clearance during transient critical and at the same time challenging. A reduced model should capture all the involved time-scales in order to reproduce the tip gap in detail correctly.

An important application of this type of analysis in engine design is the simulation of pinch points, as highlighted in Figure 4.1. During a fast shaft acceleration, like during take-off, the centrifugal speed is rapidly increased and the thermal loads that act on the turbine blade with it. The sudden increase of centrifugal force causes a rapid elongation of the blade tip due to structural deformation. Given the small size of the blade, the thermal loads will not take long to penetrate the entire blade length and cause an additional thermal deformation. The same increase of thermal loads can be found on the inner surface of the turbine casing and to a lesser extent on the rotor disc. Nevertheless, these are larger parts that have a slower response to increases of temperature, where the rotor is the slowest to deform because it is a more massive component. For this reason, in the first phase, the casing deformation at a given time instant is smaller than the one of the blades. This causes a minimum in the tip clearance indicated as a pinch point. Once the casing starts reacting, the clearance becomes more prominent than the cruise value, until the rotor disc expands as well and pushes the blade tip to its nominal value. Most of the available studies about the response of turbomachinery clearances to engine transient are performed numerically or experimentally on large engines, with relatively large running tip gaps. This work focuses on characterizing the tip gap evolution over the trajectory of a small turbojet. The engine size profoundly affects the turbine performance, as demonstrated in Chapter 2, but also changes the scales of mechanical and thermal loads.

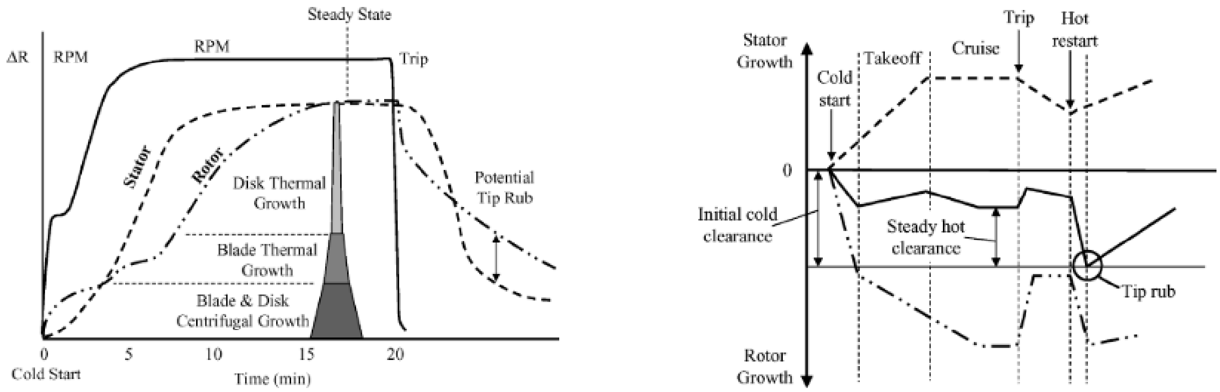

Figure 4.2: Disk and blade thermal growth [5].

The geometry considered in this section is illustrated in Figure 4.3. The simplified assembly showed on the left contains a shaft, not included in the numerical model, a solid rotor disc, half a turbine stage and a casing composed by a thin layer of abradable and a solid metal casing. A summary of the dimensions is shown in the right section of Figure 4.3, while a more detailed description of the geometrical parameters is provided in the Appendix.

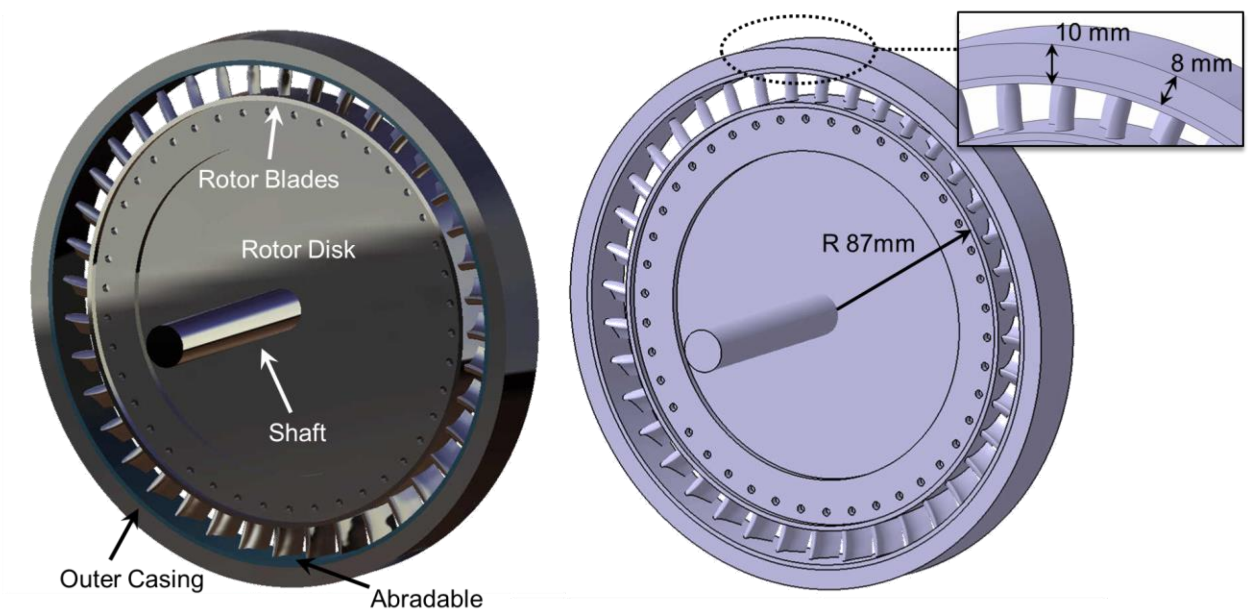

Figure 4.3: Schematic of the turbine assembly.

The first step to develop a numerical model of the engine is to characterize the time-scales of the involved phenomena to decide what can be approximated as steady and what must be characterized as an unsteady phenomenon. While some of these characteristic times are documented in the literature for large engines, it is necessary to verify which assumptions still hold for compact engine cores.

The first step is the analysis of the heat flux of the parts; it is well known that normally conduction is the slowest phenomenon in a thermal transient. In conduction problems, there are nondimensional numbers that can be used to estimate how fast the thermal response of a part will be, and which assumptions can be made. A first analysis to characterize the importance of temperature gradients within a component is based on the Biot number:

$$Bi = \frac{hL_c}{k} \tag{4.1}$$

Where h is the coefficient of convective heat flux and k is the thermal conductivity of the solid, while the characteristic length is defined as $L_c = V/A_s$ with A_s being the surface area. Bergman et al. [63] state that if the condition $Bi < 0.1$ is valid, then the temperature gradient within the solid can be neglected, or in other words, the resistance to conduction in the solid part is small compared to the resistance to convection between the fluid and solid at the body surface. In this case, the numerical approach of lumped capacitance can be adopted; this is one of the simplest methods in conduction since it considers a uniform temperature in the solid and allows to simplify significantly the differential equation describing the body temperature in a transient.

For a given component, the thermal response can be characterized based on a time constant calculate as:

$$\tau_t = \frac{\rho V c}{hA_s} \tag{4.2}$$

In this equation, c is the thermal capacity of the fluid, and ρ is the fluid density. This thermal time constant is the coefficient of an exponential law that characterizes the time needed to bring the solid to the desired temperature. In particular τ_t is the time at which the solid will achieve 63% of the final temperature, in seconds. This value will allow selecting a proper time step to characterize the temperature transient in the engine numerical model.

Table 4.1: Biot number calculation for turbine components

	Biot number	***Time scale [s]***
Rotor disc	0.12	63.62
Blades	0.03	4.03
Casing abradable	0.69	4.63
Casing metal	0.17	44.08

The Biot numbers and time constants for the four main turbine components are reported in Table 4.1. The blades are the only component for which the Biot is much smaller than 0.1 and the lumped capacitance model can be applied, while the other components will require a different modeling approach. The time scales for the blades and the thin layer of abradable in the casing are similar, below 5 seconds. We can expect them to be the first components to achieve a steady temperature during a transient. The metal casing follows with ~45 seconds, and the slowest part to respond is the rotor disc which has a time constant higher than 1 minute.

Transients in convection usually are several orders of magnitude faster than in conduction. For this reason, the boundary layer is traditionally assumed to adapt instantaneously to changes to main stream conditions in this type of numerical models. Given the peculiar flow regime in tip flows, we should assess the validity of this hypothesis. To quantify the time scale of convection, the method described in [64] was used. The time needed for the boundary layer to respond to an upstream flow change is expressed in function of flow and geometrical parameters. The aerodynamic and thermal time scales are slightly different and can both be estimated using the method described by Saavedra et al. The time scales obtained are in the order of milliseconds.

Finally, it is fundamental to understand how the tip clearance models can be used and which the requirements of these applications are. One of the primary uses of detailed tip clearance models is the design of active tip clearance control systems. Some works related to the requirements of fast active tip control are used as a reference to define the strategy of this section. In [65] and [66], the response time of actuators is discussed, and reduced models are used to characterize the design space. The time steps used in these work to run engine simulations are in the order of 0.1 s. Hence, this value is used as a reference to define the strategy for transient modeling. All the phenomena with time scales smaller than this value will be modeled using a quasi-steady approach, while the slower phenomena will be model with a full unsteady approach.

Figure 4.4 shows a summary of the time scales involved in the engine transient problem, in a base 10 logarithmic scale. The convection is fast compared to the time scales of the engine dynamic model. The blade conduction is the fastest of the conduction problems, but still close to the 0.1 seconds range.

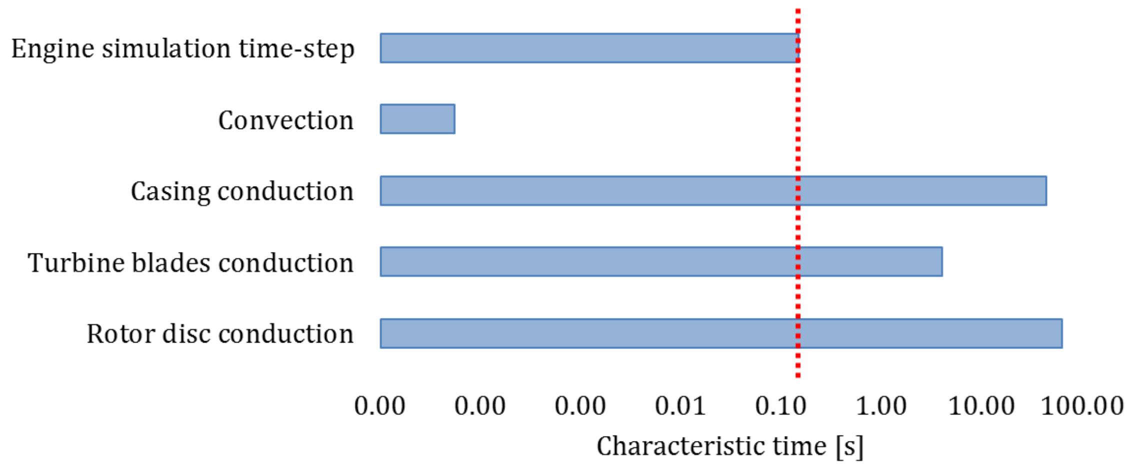

Figure 4.4: System time scales (simulations, conduction and convection).

The rotor disc and casing conduction problems are slow compared to the other time scales, with time constants of more than 10 seconds. For this reason, the conduction is modeled as fully transient while the convection, pressure and centrifugal loads are treated as quasi-steady. These loads are supposed to adapt to a time-changing boundary condition instantaneously.

4.2 Tip Clearance Modeling

4.2.1 Turbine Performance Modeling

The two modules built to estimate the turbine aerothermal performance are shown in Figure 4.5.

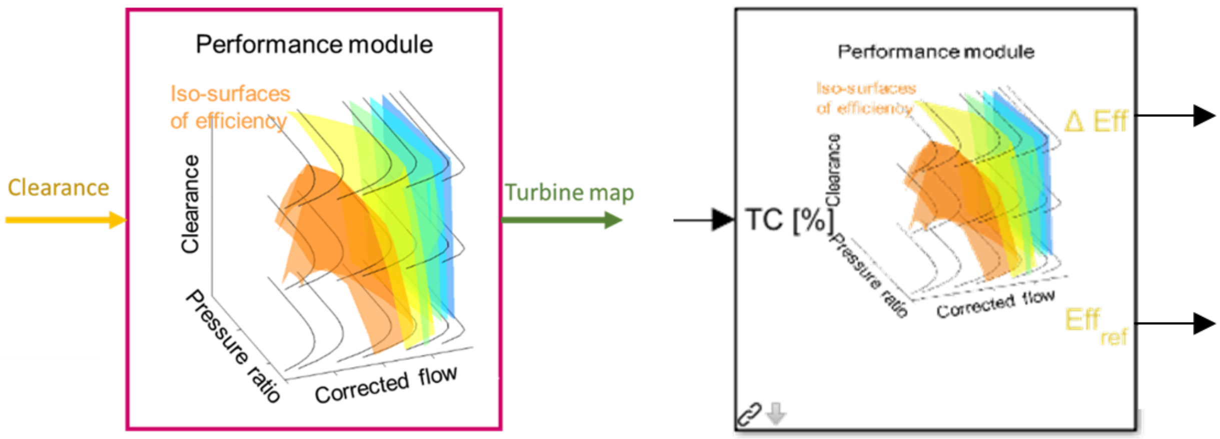

Figure 4.5: Module for turbine performance.

The two modules will be used to retrieve the turbine map and the heat transfer coefficient respectively.

The turbine map is normally expressed in 2D, with the corrected flow on the abscissa, the pressure ration on the ordinate and iso-speed lines at different rotational speeds. The points with the same value of efficiency are, in this case, simple 2D lines. When we consider the tip clearance, defining the turbine map becomes a 3D problem, where the third axis is the value of the tip gap. In the performance module, we will retrieve the surface map from the 3D one for a given input clearance at each time step.

$$\eta = \eta(\delta/h\,, tip\ geometry, \dot{m}_{cool}) \tag{4.3}$$

We have already demonstrated that the effect of efficiency depends on the tip geometry, so the first two variables need to be considered together. However, if it is assumed that the effects of clearance and of cooling are independent, the efficiency can be expressed as:

$$\eta = \eta_{ref} + \frac{\partial \eta}{\partial(\delta/h)}\bigg|_{tip} \Delta(\delta/h) + \frac{\partial \eta}{\partial \dot{m}_{cool}} \Delta \dot{m}_{cool} \tag{4.4}$$

Few models are proposed in the literature to model the effect of tip clearance. Most of the available data is based on cascade experiments on traditional large turbines. The correlations are able to distinguish between shrouded and unshrouded turbines, and some of them include non-flat tip structures but only in the case of simple squealers. One of the most adopted relations, for example the one used in [67], is based on the empirical model described by Baskharone [68].

According to this model, the effect of clearance on efficiency can be calculated as:

$$\frac{\eta}{\eta_{ref}} = 1 - K\left(\frac{\delta}{h}\right)\left(\frac{r_t}{r_m}\right) \tag{4.5}$$

Where K is a function of the Zweifel tip loading coefficient, which combines blades parameters (solidity) with flow parameters (inlet and outlet flow angles).

Additional correlations are available, still developed based on linear or annular cascade experiments. As an example, Hubert expresses changes in losses and flow angles as a function of clearance.

$$\Delta\alpha_{2,cl} = \frac{c}{g}\frac{\sin\alpha_\infty}{\delta_u \sin^2\alpha_\infty} = f\left(\frac{\delta}{c}\right) \tag{4.6}$$

Traupel follows the same structure and developed correlations based on turbine testing to include the clearance losses in the aerodynamic blade efficiency. The variation of efficiency due to tip clearance is expressed as:

$$\Delta\eta = K_\delta \frac{(\delta - 0.002c)D_T}{hD_m} \tag{4.7}$$

Where the value of K is given by an empirical correlation. According to this correlation, the efficiency variation would go to zero for a relative tip clearance of 0.2%.

In alternative, the flow deviation can be calculated as:

$$\Delta\alpha_{cl} = 70.5\frac{\delta}{h}\frac{D_T}{D_M} - 0.714\frac{g}{c} - 0.5° \tag{4.8}$$

The Ainley's equation for tip losses is

$$Y_{cl} = k\frac{\delta}{h}Z \tag{4.9}$$

where k is a constant depending on the rotor configuration (k=0.5 for unshrouded blades) and Z is the Ainley's loading factor. A further modification of this correlation was made by Dunham and Came [69] implementing the results from Hubert, and obtained:

$$Y_{cl} = k\frac{c}{h}\left(\frac{\delta}{c}\right)^{0.78} Z \tag{4.10}$$

An alternative expression to calculate the efficiency variations in turbine stages with transonic relative outlet Mach numbers is given by Kacker and Okapuu as:

$$\frac{\Delta\eta}{\eta_0} = 0.93\frac{\delta}{h\cos(90° - \alpha_2)}\frac{D_T}{D_M} \tag{4.11}$$

Where η_0 is the efficiency at zero clearance. Sjolander [70] models the tip losses with more detail, including a breakdown of the different loss components as function of the clearance. However, all the described method are based on experimental databases built on a limited range of turbine geometries. The equations above have similar structures that consider a purely linear trend of efficiency in function of the tip gap. Furthermore, none of the models is complex enough to allow the calculation of efficiency for non-traditional squealer tips.

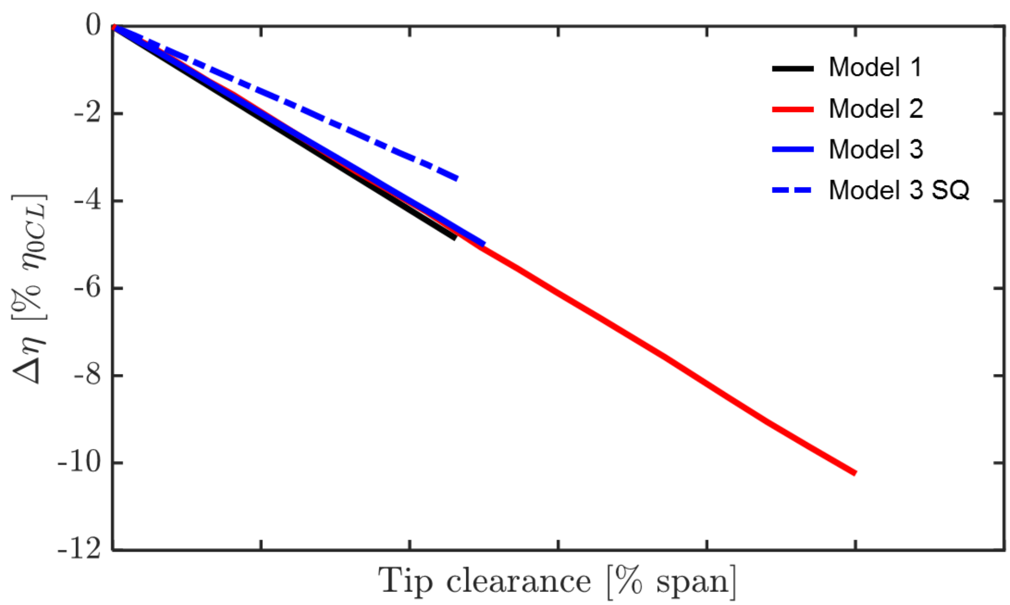

Figure 4.6: Models of efficiency change in function of tip clearance.

To show the predictions based on correlations, some of the described models are implemented and showed together in Figure 4.6. On the abscissa we find the tip gap as percentage of the blade span. On the ordinate, the variation of efficiency is expressed in percentage of the efficiency at zero clearance. These lines express the trend of efficiency loss with an increase in clearance. The three curves are based on the model (black line, indicated as Model 1), and the curve showed in Bunker's work [5] (blue lines indicated with Model 3 for flat tips in solid line and squealer in dashed line). The three models for flat tip collapse on the same trend, showing that most of the models available in the literature are based on similar or same experiment database and characterize the same family of turbines. For compact turbines, and furthermore with optimized tips, we need to verify how the trend compares with the literature one.

We must now verify how these results compare with the CFD predictions in a rotor of an HP turbine for compact core engines.

In addition to the geometries described in Figure 4.7, two additional tip configurations are selected.

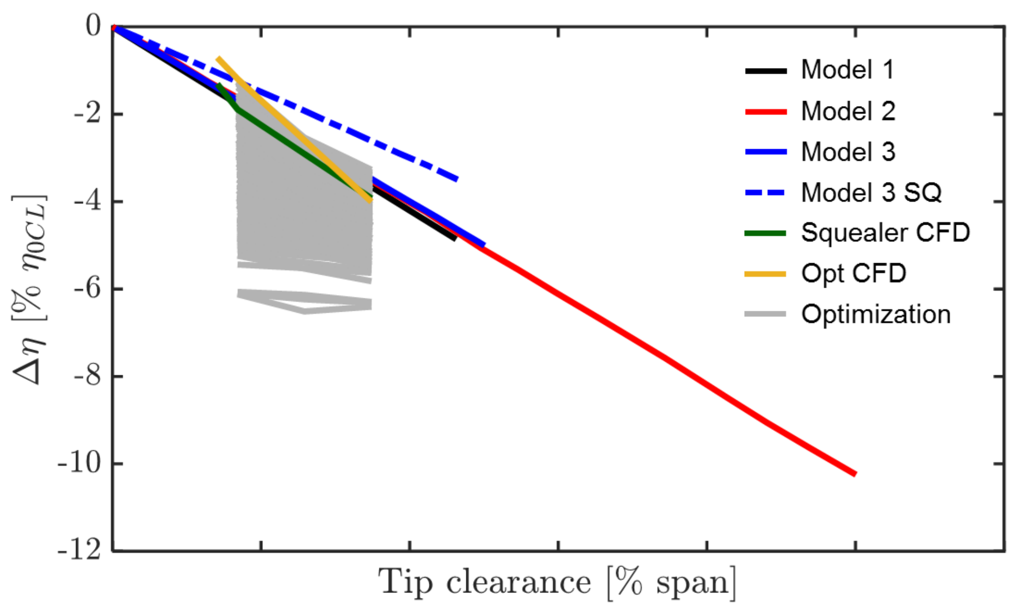

Figure 4.7: Models of efficiency change in function of tip clearance from the literature and from CFD in Chapter 2.

In total four different geometries are considered in this section:

- Baseline squealer
- Geometry with the highest efficiency from single point optimization

- Geometry with highest mean efficiency from multi-clearance optimization
- Geometry with the same efficiency as squealer but low variability from multi-clearance optimization

The four geometries are then compared to the correlation described by Baskharone [68]. Table 4.2 summarizes the variation of efficiency for the four geometries and for the empirical model from the literature in a reference clearance, a tight, medium and large ones.

Table 4.2: Summary of efficiency variations with clearance

	Δ Efficiency [%]			
	Tight	***Reference***	***Medium***	***Large***
Geometry 1	0.52	0.00	-0.90	-1.81
Geometry 2	1.05	0.62	-0.63	-1.87
Geometry 3	1.02	0.58	-0.57	-1.22
Geometry 4	-0.21	-0.35	-0.90	-1.55
Model	1.05	0.80	-0.05	-0.90

The easiest way to implement these efficiency variations into the model is to apply a variable gain to the torque output. Given a reference condition, in terms of efficiency and torque, we can write

$$\eta_{ref} = \frac{\tau_{ref}\omega}{\dot{m}\Delta H_{is}} \qquad\qquad \eta = \frac{\tau\omega}{\dot{m}\Delta H_{is}} \tag{4.12}$$

Where ref indicates a reference efficiency, i.e. the efficiency of a reference geometry at a reference clearance. The torque at each clearance can be calculated as:

$$\tau = \frac{\tau}{\tau_{ref}}\tau_{ref} = \frac{\eta}{\eta_{ref}}\tau_{ref} = \frac{\eta_{ref} + \Delta\eta}{\eta_{ref}}\tau_{ref} = \left(1 + \frac{\Delta\eta}{\eta_{ref}}\right)\tau_{ref} \tag{4.13}$$

The τ/τ_{ref} coefficient is hence expressed in function of a reference efficiency and a $\Delta\eta$ that can now be directly imposed using the database in Table 4.2.

Effect of cooling on performance

The second term in Equation (4.4) is the effect of coolant injection n the turbine performance. It is well documented that the injection of coolant in different sections of blade and platform induces a penalty of the turbine aerodynamic efficiency. Some values are documented in the literature as reference, as summarized by Kurzke [71] based on the results in [72], [73].

Based on the CFD results, we can establish a relation between cooling injection and efficiency reduction for baseline and optimal tip in a compact cooled turbine. Figure 4.8 shows the variation of efficiency for a wide range of blowing ratio.

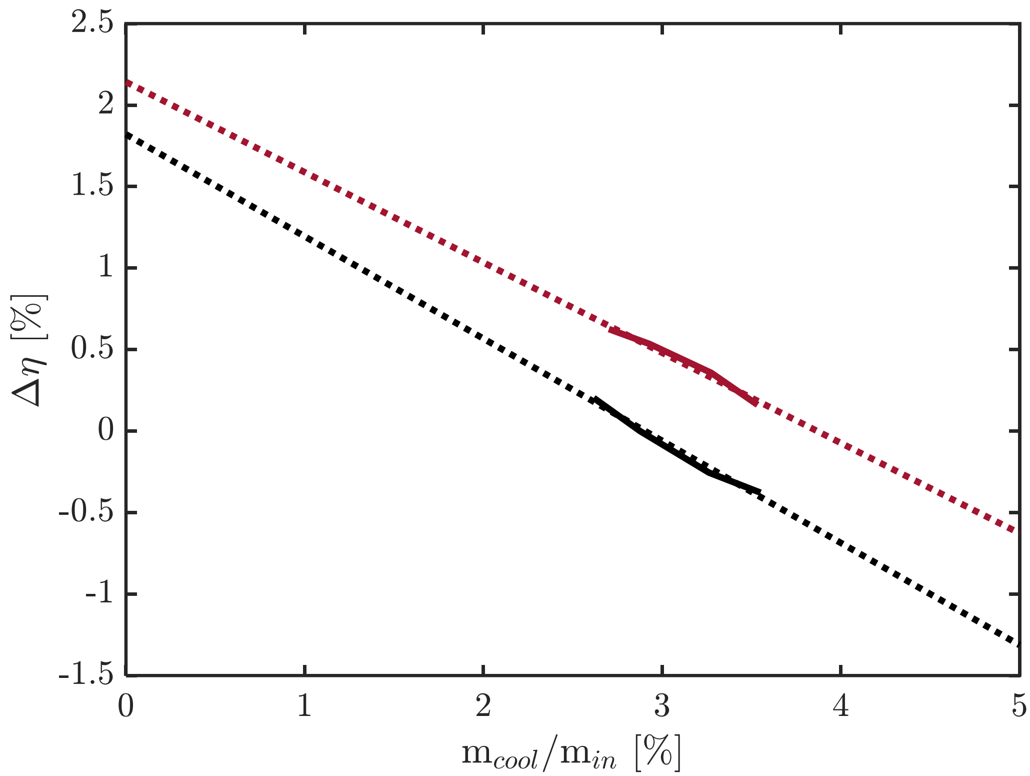

Figure 4.8: Change of efficiency as function of cooling mass flow, based on CFD results from Chapter 2, for simple squealer (black line) and optimized tip (red line).

On the abscissa, we find the ratio between total cooling flow rate and the main passage flow rate while on the ordinate, we report the change of efficiency compared to a nominal condition. The black line represents a single squealer, while the red line represents the optimized tip. The section that is actually characterized with CFD is indicated by the solid lines, while the dotted lines are an extrapolation of the trends based on the CFD results.

The range of coolant mass flows characterized with CFD ranges from 2.5% to 3.5% of the total mass flow, while thanks to the extrapolation a range of 5% can be covered starting from the extrapolated uncooled performance. It can be observed that the linear trend fits the CFD results with reasonable accuracy. In particular, the fittings have a R^2 value of 0.9875 and 0.9841 for squealer and optimized, respectively.

From this plot, we can state that the efficiency drop for a 1% change of blowing ratio is -0.63% and -0.55% for baseline and squealer respectively. The effect on the efficiency is included in the turbine performance model as:

$$\Delta\eta = C_{cool}(m_{cool} - m_{cool,\ ref})m_{in} \tag{4.14}$$

This equation is implemented in a dedicated cooling module and the change of efficiency is summed to the one due to the change of clearance.

4.2.2 Modeling of Tip Convective Heat Flux

The Green's Function module is used to implement the results from Chapter 3 into the engine model. The analysis in the convective heat transfer built on

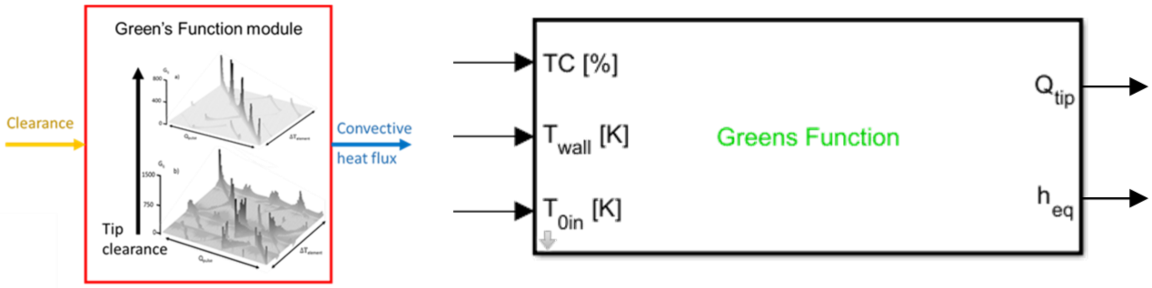

Figure 4.9: Green's Function module.

The matrices with the coefficients for different clearances are stored as parameters. Once the tip clearance is provided at each time step, the Green's Function matrix will be provided and used instead of the convective heat transfer coefficient in the calculations of the thermal expansion of blades and casing.

$$Q = Q(\delta/h\,, tip\ geometry, \dot{m}_{cool}, \dot{m}, T_0, T_w) \tag{4.15}$$

Analogously with the approach used for the efficiency, if we assume that the effect of clearance and the one of cooling are independent, the tip convective heat flux can be expressed as:

$$\frac{Q}{\Delta T} = \frac{Q}{\Delta T}\bigg|_{ref} + \frac{\partial Q}{\partial(\delta/h)}\bigg|_{tip} \Delta(\delta/h) + \frac{\partial Q}{\partial \dot{m}_{cool}}\Delta\dot{m}_{cool} + \frac{\partial Q}{\partial \dot{m}}\Delta\dot{m} + \frac{\partial Q}{\partial T_0}\Delta T_0 \tag{4.16}$$

The heat flux is now expressed in function of the difference of temperatures using the Green's Function approach described in Chapter 3.

However, the heat flux was previously described in function of the temperature at zero heat flux. This means that the reference temperature was the adiabatic wall temperature. In this model, we want to only have variables that are directly calculated from the engine model. Hence, we select the turbine inlet total temperature as our driving temperature.

$$Q = G\Delta T = G(T_w - T_0) + Q_{IsoT} \tag{4.17}$$

$$G = G(\delta/h\,, T_0/T_w) \tag{4.18}$$

After changing the reference temperature in this expression, there is a resulting offset indicated with Q_{IsoT}. The value of this offset is characterized for multiple clearances and multiple gas to wall temperature ratios. The physical meaning of this term is that for simple flows the total inlet flow would be the actual temperature driving the heat flux. For complex flows like the tip, using the total temperature as reference will induce a residual heat flux.

The tip has an effect on both heat flux intensity but also flow topology. If the heat flux coefficient was affected only in magnitude, the transformation matrices would be perfectly diagonal. However, the transformation matrices introduce a rotation of the Green's function matrices as well.

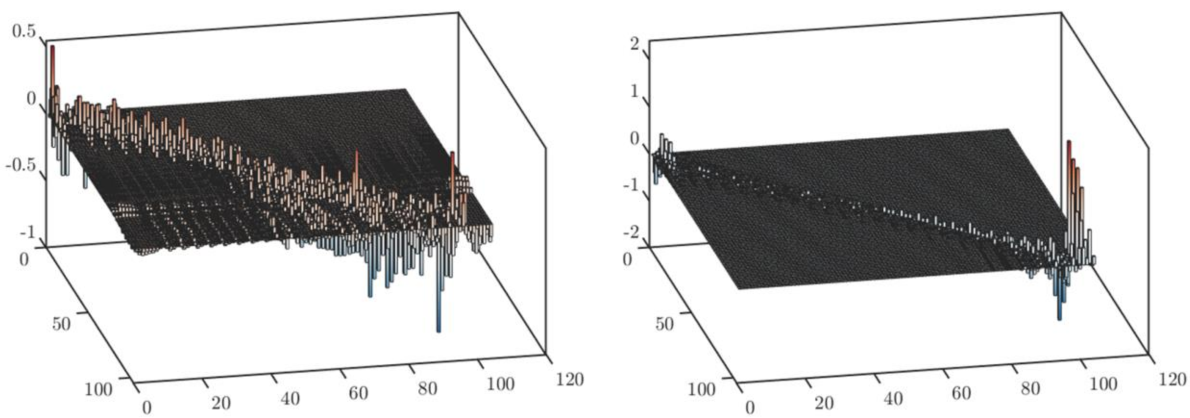

Figure 4.10: Transform matrices for tight clearances (left) and large clearances (right).

Figure 4.10 shows the two matrices used to interpolate the Green's Function matrix for any tip clearance. The matrix on the left is used for transformations from tight clearances to medium, while the one on the right is used for clearances between medium and large values.

Optionally, the matrices can be scaled to adapt to different engine conditions, following the method implemented in [66]:

$$G = G\left(\frac{\dot{m}}{\dot{m}_{des}}\right)^{0.8}\left(\frac{T}{T_{des}}\right)^{0.23} \tag{4.19}$$

Once the matrix is calculated through the Green's function module, two values are exported: a value of integral heat flux, and one value of equivalent convective heat flux coefficient, calculated in Equation (4.20):

$$h_{eq} = \frac{\sum_i (G\Delta T \cdot A_i)}{(T_0 - T_w)\sum_i (A_i)} \tag{4.20}$$

Effect of cooling

In the model, the film cooling is implemented in terms of cooling effectiveness. In the CFD, however, the wall is assumed isothermal so we cannot directly derive the cooling effectiveness from the numerical simulation. Based on the CFD, the effect on the tip heat flux will be quantified for different blowing ratios and included in the turbine performance model.

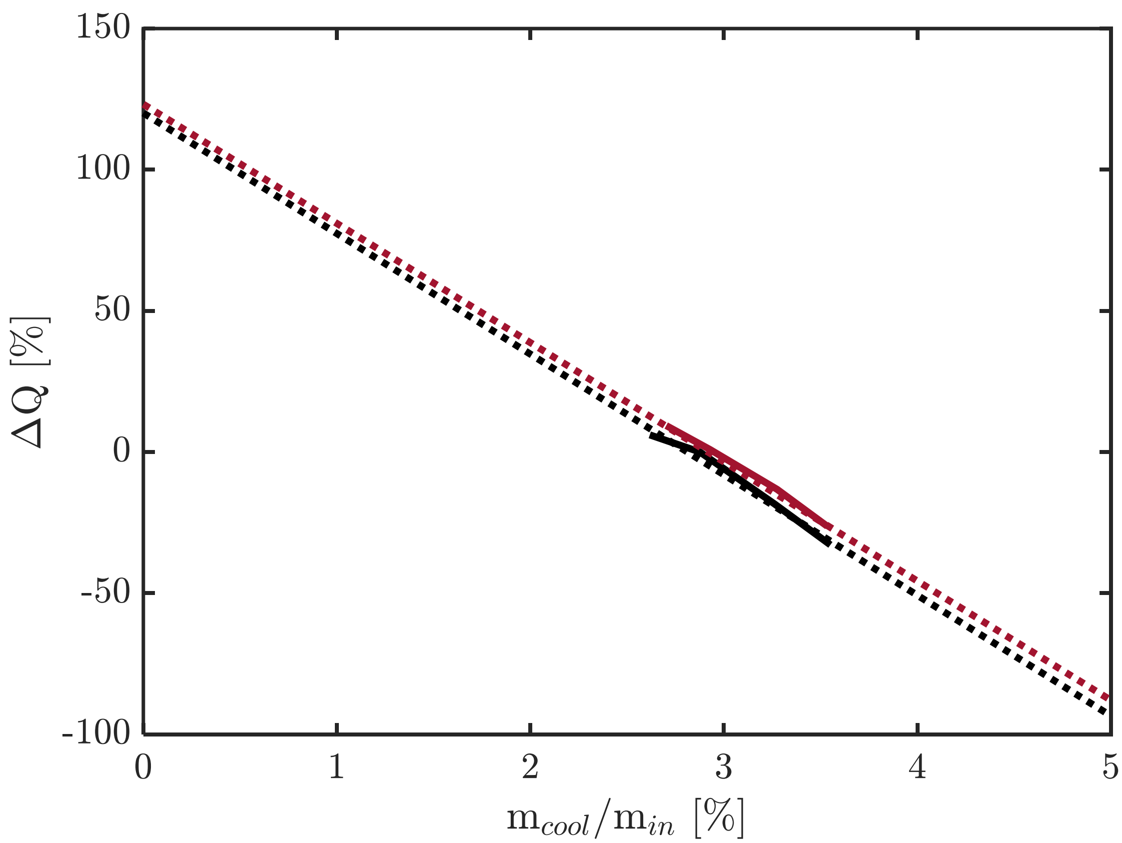

Figure 4.11: Trend of tip heat transfer in function of the coolant mass flow fraction, for simple squealer (black line) and optimized tip (red line).

Based on the scaling factor of the heat flux, we assume that this has a direct impact on the cooling effectiveness, as:

$$\frac{\eta_{cool}}{\eta_{ref,cool}} = \frac{Q_{ref}}{Q} \tag{4.21}$$

Where, consistently with the engine model, η_{cool} is the cooling effectiveness and is defined as:

$$\eta_{cool} = \frac{T_r - T_m}{T_f - T_m} \tag{4.22}$$

The compressor reference temperature is the cooling inlet temperature, the turbine temperature is the mass flow-averaged temperature at the turbine inlet, and the reference temperature is computed as the average wall temperature.

4.2.3 Mechanical and Thermal Modeling

Kypuros et al. provide a detailed guide for the time-resolved calculation of clearance variations through simplified models [74]. The work is based on the solution of the governing equations of mechanical and thermal energy, based on assumptions and boundary conditions that are specific to each component. A similar approach has been used by Chapman [67] and implemented in the library T-MATS to resolve the tip clearance integrated within an engine transient calculation.

A more detailed approach can be found in [75], where the HPT is modeled with a matricial approach. The same work is then used to develop a simplified model to predict the tip clearance.

The stochastic nature of engine performance can be characterized by modeling the clearance as a non-deterministic parameter [76].

In a simplified model, the tip clearance can be calculated as:

$$\delta(t) = r_{shroud}(t) - [r_{rotor}(t) - t_{blade}(t)] \tag{4.23}$$

Where the three terms are computed independently for the three components: blade, rotor and shroud.

Blade modeling

The centrifugal forces in the blades vary with the square of the rotational speed. The elongation of the blade is function of the initial length, the initial radius, the RPM and the material properties.

$$\Delta L_{RPM} = \frac{\rho L^2 (L + r_0)\omega^2}{E} \tag{4.24}$$

In most of the models available in the literature, the blades are considered thin compared to the other components and therefore the temperature gradients on the blade are neglected. For this reason, a lumped capacitance model can be used:

$$\Delta L_{Temp} = \alpha T_{blade} L \tag{4.25}$$

The blade temperature is calculated considering the contribution of convective heat flux and effectiveness of cooling. The cooling effectiveness is obtained from the previous analysis for different values of compressor pressure.

To summarize, the inputs necessary for the model are:

- Turbine and compressor temperature, and angular speed

While the parameters that characterize the part are:

- Cold geometry parameters (span…)
- Properties of the material
- <u>Convection coefficient</u> (this will be derived from the Green's Function)
- <u>Film cooling effectiveness</u> (from the robustness study)

Rotor disk modeling

The centrifugal force in the rotor disk varies with the square of the rotational speed. The elongation of the blade is only function of the initial length, the initial radius, the RPM and the material properties.

$$\Delta r_{RPM} = \frac{1}{4E}(1 - \nu_r)\rho_r \omega^2 {r_0}^3 \tag{4.26}$$

In this study the rotor is considered a uniform disk, where the sides are exposed to coolant and the upper surface is exposed to hot flow. The effect of windage is neglected.

For this reason, like in the case of the blades, the deformation can be expressed as:

$$\Delta r_{shroud,T} = \alpha T_{rotor} r_0 \tag{4.27}$$

The rotor temperature is calculated considering the contribution of convective heat flux and effectiveness of cooling.

To summarize, the inputs necessary for the model are:

- Compressor temperature, and angular speed

While the parameters that characterize the part are:

- Cold geometry parameters (radius)

- Properties of the material
- Rotor convection coefficient (this will be derived from the Green's Function)

Casing modeling

The casing is modeled as a rink-like structure, with the option of having different layers of material, i.e. a layer of abradable and a super alloy. Instead of using a constant heat transfer coefficient, the proposed approach to model the heat transfer on the internal casing is through the Green's function matrix. The two main contributors to the casing deflection are the thermal stresses, and the pressure differential.

To summarize, the inputs necessary for the model are:

- Turbine and compressor pressure and temperature

While the parameters that characterize the part are:

- Cold geometry parameters (radius, width…)
- Properties of the material
- Convection coefficient (this will be derived from the Green's Function)

The first step of the transient approach is to validate the dynamic model of the tip clearance, with the test case reported by Kypuros [74].

Figure 4.12 shows an increase of shaft speed from ground idle to maximum power. In the second plot we can see how the three components expand following the engine acceleration. The tip clearance, in the bottom plot, can be consequently calculated. These results are comparable with the values obtained in the paper, which are compared with experimental results.

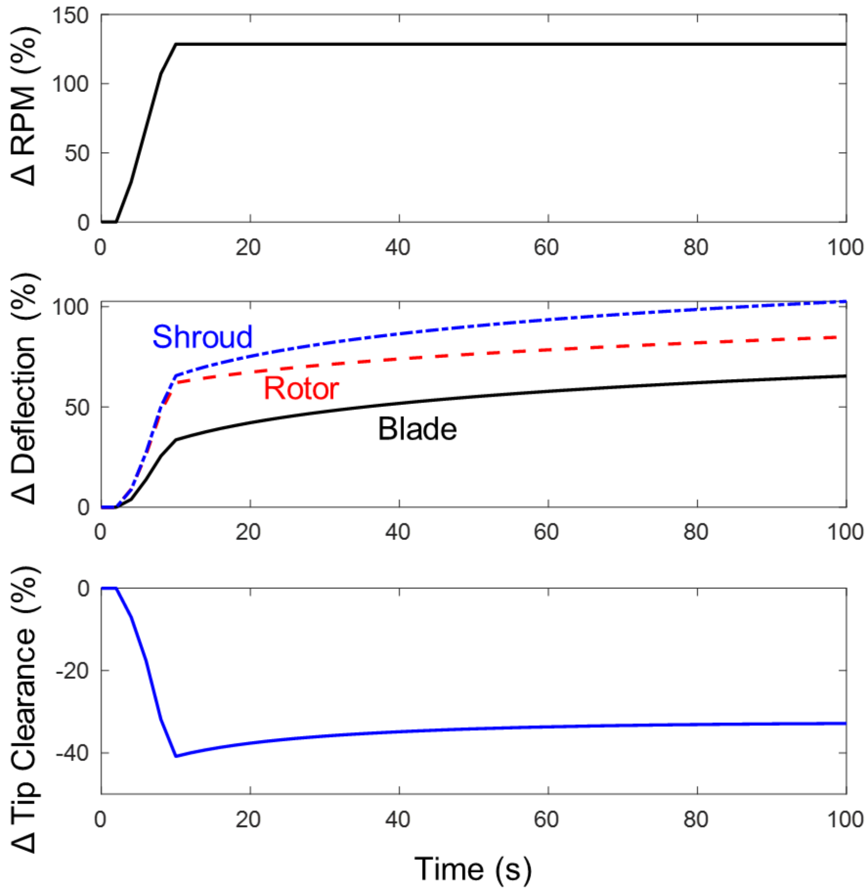

Figure 4.12: Rotor disk and blades, and shroud deformation in response to engine acceleration based on the validation test case[74].

4.3 Turbine Modeling in Engine Transient

4.3.1 Steady State Engine Modeling

For a potential application to large UAV market, a compact turbojet is considered. The engine modeled in this section is a single spool turbojet with a single-stage compressor and a single-stage turbine. The main engine parameters are summarized in Table 4.3.

Table 4.3: Summary of engine conditions

Overall pressure ratio	*Mass flow*	*RPM*	$\dot{m}_{fuel}$
4	1 kg/s	25000	0.023 kg/s

The turbine relevant parameters are selected in terms of corrected speed, corrected mass flow and Mach numbers. The hub to tip radius ratio is kept constant in the turbine scaling procedure. The mass flow is calculated once the geometrical parameters, the overall pressure ratio and the turbine parameters are constrained.

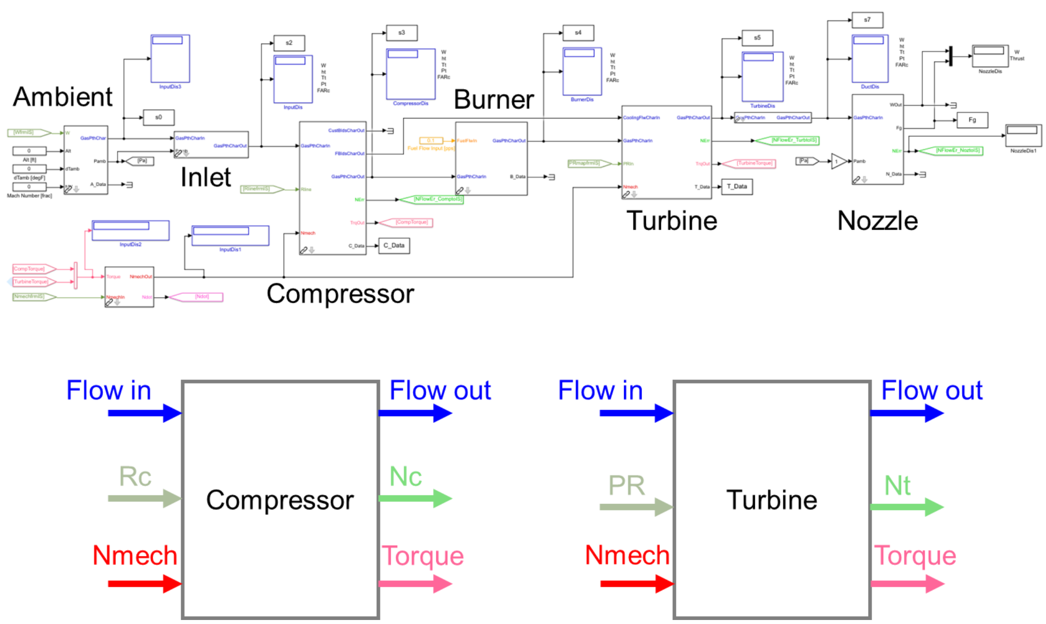

Figure 4.13: Diagram of the steady-state model.

The engine model is built using the components of the Toolbox for the Modeling and analysis of Thermodynamic Systems (T-MATS), an environment for engine modeling developed by NASA. This toolbox, integrated into Simulink, contains mathematical relations based on thermodynamics that allow for quick and reliable modeling of engine components. The T-MATS toolbox contains a solver for unsteady simulation (Newton-Raphson solver). This provides a tool to simulate the performance of the engine while continuously changing the input parameters. Figure 4.13 shows the diagram of the steady-state engine model, with a zoom of the compressor and the turbine, with their inputs and outputs. The compressor takes the inlet flow as an input. The parameter called "Rc" is an independent parameter that is fed to the component by the solver. This parameter is an auxiliary coordinate to move along an iso-speed line on the compressor map. The mechanical speed "Nmech" is computed from the difference of torque in compressor and turbine, in this single shaft configuration. The mass flow is calculated from the value of R, speed and rotational speed. For the turbine, the algorithm is analogous, but the auxiliary coordinate is replaced by the pressure ratio.

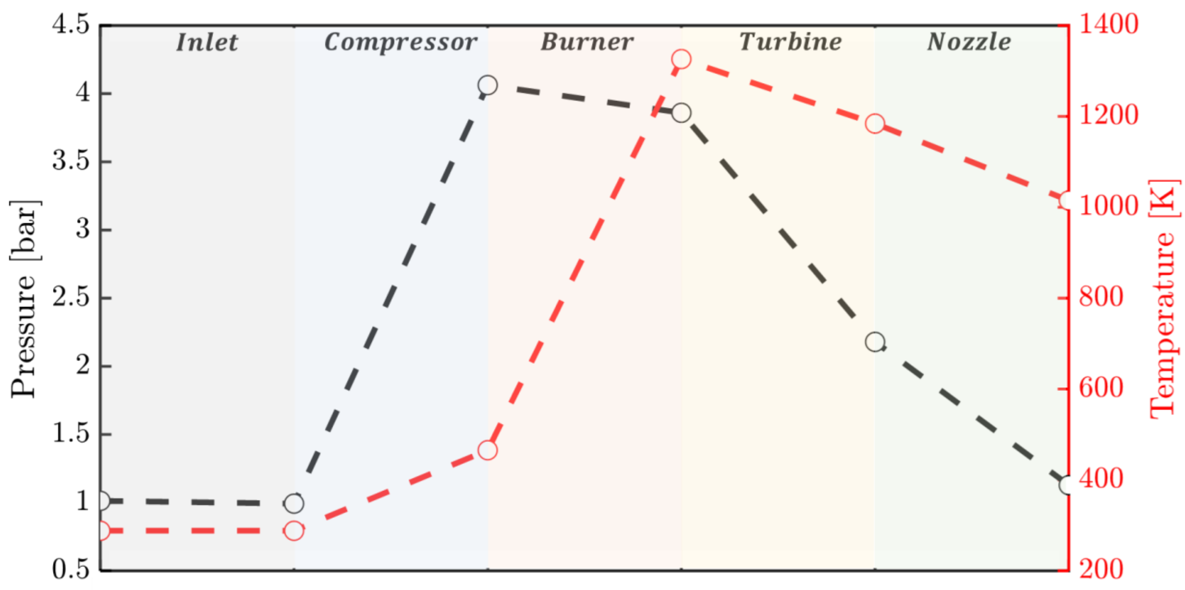

Figure 4.14: Steady-state engine model.

Figure 4.14 depicts the pressure, on the left ordinate, and the temperature, on the right ordinate, at each engine station. The first component is the inlet, where the temperature is kept constant and a pressure loss is implemented as a percentage of inlet temperature. The compressor has a pressure ratio close to four, so the pressure increases from 1 to 4 bar, while the temperature raises from ambient to a combustor outlet temperature of around 450K. In the burner, the combustion takes place at constant pressure, except for a small pressure loss through the component. The temperature on the other hand increases to a value higher than 1200K at the turbine inlet. A first expansion happens in the turbine, where the power is extracted to keep the compressor operating in this condition. Given the higher pressure and temperature at the turbine inlet, the pressure ratio needed to generate the power is lower than in the case of the compressor. Hence, the residual momentum is expanded through the nozzle and used to generate thrust. The nozzle is modeled with a constant throat area dimensioned based on the design mass flow.

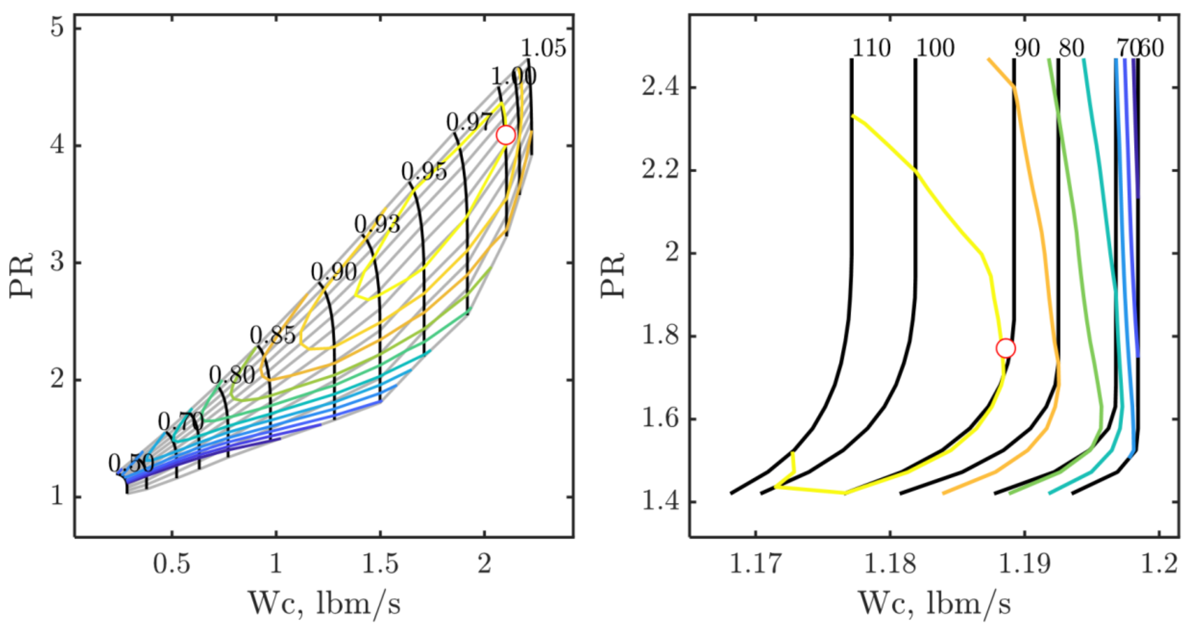

Figure 4.15: Compressor (left) and turbine (right) maps, with the steady-state point highlighted in the red-edged circle.

Figure 4.15 depicts the compressor and turbine maps on the left and right plots respectively. The black lines indicate iso-speed lines, i.e. lines with constant corrected speed defined as $\widetilde{N} = N/\sqrt{\theta}$ where θ is calculated as T_0/T_{ref}. The abscissa is expressed in terms of corrected mass flow, calculated as $\widetilde{m} = \dot{m}\sqrt{\theta}/\delta$. The ordinate is the total to total pressure ratio, calculated as an outlet to inlet ratio for the compressor and vice versa for the turbine. The maps are scaled from reference maps available in the literature following the method described by [77]. The operating point for steady design condition for both turbomachinery is indicated by the red dot. The point is selected through the design of the turbomachinery, to have room in the map for off-design conditions.

4.3.2 Engine Transient Analysis

The transient model allows an integration of the propulsive system within the airframe model and is suitable for an analysis of the aircraft with a holistic approach. In the case of a dynamic simulation, the difference between the compressor and turbine torques cannot be set to zero. The excess or lack of power is translated into an acceleration or deceleration for the following time-step. For this reason, the way to control the convergence in the internal loop is by setting the maximum number of iterations. The outer loop is based on a Newton-Raphson method with Jacobian calculation. A detailed explanation of the algorithm implemented by T-MATS is described by Chapman [78].

A deceleration-reacceleration trajectory is generated in this section by changing the fuel flow injected in the combustor. Figure 4.16 illustrates the same two maps used for the steady model, exposed to a time-varying trajectory.

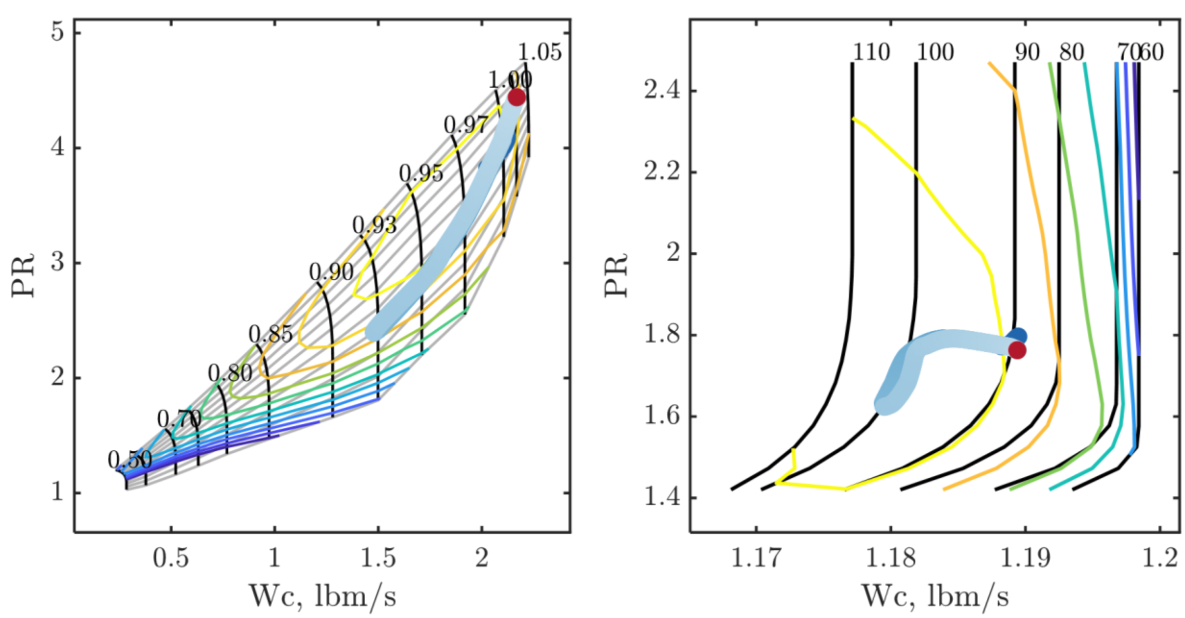

Figure 4.16: Compressor map (on the left) and turbine map (on the right) with operating conditions over an engine transient.

Starting from the compressor map, the design point was located at a speed of 100% of the reference speed. As the fuel flow is reduced, the shaft speed drops as well. Since the compressor inlet temperature is constant, because there is no temperature change through the inlet, a decrease in mechanical speed corresponds to a decrease in corrected speed. For the turbine, on the right, the design corrected speed is selected to be 90% of the design speed. During the transient, the shaft speed that of course equals the compressor rotational speed, initially decreases and then increases. However, a change in fuel flow affects the turbine inlet temperature. A decrease in fuel, and consequent decreases in speed, are compensated by a decrease in turbine inlet temperature and therefore an increase of corrected speed.

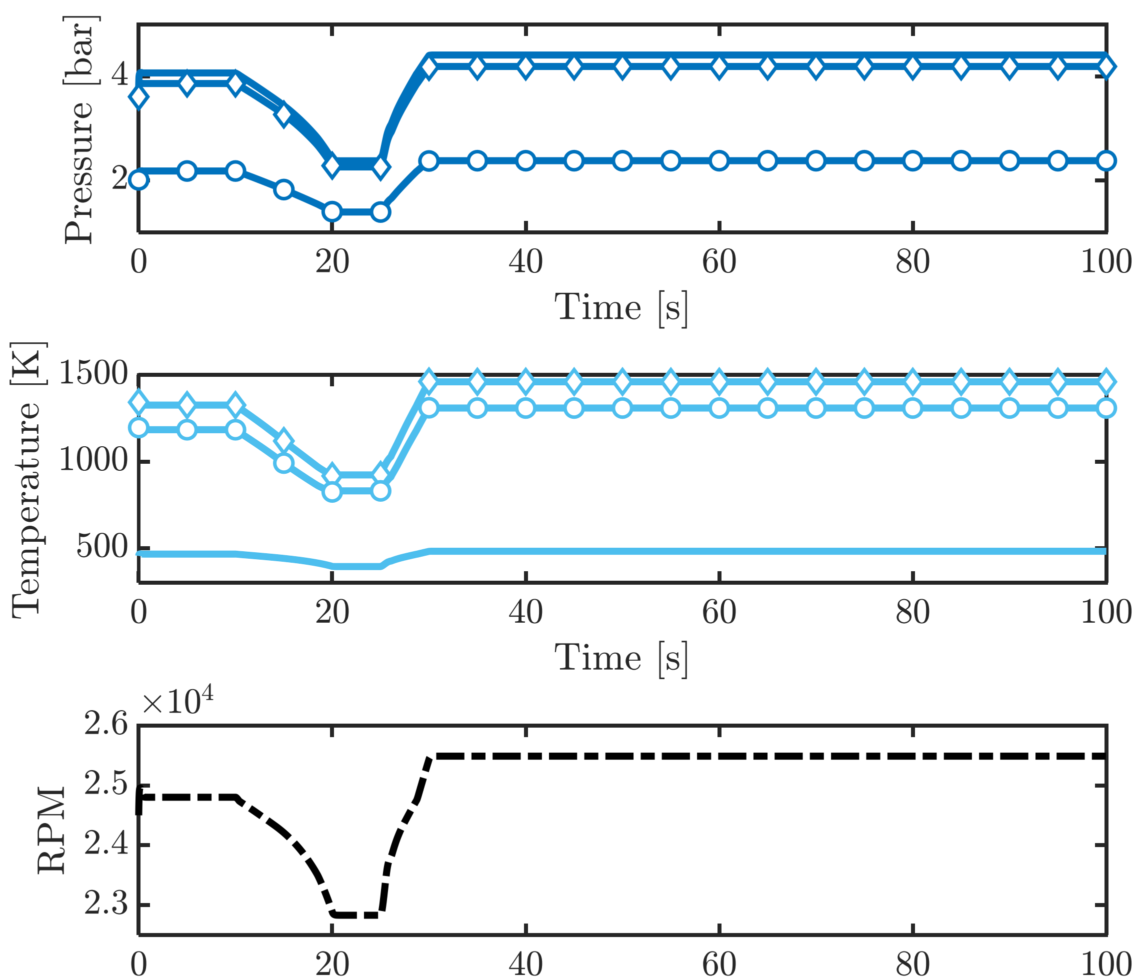

Figure 4.17: On the top: pressure at compressor outlet (solid line), turbine inlet (diamonds) and turbine outlet (circles). Middle: temperature at compressor outlet (solid line), turbine inlet (diamonds) and turbine outlet (circles). Bottom: RPM and specific fuel consumption in time.

Figure 4.17 shows the trends of pressure and temperature in time, due to an imposed sequence of fuel flow. On the top graph, the pressure at compressor outlet (solid line), turbine inlet (diamonds) and turbine outlet (circles) are shown. The highest pressure is always the compressor outlet, which at the initial instant starts at four bar, drops at 2.5 bar when the fuel is decreased, and increases back to the initial value once the fuel is brought back to a value higher than the design value. The pressure at the exit of the combustor is close to the compressor, except for a minor loss, and the turbine outlet pressure marked with circles, is the inlet divided by the pressure ratio that is in the range of 2. The middle graph is the trend of temperature in time. The lowest temperature is the compressor outlet, followed by the turbine outlet and then the turbine inlet. The drop in fuel flow that takes place between 20 and 30 seconds induces a decrease in turbine inlet temperature of about 500K. Finally, the bottom figure shows the trend in terms of shaft mechanical speed, in rounds per minute.

4.3.3 Engine Sensitivity to Turbine Performance

A brute force Monte Carlo approach similar to the methodology described by Bunker [79] was adopted. Montomoli et al. [80] clarify that the Monte Carlo method coupled with a Meta-Model is the main reference for stochastic studies. The method converges to the theoretical solution as long as the number of samples (and consequent calculations) is large enough to characterize the entire design space. An example of how this approach can be used to assess the effect of tip flow on turbine performance is provided in [81].

In the case of this analysis, the curse of dimensionality normally associated with uncertainty quantification problems is avoided by treating all the parameters except for the turbine tip clearance as deterministic. The tip clearance and the consequent efficiency variations are modeled using a stochastic approach. Given the unknown tip clearance distribution, a normal distribution with a given mean and standard deviation is used.

Figure 4.18 left, shows the distribution of tip clearance that is used for the stochastic analysis of the engine. The abscissa indicates the value of tip clearance as percentage of the blade span, while the ordinate shows the probability calculated as the ratio between the relative frequency and the total count of samples.

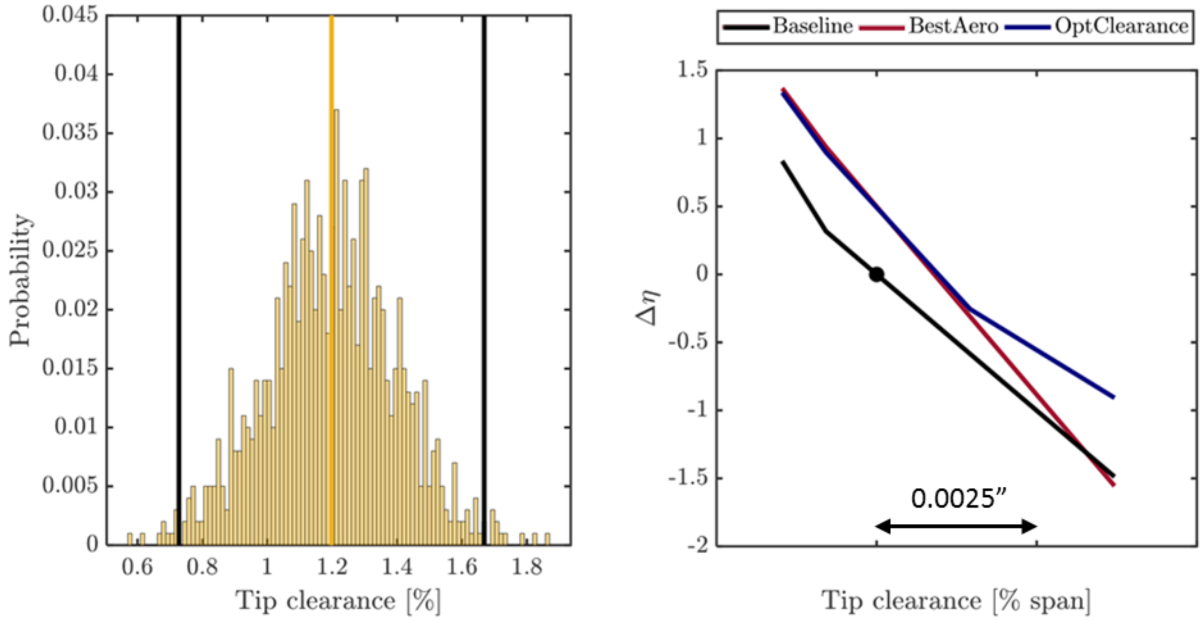

Figure 4.18: Left, probability distribution of tip clearance with 95% confidence interval. Right, effect of tip clearance on the efficiency in three different tip geometries: baseline squealer (black line), best efficiency from single clearance optimization (red line), best efficiency from multi-clearance optimization (blue line).

The mean value of tip clearance is selected as $\mu = 1.2\%$ with a standard deviation of $\sigma = 0.2\%$. Figure 4.18 on the right, summarizes the results derived in Chapter 2 about the effect of tip gap on the turbine efficiency for three different geometries. In particular, three configurations are analyzed in this section: the baseline squealer, which is considered our reference design, the geometry with the highest efficiency designed with a single tip gap optimization (marked with ‘a’ in Figure 2.16) and the geometry with the highest efficiency designed with a multi-clearance optimization (marked with ‘a’ in Figure 2.21). A total number of 1000 samples are selected to characterize the distribution of tip clearance, and for each value the variation of efficiency is calculated. Figure 4.19 shows the results in terms of probability of efficiency for each design.

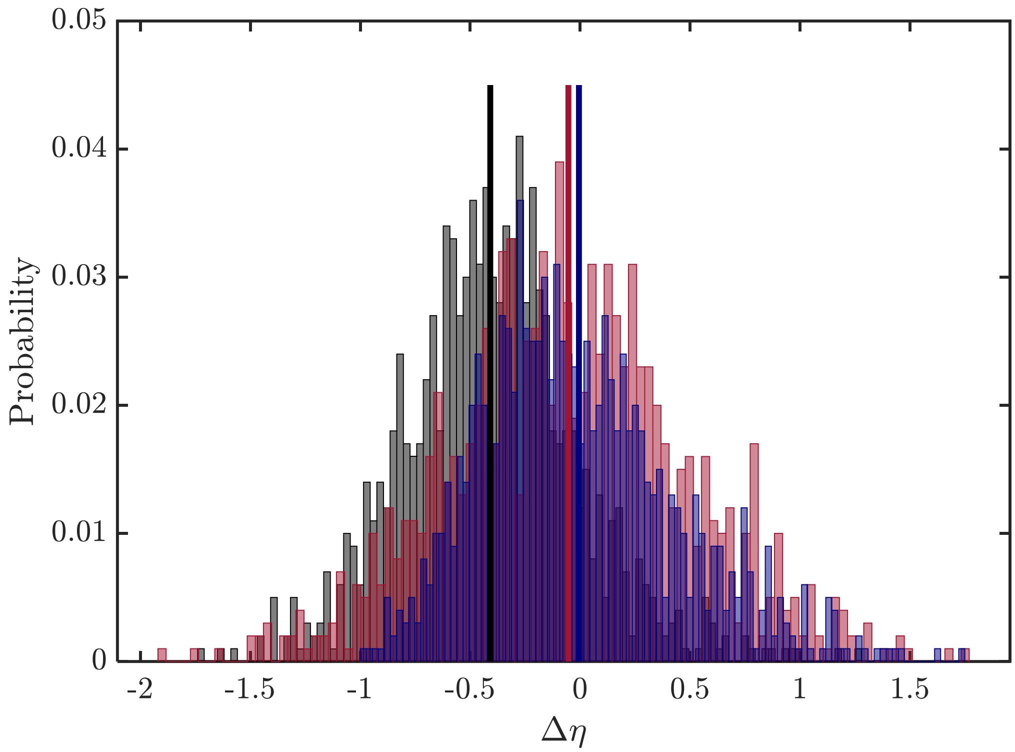

Figure 4.19: Histogram of efficiency for three different tip configurations: baseline squealer (black), best efficiency from single clearance optimization (red), best efficiency from multi-clearance optimization (blue). The solid lines indicate the mean values for each distribution.

The distribution is then fed to the steady engine model, which calculates the engine operating condition under each turbine efficiency. Figure 4.20 shows the final results from the stochastic engine analysis in terms of thrust. We can see that the mean values are consistent with the trends identified in the mean values of efficiency. However we can see some distortion in the distributions due to the nonlinearity of the engine model and turbomachinery coupling.

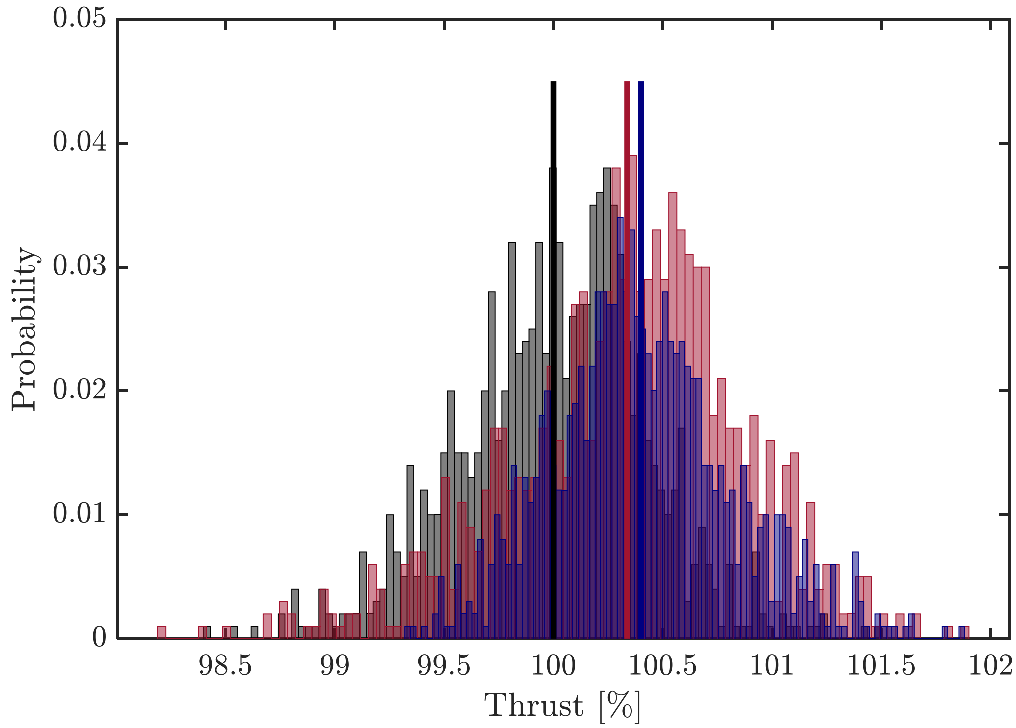

Figure 4.20: Thrust variations due to efficiency uncertainty for three different tip configurations: baseline squealer (black), best efficiency from single clearance optimization (red), best efficiency from multi-clearance optimization (blue). The solid lines indicate the mean values for each distribution.

In particular, we can see that while the mean values of thrust in the two optimal design are approximately the same, the tip optimized over a range of clearances offers a more narrow distribution of thrust. This means that from a stochastic perspective, the uncertainty in the performance of this component is smaller.

An additional geometry is used for the engine analysis, this time with the same mean efficiency as the simple squealer, but with less efficiency variability over clearance. This geometry is the one marked with ‘f’ in Figure 2.21. Figure 4.21 shows the stochastic response of the engine model in terms of turbine efficiency variation and thrust percentage.

The results show that, as expected, the two mean efficiencies (left graph) and thrust (right plot) are very similar. The values are identified with black and purple solid lines for the squealer and optimized geometry respectively. However, the variability of the performance in the case of the optimized tip is almost halved. This conclusion can be made qualitatively by looking at the area covered by the grey histogram (baseline) compared the purple one (optimized). The quantitative results, in terms of confidence interval, are shown in Table 4.4.

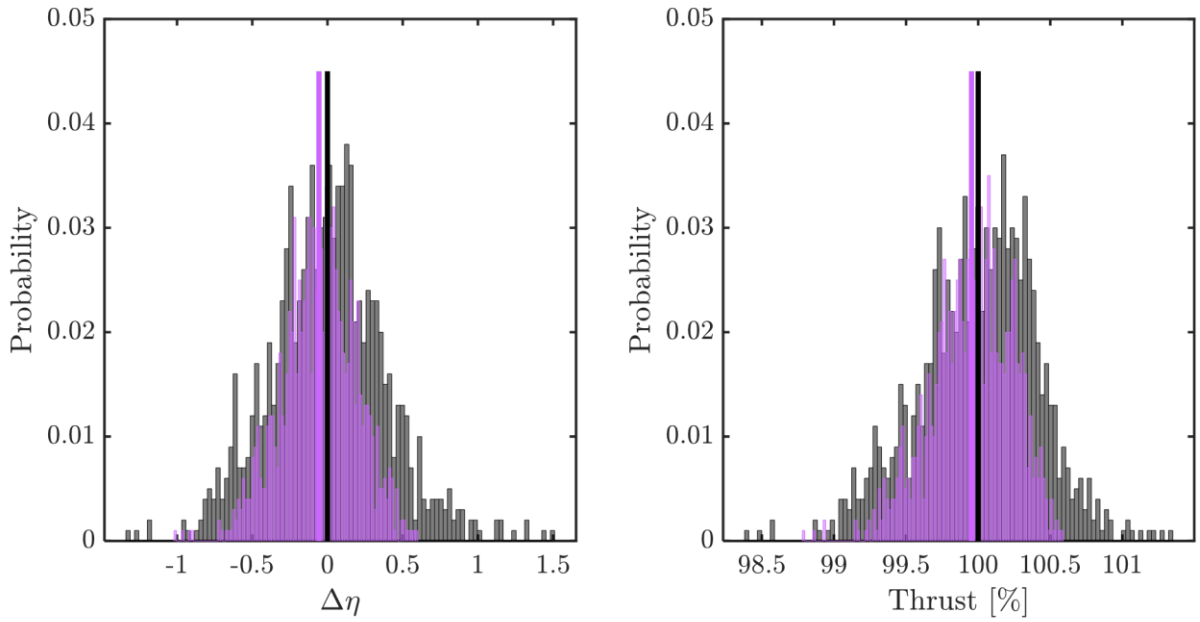

Figure 4.21: Probability of efficiency and thrust for baseline squealer and marked with 'f' in Figure 2.21.

After having assessed the effect of uncertainty on turbine efficiency, we must assess the effect on the stage mass flow. It has been observed in Chapter 2 that changes in clearance have an effect on leakage and passage flow angle, and consequently on exit flow angle and mass flow. This uncertainty is added into the model as shown in Figure 4.22.

Analogously to the approach used for the efficiency, the changes in tip clearance are propagated to the calculation of passage mass flow, based on the results shown in Figure 2.6. The turbine map is updated using a correction factor that is function of clearance. The updated map is then fed back into the model, where the effect on the gas turbine performance is calculated. By using this approach, the turbine map is no longer defined as a deterministic entity but a stochastic one instead.

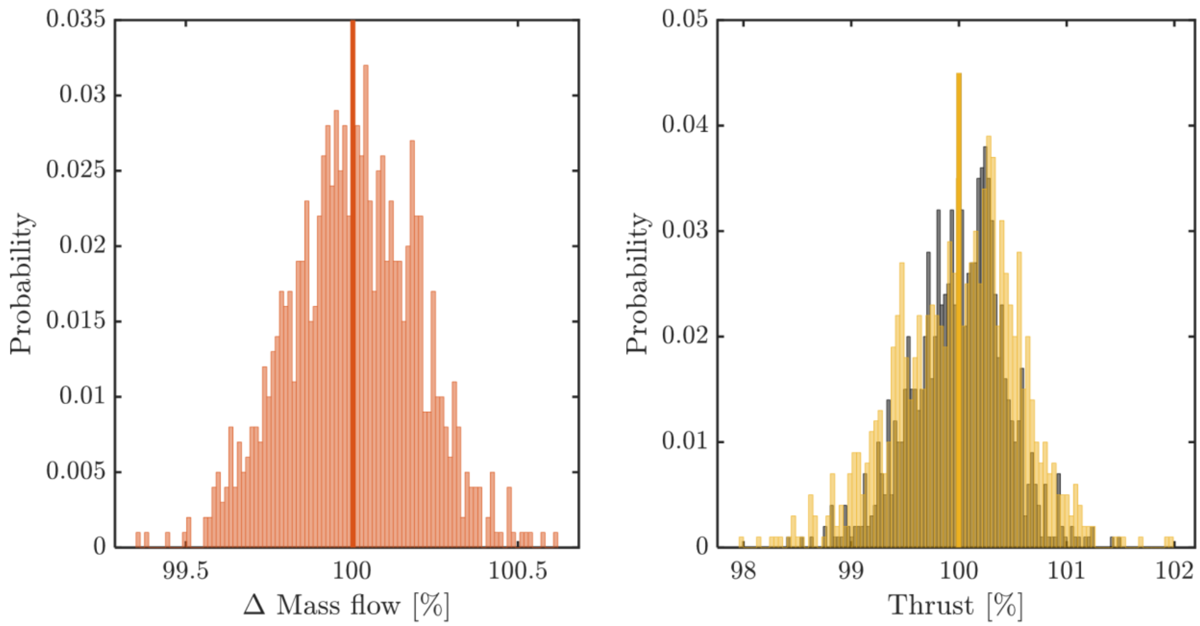

Figure 4.22: Uncertainty on mass flow induced by clearance variation (left) and effect on thrust distribution (right).

The additional uncertainty on engine gross thrust can be identified in the right plot as the difference between the grey histogram, where the mass flow changes are neglected, and the yellow histogram. Finally, the results are summarized in Table 4.4. The standard deviation is calculated based on 1000 samples for each case.

Table 4.4: Summary of the sensitivity to tip clearance.

	Mean value [%]	Standard deviation [%]
Baseline	100.00	0.43
Best Aero Opt 1	100.33	0.53
Best Aero Opt 2	100.40	0.40
Best Aero Opt 3	99.95	0.28
Baseline + mass flow	100.00	0.56

Consistently with the previous section, the baseline indicates the simple squealer. 'Best Aero Opt 1', '2' and '3' indicate the geometry with highest efficiency from single point optimization, the geometry with highest mean efficiency from multi-clearance optimization and the geometry with the same efficiency as squealer but low variability from multi-clearance optimization respectively. The optimal geometries 1 and 2 offer high mean values of thrust, but geometry 2 also offers a smaller standard deviation. The highest standard deviation is calculated when the uncertainty in both efficiency and mass flow is considered.

4.3.4 Turbine Tip Effects over an Engine Transient

The models of the tip clearance for performance, convective heat flux and structural deformation are integrated within the engine model as conceptually illustrated in Figure 4.23. The mechanical components take as input the predicted convective heat flux and cooling effectiveness and will output the dynamic tip clearance. Based on the tip clearance, the turbine aerothermal performance will be retrieved and fed to the model to correct the baseline turbine map.

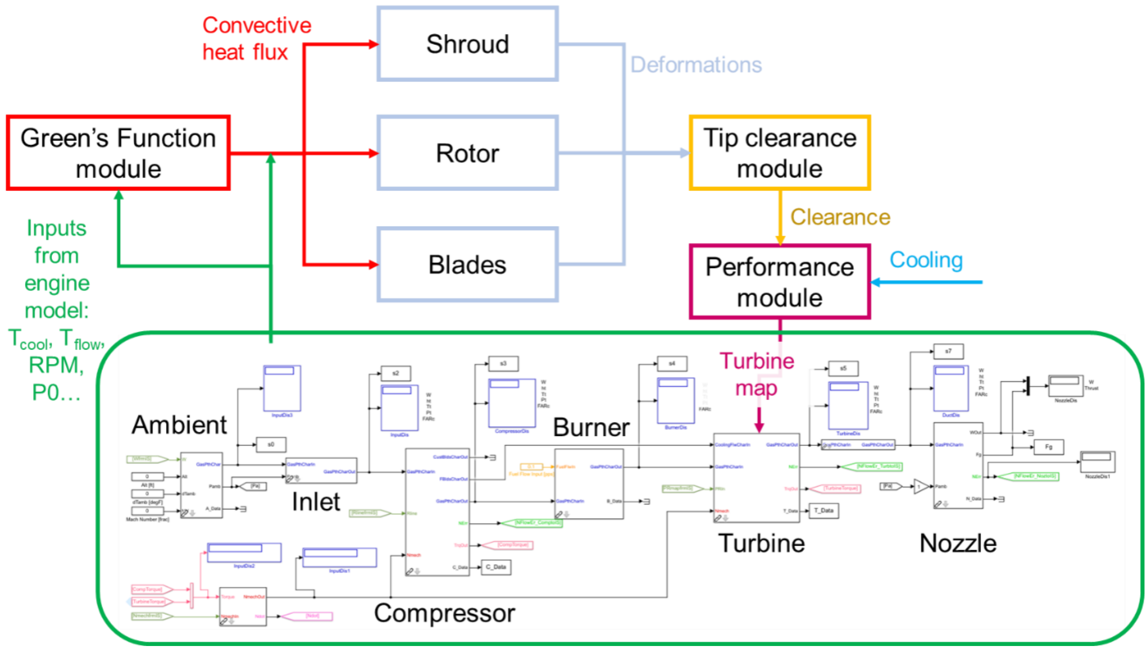

Figure 4.23: Conceptual diagram of the engine model integrated with the clearance mechanical and aerothermal.

The engine model has two solvers: one for the internal iterations on each time step, and the other to iterate in time.

Cruise condition

The first step is to use a simple model for a quick assessment of clearance changes. The model described in the previous section is implemented into the T-MATS based transient engine model and used to select the geometries parameters that would allow a rub-safe operation in cruise.

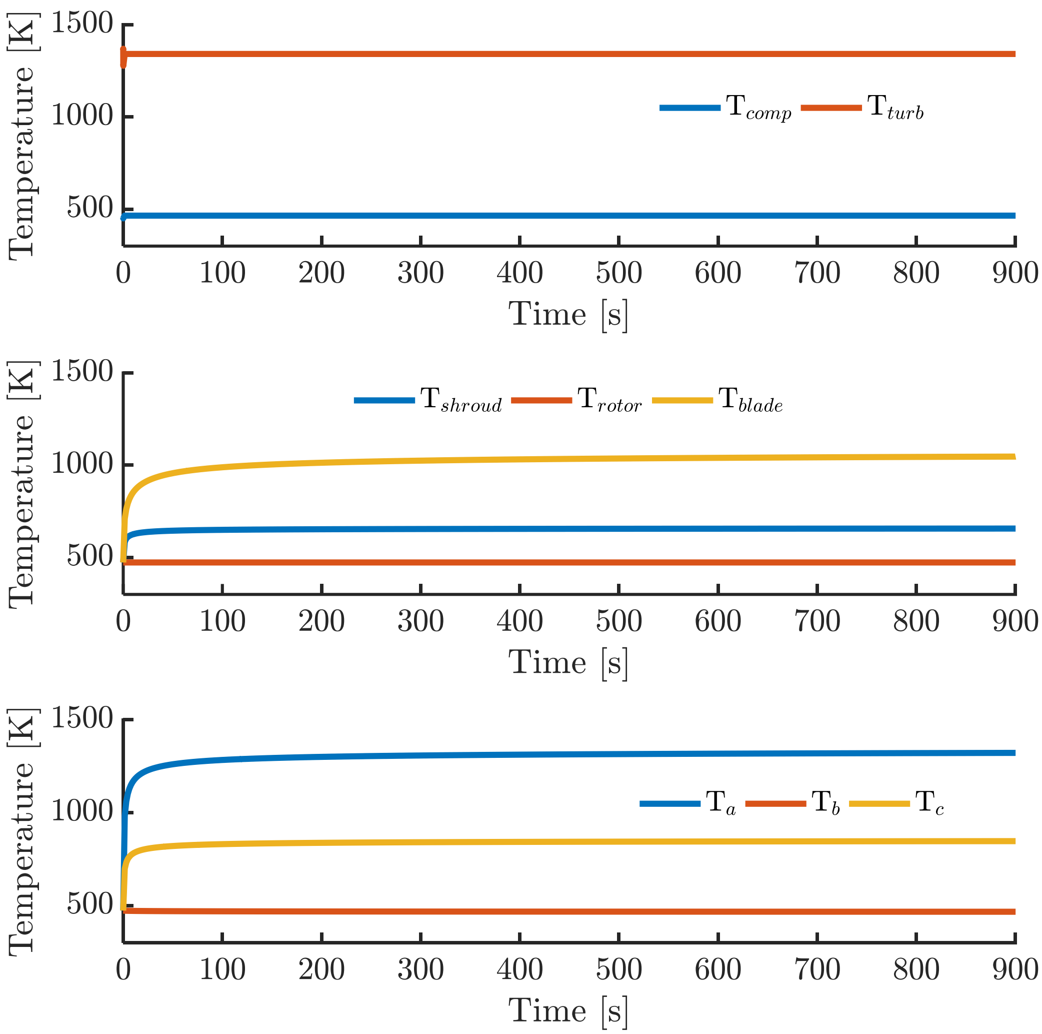

Figure 4.24: Calculation of steady conditions in terms of temperatures. Top: turbine and compressor temperature. Middle: shroud, rotor and blades temperature. Bottom: three temperatures in the casing, ‘a’ for inner radius, ‘b’ for outer radius and ‘c’ for intermediate radius.

The input is a constant vector of fuel flow in time. Given an initial guess for shaft speed, the engine will tend to go to an equilibrium shaft speed that could be identified as cruise condition. The purpose of these simulations is to run for a long time and let the components go to thermal steady state. In this way the steady state running clearance can be identified.

Figure 4.24 shows the temperature trends over a trajectory to achieve steady state. On the top, the gas temperatures at the exit of the compressor and at the inlet of the turbine are showed. As expected, since the fuel mass flow is constant over time, the temperatures will tend to stabilize to a constant value.

The middle plot depicts the temperatures on shroud, blade and rotor disc, indicated with “rotor”. The simulation is run for more than 1000 seconds to allow to achieve steady state. The initial temperatures of shroud and rotor disc are close to their final steady state temperature and therefore they do not take long to get to a constant temperature, despite their larger size. The blades are the smaller components, but they are also the most exposed to the flow. They reach a temperature higher than 1000 K and this implies a longer temperature transient.

The bottom plot highlights the temperature gradient within the casing. The temperature in the abradable section, marked as “Ta”, is the highest since it’s directly exposed to the hot flow. The “Tb” indicates the temperature of the metallic casing on the outer shroud. The intermediate temperature “Tc” is the temperature at the intersection calculated based on the semi-infinite body analytical solution.

Figure 4.25 shows the consequent component deformations. The top figure shows the trends of deformations of the three main components in function of time. The deformations are reported in absolute dimensions (in millimeters). The shroud has the largest expansion, followed by the rotor disc and lastly by the blade. The rotor would normally expand similarly to the casing, but in this case the initial temperature is selected close to the final value so the variations are smaller. The transient behavior follows the trends previously observed in the temperatures. This is caused by the pressure and centrifugal forces responding immediately to changes in the operating conditions, while the thermal loads, as previously demonstrated, are the slowest to respond.

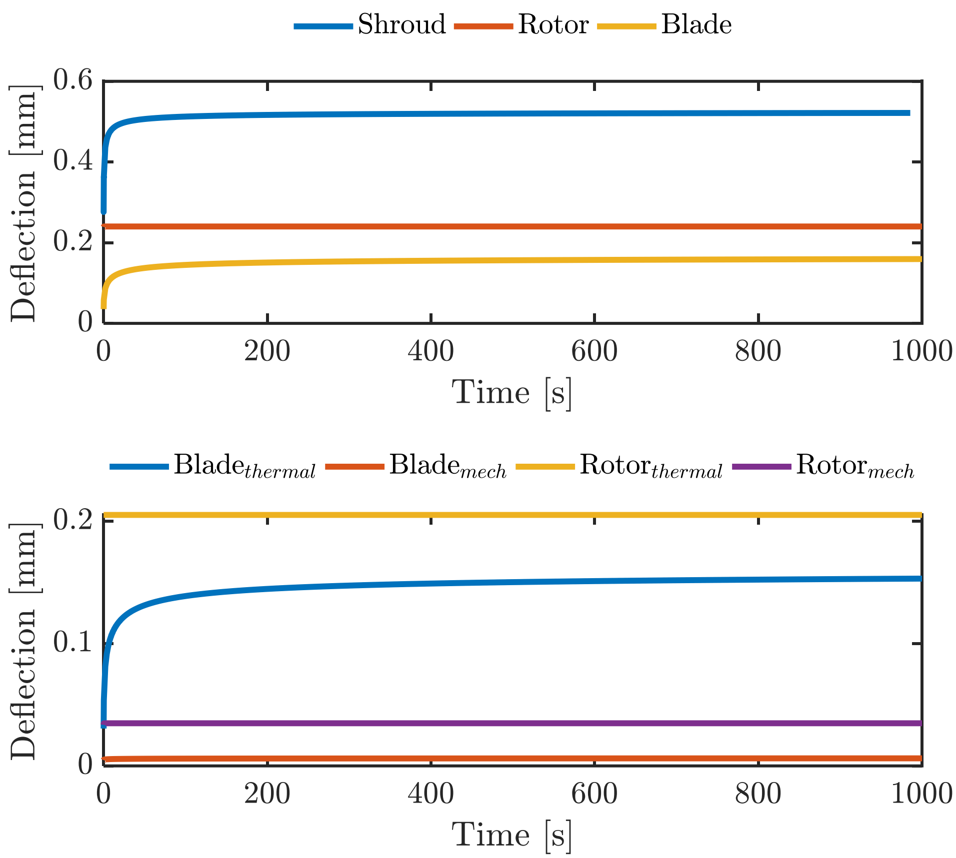

Figure 4.25: Trends of deflections over time. Top: shroud, rotor and blade deflections. Bottom: mechanical and thermal deflections in blades and rotor.

Finally, Figure 4.26 on the left shows the shaft speed in function of time. Given an initial guess of speed, the system evolves to a steady value very close to 25000 RPM that was the design target speed.

On the right, the deflections are used to calculate the running clearance over time. On the left ordinate the clearance is expressed in absolute terms, with units in millimeters. On the right ordinate, the clearance is expressed in percentage of the blade span. This is the value that will be fed to the performance module. The tip clearance starts from a minimum of 0.4% up to almost 1.4% to then stabilize at around 1.3%. This is selected as an acceptable operation at steady condition and the unstressed parameters are fixed to proceed with the transient analysis.

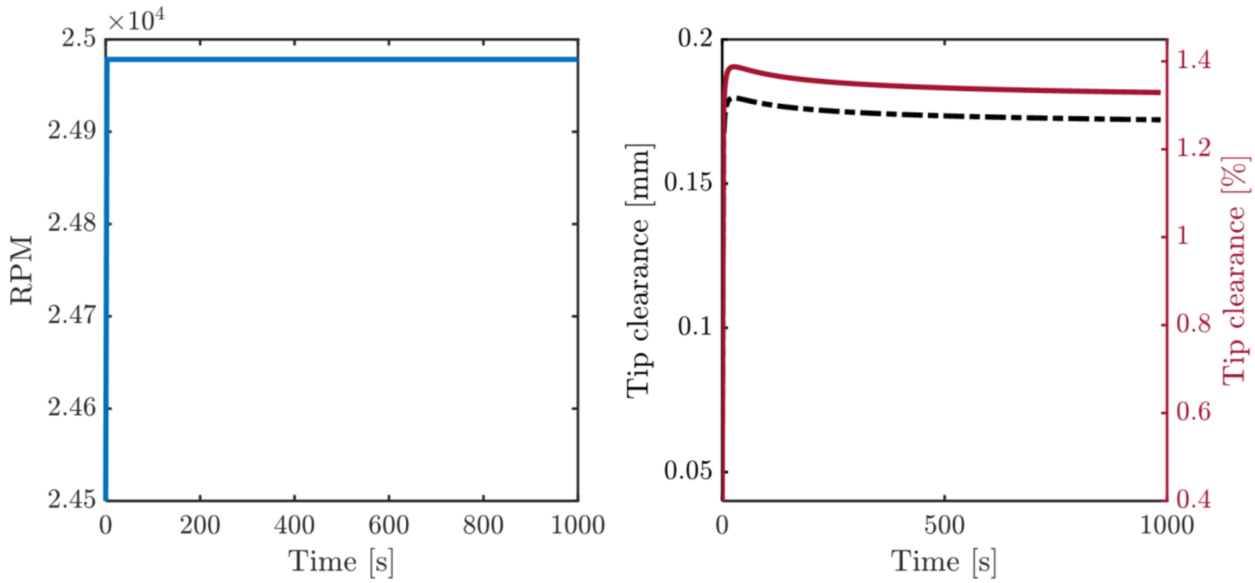

Figure 4.26: Left, evolution of shaft speed over time. Right, change of tip clearance over time in absolute dimension on the left ordinate and relative dimension in the right ordinate.

Deceleration-reacceleration trajectory

One of the critical trajectories for a gas turbine operation is the cold restart. This represents a challenge from a tip clearance control perspective. This is due to the different time scales involved in pressure, centrifugal and thermal loads. In this work we focus on compact engines, and therefore compact turbomachinery. The components sizes affect in multiple ways each of these loads and the consequent deformations. To characterize the relative importance of these phenomena in compact engines, the ratio between deformations due to centrifugal force and to thermal expansions can be derived as:

$$u_{ratio} = \frac{u_{RPM}}{u_{thermal}} \tag{4.28}$$

This ratio expresses how large are the deformations due to the changes in RPM compared to the changes in temperature. This number is relevant to assess the probability of having a pinch point. In case this number is very large, then thermal loads can be neglected and the system will be dominated by centrifugal loads. In this case, the initial clearance must be large and then it will be sealed by the growth of rotor disc and blades. In case this nondimensional number is small, the changes of tip clearances due to changes in shaft speed can be neglected. This diminishes the danger of having a pinch point because the rotating and stationary point will be deforming with similar time scales and the change of elongations due to centrifugal forces are not sufficient to cause a drastic reduction of tip gap.

To quantitatively estimate the value of u_{ratio} in the case of the rotor, considering the equations for centrifugal and thermal deformations, we can express it as:

$$u_{ratio} = \frac{\frac{1}{4E}(1-\nu_r)\rho_r \omega^2 {r_0}^3}{\alpha T_{rotor} r_0} = \frac{\rho(1-\nu_r)}{4\alpha E}\frac{\omega^2}{T_{rotor}}{r_0}^2 = \frac{\rho(1-\nu_r)}{4\alpha E}\left(\frac{T_0}{T_w}\right)\frac{\omega^2 {r_0}^2}{T_0} \tag{4.29}$$

On the right hand side of Eq. (4.29), the ratio is expressed as the product of three main terms: the first terms are mainly a function of the material, the second term is the gas-to-wall temperature ratio, whose range of values is normally characterized for cooled and uncooled turbine stages. Finally, the last term is function of the rotor disc geometry and the operating conditions. In particular the ratio is directly proportional to the square of the RPM and to the square of the disc outer radius, while it is inversely proportional to the turbine inlet temperature.

Analogously, the same nondimensional number can be written for the blade as:

$$u_{ratio} = \frac{\frac{\rho L^2 (L+r_0)\omega^2}{E}}{\alpha T_{blade} L} = \frac{\rho}{\alpha E}\frac{\omega^2}{T_{blade}} L(L+r_0) \tag{4.30}$$

Considering a blade with a fixed hub to tip ratio, this can be rewritten as

$$\begin{aligned} u_{ratio} &= \frac{\rho}{\alpha E}\frac{\omega^2}{T_{blade}}(r_t - r_0)\big((r_t - r_0) + r_0\big) = \frac{\rho}{\alpha E}\frac{\omega^2}{T_{blade}} r_t (r_t - r_0) \\ &= \frac{\rho}{\alpha E}\left(\frac{T_0}{T_w}\right)\frac{(1 - r_h/r_t)}{(r_h/r_t)^2}\frac{\omega^2 {r_0}^2}{T_0} \end{aligned} \tag{4.31}$$

The right-hand side of the equation is similar to the one derived for the rotor disc. In this case however, the hub to tip ratio is an additional parameter to consider. By performing a parametric study on these two nondimensional number, we can characterize different families of engines.

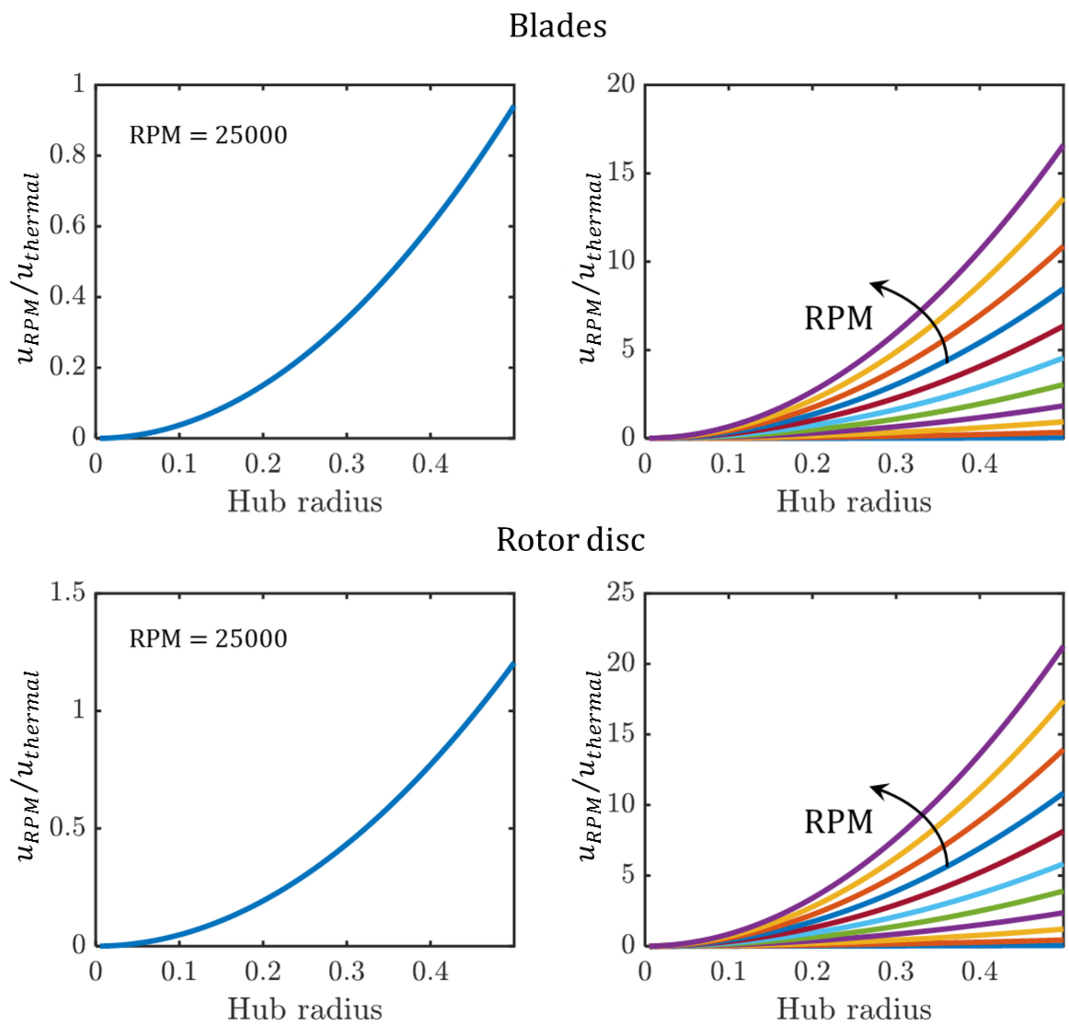

Figure 4.27: Ratio between deformation due to centrifugal forces and thermal load for rotor, on top row, and blades, bottom row. Values are provided for fixed shaft speed on the left and for variable shaft speed on the right.

The left column on Figure 4.27 shows how the ratio between centrifugal and thermal deformations for a fixed shaft speed in blades (on the top column) and rotor disc (on the bottom column). As clear in the two formulas, this dimensionless number has a quadratic dependence with the hub radius. When the turbine is small, like in this work where the turbine radius is less than 0.1 m, the deformations due to RPM are less than 5% of the thermal ones in both blades and rotor. However, if we move to a more traditional larger turbine size, like 0.4 m, the ratio becomes 60% and 80% for blades and rotor respectively. The implication of this different behavior is that in a large engine, the centrifugal force can double or halve the tip gap, while in a small engine the variability of tip gap due to RPM can be even negligible.

We want to assess the turbine performance over a wide range of clearances and operating conditions. This is achieved with a deceleration-reacceleration trajectory, generated by imposing changes in injected fuel flow over time. In this case, the fuel is kept constant to design fuel-to-air ratio for the first 25 seconds. Please note that the initial conditions are set so that the duration of the thermal transient is minimized. For this reason, the final temperatures calculated in cruise conditions in the previous sections are imposed in this case at time 0 seconds. This means that in the very few seconds, the components have already achieved a steady stressed dimension.

Figure 4.28 depicts the trend of engine shaft speed over time for one of the turbine geometries. The initial velocity, set as an initial guess, quickly adapts to a steady value that is kept constant for the first 25 s. As the fuel flow is dropped, the shaft speed starts dropping as well, with a small delay caused by the rotor inertia. At the end of the deceleration phase, the fuel is kept at a minimum level for approximately 50 seconds, from 40 to 90 seconds. Afterwards, the fuel level is increased to a value that exceeds that nominal value, and is kept constant until the end of the simulation.

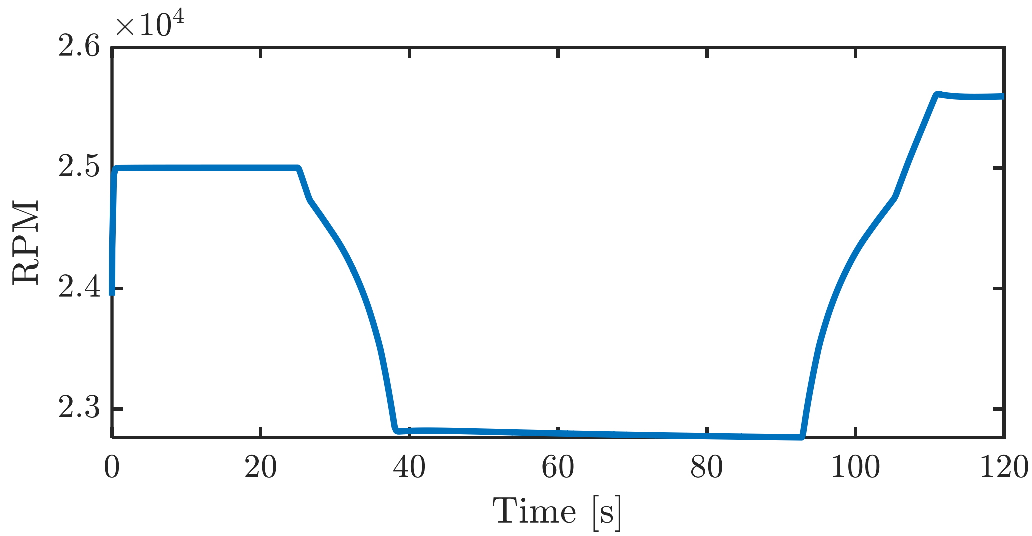

Figure 4.28: Shaft speed over time in a deceleration-reacceleration trajectory.

This type of trajectory causes the engine to explore a range of rotational speeds of approximately 10% of the design speed. The aim of this trajectory is to quantify the variations of tip clearance due to the different time scales between thermal and mechanical deformations and the effect on turbine performance. The performance module is linked to the engine model and three different geometries are used in the simulation, together with the correlation modeled by [67]. The trajectory is fully simulated with each of the geometry and performance and component deformations are extracted. Figure 4.29 shows the system response in terms of tip clearance.

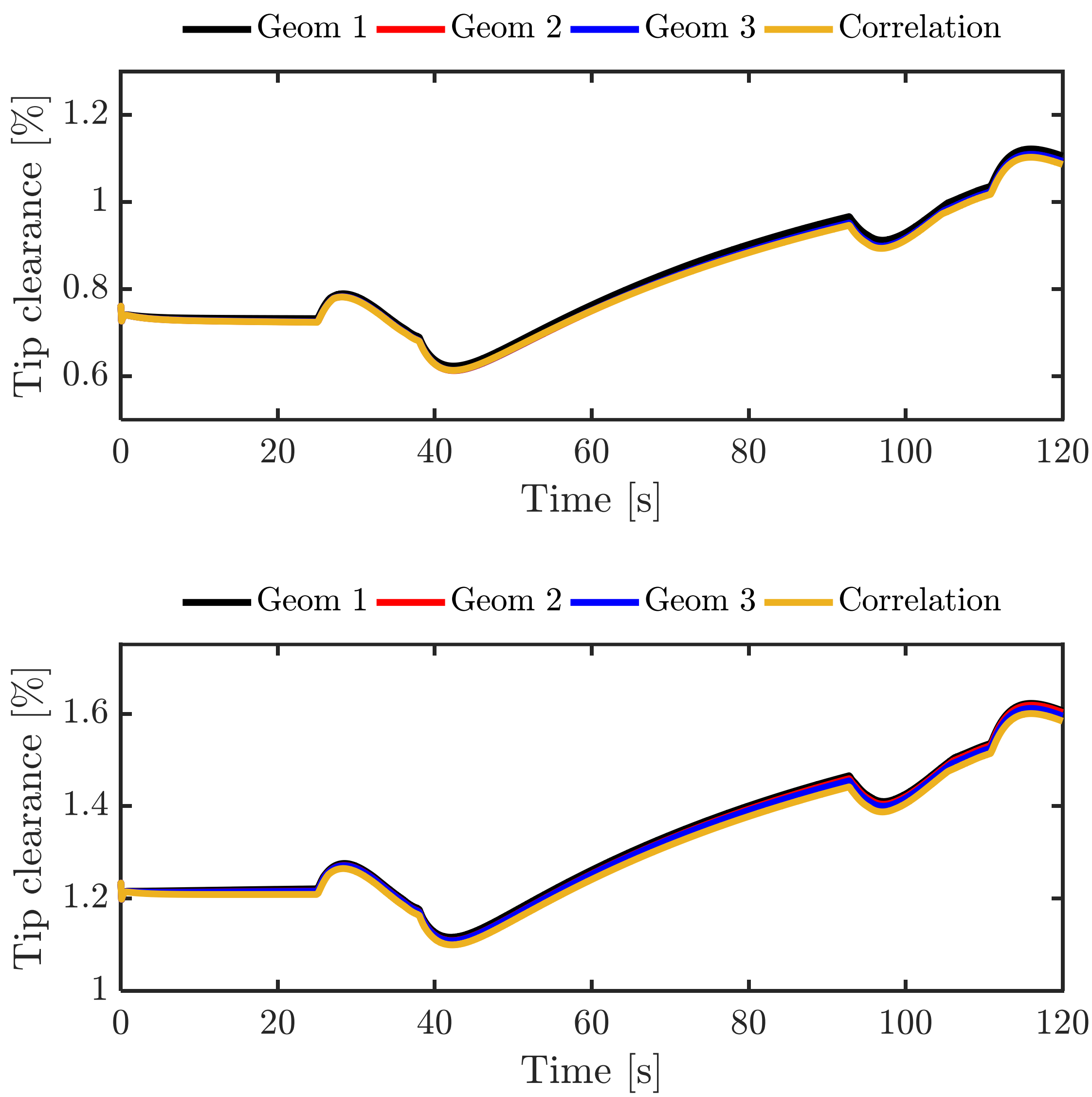

Figure 4.29: Tip clearance evolution over time. Top: trajectory with tight clearance. Bottom: trajectory with large clearance.

To extend the range of clearances investigated, two sets of simulations are performed; the difference between the two sets lies on the initial blade length. The case with a nominal clearance of 0.75% is shown on the top of Figure 4.29, while the bottom graph refers to the initial condition that provides a cruise running clearance of around 1.15%.

In the top, clearance covers a range between a minimum of 0.6% and a maximum of 1.1% during the transient. This is the range that in Chapter II was defined as tight or medium. On the bottom plot, the clearance ranges from 1% to 1.55%, covering the range that would be identified as medium or large.

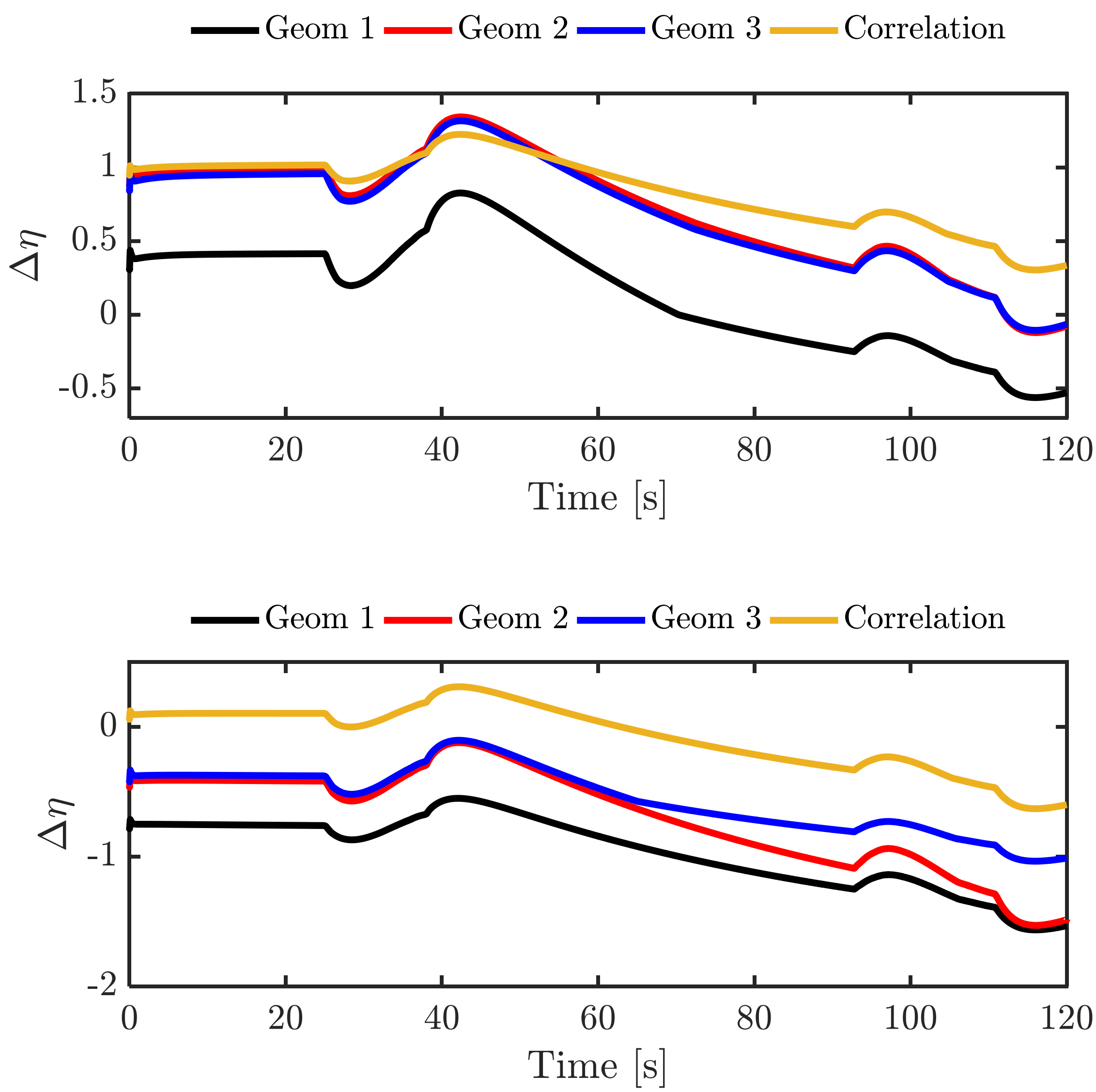

Figure 4.30: Turbine performance vs. time for tight clearance (top) and large clearance (bottom).

Figure 4.30 shows the turbine responses to the change of tip clearance. As in the previous figure, the graph on top represents a trajectory with tight clearance and the one on the bottom a large clearance range. The black geometry is the reference geometry, i.e. the simple squealer. The geometries 2 and 3 are the optimal geometries designed through a single-clearance and a multi-clearance optimization respectively.

The correlation, solid gold line, implements the model described by Baskharone [68]. Initially, in the top graph, the two optimized turbines and the correlation lie almost on top of each other, while the simple squealer has a negative offset of approximately 0.5%. This is consistent with the results from the optimizations. As the clearance starts to change during the transient, all the efficiencies drop for slightly less than 1%. It is worthy to notice that the drop calculated with the correlation is half of the values calculated with CFD. This means that the correlation systematically overestimates the efficiency in this case. The offset becomes even larger in the bottom graph, where the distance between the optimal geometries and the correlation is as large as the difference compared with the squealer. It is relevant that while the red and blue lines are overlapping in most of the range, the blue line, i.e. the optimal geometry at multiple clearances, will hold the performance at the end while the red line will decay to meet the black one.

4.4 Development of Experimental Procedures

This section will describe the development of an experiment that would provide a global validation of the described methodology. The validation will focus on:

- Validation of thermodynamic, mechanical and thermal components used in the engine model through the modeling of the wind tunnel
- Validation of turbine tip flow prediction with steady and unsteady pressure measurements
- Validation of the Green's Function approach through heat flux measurements

The validation experiment is designed for the annular wind tunnel, at the Purdue Experimental Aerothermal Lab. The laboratory contains two wind tunnels connected in parallel: a linear, and an annular test section. A high-pressure tank, with a total available volume of $51 m^3$ stores air at 150 bar. The system is coupled with an air heater that can increase the flow temperature up to 1100 K. The air can be discharged to a vacuum tank of $253\ m^3$ or directly to the atmosphere. The large capabilities of the Zucrow facility, allow to have a unique range of Mach and Reynolds number in the wind tunnels, and to produce both subsonic and supersonic flow. The annular test section has two separate disks for vane and rotor, in order to allow for movement with slow rotational speed if a preswirler is needed.

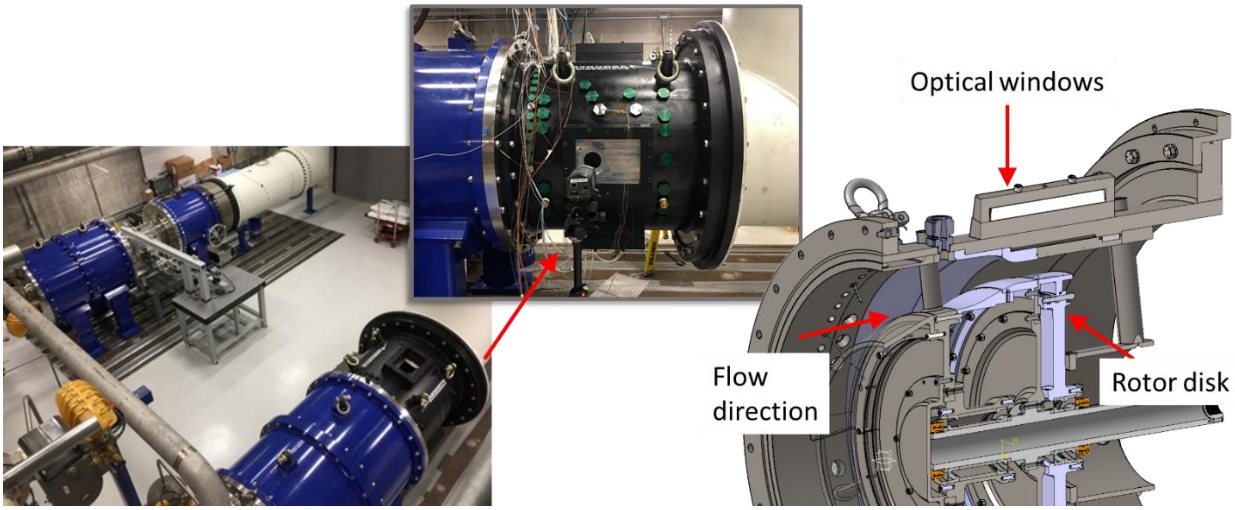

Figure 4.31: View of annular test section, and detail of the 3D model.

The test section is designed with large windows for optical access and multiple slots for overtip instrumentation. Three large slots, that cover a sector of more than 100 degrees, provide access to traverse in the angular and radial direction, both upstream and downstream of the rotor row.

4.4.1 Numerical Model of the Wind Tunnel

The wind tunnel model is built using Numerical Propulsion System Simulation (NPSS), initially developed by NASA Glenn Research Center to model engines at steady-state and transient operation. The models are based on the same thermodynamic equations implemented in T-MATS [82], so the models used for the wind tunnel and for dynamic engine analysis are comparable. The simulation software is built using an object-oriented approach, based on the programming language C++. In general, physical components can be included in the model as “elements” or “subelements”. Figure 4.32 represents a schematic of an engine model. The different mechanical components like compressor, turbine… are indicated as elements. These components are linked together through the use of ports, which are programmed within the element. According to the function of each element, a variable amount of ports can be included in the definition. The main flow path would be computed at each fluid port, but also secondary flow ports, shaft ports are available to build the respective connections. Additionally, sockets may be included in the component. These are channels were calculations that support the element can be plugged in. One example is the calculation of the turbine map, or the loss coefficient in a pipe.

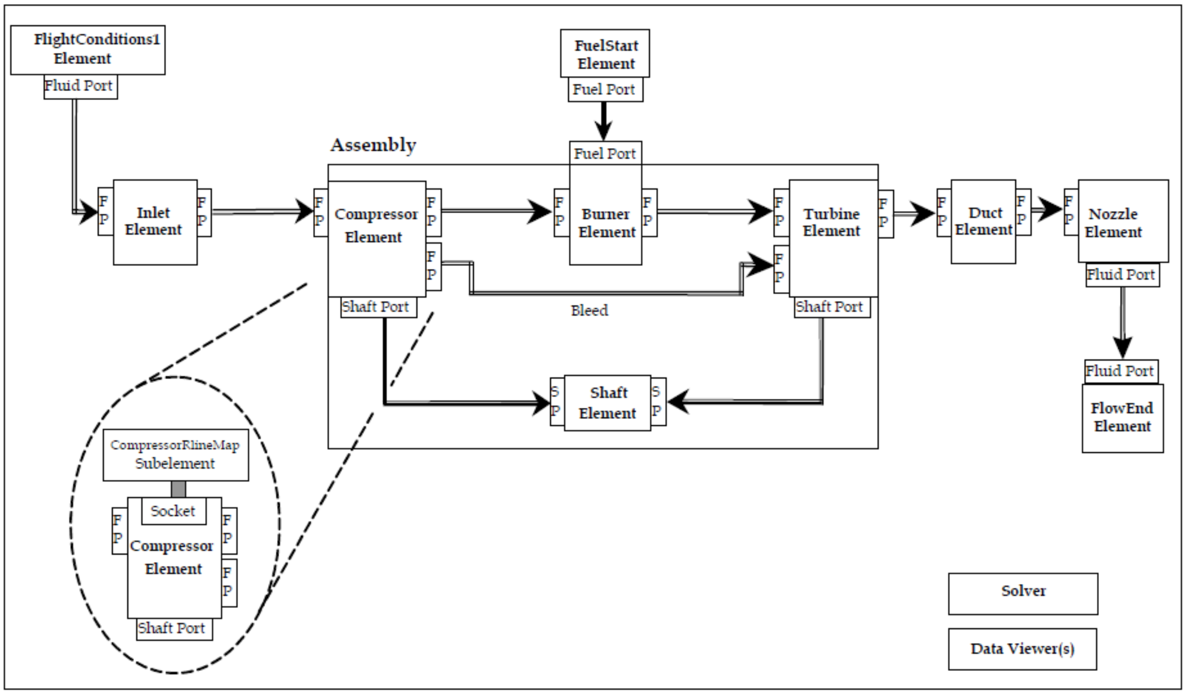

Figure 4.32: Schematic of an engine model from [83].

The solver in NPSS can handle both steady-state and transient operation, at design and off-design conditions. All the system variables are divided into independent and dependent variables; the correct identification of this attribute is fundamental for the convergence and reliability of the simulation. At each solver iteration, the independent variables are varied until the condition on the dependent ones is met. Transient simulations are computed as a series of steady-state solutions at discrete time steps. The time step can be selected to be constant, or to become smaller in case of fast transients. The transient can be solved with different integration methods, implicit or explicit.

4.4.1.1 Component Validation

In order to understand the behavior of the components, the system is broke down into smaller subsystems easier to analyze and troubleshoot. In particular we are interested in identifying a component able to reproduce the phenomena of mass and energy accumulation, and orifice components able to include the choked flow limitation.

Comparison between Valve, Pipe and Duct

The first test case is to verify that the orifice can reproduce the constraint on the mass flow due to choking. A simple way to test this capability is to build a simple model composed by an inlet infinite reservoir (“Flow start”), an outlet infinite reservoir (“Flow end”) and a duct, pipe or valve in between. The back pressure of the outlet is initially constant, as can be seen in Figure 4.33 on the left. The value is low enough to obtain a pressure ratio above the critical value. After several seconds of steady operation, we start decreasing the back pressure, till half of the initial value. Since the component between the two reservoirs was already choked, a further decrease in back pressure should not increase the mass flow. As shown in on the right, this happens only when the component is a pipe. In the case of valves and ducts, the mass flow shows a small increase, meaning that the choking limitation is not included in the component.

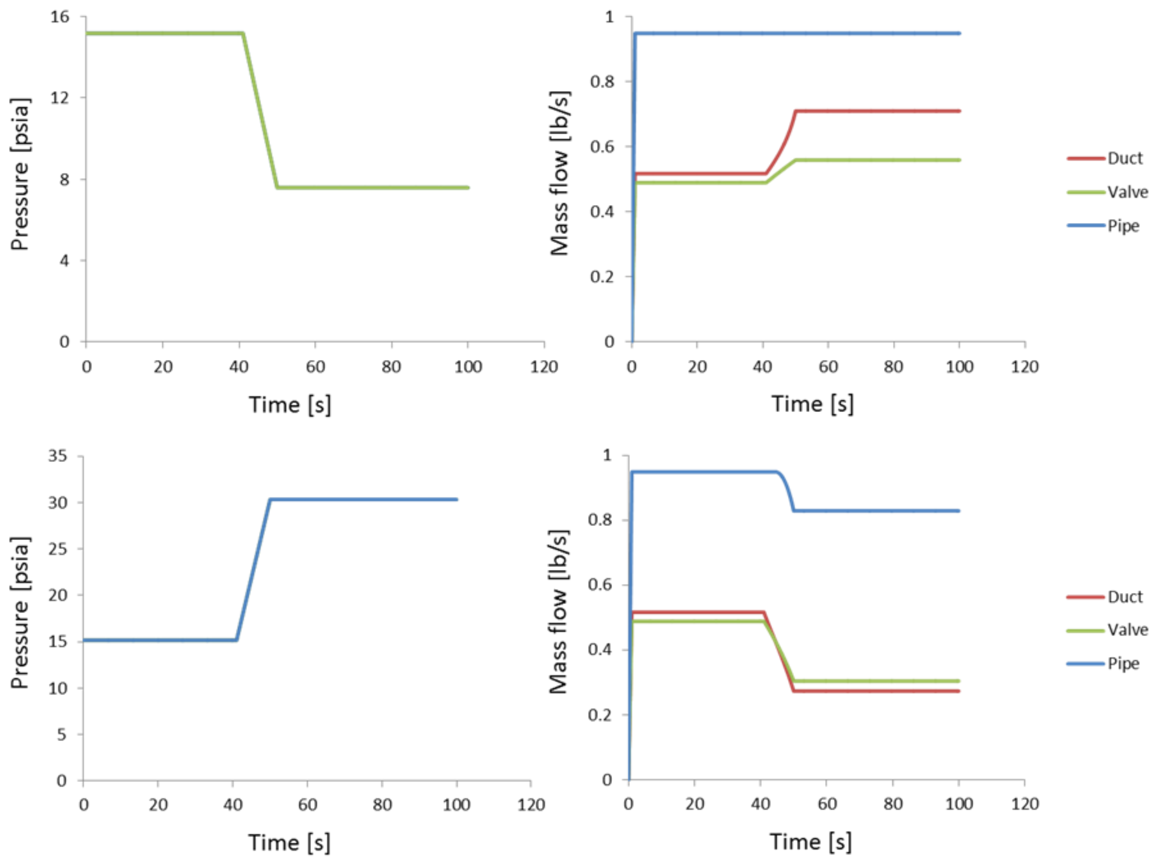

Figure 4.33: Response of pipes, valves and ducts to a decreasing and increasing pressure transient.

Analogously we want to test the mechanism of unchoking of the pipes. In Figure 4.33 we show a second test case, but this time the pressure increases in time. On the right, we can see how the mass flow changes as we increase the back pressure for the three components. However, for the pipe element, the mass flow starts adapting only after the pressure ratio is above a certain value. This means that the pipe has first to unchoke. After that point, the mass flow starts depending on the outlet pressure as well as on the inlet one.

Volumes in transient operation

The next step is to test the behavior of volumes under transient conditions. In particular we are interested in the capability of replicating mass and energy accumulation. This is critical to reproduce the trends of pressure and temperature in the wind tunnel. We have observed in previous work that some features observed in experiments, like temperature overshoots and pressure transients, are correctly modelled only if the volumes of the components are considered.

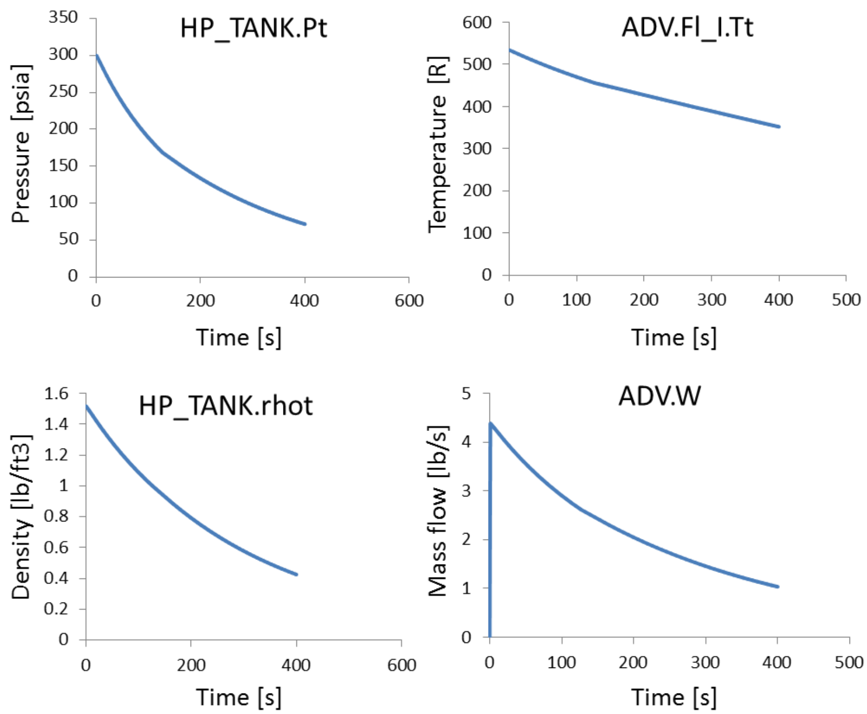

Figure 4.34: Transient simulation of a high pressure reservoir.

In Figure 4.34 we show the results of a simple model composed by a high-pressure reservoir, a pipe and a discharge to atmosphere. What we can see is that as the small reservoir depletes, the pressure, temperature and density decrease. Consequently, the mass flow will decrease as well, due to a lower inlet total pressure in the valve. These simulations show how the volume elements can reproduce the changes in gas properties due to an unbalance of mass flow and energy entering and leaving the control volume. The following test case was reproduced at higher and lower pressure levels, to make sure that the behavior is consistent in all the ranges covered by the gas properties database. One thing that has been observed to be critical for the reproduction of the transient is the selection of time-step and tolerances. This means that when volumes are included in the model, we must perform sensitivity studies on these parameters.

Wind tunnel model

An initial model of the wind tunnel is built using an alternation of volumes and pipes. A schematic of the wind tunnel is summarized in Figure 4.35. The tank and all the pipes, settling chamber and test section are modeled using Volume elements in NPSS; the valves and orifices are modeled using Pipe elements in NPSS. These decisions are based on the results of the single component validations. The model can be simulated based on different strategies, analogous to the control strategy of the wind tunnel. The simplest approach is to set a fixed value for the area of the admission valve. This means that the mass flow will decrease as the reservoir depletes. This is the modeled used for the results in Figure 4.35.

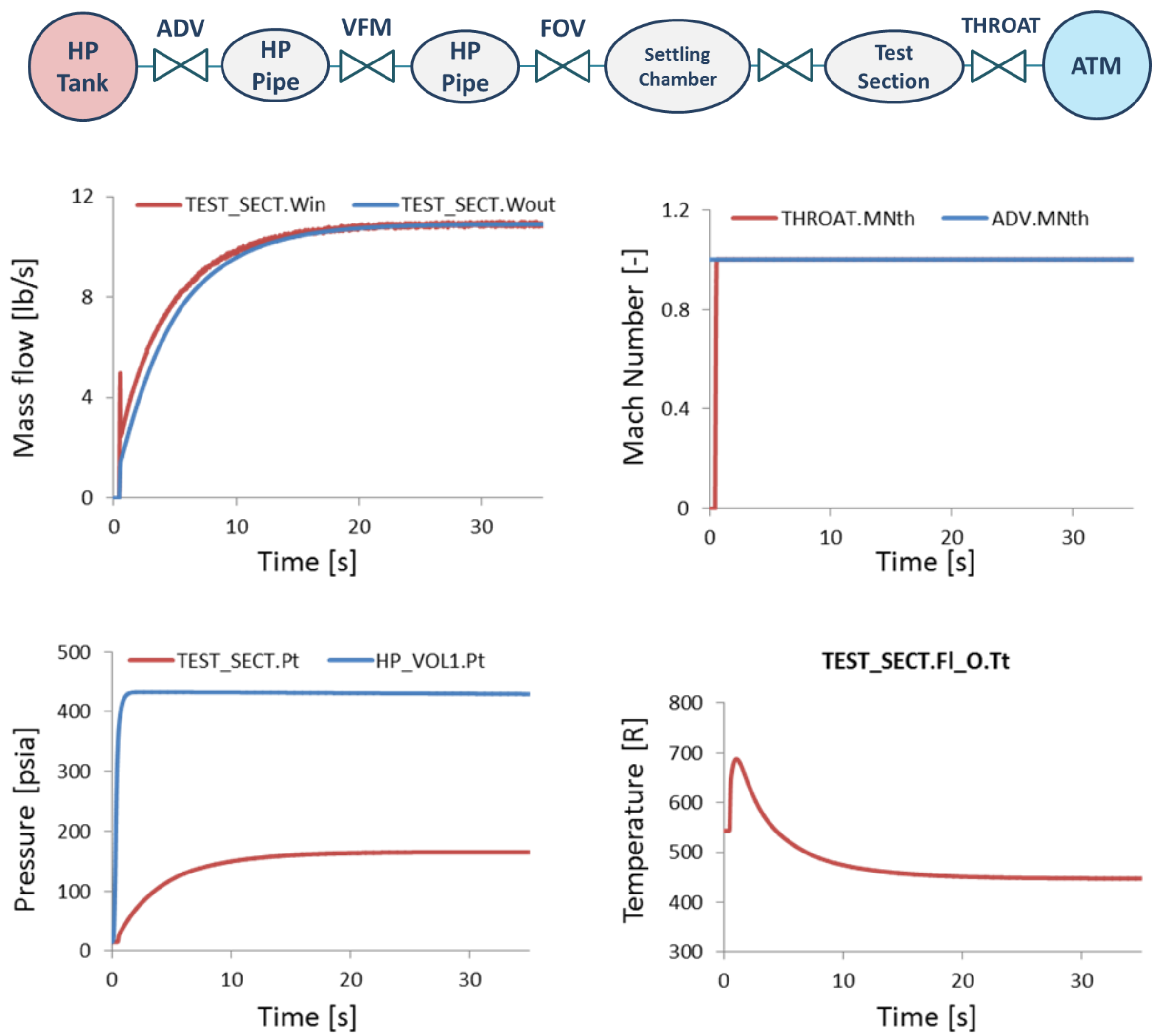

Figure 4.35: NPSS transient simulation of the wind tunnel model.

On the top left we can see how the air starts flowing in the test section only after the fast opening valve located right upstream of the settling chamber opens. The difference between the incoming and ejected mass flows in the test section produces mass and energy accumulation; this causes compression in the test section till a steady state value (in the figure at the bottom left) and an initial temperature overshoot (in the figure at the bottom right). We can see on the top right how the admission valve and the sonic throat operate at critical conditions during the entire duration of the experiment.

4.4.1.2 Annular Wind Tunnel Model Calibration

The model of the wind tunnel is initially calibrated based on steady state value. This is used as first approach because steady numerical models are faster to run. For this reason a set of more than 20 experiments are analyzed and the flow quantities at steady conditions are extracted. The values are used to calibrate pressure losses in valves and pipes. As an example, Figure 4.36 shows the calculated discharge coefficient in function of a nondimensional number that characterizes the valve Reynolds number. The discharge coefficient is computed as the ratio between the effective are (that depends on the flow conditions) and the geometrical area.

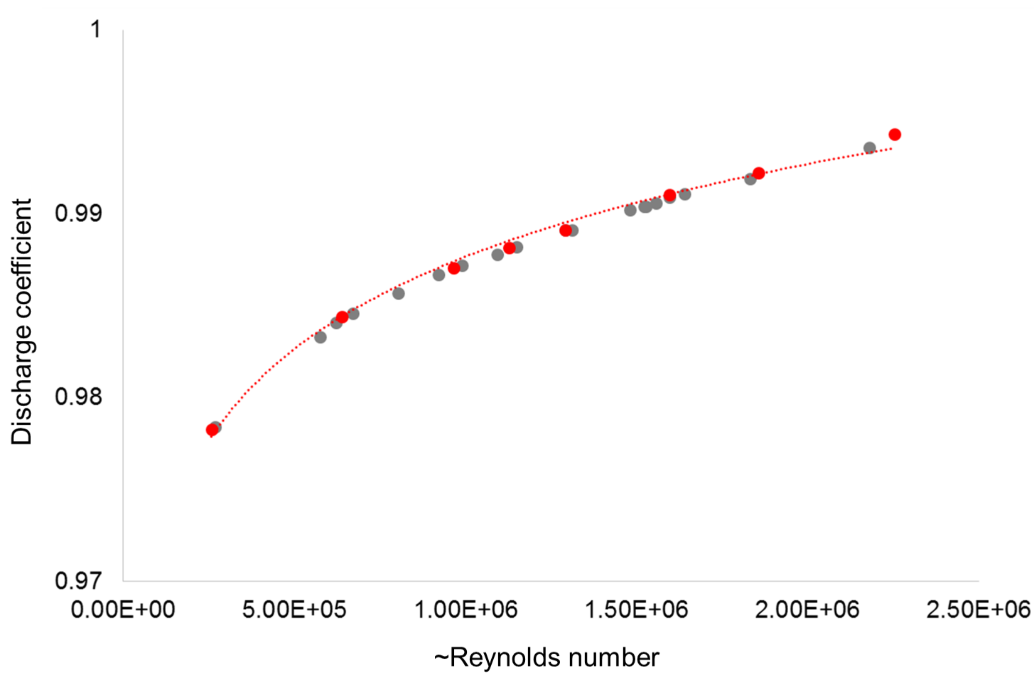

Figure 4.36: Model steady calibration. Discharge coefficient of the Venturi flow meter.

Some of the experiments, marked with red dots, are used as training dataset to develop the model. The trend of discharge coefficient in function of Reynolds number is built by polynomial fitting, indicated with red dotted line, and fed back into the NPSS model of the wind tunnel. The remaining data, indicated with grey dots, is then used as a validation dataset. The fitting, even though based on a few experiments, shows a satisfactory matching. The same operation is repeated for the other valves and orifices present in the system.

Once the system losses are calibrated with a steady approach, we need to perform an unsteady calibration to characterize transient phenomena like mass accumulation and heat transfer.

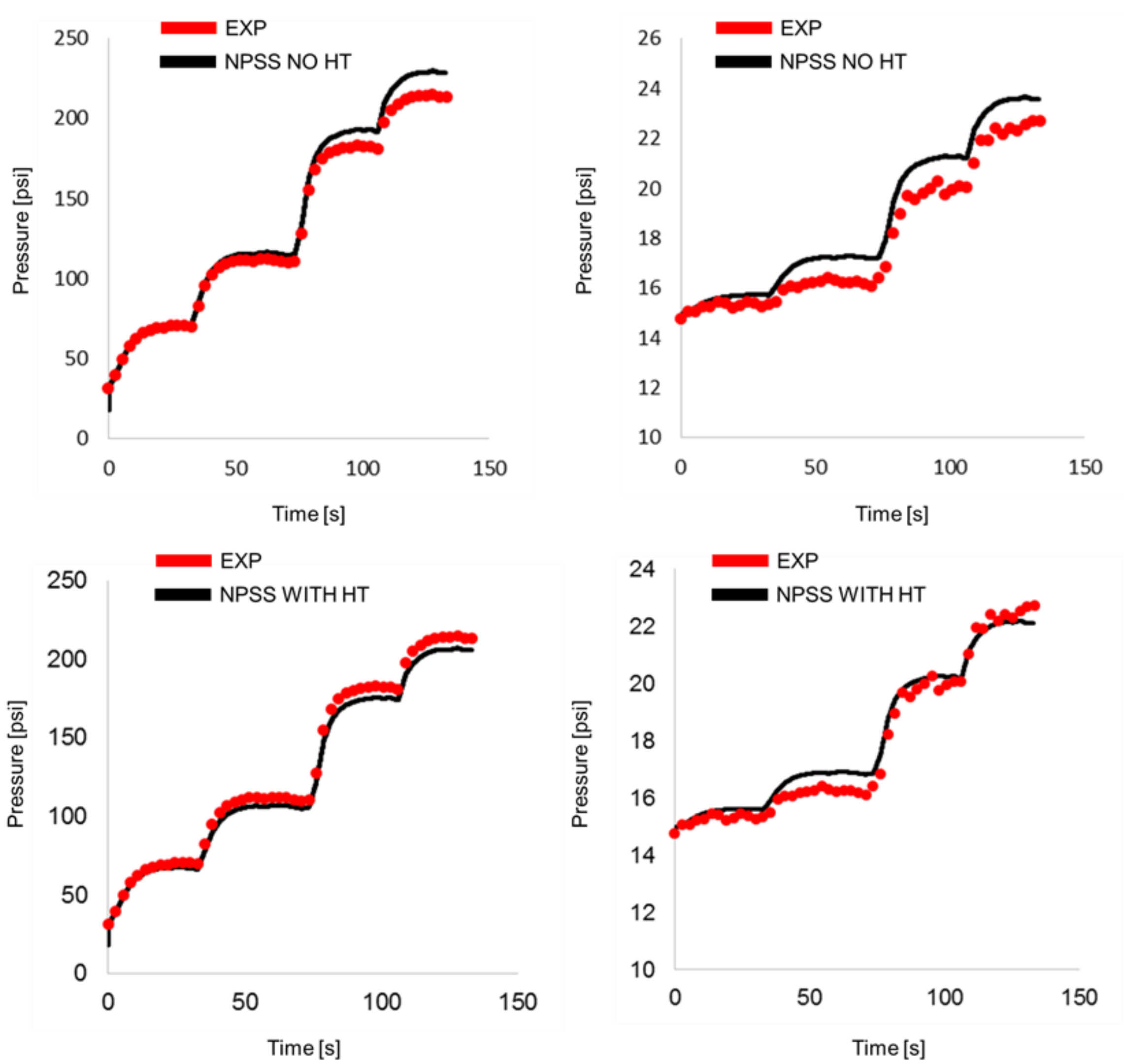

Figure 4.37: Model transient calibration without and with heat transfer through the components.

Figure 4.37 shows the experimental results and the model predictions with and without heat transfer effects. A transient experiment is replicated, where over approximately 120 seconds the mass flow is progressively ramped up in steps from a value of 1.5 kg/s to a final value of 12 kg/s. On the top row we can see the comparison between the experiments (marked in red) and the facility model where component heat transfer is neglected (marked in black). On the left the graph shows the pressure upstream of the Venturi flow meter in function of time, while on the right we can find the total pressure upstream of the test section. The same comparison is then proposed in the bottom row, where this time the model includes heat transfer effects in pipes and volumes. In the top plots there is a difference between the black line and the red dots, which grows larger as time and mass flow increase. Since the operation of the wind tunnel is mainly driven by valve and orifice choking, and remembering the formula for choked mass flows, it is logical that if temperature drops over time the pressure will be affected. In particular, if the flow temperature drops because of heat transfer through the wall, the flow pressure will have to drop as well to maintain a given (imposed) mass flow.

For this principle, when we introduce heat flux and replicate in the model the actual temperature decay that we observe in the experiment, the difference between pressure in experiments and simulations is reduced.

This can be observed in the two bottom graphs in Figure 4.37, where the red dots (coming from experimental measurements) lie almost on top of the numerical predictions (black lines).Figure 4.38 shows the temperature transient measured in the pipe downstream of the Venturi flow meter. In a first NPSS model, where the heat flux through the pipes was neglected, the temperature is calculated to be rather constant over time. This, as previously observed, induces a miscalculation of the pressure in the wind tunnel. However, once the calculations in the model include the hat flux in the wind tunnel components, the model is able to replicate the decay if flow temperature measured in the experiments. This trend is indicated with the black line, while the experimental temperature is marked with red dots.

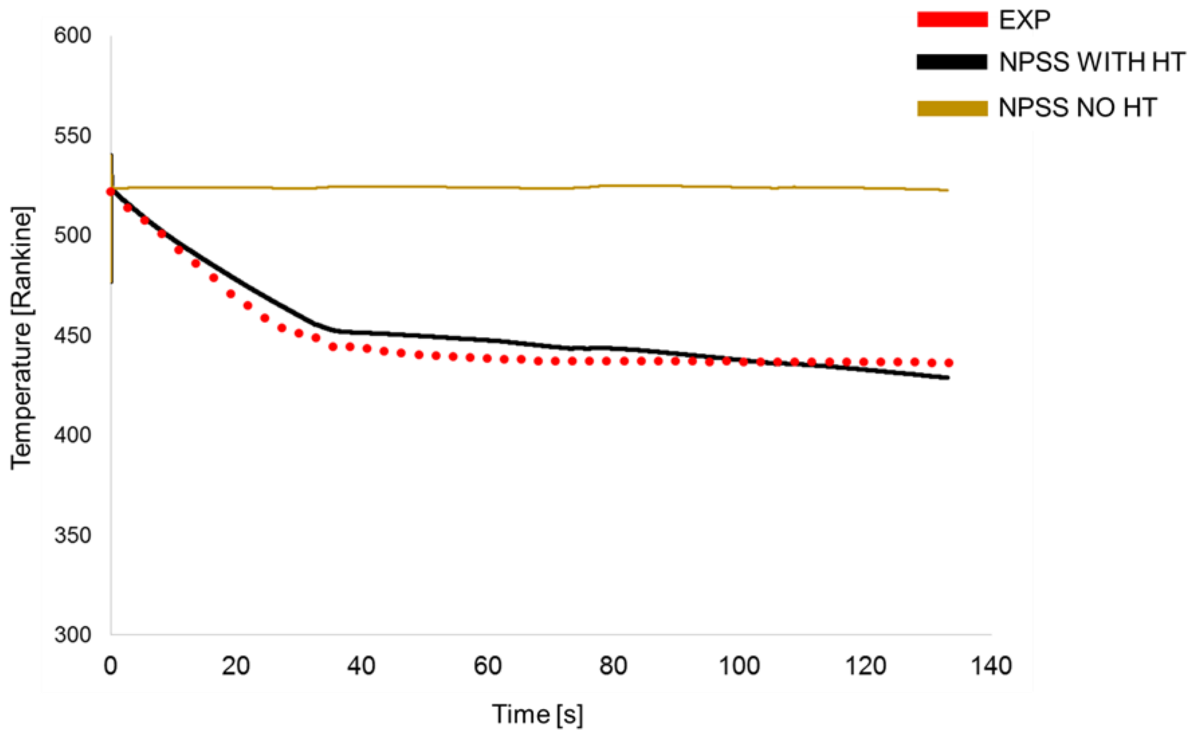

Figure 4.38: Temperature transient in pipes.

4.4.1.3 Rotating Wind Tunnel Model

Once the numerical model of the wind tunnel has been validated against experiments in the existing wind tunnel, we can plug the model of the turbine and simulate the future operation of the rotating rig. There are several options to operate a rotating wind tunnel; one mode is to leave the turbine free to spin and generate the transient using a blowdown facility. In this operation mode, as modeled in [84], the turbine is initially accelerated to an initial shaft speed lower than the design value. Afterward, a valve is suddenly opened and the turbine is hit by a sudden discharge of mass flow which causes a turbine acceleration. This acceleration is used to produce a transient in RPM and get to the final design speed desired for the experiment. Alternatively, the turbine can be connected to an electric motor that can generate or absorb the power in different phases of the test. In this operating mode, the shaft speed can be controlled to achieve a constant value over time, or an imposed trend of transient speed over time. In both cases, the model of the wind tunnel needs an accurate simulation of the turbine performance. The method used to include the turbine performance in the NPSS model is similar to the approach used to represent turbomachinery into the T-MATS engine model. Figure 4.39 shows the numerical prediction of the turbine performance in the two described operating modes.

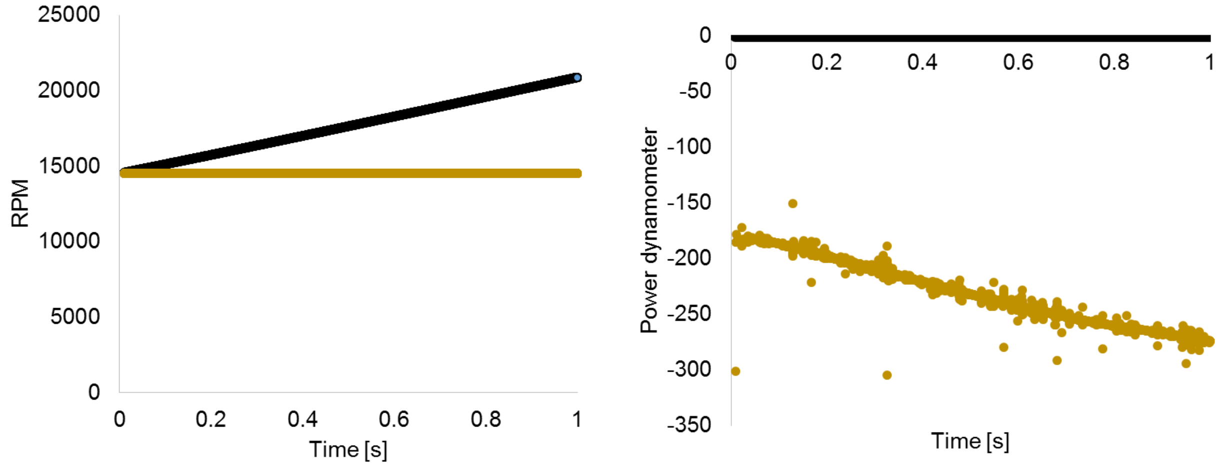

Figure 4.39: Numerical simulations of the operation of the rotating wind tunnel. Left: shaft speed over time. Right power generated or absorbed by the dynamometer.

In these simulations, a ramp of mass flow is imposed on the admission valve, and the area of the inlet valve is adjusted to match the desired values. Once this mass flow reaches the turbine, the different operating conditions of the turbine in terms of shaft speed and upstream flow quantities continuously change over the transient. Hence the mass flow through the turbine will keep changing to operate at a given corrected flow value. The difference between inlet and outlet mass flow will be stored in the upstream components and induce pressure and temperature change due to mass accumulation.

Figure 4.40 shows the evolution of mass flow over time in the wind tunnel. In red, the mass flow through the admission valve is represented. This flow is imposed to the system, and the black and gold line shows the turbine response in the case without and with dynamometer respectively.

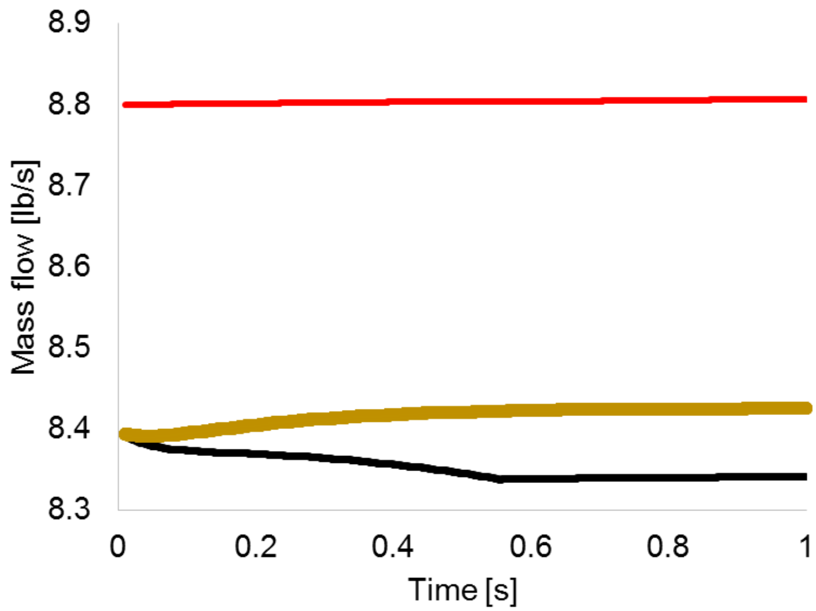

Figure 4.40: Mass flow in the admission valve (red) and in the turbine (black without dynamometer and gold with dynamometer).

4.4.2 Development of Experimental Procedure to Identify Tip Loss Mechanism

In this section, we want to outline an experimental procedure to identify the dominant physical mechanism in tip flows based on the insights given by the numerical analysis. The purpose is to develop a testing strategy for future experiments focused on tip flows in a stationary and rotating rig.

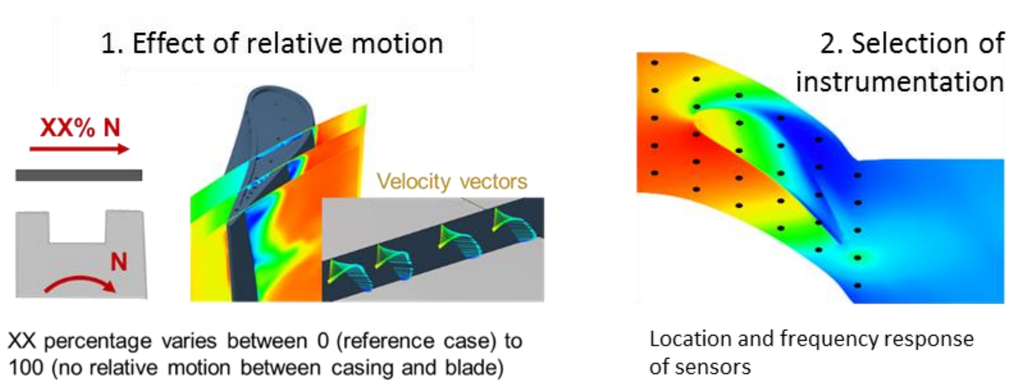

Figure 4.41: Methodology to design tip flow experiments in stationary and rotating environment.

For this purpose, we will first investigate the effect of testing turbine tips in a non-rotating environment, and consequently propose a strategy to optimally select the instrumentation.

4.4.2.1 Tip Flows in an Annular Cascade

To design an experiment in an annular cascade, the first factor to understand is the importance of the relative motion between the blade and the casing. Being the gap so small, and being the flow dominated by viscous effects, the characteristics of the leakage flow will be affected by the shear between the stationary and rotating surfaces.

First, the baseline and optimal geometries will be first simulated in rotation at design condition. Then, the casing will be rotated in the same direction of the blade, in order to eliminate the relative motion.

Figure 4.42 shows the trends of turbine efficiency for different casing rotational speed. On the abscissa, the shaft speed is reported in percentage of the blade rotational speed, while on the ordinate the plot shows the variation of efficiency with respect to the reference case (simple squealer at design conditions). The red lines indicate the optimal geometry while the black line is the simple squealer.

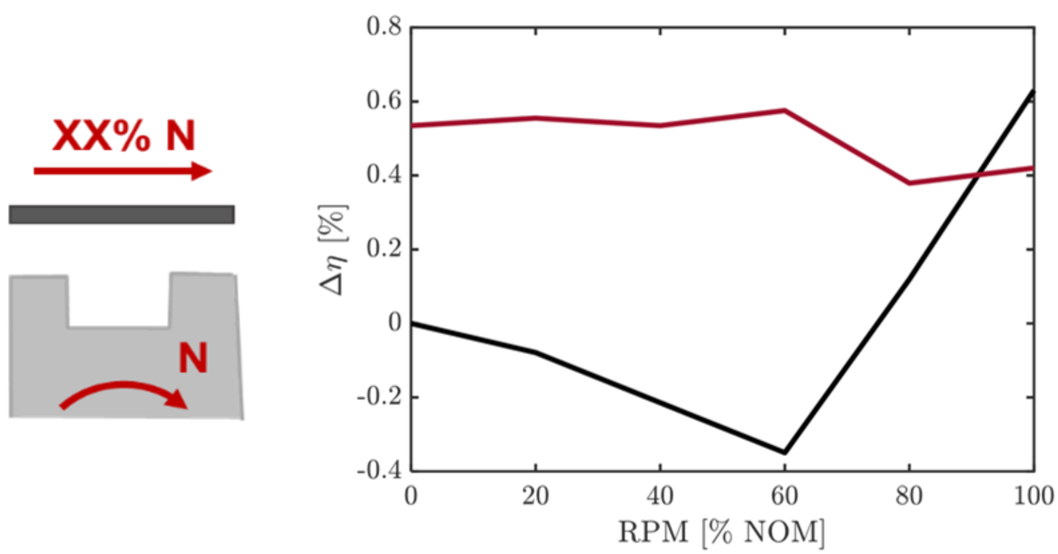

Figure 4.42: Effect of relative motion between blade and casing.

The difference between the two lines at zero RPM is the efficiency improvement that was obtained with the single-clearance optimization. The red line, initially at 0.5%, maintains a constant value till shaft speed of 80% and 100% where the value drops to 0.4%. The black lines on the other hand, i.e. the simple squealer, decreases monotonically in the range 0% to 60% shaft speed. In this region, the efficiency variation drops from 0 to -0.4%. For shaft speeds higher than the 60%, the difference of efficiency starts increasing till the squealer outperforms the optimized blade of a 0.2% for shaft speed equal to design speed. This indicates that the squealer performance is heavily penalized by the flow structure induced by the relative casing motion. This penalty is maximized for a casing RPM of 60%.

To gather a better understanding of the cause of these results, we analyze the overtip flow topology analogously with the method applied in Chapter 2. The overtip surface is discretized in small portions and the mass flow and mass flow-averaged quantities are extracted in each element. Initially we look at the trends of leakage flow on the suction side, represented in Figure 4.43. On the left, the leakage flow in the baseline geometry is represented, while on the right, the optimized tip is analyzed. In each figure, the line colors range from dark to light, as the shroud RPM increases from o to 100%. Hence for example on the left graph the black line will be the baseline case with rotating blade and stationary casing, while the light grey line represents the opposite extreme case, where the casing rotates together with the blades at the same shaft speed. This implies that the difference between the two curves is entirely due to the relative motion between the casing and blade.

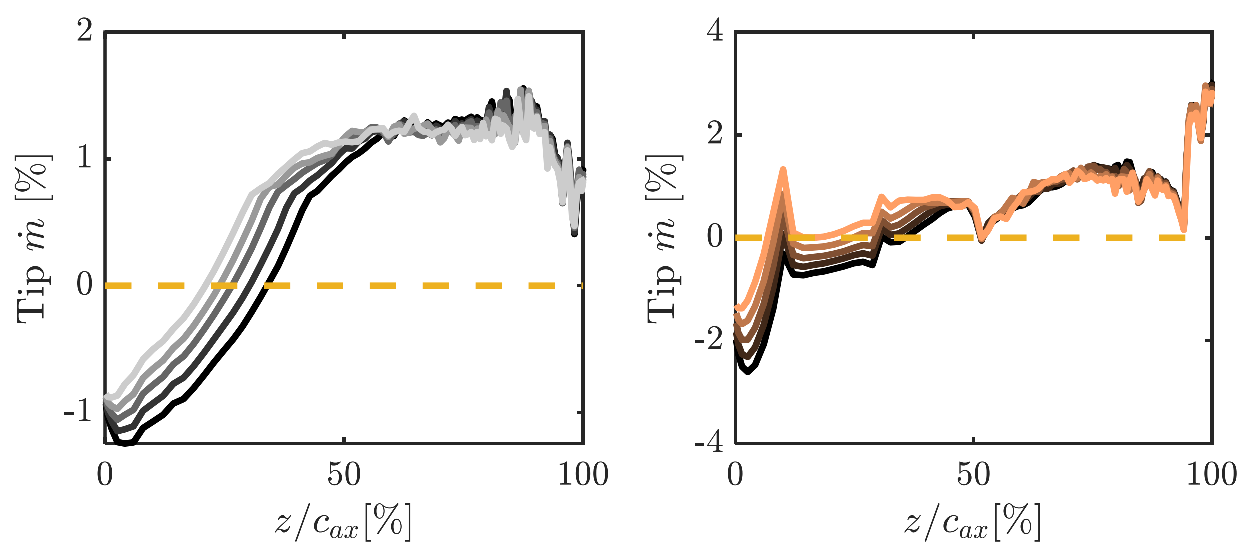

Figure 4.43: Axial distribution of leakage mass flow for different casing RPM (baseline on the left, optimized on the right).

The first feature that can be observed on the left graph is the axial location at which the lines cross the zero leakage flow. This point represents the location where the suction side switches from being an inlet to being an outlet. From this point downstream, the leakage flow is ejected on the suction side and mixes with the main flow, generating mixing losses. In the baseline case this point is located at around the 40% of the axial chord, meaning that only the 60% rear portion of the blade is effectively acting as a leakage region. As the casing starts to move in the same direction of the blade, the blockage due to friction is reduced. For this reason, the point where the leakage switches from negative (inward) to positive (outward) moves upstream. In the limit case where the casing moves with the blades, the suction side behaves as an inlet only in the front 20%, leaving the remaining 80% of the axial chord acting as leakage outlet section. If we consider the front portion of the blade, it can be noticed that for stationary casing the leakage flow entering the overtip region is higher compared to the rotating shroud case. This means that the viscous forces, which push the flow from suction to pressure side, are larger than the pressure gradient effect. This confirms that the large region at the front of the blade that acts as an inlet is mainly driven by the relative motion between blade and casing. It is interesting to notice that the leakage flow in the rear half of the blade appears not to be affected by the casing rotation. Analogous considerations may be made for the optimal geometry, whose leakage flow is depicted on the right. The front section that acts as an inlet is heavily reduced as the shroud starts to move with the blade. The definition of a unique point where the leakage flow becomes positive is not possible in optimized blade tips. The leakage flow changes sign in multiple locations, due to the presence of multiple rims and open sections. However we can observe that the inlet section is larger in the case of the stationary casing, reducing the length of the outlet section.

Figure 4.44 shows the distribution of Mach number along the tip border, going from leading to trailing edge on the suction side. For the baseline geometry, depicted on the left graph, most of the effects are seen on the rear 80% of the blade. This result is opposite to what concluded for the leakage mass flow; it means that even though the leakage flow is not affected by the rotation in the rear side of the blade, the Mach number is. Hence, the change in flow angle must play a role as well.

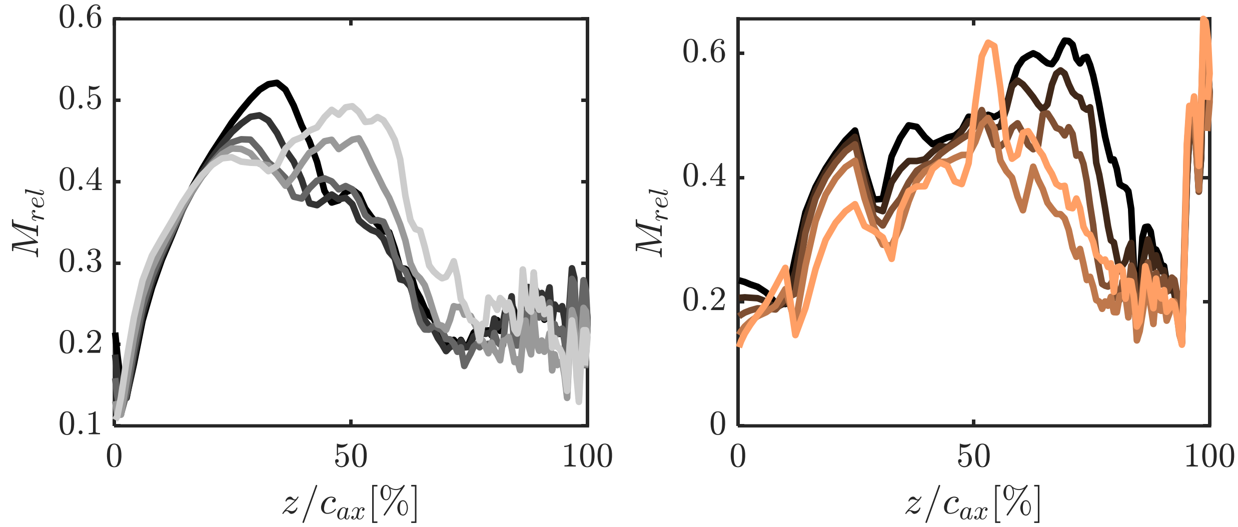

Figure 4.44: Axial distribution of relative Mach number for different casing RPM (baseline on the left, optimized on the right).

The flow topology in the optimized tip is more complex, but it can be observed that moving the case in the same direction of the blade reduces the Mach number in both inlet and outlet portion of the suction side. This trend is opposite to the behavior of the simple squealer on the second blade half (light grey line on the left plot).

Finally, Figure 4.45 shows the distribution of flow relative angle with respect to the axial direction. On the left we report the distribution for the simple squealer while on the right the results for the optimized tip. For the baseline geometry the impact of the case rotation on the flow angle is minimal on the front part. It can be noted that in the front 50% of the suction side the flow exits, or enter the gap, with a flow angle that is close to zero. In this region, the variation between lines at different casing rotational speeds is maximum 10 degrees. In the rear part of the suction side, the effect of the change in shroud speed has a large impact on the flow angle. For the nominal condition the flow angle is negative and is around -50 degrees in the last 30% of the blade. However, when the shroud starts to move the flow angle changes sign and has an average value of 40 degrees. It must be noted that the mass flow-averaged relative angle of the main passage flow in that region was discussed in Section 2.3.4. Hence, the absence of viscous effects makes the leakage flow more aligned to the main flow and the turbine stage more efficient.

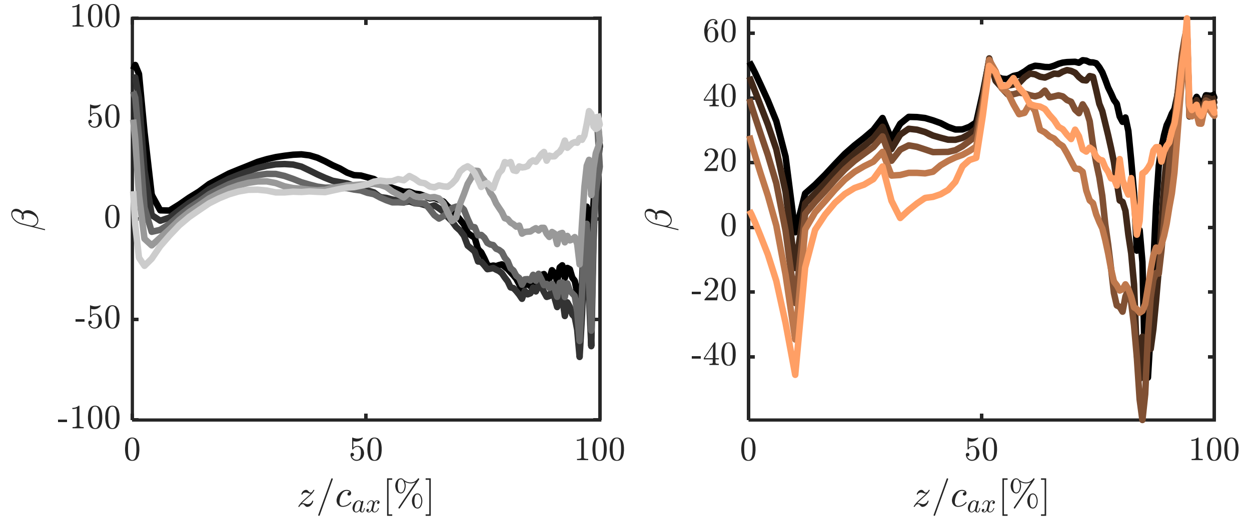

Figure 4.45: Axial distribution of relative flow angle for different casing RPM (baseline on the left, optimized on the right).

On the right graph, large differences can be identified both on the front and on the rear section of the airfoil. The value of β decreases in all the front 50% of the airfoil with the increase of casing rotational speed. The optimized blade in nominal condition has a flow angle of around 40% between 50% and 80% of the axial chord. This value, as seen in Chapter 2, is close to the flow angle in the main passage. However, when the shroud rotational speed increases this value starts dropping to achieve values similar to the ones in the baseline geometry. These considerations, and the effect on the mixing losses as calculated in Chapter 2, may explain why the simple squealer outperforms the optimized blade in the absence of relative motion between casing and blade.

These results suggest that in order to replicate the flow features that make the optimal tip more efficient than a squealer, we need do either rotate the blade or the casing. However, as seen in Figure 4.42, this velocity can be as little as the 20% of the shaft design speed.

4.4.2.2 Experimental Setup for Tip Flow Testing

Given the location and type of access in the wind tunnel, it is possible to optimally select the location of the instrumentation.

The purpose of this section is to propose an experiment that would allow to:

- Characterize the flow features in the tip gap
- Capture the differences due to the different tip geometries

Spatial characterization in a stationary wind tunnel

In order to fulfill the first requirement, a first step is to extract the static pressure at the casing and select an optimal combination of number and location of static pressure taps to characterize it.

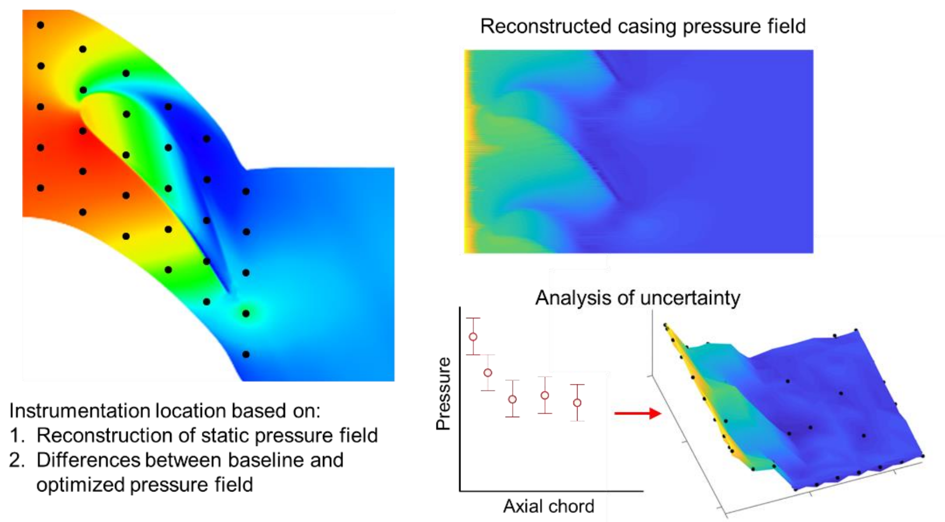

Figure 4.46: Methodology to choose the experimental setup and quantify uncertainty propagation.

The method used to perform this section, based on the analysis reported in [85], is based on the analysis of CFD results:

- The wall pressure in the casing and the tip is extracted and considered the "real" pressure
- Limitations due to measurement techniques are considered
- The location of the measurement points is selected

The wall pressure on the stationary casing is analyzed for both baseline and optimized tip geometry to identify the flow features and the difference between the two cases. Figure 4.47 shows the contour of static pressure fields with the same range. The distribution of pressure upstream of the leading edge is similar in both contours: a region of acceleration, with lower pressure can be identified towards the suction side, where on the contrary the pressure starts rising close to the pressure side due to flow deceleration. However, since the optimized geometry has an open rim on the front part of the pressure side, a major difference can be noticed in this region. On the left, the flow accelerates due to area reduction induced by the presence of the rim, while on the right the high-pressure flow proceeds almost uniformly towards the center of the blade without major velocity changes.

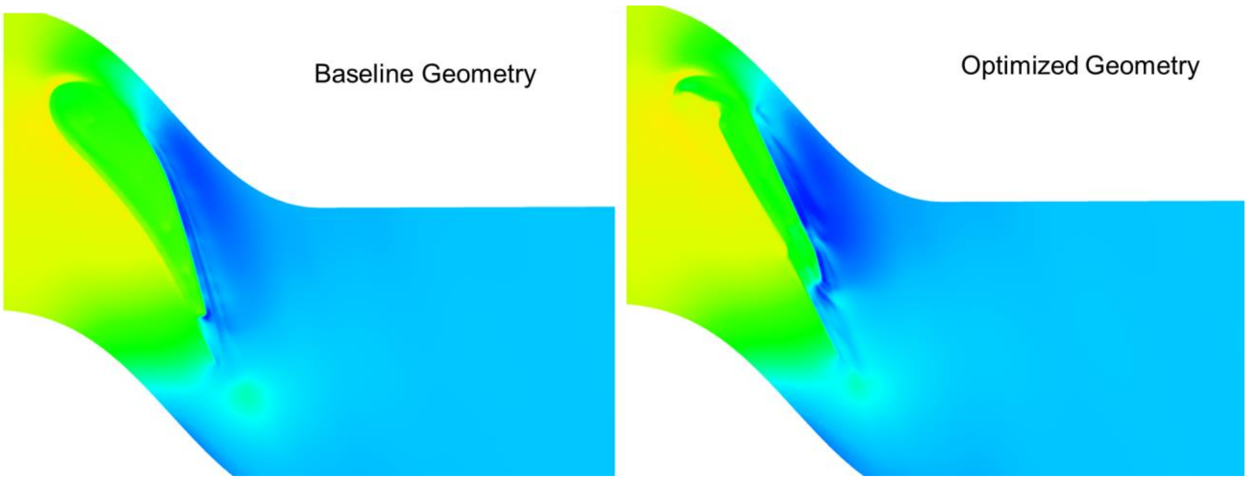

Figure 4.47: Contours of static pressure on the rotor casing for baseline geometry (left) and optimal tip geometry (right).

An analogous consideration can be made for the suction side region. The optimized tip has a pocket that allows the flow to have a first expansion on the cavity floor before mixing with the passage flow. This behavior can be identified by a sudden drop of wall static pressure on the casing on the SS of the right contour. Finally, the two geometries show different trends on the trailing edge where the optimized blade has no rim, which allow for a direct injection of coolant into the main flow.

Using the data represented in Figure 4.47 as an input, a code is developed to fit the pressure fields based on only a few measurement points. The reasoning behind this is that few optical techniques can provide a fully spatially characterized pressure field (for example pressure-sensitive paint). In alternative, we need to rely on traditional pressure measurements in a few discrete locations. The measurement location is bounded to be right upstream of the leading edge, and downstream of the trailing edge. We fix the number of axial locations of the measurements to 5 and we proceed to vary the number of tangential locations in multiples of 5 and assess how the total number of points affect the fitting. The surface interpolation is based on a scattered interpolant using a natural algorithm.

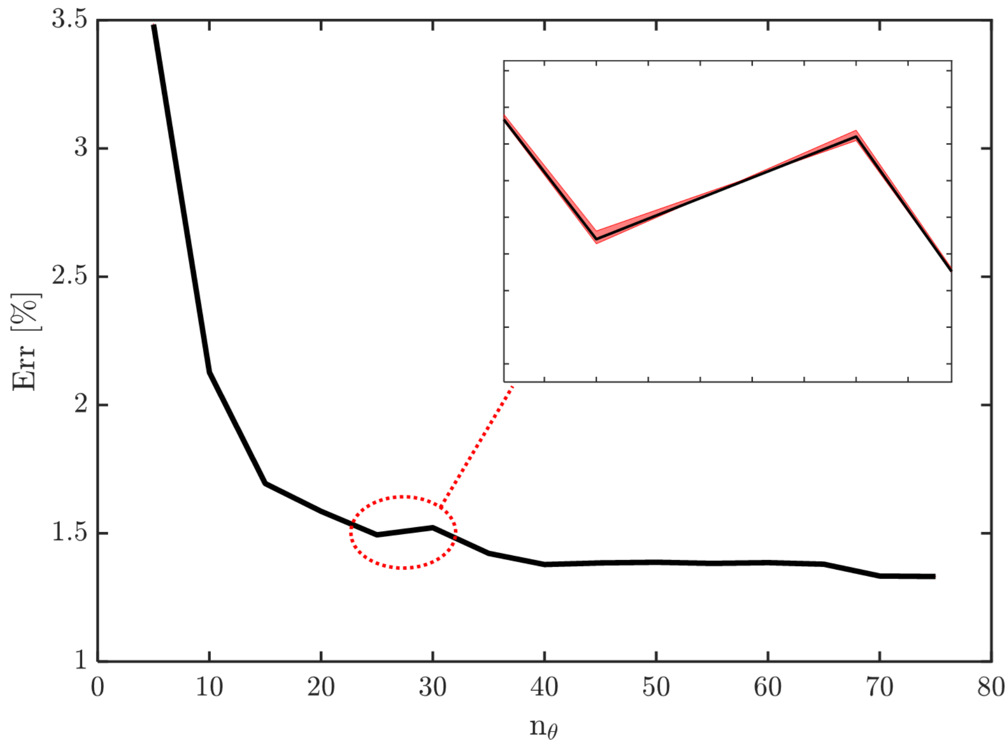

Figure 4.48: Fitting error vs. number of measurement points in the tangential direction.

The error fitting, showed in Figure 4.48, is calculated on each CFD point as:

$$Err[\%] = \frac{\sqrt{\sum\left(\hat{P} - P\right)^2}}{n_{CFD}} \frac{100}{P_0} \tag{4.1}$$

The error is initially calculated for a total of 25 points and has a value of 3.5%. As the number of measurement locations increases, the error starts to drop to finally stabilize to a value around 1%. We should highlight that this kind of approach provides a global quantification of the fitting error. However, if we are interested in capturing a few flow features, a local fitting approach can be used that could further reduce the error. The uncertainty on the pressure measurements is considered to calculate an uncertainty error bar on the fitting error. The zoomed region of Figure 4.48 shows the red area which indicates the uncertainty on the curve. The lower and upper bounds are obtained by applying a constant offset to the measurement equal to the direct measurement uncertainty, which on current measurement is approximately 50Pa.

Time-resolved unsteady pressure in a rotating wind tunnel

In this section, the effect of sensor frequency response on the measured tip flow features will be assessed. Different frequencies, typical of multiple pressure measurement techniques like Pressure Sensitive Paint (PSP), will be considered. For the rotor analysis, the first step is to translate steady results coming from RANS-based CFD to the reconstruction of unsteady measurement that could be collected in a turbine rig. The traces due to the passing of the airfoils can be seen in Figure 4.49, left. The color contour depicts the distribution of static pressure on the rotor shroud as seen from the relative frame of the rotor, i.e. an instantaneous snapshot seen from the absolute frame of the casing. Observed from the casing, this color contour would be rotating with speed equal to ωr_{shroud}, where ω is the rotational speed and r_{shroud} is the radius at the inner casing wall. This transformation allows us to go from a space coordinate (the tangential direction in the relative frame, as shown by the dashed lines in Figure 4.49, right) to a time coordinate (the measurement in time in a single point).

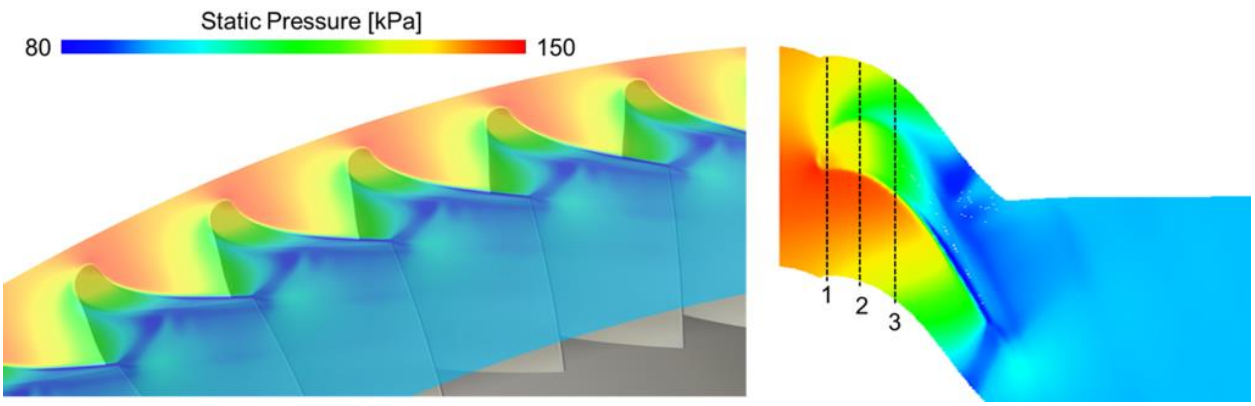

Figure 4.49: Left, over tip casing pressure contour. Right, sections where static pressure profiles are extracted.

Figure 4.50, left illustrates the static pressure trend at three axial locations. The blue, orange and yellow curves are extracted along section 1, 2 and 3 respectively. These lines indicate the variations of static pressure across the blade in a single passage. By replicating a single trace (black line in Figure 4.50, right) in a periodic fashion, the entire annulus can be reproduced. This reconstructed signal (red dashed line in Figure 4.50, right) simulates the unsteady pressure that we could measure in a fixed point on the stationary casing over time. The signal is repeated for multiple annulus so that our signal is long enough for the analysis.

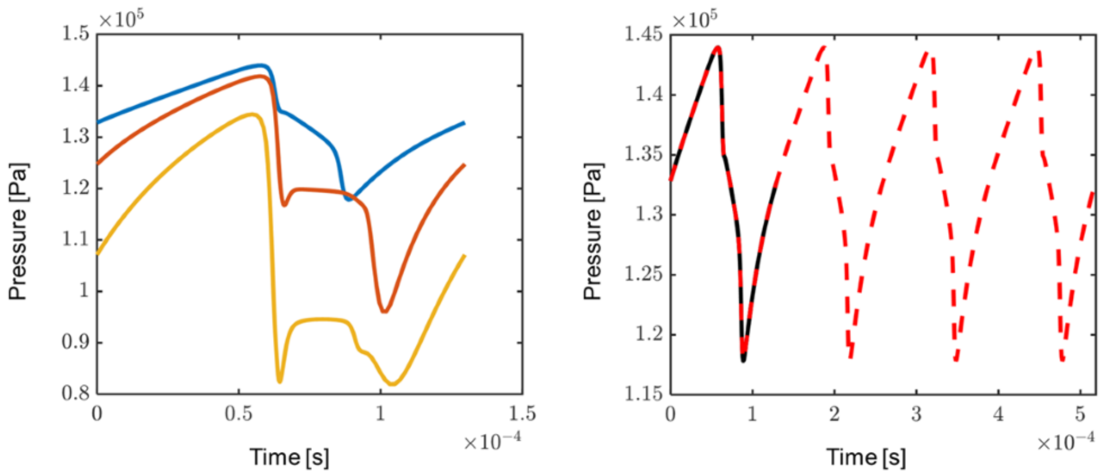

Figure 4.50: Left, wall pressure distribution at three axial locations (blue, orange and yellow lines are sections 1, 2, and 3 in Figure 5 respectively). Right: single signal coming from steady CFD (black solid line) repeated periodically to simulate blade trace over time (red dashed line).

Given that the signal in Figure 4.50, right is the actual pressure to measure in a single point in section 1, we need to verify that the frequency response offered by PSP is sufficient to reconstruct the time-resolved pressure distribution. In order to simulate the delay due to the response of the measurement system, a series of low-pass filters is implemented at frequencies of 5, 10 and 20 kHz. In this way we can quantify how much frequency content in the signal is getting lost when the high-frequency PSP becomes slower.

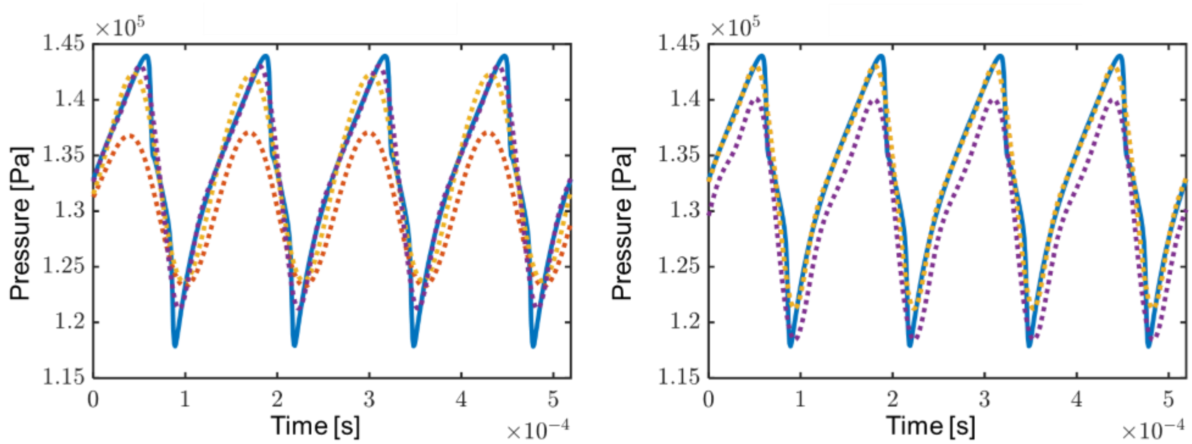

Figure 4.51: Left, static pressure trace in section 1 (blue) filtered with cutoff frequencies of 5, 10 and 20 kHz (orange, yellow and purple lines respectively. Right: signal filtered at 20 kHz, with three different steepness levels.

Figure 4.51, left shows the original signal in section 1 (blue line) compared with the three filtered signals. It can be noticed that for all three frequencies the period is correctly predicted which means that the blade passing is detected and we can distinguish between pressure and suction side. However, the slowest response (filter of 5 kHz indicated with orange line) is not sufficient to actually get the negative and positive peaks of pressure. On the other hand, the 20 kHz filter allows to accurately capture both location and amplitude of the local maxima and minima of pressure. This indicates that a verified frequency response of 20 kHz from PSP would provide a fully resolved trace of overtip pressure.

Besides the cut off frequency, the steepness of the filter plays a relevant role in the attenuation of the high-frequency content. Figure 4.51, right shows the signal filtered with the same cut off frequency (20 kHz) but with different slopes. It can be noticed that if the slope is too high, the high-frequency content is again missed. This indicates that a detailed dynamic calibration of the PSP is needed to verify that relevant components of the signal are not damped.

Finally, in Figure 4.52, it can be verified how the frequency content of the pressure signal (the original is colored in blue) is reduced as we filter the signal. The first three harmonics of the blade passing frequency seems to be conserved by the 20 kHz filter (purple lines) while are damped for smaller cut off frequencies.

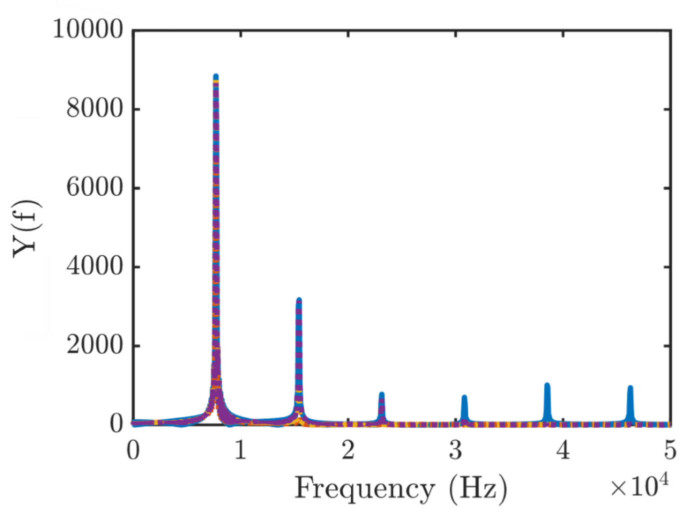

Figure 4.52: FFT analysis of the original signal in section 1, and three filtered signals (cutoff frequencies of 5, 10 and 20 kHz indicated with orange, yellow and purple lines respectively).

Finally we analyze the frequency requirements to measure pressure traces in the small rotating turbine rig, on optimized tips. In this rig the rotational speed is higher and the blades are smaller. This makes the measurement more challenging. Two tip geometries are considered, a simple squealer and an optimized tip.

The described approach is used to transform the steady profile into an unsteady pressure trace measured in a single point.

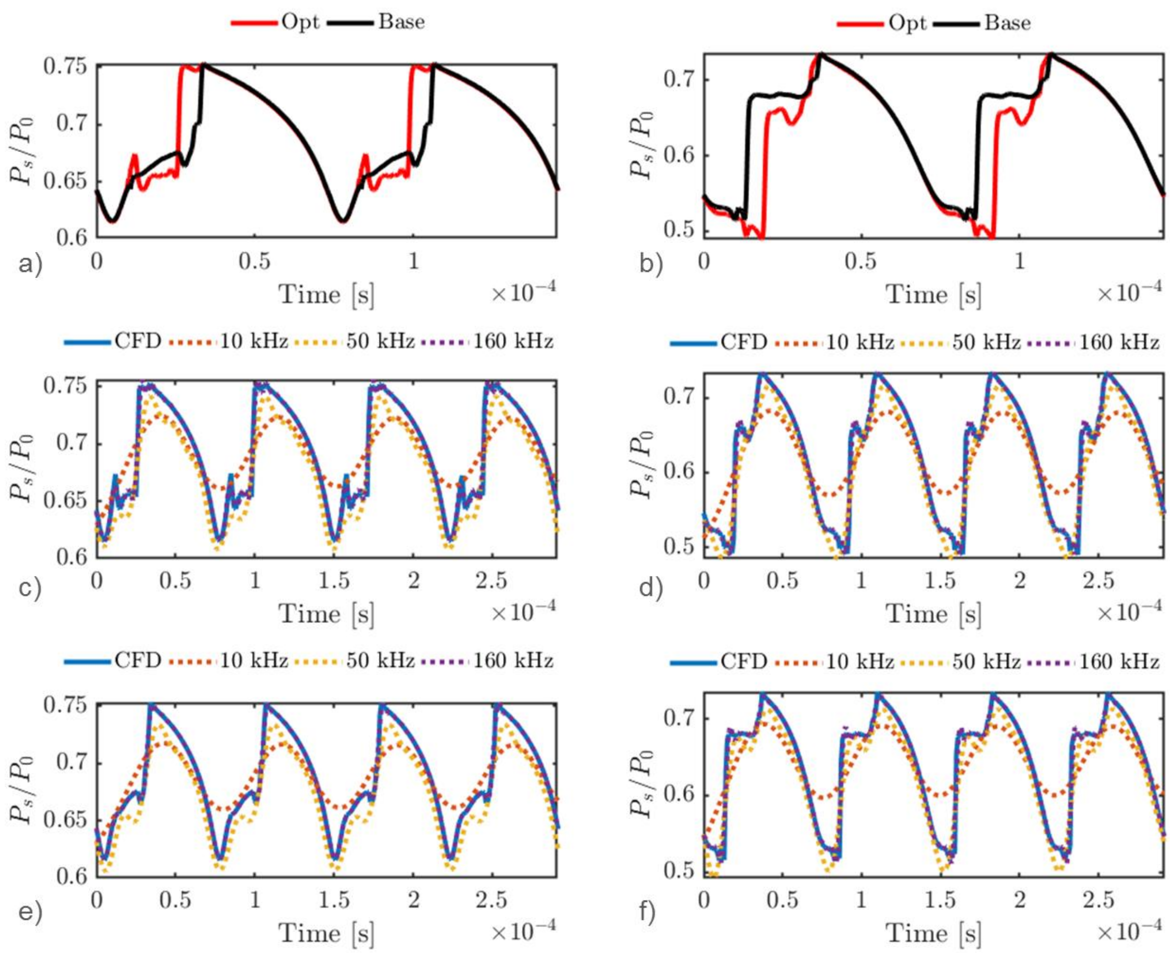

Figure 4.53: Static pressure extracted at 25% of axial chord (a) and 50% of axial chord (b) for the optimal tip and baseline tip (red and black line respectively. Filtered signals for optimal and baseline tips at 25% ('c' and 'e' graphs) and filtered signals for optimal and baseline tips at 50% ('d' and 'f' graphs).

Figure 4.53 on top (graphs 'a' and 'b') shows the pressure trace on a fixed axial location at 25% of the axial chord and 50% of the axial chord respectively. At the 25% the main difference between the blade tips is on the pressure side, where the squealer has a single rim that continuously covers the airfoil bored, while the optimized geometry has a recessed rail. Similar considerations were made in the description of Figure 4.47. At the 50% of the axial chord, the main differences are in both recesses on the pressure and suction side for the optimized tip. This can be seen in graph ‘b’ where the red line shows a deeper fall in the initial descend and also an earlier expansion close to the suctions side.

The plots from ‘c’ to ‘f’ depict the filtered signals with three cut-off frequencies: 10 kHz, 50 kHz, and 160 kHz. The first frequency can be achieved by PSP while the last one corresponds to the cut-off frequency of fast pressure transducers like Kulite. In all the 4 cases, the curve with the highest frequency is able to fully capture the dynamic behavior of the static pressure in the casing. The lowest frequency however filters most of the highest frequency features, making the blade passing the main phenomenon captured. The 50 kHz frequency provides signals that are still far from the original CFD signals, but can provide additional features that allow distinguishing the optimized blade from the baseline geometry.

4.4.3 Design of Experiments for Validation of Turbine Tip Green's Function*

The aim of measuring heat flux in a wind tunnel environment is to eventually retrieve the actual heat load on the turbine in engine operation. The accurate reproduction of the aerothermal phenomena at scaled conditions is one of the challenges in turbine experimental heat transfer. This section focuses on how to use facility measurement to retrieve the convective heat flux in the engine. In this approach, we compute the Green Functions coefficient matrix using heat flux pulses used to retrieve the increase of temperature in the inner surface of the casing. This coefficients matrix is obtained using data with the wind tunnel boundary conditions, and then the matrix is applied to the scaled engine conditions, which is the validation case. The method is designed to be potentially coupled with an inverse methodology to retrieve the heat flux in the inner casing from measurements of temperature on the outer casing.

4.4.3.1 Application of Green's Function Method to Test in the Annular Wind Tunnel

First, we need to scale the wind tunnel boundary conditions to get the corresponding engine conditions. The inlet and outlet quantities are varied to ensure the matching of the relevant non-dimensional numbers.

In particular, pressure ratio (total to static), vane Reynolds number, dimensionless velocity triangles, corrected speed and gas to wall temperature ratio in the engine replicate the ones used for the wind tunnel. The geometrical parameters were maintained to guarantee geometrical similarity, so only the flow parameters and the rotational speed were adjusted. Figure 4.54 shows the contours of Mach number at midspan obtained at engine condition (on the top) and wind tunnel condition (on the bottom). The results show an excellent agreement between the two Mach distributions, which confirms the correct scaling of the flow field. Since the focus of this work is the heat flux, we should compare the casing heat flux characteristics in the two cases.

* Section partially published in Cuadrado, D. G., Lozano, F., Andreoli, V., & Paniagua, G. (2019). Engine-Scalable Rotor Casing Convective Heat Flux Evaluation Using Inverse Heat Transfer Methods. Journal of Engineering for Gas Turbines and Power, 141(1), 011012.

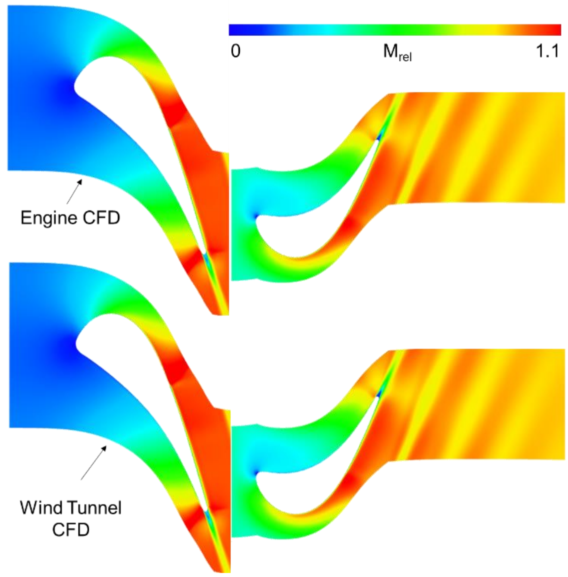

Figure 4.54. Mach distribution comparison between the engine simulation and the scaled wind tunnel simulation.

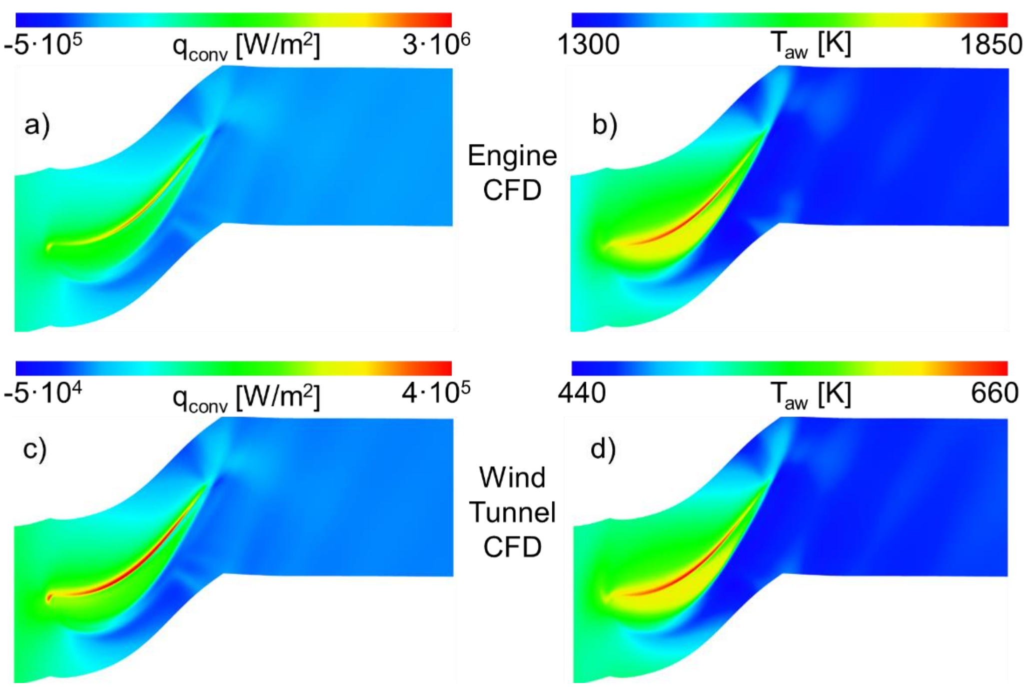

Figure 4.55: Convective heat flux in an isothermal CFD and adiabatic wall temperature at engine and facility conditions.

Figure 4.55a) illustrates the convective heat flux on the rotor shroud calculated from CFD at engine conditions. Analogously, Figure 4.55c shows the heat flux at wind tunnel conditions.

Both results are calculated imposing isothermal walls at the same gas to wall temperature ratio. Even though the ranges are different, due to higher inlet temperature in the engine conditions, similar heat flux distributions can be identified.

In both cases, the regions of highest heat flux can be encountered on top of the blade leading edge region and along the pressure side. On top of the blade tip, we can identify a region of average and uniform heat distribution. Areas of lower heat flux can be found in the passage close to the suction side where high Mach numbers are achieved. Figure 4.55b and Figure 4.55d depict the contours of adiabatic wall temperature for the engine and wind tunnel CFD respectively.

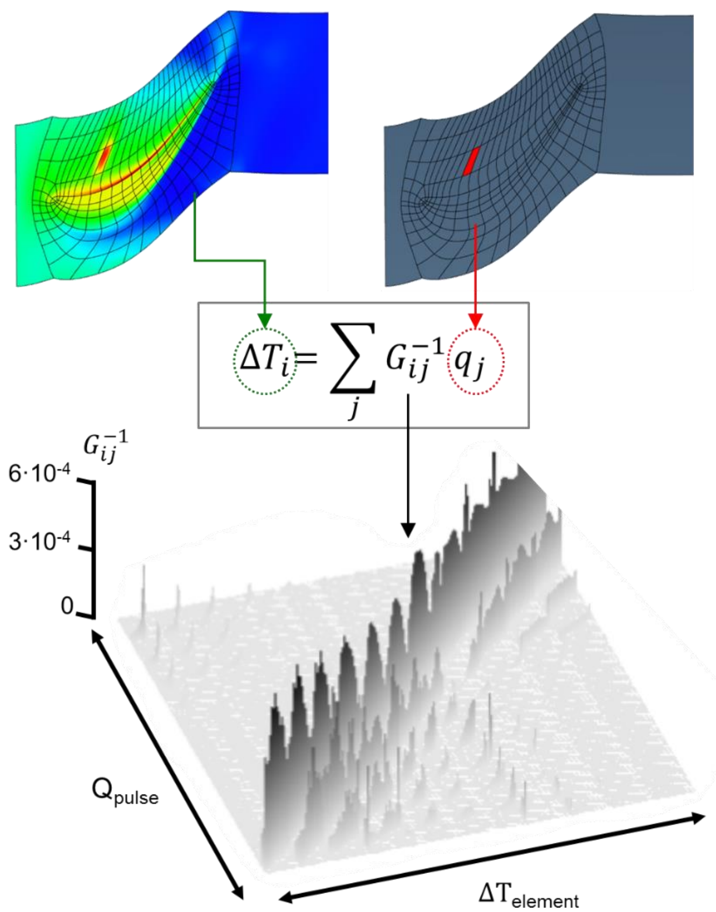

Figure 4.56: Green’s function matrix at experiments conditions.

These values are retrieved by imposing adiabatic boundary conditions for blade and endwalls. Again, the contours depict similar trends while ranges are different due to the higher driving temperature in the engine case.

Once the tool to compute the engine heat transfer has been assessed, we can evaluate how to retrieve the values starting from wind tunnel-based temperature measurements. The approach that we propose is based on the Green Function methodology. The full description of the procedure can be found in [42] and its application to turbine tips can be found in [86]. The basic idea is to discretize the internal casing into small surfaces and to build a superposition matrix that characterizes how the temperature in each element affects the heat flux on each other surface. This matrix, called superposition Kernel, reproduces the cross-talking between different regions of the casing; this is a very relevant phenomenon when the wall has non-homogeneous temperature [39]. Figure 4.56 shows the procedure to compute the matrix of the Green Function coefficient, and the coefficients obtained for wind tunnel conditions. The diagonal terms relate the local increase of temperature with the local heat flux. These terms are normally modeled using a conventional approach based on Newton's law of cooling. The extra-diagonal terms quantify the relevance of each element on the other casing areas. The matrix can be then used to retrieve the heat flux distribution on the casing, based on measurement of temperature.

4.4.3.2 Uncertainty Quantification

One of the purposes of this work is to explore the experimental feasibility of the DGF approach in a turbine testing environment, an alternative procedure for the retrieval of the reference wall temperature was tested.

The first point is to propose a methodology to retrieve the adiabatic wall temperature. Instead of retrieving the adiabatic wall temperature from the adiabatic simulation, the temperature is retrieved from an isothermal simulation. The same exact procedure could be used to derive the T_{aw} distribution from an experiment with heating at constant values. The future work consists in assessing what is the error on the heat flux, if we used an adiabatic wall temperature retrieved experimentally.

Another key factor while doing experiments is the propagation of uncertainty from the direct measurements to the derived quantities. The uncertainty associated with this methodology was evaluated considering the effect of the temperature and heat flux measurements. Using the backward facing step, we analyzed the effect of the magnitude of the pulse applied to retrieve the coefficients of the Green Functions matrix in each point. The uncertainty is mainly related to the uncertainty associated with the temperature readings since this methodology is very sensitive to temperature variation. In the case of the backward facing step, we consider that the temperature uncertainty is 0.5K and we performed calculations imposing pulses of 10, 100, 1000 and 10000 W/m^2.

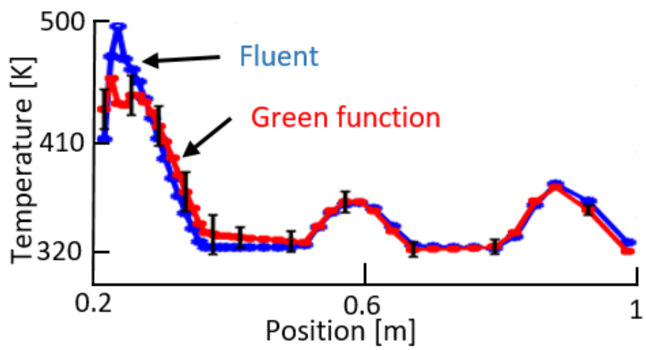

Figure 4.57. Uncertainty in the wall temperature estimation associated with a heat flux pulse of 10000 W/m2 and uncertainty in the temperature measurement of 0.5K.

Figure 4.57 represents the uncertainty associated with heat pulses of 10000W/m^2 for the backward facing step discussed in Chapter 3. There is a clear dependence on the size of the pulse with respect to the uncertainty associated with the method. The larger the pulse, the larger the increment of temperature and therefore the smaller the uncertainty. If the pulse is below a certain threshold the increment of temperature falls into the uncertainty of the temperature measurement and it is unfeasible to apply the method accurately. The uncertainty associated with the calculation with 10W/m^2 is over 400%, being even larger in the smaller elements where the recirculation is placed. This is related to the area of the elements, since applying the same heat flux in each element, the heat rate is smaller is the elements with a smaller area, which leads to a smaller increment of temperature. This dependency of the area may be avoided by imposing similar heat rates in all the elements. With larger pulses, the uncertainty is drastically reduced, reaching values of 5% in for the case with 10000 W/m^2 of pulse magnitude.

The uncertainty in the blade tip was evaluated using two different techniques: the sensitivity method and the Monte Carlo approach, which is based in the repeatability of the experiments. The sensitivity methodology consists of imposing the sensitivity of the measurement techniques to the mean level and compare the results using the same procedure. The uncertainty imposed in this case is 0.2K for the temperature measurements and 100 W/m^2 for the imposed heat flux. The heat flux pulse applied to calculate the coefficients is $2{\cdot}10^5$ W/m^2.

Figure 4.58 a) and b) display the level of uncertainty associated with the calculation of the temperature using this method with 1% of clearance and 0.1% respectively.

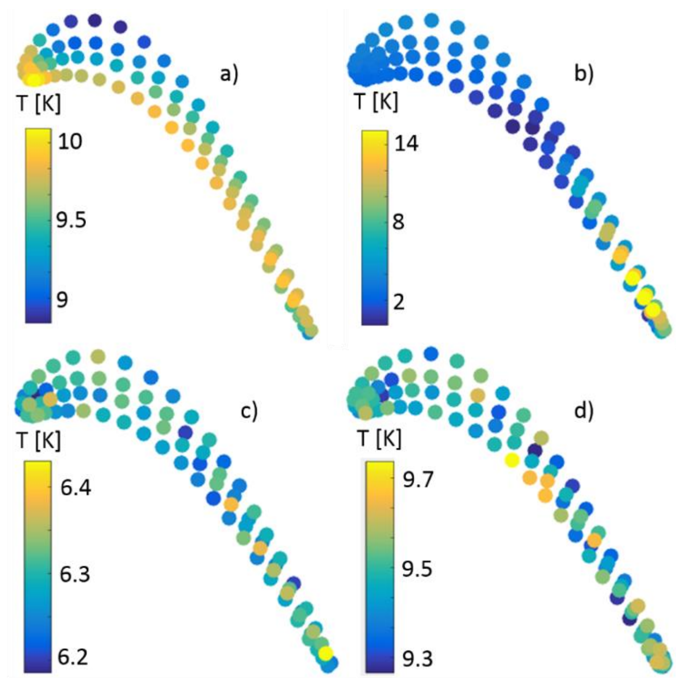

Figure 4.58. a) Uncertainty associated to the 1% clearance blade tip temperature calculation using sensitivity estimation. b) Uncertainty associated to the 0.1% clearance blade tip temperature calculation using sensitivity estimation. c) Uncertainty associated to the 1% clearance blade tip temperature calculation using Monte Carlo approach. d) Uncertainty associated to the 0.1% clearance blade tip temperature calculation using Monte Carlo approach.

The values are slightly higher in the case of the tight clearance in the region of the trailing edge, while in the case of the 1% clearance, the uncertainty is more distributed along the blade. It is particularly interesting that the higher uncertainty values for the 1% clearance are located along the pressure side of the blade. Further analysis of that region shows that the shear stress lines are following the pressure side since there is a vortex along this pressure line, and therefore the temperature is higher. In the case of the tight clearance, this vortex is not present but the higher temperature in the adiabatic case is located in the trailing edge, where the maximum uncertainty is also localized. This shows a clear dependency of the method on the aerothermal phenomena occurring in the over-tip region.

A second methodology was applied in order to evaluate only the method accuracy and uncertainty based only in the calculation and independent on the fluid singularities present in the over-tip region. A Monte Carlo approach was implemented by numerically adding a large number of experiments with random error normally distributed [87]. The uncertainty used for this method was 0.2K for temperature measurements and 100 W/m^2 for imposed heat flux. In every simulated experiment, we allow variations of the measured quantities in a normally distributed fashion with the specified standard deviation. The heat flux variation is imposed in each one of the pulses in the calculation of the coefficient of the matrix and in the imposed heat flux of the validation case. Regarding the temperature, the random error is introduced in the calculation of the reference temperature, in the measured temperature of the validation case and in the measured temperature of the pulses simulations.

This method is more experimentally related and make the uncertainty calculation independent of the conditions of the flow. Figure 4.58 c) and d) show the results of this calculation for the nominal 1% clearance and for the tight 0.1% clearance, respectively. The uncertainty associated to the random error is higher in the case of the tight clearance by 3K but the uncertainty on the tip of the blade is constant in all points, since for this estimation, all the random variations in all the assessed elements have been included. This is the reason of the randomly distributed error along the blade tip.

4.5 Conclusions

A turbine representation suitable for an engine transient has been derived and implemented into a modeling software. The approach for dynamic engine modeling has been established based on the time scales of the phenomena involved. An engine has been designed for this purpose, both in terms of the cycle analysis and detailed turbine design. The engine cycle has been simulated at design and off-design using steady and dynamic numerical tools.

Three dedicated computing modules have been implemented and individually tested. A performance module is used to calculate the efficiency variations in function of variations of clearance and cooling. A heat flux module implements the Green's function-based matrix, a function of clearance, to calculate the tip heat flux based on gas and wall temperatures. The module also updates the cooling effectiveness based on the injected cooling fraction. A thermomechanical component computes the mechanical and thermal loads acting on the turbine components, and derive the time-resolved running clearance as a result of each component's deformation.

A sensitivity study is performed to characterize the tip clearance and the consequent turbine performance as stochastic quantities. This study allows defining an averaged engine performance with an error band based on uncertainty quantification.

Finally, the global model is used to study the clearance and performance variations that a compact engine undergoes to during a transient in a specific mission.

CHAPTER 5. CONCLUSIONS

This manuscript presented a methodology to link detailed tip clearance aerothermal analysis and optimization to the dynamic model of a compact aircraft engine. While the three different objectives were achieved, a number of additional lessons were obtained.

1) Aerothermal optimization of the tip shape for a cooled high-pressure turbine.

- The effect of tip gap on a compact turbine was investigated, and the relevance of viscous effects was quantified.
- A single clearance optimization strategy was presented, together with the results and a set of optimized geometry. Through the tip optimization, the efficiency can be improved by 0.53% or the heat load can be reduced by 70%.
- A robustness analysis has been conducted, to highlight the sensitivity of the rotor efficiency to tip clearance.
- Based on the lessons learned, a strategy to optimize the tip shape considering transient operation is proposed. The optimization has been implemented, so the future work is to run the calculations and analyze the results.
- The main features of the overtip flow have been analyzed to understand the origin of the improvement of performance. Detailed quantification of leakage flow and a breakdown of losses was performed.
- The sensitivity to coolant conditions has been quantified in terms of variations of efficiency and tip heat transfer. For those two quantities, a variation of -10% of coolant total pressure corresponds to a decrease in the efficiency of 0.3% and a heat load reduction of 20%.

2) Scalable models of turbine tip convective heat flux

- A model based on Green's Function applicable to turbine tip has been developed. The routine to calculate the matrices and retrieve the heat flux has been implemented and tested in a simple test-case.
- The tip heat flux is analyzed and the Green's function methodology has been implemented to retrieve the convective heat flux in a turbine environment.

- The Green’s Function matrix has been calculated for different tip gaps and the features of the heat transfer in the turbine tip were discussed.
- The scaling of the method has been discussed with respect to the tip gap and the flow temperature.

3) Evaluate tip clearance effects in a compact engine during transient

- A methodology to implement tip clearance variations into a dynamic engine model was developed to simulate engine transients. A baseline cycle has been selected and the engine has been designed, focusing on the turbine. A steady-state model has been developed to run design and off-design analysis.
- A performance module has been programmed to calculate the efficiency variations in function of variations of clearance and cooling. A heat transfer module has been implemented to retrieve the convective heat flux through Green’s function-based matrix, as a function of clearance. The module also updates the cooling effectiveness based on the injected cooling. A thermomechanical component computes the mechanical and thermal loads acting on the turbine components and is used to compute the deformations and the clearance.
- The dynamic model has been integrated with the three components and used to quantify the turbine performance for varying clearance during a given mission.
- Using a steady model, the sensitivity of gas turbine performance to tip clearance has been quantified. The results indicate the need for defining the clearance as a stochastic quantity rather than deterministic.
- The final step is to design the experiment for future validations. A dynamic wind tunnel model has been built to validate the modeling of the turbine experimentally. Considerations on turbine tip testing in stationary conditions are made based on the CFD results. Additionally, the numerical simulations have been used to decide the location and characteristics of the instrumentation. Analogously, an experiment to derive turbine Green’s Function has been proposed, considering the uncertainties associated with the experimental measurements and the scaling.

APPENDIX

APPENDIX A. SOLVERS VALIDATION

In this section, validation data is reported for the CFD solvers used in this thesis. Figure A. 1 depicts the experimental data and the CFD results from Numeca FINE/Turbo in function of the non-dimensional curvilinear coordinate along the rotor blade surface, zero at the leading edge, negative along the pressure side, and positive along the suction side. Figure A.1 a) represents the isentropic Mach number at the 85% of the blade span for both pressure and suction side, while Figure A. 1 b) illustrates the Nusselt number. The leading edge, at minimal Isentropic Mach experiences the maximum level of heat flux, and therefore of Nusselt number. As the flow field accelerates along the front pressure and suction side, the boundary layer thickens, resulting in a reduction of the Nusselt number. Along the front pressure side, the flow is rapidly accelerated in the convex surface resulting in a substantial decrease of the Nusselt number, which remains practically constant further downstream Nu =700, revealing a laminar/transitional state of the boundary layer. Overall the CFD exhibits a good agreement with the experimental results, considering the experimental uncertainty.

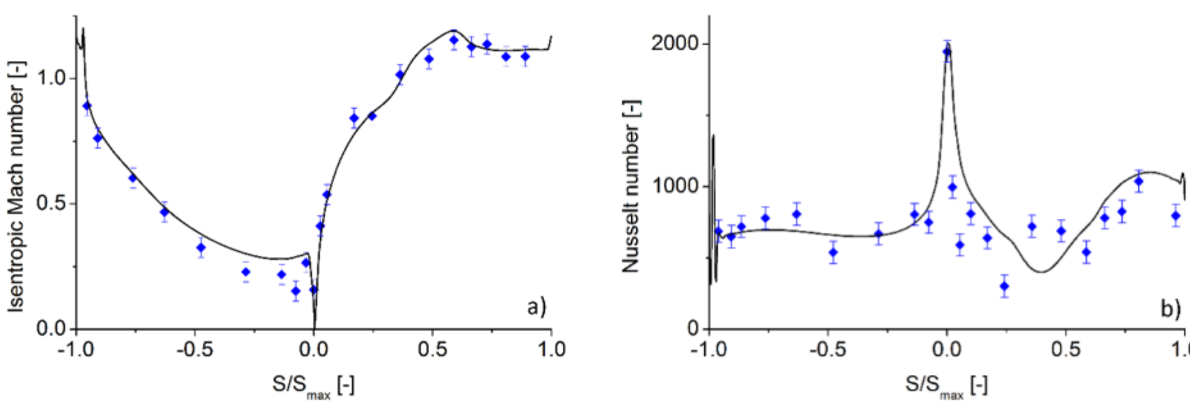

Figure A. 1: a) Isentropic Mach number (experiments - blue dots, CFD – continuous black line) at 85% of the blade span. b) Nusselt number (experiments - blue dots, CFD – continuous black line) at 85% of the blade span.

Numeca FINE/Open was validated in previous works on a cooled turbine [88]. Figure A. 2, from De Maesschalck et al., shows the Nusselt number on the overtip casing of the turbine. Overall, the heat flux features compare well between the CFD and the experiments.

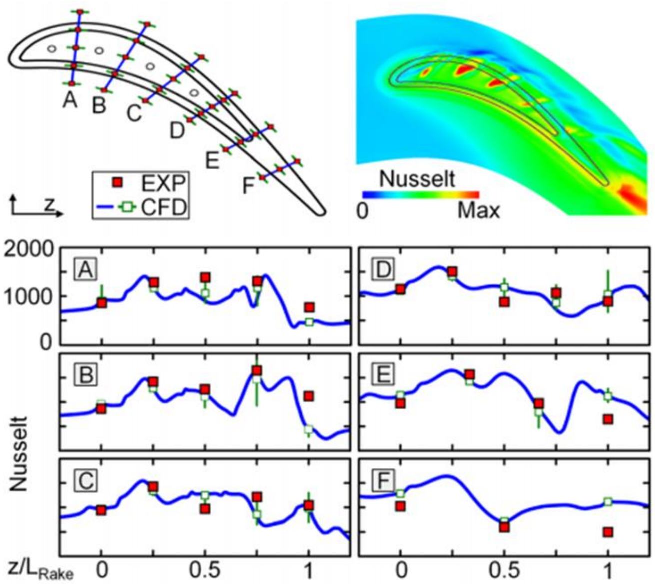

Figure A. 2: Validation of the Nusselt number on the overtip casing [17]

APPENDIX B. ENGINE MODEL INPUT

Section 'a' - abradable			
w	0.025	m	Width
r_{in}	0.1	m	Inner radius
r_{out}	0.102	m	Outer radius
t	0.002	m	Thickness
A	0.0157	m^2	Inner surface area
A_s	0.0157	m^2	Exposed area
V	3.17E-05	m^3	Volume
L_c	0.0020	m^2	Characteristic length
h	1000	W/m^2K	Heat transfer coefficient
Material	Zirconium Oxide	-	Properties from Appendix B
Section 'b' - metal			
w	0.025	m	Width
r_{in}	0.102	m	Inner radius
r_{out}	0.11	m	Outer radius
t	0.008	m	Thickness
A	0.0160	m^2	Inner surface area
A_s	0.0320	m^2	Exposed area
V	1.33E-04	m^3	Volume
L_c	0.0083	m^2	Characteristic length
h	500	W/m^2K	Heat transfer coefficient
Material	Inconel 718	-	Properties from Appendix B
Blade parameters			
L	0.0129	m	Blade length
M	0.168	m	Outer radius
A_s	0.027	m	Thickness
V	2.04E-05	m^2	Inner surface area
L_c	0.00076	m^2	Exposed area
h	1000	W/m^2K	Heat transfer coefficient
Material	Inconel 718	-	Properties from Appendix B
Rotor parameters			

w	0.006	m	Width
r_{out}	0.085	m	Outer radius
A	0.024	m^2	Inner surface area
A_s	0.048	m^2	Exposed area
V	1.43E-04	m^3	Volume
L_c	0.006	m^2	Characteristic length
h	500	W/m^2K	Heat transfer coefficient
Material	Inconel 718	-	Properties from Appendix B

APPENDIX C. MATERIAL PROPERTIES

- Inconel 718

MatData.T_vec = [21.1111 37.7778 93.3333148.8889 204.4444260 315.5556371.1111 426.6667 482.2222537.7778 593.3333648.8889 704.4444760 815.5556 871.1111 926.6667 982.2222 1037.7778 1093.3333];

MatData.rho = ones(1,length(MatData.T_vec)).*8193.2518; % kg/m^3, density

MatData.nu = [0.2940 0.291 0.288 0.28 0.28 0.275 0.272 0.273 0.271 0.272 0.271 0.276 0.283 0.292 0.306 0.321 0.331 0.334 0.341 0.366 0.4020]; % Poissons ratio

MatData.c = ones(1,length(MatData.T_vec)).*435; % J/Kg-C, specific heat

MatData.alpha = [1.27726E-05 1.28E-05 1.31E-05 1.33E-05 1.35E-05 1.37E-05 1.39E-05 1.42E-05 1.44E-05 1.46E-05 1.48E-05 1.50E-05 1.53E-05 1.55E-05 1.57E-05 1.59E-05 1.62E-05 1.64E-05 1.66E-05 1.68E-05 1.70344E-05];

MatData.k = [11.1972 11.4644 12.3549 13.2455 14.1361 15.0267 15.9173 16.8079 17.6985 18.5891 19.4797 20.3703 21.2609 22.1515 23.0421 23.9326 24.8232 25.7138 26.6044 27.495 28.3856]; % W/m-K, thermal conductivity

MatData.E = [199947961502.1710 1.98569E+11 1.95811E+111.93053E+11 1.90295E+11 1.86848E+11 1.8409E+11 1.80643E+11 1.77885E+11 1.74437E+11 1.7099E+11 1.66853E+11 1.63406E+11 1.58579E+11 1.53753E+11 1.46858E+11 1.39274E+11 1.29621E+11 1.19969E+11 1.09627E+11 98595029292.4498]; % Pa, modulus of elasticity

- Zirconium Oxide

MatData.T_vec = [21.1111 37.7778 93.3333148.8889 204.4444260 315.5556371.1111 426.6667 482.2222537.7778 593.3333648.8889 704.4444760 815.5556 871.1111 926.6667 982.2222 1037.7778 1093.3333];

MatData.rho = ones(1,length(MatData.T_vec)).*5.03/1000*100^3; % kg/m^3

MatData.nu = ones(1,length(MatData.T_vec)).*0.4; % poissons ratio

MatData.c = ones(1,length(MatData.T_vec)).*0.109*4184; % J/kg-K

MatData.alpha = ones(1,length(MatData.T_vec)).*8.2e-6; % 1/K, thermal expansion coef.

MatData.k = ones(1,length(MatData.T_vec)).*2.93; % W/m-K

MatData.E = ones(1,length(MatData.T_vec)).*139e9; % Pa, modulus of elasticity

REFERENCES

[1] S. J. Khalid, "Role of dynamic simulation in fighter engine design and development," *J. Propuls. Power*, vol. 8, no. 1, pp. 219–226, Jan. 1992.

[2] S. Khalid and R. Hearne, "Enhancing dynamic model fidelity for improved prediction of turbofanengine transient performance," *16th Jt. Propuls. Conf.*, 1980.

[3] W. P. J. Visser and I. D. Dountchev, "Modeling Thermal Effects on Performance of Small Gas Turbines," in *Volume 1: Aircraft Engine; Fans and Blowers; Marine*, 2015, p. V001T01A014.

[4] A. Rolt *et al.*, "Scale effects on conventional and intercooled turbofan engine performance," *Aeronaut. J.*, vol. 121, no. 1242, pp. 1162–1185, Aug. 2017.

[5] R. S. Bunker, "Axial Turbine Blade Tips: Function, Design, and Durability," *J. Propuls. Power,* vol. 22, no. 2, pp. 271–285, 2006.

[6] M. W. Wiseman and Ten-Huei Guo, "An investigation of life extending control techniques for gas turbine engines," in *Proceedings of the 2001 American Control Conference. (Cat. No.01CH37148),* 2001, pp. 3706–3707 vol.5.

[7] C. H. Gay, "Thermal Response Turbine Shroud.," Nov. 1979.

[8] R. S. Bunker, "A Review of Turbine Blade Tip Heat Transfer," *Annals of the New York Academy of Sciences*, vol. 934, no. 1. pp. 64–79, 2001.

[9] W. A. Howard, W.D. and Fasching, "CF6 jet engine diagnostics program. High pressure turbine roundness/clearance investigation," 1982.

[10] N. W. Harvey, "Aerothermal implications of shroudless and shrouded blades," in *VKI LS 2004-02, Turbine blade tip design and tip clearance treatment, ISBN 2-930389-51-6*.

[11] J. D. Coull, N. R. Atkins, and H. P. Hodson, "Winglets for Improved Aerothermal Performance of High Pressure Turbines," *J. Turbomach.*, vol. 136, no. 9, p. 091007, May 2014.

[12] D. O. O'Dowd *et al.*, "Aero-Thermal Performance of a Winglet at Engine Representative Mach and Reynolds Numbers," in *Volume 4: Heat Transfer, Parts A and B,* 2010, pp. 357–367.

[13] G. Paniagua *et al.*, "Design of the Purdue Experimental Turbine Aerothermal Laboratory for Optical and Surface Aerothermal Measurements," *J. Eng. Gas Turbines Power*, vol. 141, no. 1, 2019.

[14] Q. Zhang, D. O. O'Dowd, L. He, A. P. S. Wheeler, P. M. Ligrani, and B. C. Y. Cheong, "Overtip Shock Wave Structure and Its Impact on Turbine Blade Tip Heat Transfer," *J. Turbomach.*, vol. 133, no. 4, p. 041001, 2011.

[15] C. De Maesschalck, S. Lavagnoli, G. Paniagua, and N. Vinha, "Aerothermodynamics of tight rotor tip clearance flows in high-speed unshrouded turbines," *Appl. Therm. Eng.*, vol. 65, no. 1–2, pp. 343–351, Apr. 2014.

[16] Q. Zhang and L. He, "Tip-Shaping for HP Turbine Blade Aerothermal Performance Management," *J. Turbomach.*, vol. 135, no. 5, p. 051025, 2013.

[17] C. De Maesschalck, S. Lavagnoli, G. Paniagua, T. Verstraete, R. Olive, and P. Picot, "Heterogeneous Optimization Strategies for Carved and Squealer-Like Turbine Blade Tips," *J. Turbomach.*, vol. 138, no. 12, p. 121011, Jul. 2016.

[18] M. G. Dunn, "Convective Heat Transfer and Aerodynamics in Axial Flow Turbines," *J. Turbomach.*, vol. 123, no. 4, p. 637, 2001.

[19] Z. Wang, Q. Zhang, Y. Liu, and L. He, "Impact of Cooling Injection on the Transonic Over-Tip Leakage Flow and Squealer Aerothermal Design Optimization," *J. Eng. Gas Turbines Power*, vol. 137, no. 6, p. 062603, Jun. 2015.

[20] S. Mhetras, D. Narzary, Z. Gao, and J.-C. Han, "Effect of a Cutback Squealer and Cavity Depth on Film-Cooling Effectiveness on a Gas Turbine Blade Tip," *J. Turbomach.*, vol. 130, no. 2, p. 021002, 2008.

[21] J. D. Denton, "Loss Mechanisms in Turbomachines," *J. Turbomach.*, vol. 115, no. October 1993, pp. 621–656, 1993.

[22] J. P. Bindon, "The Measurement and Formation of Tip Clearance Loss," *J. Turbomach.*, vol. 111, no. 3, p. 257, 1989.

[23] N. R. Atkins and R. W. Ainsworth, "Turbine Aerodynamic Performance Measurement Under Non-Adiabatic Conditions," *Vol. 6 Turbo Expo 2007, Parts A B*, vol. 134, no. November 2012, pp. 493–501, 2007.

[24] G. Hubert, "Untersuchungen über die Sekundärverluste in axialen Turbomaschinen," *VDI ForschHft 496*, vol. 5, 1963.

[25] T. Verstraete, S. Amaral, R. Van den Braembussche, and T. Arts, "Design and Optimization of the Internal Cooling Channels of a High Pressure Turbine Blade—Part II: Optimization," *J. Turbomach.*, vol. 132, no. 2, p. 021014, 2010.

[26] K. Deb, A. Pratap, S. Agarwal, and T. Meyarivan, "A fast and elitist multiobjective genetic algorithm: NSGA-II," *IEEE Trans. Evol. Comput.*, vol. 6, no. 2, pp. 182–197, Apr. 2002.

[27] D. C. Montgomery, *Design and Analysis of Experiments*. John wiley & sons, 2017.

[28] T. Yasa, G. Paniagua, and A. Bussolin, "Performance analysis of a transonic high-pressure turbine," *Proc. Inst. Mech. Eng. Part A J. Power Energy*, vol. 221, no. 6, pp. 769–778, Jan. 2007.

[29] C. De Maesschalck, C. Lacor, G. Paniagua, S. Lavagnoli, A. Remiot, and L. Bricteux, "Performance Robustness of Turbine Squealer Tip Designs Due to Manufacturing and Engine Operation," *J. Propuls. Power*, vol. 33, no. 3, pp. 740–749, 2017.

[30] P. Seshadri, S. Shahpar, and G. T. Parks, "Robust Compressor Blades for Desensitizing Operational Tip Clearance Variations," in *Volume 2A: Turbomachinery*, 2014, p. V02AT37A043.

[31] and P. M. Hunt, Julian CR, Alan A. Wray, "Eddies, Streams, and Convergence Zones in Turbulent Flows," 1988.

[32] P. CHAKRABORTY, S. BALACHANDAR, and R. J. ADRIAN, "On the relationships between local vortex identification schemes," *J. Fluid Mech.*, vol. 535, pp. 189–214, Jul. 2005.

[33] N. L. Key and T. Arts, "Comparison of Turbine Tip Leakage Flow for Flat Tip and Squealer Tip Geometries at High-Speed Conditions," *J. Turbomach.*, vol. 128, no. 2, p. 213, 2006.

[34] N. W. Harvey and K. Ramsden, "A Computational Study of a Novel Turbine Rotor Partial Shroud," *J. Turbomach.*, vol. 123, no. 3, p. 534, 2001.

[35] J. D. Coull and N. R. Atkins, "The Influence of Boundary Conditions on Tip Leakage Flow," *J. Turbomach.*, vol. 137, no. 6, p. 061005, 2015.

[36] M. Pátý, B. C. Cernat, C. De Maesschalck, and S. Lavagnoli, "Experimental and Numerical Investigation of Optimized Blade Tip Shapes—Part II: Tip Flow Analysis and Loss Mechanisms," *J. Turbomach.*, vol. 141, no. 1, p. 011006, 2018.

[37] V. Pinilla, J. P. Solano, G. Paniagua, and R. J. Anthony, "Adiabatic Wall Temperature Evaluation in a High Speed Turbine," *J. Heat Transfer*, vol. 134, no. 9, p. 091601, 2012.

[38] J. Sellars, M. Tribus, and J. Klein, “Heat Transfer to Laminar flow in a Round Tuber or Flat Conduit - The Graetz Problem Extended,” 1954.

[39] a. M. Anderson and R. J. Moffat, “The Adiabatic Heat Transfer Coefficient and the Superposition Kernel Function: Part 2—Modeling Flatpack Data as a Function of Channel Turbulence,” *J. Electron. Packag.*, vol. 114, no. 1, p. 22, 1992.

[40] J. M. Hacker and J. K. Eaton, “Measurements of heat transfer in a separated and reattaching flow with spatially varying thermal boundary conditions,” *Int. J. Heat Fluid Flow*, vol. 18, no. 1, pp. 131–141, 1997.

[41] B. Vick, J. H. Beale, and J. I. Frankel, “Integral Equation Solution for Internal Flow Subjected to a Variable Heat Transfer Coefficient,” *J. Heat Transfer*, vol. 109, no. 4, p. 856, 1987.

[42] R. J. Moffat, “What’s new in convective heat transfer?,” *Int. J. Heat Fluid Flow*, vol. 19, no. 2, pp. 90–101, 1998.

[43] C. Booten and J. K. Eaton, “Discrete Green’s Function Measurements in Internal Flows,” *J. Heat Transfer*, vol. 127, no. 7, p. 692, 2005.

[44] C. W. Booten and J. K. Eaton, “Discrete Green’s Function Measurements in a Serpentine Cooling Passage,” *J. Heat Transfer*, vol. 129, no. 12, p. 1686, 2007.

[45] D. Mukerji and J. K. Eaton, “Discrete green’s function measurements in a single passage turbine model,” *J. Heat Transfer*, vol. 127, no. 4, pp. 366–377, 2005.

[46] C. Zhou, “Aerothermal Performance of Different Tips in Transonic Turbine Cascade with End-Wall Motion,” *J. Propuls. Power*, vol. 30, no. 5, pp. 1316–1327, 2014.

[47] S. K. Krishnababu *et al.*, “Aero-Thermal Investigations of Tip Leakage Flow In Axial Flow Turbines: Part I — Effect of Tip Geometry and Tip Clearance Gap,” *Vol. 4 Turbo Expo 2007, Parts A B*, vol. 131, no. January 2009, pp. 727–738, 2007.

[48] S. J. Thorpe, S. Yoshino, G. A. Thomas, R. W. Ainsworth, and N. W. Harvey, “Blade-tip heat transfer in a transonic turbine,” *Proc. Inst. Mech. Eng. Part A J. Power Energy*, vol. 219, no. 6, pp. 421–430, Jan. 2005.

[49] S. Lavagnoli, G. Paniagua, C. De Maesschalck, and T. Yasa, “Analysis of the Unsteady Overtip Casing Heat Transfer in a High Speed Turbine,” *J. Turbomach.*, vol. 135, no. 3, p. 031027, 2013.

[50] M. D. Polanka, D. A. Hoying, M. Meininger, and C. D. MacArthur, "Turbine Tip and Shroud Heat Transfer and Loading—Part A: Parameter Effects Including Reynolds Number, Pressure Ratio, and Gas-to-Metal Temperature Ratio," *J. Turbomach.*, vol. 125, no. 1, p. 97, 2003.

[51] V. Shyam, A. Ameri, and J.-P. Chen, "Analysis of Unsteady Tip and Endwall Heat Transfer in a Highly Loaded Transonic Turbine Stage," *Vol. 4 Heat Transf. Parts A B*, vol. 134, no. July 2012, pp. 645–656, 2010.

[52] F. Zhong, C. Zhou, H. Ma, and Q. Zhang, "Heat Transfer of Winglet Tips in a Transonic Turbine Cascade," in *Volume 5A: Heat Transfer*, 2016, p. V05AT13A014.

[53] C. H. Sieverding, T. Arts, R. Dénos, and F. Martelli, "Investigation of the Flow Field Downstream of a Turbine Trailing Edge Cooled Nozzle Guide Vane," *J. Turbomach.*, vol. 118, no. 2, p. 291, 1996.

[54] K. A. Batchelder and J. K. Eaton, "Practical Experience With the Discrete Green's Function Approach to Convective Heat Transfer," *J. Heat Transfer*, vol. 123, no. 1, p. 70, 2001.

[55] Numeca International, "Autogrid5™ v9 User Manual," no. December, pp. 1–475, 2014.

[56] "Procedure for Estimation and Reporting of Uncertainty Due to Discretization in CFD Applications," *J. Fluids Eng.*, vol. 130, no. 7, p. 078001, 2008.

[57] Numeca International, "FINE™/TURBO v9.1 Theoretical Manual," no. November, p. 156, 2014.

[58] F. Didier, R. Dénos, and T. Arts, "Unsteady Rotor Heat Transfer in a Transonic Turbine Stage," *Vol. 3 Turbo Expo 2002, Parts A B*, vol. 124, no. June, pp. 319–329, 2002.

[59] S. Lavagnoli, C. De Maesschalck, and G. Paniagua, "Analysis of the Heat Transfer Driving Parameters in Tight Rotor Blade Tip Clearances," *J. Heat Transfer*, vol. 138, no. 1, p. 011705, 2015.

[60] R. Maffulli and L. He, "Impact of Wall Temperature on Heat Transfer Coefficient and Aerodynamics for Three-Dimensional Turbine Blade Passage," *J. Therm. Sci. Eng. Appl.*, vol. 9, no. 4, p. 041002, Apr. 2017.

[61] R. Maffulli and L. He, "Wall Temperature Effects on Heat Transfer Coefficient for High-Pressure Turbines," *J. Propuls. Power*, vol. 30, no. 4, pp. 1080–1090, 2014.

[62] S. Lattime and B. Steinetz, "Turbine Engine Clearance Control Systems: Current Practices and Future Directions," *38th AIAA/ASME/SAE/ASEE Jt. Propuls. Conf. & Exhib.*, no. July, 2002.

[63] A. S. L. Theodore L. Bergman, Frank P. Incropera, David P. DeWitt, *Fundamentals of Heat and Mass Transfer*. 2011.

[64] J. Saavedra, G. Paniagua, and S. Lavagnoli, "On the transient response of the turbulent boundary layer inception in compressible flows," *J. Fluid Mech.*, vol. 850, pp. 1117–1141, Sep. 2018.

[65] J. DeCastro and K. Melcher, "A Study on the Requirements for Fast Active Turbine Tip Clearance Control Systems," in *40th AIAA/ASME/SAE/ASEE Joint Propulsion Conference and Exhibit*, 2004, no. July, pp. 1–14.

[66] J. L. Kratz and J. W. Chapman, "Active Turbine Tip Clearance Control Trade Space Analysis of an Advanced Geared Turbofan Engine," in *2018 Joint Propulsion Conference*, 2018.

[67] J. W. Chapman, T.-H. Guo, J. L. Kratz, and J. S. Litt, "Integrated Turbine Tip Clearance and Gas Turbine Engine Simulation," *52nd AIAA/SAE/ASEE Jt. Propuls. Conf.*, no. October 2016, 2016.

[68] E. A. Baskharone, "Axial-Flow Turbines," in *Principles of Turbomachinery in Air-Breathing Engines*, Cambridge: Cambridge University Press, 2014, pp. 250–346.

[69] J. Dunham and P. M. Came, "Improvements to the Ainley-Mathieson Method of Turbine Performance Prediction," *J. Eng. Power*, vol. 92, no. 3, p. 252, 1970.

[70] M. I. Yaras and S. A. Sjolander, "Prediction of Tip-Leakage Losses in Axial Turbines," *J. Turbomach.*, vol. 114, no. 1, p. 204, 2008.

[71] J. Kurzke and I. Halliwell, *Propulsion and Power*, no. September. Cham: Springer International Publishing, 2018.

[72] P. P. Walsh, *Gas turbine performance*. 2004.

[73] J. W. Gauntner, "Algorithm for Calculating Turbine Cooling Flow and the Resulting Decrease in Turbine Efficiency," *NASA Tech. Memo.*, vol. 81453, 1980.

[74] J. A. Kypuros and K. J. Melcher, "A Reduced Model for Prediction of Thermal and Rotational Effects on Turbine Tip Clearance," no. March, 2003.

[75] R. Merkler, S. Staudacher, M. Schölch, H. Schulte, and K.-J. Schmidt, "Simulation of Clearance Changes and Mechanical Stresses in Transient Gas Turbine Operation by a Matrix Method," in *41st AIAA/ASME/SAE/ASEE Joint Propulsion Conference & Exhibit*, 2005, no. July, pp. 1–13.

[76] C. W. Fei, W. Z. Tang, G. C. Bai, and Z. Y. Chen, "A dynamic probabilistic design method for blade-tip radial running clearance of aeroengine high-pressure turbine," *Proc. Inst. Mech. Eng. Part C J. Mech. Eng. Sci.*, vol. 229, no. 10, pp. 1861–1872, 2015.

[77] V. Fernandez-villace and G. Paniagua, "Numerical Model of a Variable-Combined-Cycle Engine for Dual Subsonic and Supersonic Cruise," pp. 839–870, 2013.

[78] J. W. Chapman, T. M. Lavelle, R. D. May, J. S. Litt, and T. Guo, "Toolbox for the Modeling and Analysis of Thermodynamic Systems (T-MATS) User' s Guide," 2014.

[79] R. S. Bunker, "The Effects of Manufacturing Tolerances on Gas Turbine Cooling," *J. Turbomach.*, vol. 131, no. 4, p. 041018, 2009.

[80] F. Montomoli, M. Carnevale, A. D'Ammaro, M. Massini, and S. Salvadori, *Uncertainty Quantification in Computational Fluid Dynamics and Aircraft Engines*. 2015.

[81] F. Montomoli, M. Massini, and S. Salvadori, "Geometrical uncertainty in turbomachinery: Tip gap and fillet radius," *Comput. Fluids*, vol. 46, no. 1, pp. 362–368, 2011.

[82] J. W. Chapman, T. M. Lavelle, J. S. Litt, and T.-H. Guo, "A Process for the Creation of T-MATS Propulsion System Models from NPSS data," *50th AIAA/ASME/SAE/ASEE Jt. Propuls. Conf.*, no. November, 2014.

[83] Numerical Propulsion System Simulation Consortium, "NPSS User Guide," 2012.

[84] V. Andreoli, S. Lavagnoli, G. Paniagua, and V. Fernandez Villace, "Robust model of a transient wind tunnel for off-design aerothermal testing of turbomachinery," *Meas. J. Int. Meas. Confed.*, vol. 82, pp. 323–333, 2016.

[85] C. De Maesschalck, S. Lavagnoli, and G. Paniagua, "Integration of CFD to Design Experiments for Enhanced Spatial and Temporal Discretization," in *Volume 6: Ceramics; Controls, Diagnostics and Instrumentation; Education; Manufacturing Materials and Metallurgy*, 2017, p. V006T05A032.

[86] V. Andreoli, D. G. Cuadrado, and G. Paniagua, "Prediction of the turbine tip convective heat flux using discrete green's functions," *J. Heat Transfer*, vol. 140, no. 7, 2018.

[87] S. Lavagnoli, C. De Maesschalck, and G. Paniagua, “Uncertainty analysis of adiabatic wall temperature measurements in turbine experiments,” *Appl. Therm. Eng.*, vol. 82, pp. 170–181, May 2015.

[88] C. De Maesschalck, S. Lavagnoli, G. Paniagua, T. Verstraete, R. Olive, and P. Picot, “Heterogeneous Optimization Strategies for Carved and Squealer-Like Turbine Blade Tips,” *Vol. 5B Heat Transf.*, p. V05BT13A012, 2015.

VITA

Valeria Andreoli earned a Bachelor Degree in Aerospace Engineering from Politecnico di Milano in 2010. For her Bachelor Thesis, Valeria completed an internship at AgustaWestland in Cascina Costa di Samarate (Varese, Italy). Her work focused on the design of a centrifugal fan for the cooling of a helicopter transmission system. She furthered her studies with a Master Degree in Aerospace Engineering from Politecnico di Milano. Her thesis work was carried out at the von Karman Institute for Fluid Dynamics at Rhode-Saint-Genèse in Belgium. Afterward, she received a Research Master at the von Karman Institute for Fluid Dynamics in the department of Turbomachinery and Propulsion. For her research work, she investigated turbine tip flows numerically, and work on the preparation of the experiments to carry out experimental research on tip flows in a blowdown rotating turbine rig. For her work, she gained the "Excellence in Numerical

She began her graduate studies at Purdue University in the School of Mechanical Engineering, where she works as Research Assistant at Zucrow Laboratories. Her first year of Ph.D. was partially funded but the American Association of International Women. During her Ph.D., she spent one summer employed as Turbine Analyst by Belcan TechServices with an assignment at Rolls-Royce Corporation, in Indianapolis. She received several awards for her work, including multiple ASME travel grants, the "Purdue College of Engineering Outstanding Research Award."

PUBLICATIONS

Patents

i. Bloxham, M. J., Ebacher, J. V., Paniagua , G., Andreoli, V., De Maesschalck, C. G. M., Braun,J., " Tip Structure for a Turbine Blade with Pressure Side and Suction Side Rails", United States Patent Application 20180245469.

ii. Paniagua, G., Cuadrado, D.G., Braun, J., Andreoli, V., Liu, Z., " Directional Probe for High Temperature Flows", Provisional Application; 68020-01; 62/571774.

Journal Articles

i. Andreoli, V., Cuadrado, D.G. and Paniagua, G., "Prediction of the Turbine Tip Convective Heat Flux Using Discrete Green's Functions", Journal of Heat Transfer, 140(7), p.071703.

ii. Cuadrado, D.G., Lozano, F., Andreoli, V. and Paniagua, G., "Engine-Scalable Rotor Casing Convective Heat Flux Evaluation Using Inverse Heat Transfer Methods", J. Eng. Gas Turbines Power, 2018.

iii. Paniagua, G., Cuadrado, D., Saavedra, J., Andreoli, V., Meyer, T., Solano J.P., Herrero R., Meyer, S. and Lawrence, D., "Design of the Purdue Experimental Turbine Aerothermal Laboratory for Optical and Surface Aero-Thermal Measurements", J. Eng. Gas Turbines Power, 141(1), 012601, 2019.

iv. Andreoli, V., Lavagnoli, S., Paniagua, G., Fernandez Villace, V., "Robust Model of a Transient Wind Tunnel for Off-Design Aerothermal Testing of Turbomachinery", Measurement, Volume 82, March 2016, p. 323-333.

v. Andreoli, V., Braun, J., Paniagua, G., De Maesschalck, C., Bloxham, M., Cummings, W. and Langford, L., "Aerothermal Optimization of Fully Cooled Turbine Blade Tips", Recommended for Journal of Turbomachinery.

vi. Lavagnoli, S., C. De Maesschalck, and V. Andreoli. "Design considerations for tip clearance control and measurement on a turbine rainbow rotor with multiple blade tip geometries." Journal of Engineering for Gas Turbines and Power 139, no. 4 (2017): 042603.

Conference Papers

i. Cis De Maesschalck, C., Andreoli, V., Paniagua, G., Gillen, T., Barker, B., “Aerothermal Optimization of Turbine Squealer Tip Geometries With Arbitrary Cooling Injection“, ASME Turbo Expo 2019: Turbomachinery Technical Conference and Exposition, American Society of Mechanical Engineers (*in progress*)

ii. Wallace, A., Johnson, D., Cuadrado, D. G., Aye-Addo, N., Andreoli, V., Bhatnagar, L., Lozano, F., Fisher, J., Saavedra, J., Paniagua, G., Meyer, T., Clemens, E., Stults, B., White, T., “Purdue Small Turbine Aerothermal Research Rig (STARR)”, 55th AIAA/ASME/SAE/ASEE Joint Propulsion Conference and Exhibit, 2019 (*in progress*)

iii. Athmanathan, V., Fisher, J., Ayers, Z., Cuadrado, D., G., Andreoli, V., Braun, J., Meyer, T., Paniagua, G., Fugger, C., Roy, S., “Turbine-integrated High-pressure Optical RDE (THOR) for injection and detonation dynamics assessment”, 55th AIAA/ASME/SAE/ASEE Joint Propulsion Conference and Exhibit, 2019 (*in progress*)

iv. Aye-Addo, N., Andreoli, V., Long, N., Paniagua, G., “CFD-based design of optical diagnostic techniques for turbine vane testing”, 55th AIAA/ASME/SAE/ASEE Joint Propulsion Conference and Exhibit, 2019 (*in progress*)

v. Bhatnagar, L., Braun J., Andreoli V., Gonzalez Cuadrado D., Liu Z., Paniagua G., “Development in high frequency directional probes for high temperature applications”, XXIV Biennial Symposium on Measuring Techniques in Turbomachinery, 2018, Prague, Czech Republic.

vi. Andreoli, V., Braun, J., Paniagua, G., De Maesschalck, C., Bloxham, M., Cummings, W. and Langford, L., “Aerothermal Optimization of Fully Cooled Turbine Blade Tips”, ASME Turbo Expo 2018: Turbomachinery Technical Conference and Exposition (pp. V05CT22A001-V05CT22A001). American Society of Mechanical Engineers.

vii. Cuadrado, D.G., Lozano, F., Andreoli, V. and Paniagua, G., “Engine-Scalable Rotor Casing Convective Heat Flux Evaluation Using Inverse Heat Transfer Methods”, In ASME Turbo Expo 2018: Turbomachinery Technical Conference and Exposition, American Society of Mechanical Engineers.

viii. Vyas, Udit, Valeria Andreoli, Guillermo Paniagua, “Effect of transonic inlet design on the performance of a micro-turbojet engine”, In 2018 AIAA Aerospace Sciences Meeting, p. 1624. 2018.

ix. Cuadrado, D. G., Saavedra, J., Andreoli, V., Paniagua, G., “Experimental Calibration of a High Speed Blowdown Tunnel”, International Society for Air Breathing Engines 2017, Manchester, United Kingdom.

x. Andreoli, V., Cuadrado, D. G., Paniagua, G., “Prediction of the Turbine Tip Convective Heat Flux Using Discrete Green Functions”, 2017 ASME TurboExpo Conference, GT2017-64080.

xi. Paniagua, G., Cuadrado D. G., Saavedra, J., Andreoli, V., Meyer, T., Meyer, S., Lawrence, D., “Design of the Purdue Experimental Turbine Aerothermal Laboratory for Optical and Surface Aerothermal Measurements”, 2016 ASME TurboExpo Conference, GT2016-58101.

xii. Lavagnoli, S., De Maesschalck C., Andreoli, V., “Design Considerations for Tip Clearance Control and Measurement on a Turbine Rainbow Rotor with Multiple Blade Tip Geometries”, 2016 ASME TurboExpo Conference, GT2016-56544.

xiii. Lavagnoli, S., De Maesschalck C., Andreoli, V., Paniagua, G., G. Cuadrado,D., “ Wind Tunnel Testing of Turbine Blade Tip Flows”, 54th AIAA Aerospace Sciences Meeting, Proceedings of the 54th AIAA Aerospace Sciences Meeting. San Diego, California, USA.

xiv. Lavagnoli, S., Andreoli, V., Paniagua, G., Fernandez Villace, V., “High-Fidelity Model of a Transient Turbine Facility for Off-Design Aerothermal Testing”, Proceedings of the AIAA Science and Technology Forum and Exposition, AIAA-2014-1309, National Harbor, USA, Jan 2014.